



University of Kentucky
UKnowledge

Theses and Dissertations--Physics and
Astronomy

Physics and Astronomy

2012

DECIPHERING THE ARRANGEMENT OF DUST IN THE CLUMPY TORI OF ACTIVE GALACTIC NUCLEI

Grant David Thompson
University of Kentucky, grant.thompson@uky.edu

[Right click to open a feedback form in a new tab to let us know how this document benefits you.](#)

Recommended Citation

Thompson, Grant David, "DECIPHERING THE ARRANGEMENT OF DUST IN THE CLUMPY TORI OF ACTIVE GALACTIC NUCLEI" (2012). *Theses and Dissertations--Physics and Astronomy*. 4.
https://uknowledge.uky.edu/physastron_etds/4

This Doctoral Dissertation is brought to you for free and open access by the Physics and Astronomy at UKnowledge. It has been accepted for inclusion in Theses and Dissertations--Physics and Astronomy by an authorized administrator of UKnowledge. For more information, please contact UKnowledge@lsv.uky.edu.

STUDENT AGREEMENT:

I represent that my thesis or dissertation and abstract are my original work. Proper attribution has been given to all outside sources. I understand that I am solely responsible for obtaining any needed copyright permissions. I have obtained and attached hereto needed written permission statements(s) from the owner(s) of each third-party copyrighted matter to be included in my work, allowing electronic distribution (if such use is not permitted by the fair use doctrine).

I hereby grant to The University of Kentucky and its agents the non-exclusive license to archive and make accessible my work in whole or in part in all forms of media, now or hereafter known. I agree that the document mentioned above may be made available immediately for worldwide access unless a preapproved embargo applies.

I retain all other ownership rights to the copyright of my work. I also retain the right to use in future works (such as articles or books) all or part of my work. I understand that I am free to register the copyright to my work.

REVIEW, APPROVAL AND ACCEPTANCE

The document mentioned above has been reviewed and accepted by the student's advisor, on behalf of the advisory committee, and by the Director of Graduate Studies (DGS), on behalf of the program; we verify that this is the final, approved version of the student's dissertation including all changes required by the advisory committee. The undersigned agree to abide by the statements above.

Grant David Thompson, Student

Dr. Moshe Elitzur, Major Professor

Dr. Tim Gorringer, Director of Graduate Studies

DECIPHERING THE ARRANGEMENT OF DUST IN THE CLUMPY TORI OF
ACTIVE GALACTIC NUCLEI

DISSERTATION

A dissertation submitted in partial
fulfillment of the requirements for
the degree of Doctor of Philosophy
in the College of Arts and Sciences
at the University of Kentucky

By
Grant David Thompson
Lexington, Kentucky

Director: Moshe Elitzur, Professor of Physics and Astronomy
Lexington, Kentucky 2012

Copyright © Grant David Thompson 2012

ABSTRACT OF DISSERTATION

DECIPHERING THE ARRANGEMENT OF DUST IN THE CLUMPY TORI OF ACTIVE GALACTIC NUCLEI

In the framework of active galactic nuclei (AGNs), a galaxy's supermassive black hole is surrounded by a dusty torus whose clumpy configuration allows for either direct or obscured views toward the central engine. Viewing AGNs from different angles gives rise to a variety of AGN classifications; for example, the generic Type 1 AGN class requires the detection of optically broad emission lines, which arise from quickly moving material within the torus, whereas Type 2 AGNs lack these observations. While these viewing angles are not directly observable, synthetic torus models generated with CLUMPY provide a means to determine them along with other parameters that describe the nature and characteristics of the torus in general. Employing CLUMPY models with mid-infrared spectroscopic observations of a large sample of both Type 1 and Type 2 AGNs allows us to acquire a further understanding of the clumpy torus structure and its viewing angles.

KEYWORDS: Active Galactic Nuclei, Galaxies, Seyfert, Infrared, Radiative Transfer

Author: Grant David Thompson

Date: August 1, 2012

DECIPHERING THE ARRANGEMENT OF DUST IN THE CLUMPY TORI OF
ACTIVE GALACTIC NUCLEI

By

Grant David Thompson

Moshe Elitzur

Director of Dissertation

Tim Gorringe

Director of Graduate Studies

August 1, 2012

Date

I dedicate this dissertation to my loving and supportive family.

ACKNOWLEDGMENTS

I extend my appreciation to all of those who have influenced my academic achievements. I thank Professor Moshe Elitzur for welcoming me into his research group with open arms. Your graciousness in providing me the opportunity, a multitude of suggestions that greatly improved the research, and guidance throughout the process will always be remembered and appreciated; I am truly thankful. I must also thank Dr. Nancy Levenson for allowing me to conduct research under her supervision, from which a wealth a knowledge was gained and unforgettable situations experienced. I too must thank my committee members Professors Thomas Troland and John P. Selegue for continued support and more than helpful suggestions. I would additionally like to thank research group members Drs. Robert Nikutta and Frank Heymann who always offered most valuable insight, suggestions, and explanations.

A special thanks goes to my friends and classmates Ben, Emily, Erin, and Gretchen who have always been a source of encouragement and support. Finally, I extend a heartfelt thank you to my family who has always supported and helped me to achieve my goals. Kristen, I am so thankful we got to go on this journey together, and I truly appreciate everything you have done for me throughout the entire process. Thank you Mom and Dad for raising me in a loving and providing home and for showing me how hard work and determination pay off. To my siblings Chad, Inga, and Tony, you all highlighted the path I have followed; thank you for your directions and guidance. Thank you Grandma Doris for always being there, supporting me in every aspect of my life. To Grandpa Vernie, Grandpa Frank, and Grandma Mitchell, thank you for being here with me and for always believing in me. Thank you all.

TABLE OF CONTENTS

Acknowledgments	iii
Table of Contents	iv
List of Tables	vii
List of Figures	viii
Chapter 1 Introduction	1
1.1 Active Galactic Nuclei	1
1.2 Structure	2
1.3 AGN Classifications	3
1.3.1 Quasars and QSOs	4
1.3.2 Seyfert Galaxies	4
1.4 Project Overview	5
Chapter 2 Radiative Transfer and Polarization	6
2.1 Equation of Radiative Transfer	6
2.2 Constant Temperature Medium	8
2.3 Emission of a Variable Temperature Medium	10
2.4 Polarization	11
2.4.1 Types of Polarization	11
2.4.2 Methods of Producing Polarization	13
Chapter 3 Astronomical Dust and Its Properties	15
3.1 Dust Formation	15
3.2 Grain Size and Composition	16
3.3 Dust Extinction	17
3.4 Silicate Dust	18
3.5 Polycyclic Aromatic Hydrocarbons	20
Chapter 4 CLUMPY Models	22
4.1 CLUMPY Torus Parameters	22
4.2 General Background	23
4.3 CLUMPY Model Fitting	25
4.4 Bayesian Analysis	27
Chapter 5 Previous Studies Concerning AGN	29
5.1 Smooth Torus	29
5.2 Clumpy Torus	30
5.3 Torus Models and Observations	31

Chapter 6	Dust Emission from Unobscured Active Galactic Nuclei	34
6.1	Introduction	34
6.2	Sample and Data Reduction	35
6.3	Results	36
6.3.1	Broadband Spectral Characteristics	36
6.3.2	Type 1 AGN Silicate Emission	41
6.3.3	AGN-Star Formation Connection	44
6.4	Dust Geometry from Silicate Features	47
6.5	Conclusions	61
Chapter 7	Determining the AGN Viewing Angle with Spectropolarimetry and MIR Emission	64
7.1	Spectropolarimetry	64
7.1.1	Spectropolarimetry in the Realm of AGNs	64
7.1.2	Type 2 Scattering Geometry	65
7.1.3	Type 1 Scattering Geometry	66
7.1.4	Interpretation of the Different Scattering Regions	67
7.1.5	Polarization Properties	68
7.1.6	Polarization Classes	71
7.1.7	Conclusions	72
7.2	Utilizing the Mid-Infrared	74
7.2.1	Sample and Data Reduction	75
7.2.2	Star Formation and Emission Line Removal	77
7.3	Constraining the MIR Sample with Ground-Based Observations	79
7.3.1	Ground-Based Sample and Data Reduction	80
7.3.2	Analysis of Ground-based Observations: 2-D Spectrum	81
7.3.3	Spectral Extractions	85
7.3.4	<i>Spitzer</i> vs <i>Gemini</i> Observations	86
7.3.5	Conclusions	92
7.4	CLUMPY Model Fitting of MIR Emission	94
7.4.1	Seyfert 1 Analysis	96
7.4.2	Seyfert 2 Analysis	104
7.5	Comparing the Analyses of Mid-Infrared Emission and Polarization	108
7.5.1	Seyfert 1 Analysis	109
7.5.2	Seyfert 2 Analysis	117
7.5.3	Overall Sample Analysis	121
Chapter 8	Integrating Previous Two Studies	127
8.1	Feature-Feature Diagram Revisited	127
8.2	CLUMPY fits of Seyferts and Quasars	128
Chapter 9	Summary and Outlook	131

Appendix A: CLUMPY Torus Model Fittings	134
A.1 Seyfert 1 Source Summaries	134
A.2 Seyfert 2 Source Summaries	179
A.3 Poorly Fit Sources	197
Bibliography	207
VITA	213

LIST OF TABLES

4.1	Parameters of the CLUMPY Torus Models.	23
6.1	Observations and Galaxy Data	37
6.2	Average Type 1 AGN Spectra	39
6.3	Spectral Measurements	43
7.1	Polarization Classes.	73
7.2	Observations and Galaxy Data for Seyfert 1s	76
7.3	Observations and Galaxy Data for Ground-Based Sources	80
7.4	Fractional Contribution of Total Flux per Component in Seyfert 1s	101
7.5	Observations and Galaxy Data for Seyfert 2s	106
7.6	Fractional Contribution of Total Flux per Component in Seyfert 2s	107
7.7a	Fitted Torus Model Parameters for Seyfert 1s	115
7.7b	Fitted Torus Model Parameters for Seyfert 1s (cont.)	116
7.8	Fitted Torus Model Parameters for Seyfert 2s	120
7.9	Measurements of Seyfert 1s	125
7.10	Measurements of Seyfert 2s	126

LIST OF FIGURES

1.1	Schematic of AGN	3
2.1	Slab Geometry of Radiative Transfer	7
2.2	Dust Cross Section	9
2.3	Electromagnetic Wave Components	12
2.4	Types of Polarization	12
3.1	Silicate Dust Cross Section	20
4.1	Schematic of Clumpy Torus	24
6.1	Average Seyfert 1 Spectrum	38
6.2	Average Quasar Spectrum	40
6.3	Continuum Fitting Technique	42
6.4	Silicate Strengths	45
6.5	Neon - 5 μ m Luminosity Relation	46
6.6	Feature-Feature Diagram	48
6.7	CLUMPY Spherical Distributions	53
6.8	Schematic of Clumpy Torus	54
6.9	CLUMPY Torus Models as a Function of Y	56
6.10	CLUMPY Torus Models as a Function of q	57
6.11	CLUMPY Torus Models as a Function of σ	58
6.12	CLUMPY Torus vs Sphere	62
7.1	Polarization Properties	70
7.2	Polarization Classification and Orientation	71
7.3	Star Formation Removal	78
7.4	<i>Spitzer</i> vs <i>Gemini</i> : NGC 2992	82
7.5	2D Spectrum of IC 5063	83
7.6	2D Spectrum of NGC 4388	83
7.7	2D Spectrum of NGC 5506	84
7.8	2D Spectrum of NGC 4151	84
7.9	Spectral Extractions NGC 4151	85
7.10	<i>Spitzer</i> vs <i>Gemini</i> : IC 5063	87
7.11	<i>Spitzer</i> vs <i>Gemini</i> : NGC 1068	88
7.12	<i>Spitzer</i> vs <i>Gemini</i> : NGC 2992	89
7.13	<i>Spitzer</i> vs <i>Gemini</i> : NGC 4388	90
7.14	<i>Spitzer</i> vs <i>Gemini</i> : NGC 5506	91
7.15	<i>Spitzer</i> vs <i>Gemini</i> : NGC 4151	92
7.16	Single- or Double- Component Model	97
7.17	CLUMPY Model Fit Analysis: Mrk 1239	98
7.18	CLUMPY Torus Parameter Distribution for Seyfert 1s and 2s	103

7.19	CLUMPY Model Fit Analysis: NGC7469	111
7.20	'First Class' CLUMPY Torus Parameter Distribution	117
7.21	'Second Class' CLUMPY Torus Parameter Distribution	118
7.22	Luminosity Comparison	123
8.1	Updated Feature-Feature Diagram	129
8.2	Seyfert 1 and Type 1 Quasar CLUMPY Torus Parameter Distributions .	130

Chapter 1

Introduction

A massive collection of galaxies sprawl across the universe. Many share similar properties, and thus classification systems have been amassed. A general discrimination of galaxies describes them as active or quiescent, where active galaxies are those that have higher levels of activity, perhaps orders of magnitude, within them as compared to the quiescent galaxy. Regardless of their activity level, galaxies contain in their centers a supermassive black hole with masses ranging from $M_{BH} \sim 10^6 - 10^{10} M_{\odot}$, where M_{\odot} is the mass of the Sun. Intense energy output emanating from this central core region of the galaxy, collectively referred to as the active galactic nucleus, is the keystone difference between active and quiescent galaxies. In this section, we will introduce the nomenclature of the galaxies in which we are most interested, active galactic nuclei.

1.1 Active Galactic Nuclei

An active galactic nucleus (AGN) is the general term for a galaxy where a significant amount of the emitted energy comes from non-stellar sources within and around the central core region. The centers of galaxies contain supermassive black holes with masses of millions to billions of solar masses. Accretion of vast quantities of matter onto these central black holes converts the gravitational energy of the infalling material into radiative energy, which is eventually released as electromagnetic radiation, or light. This accretion process is responsible for the intense energy output distinguishing active galaxies. These sources are characterized by enormous luminosities coming from compact volumes and radiate over the entire electromagnetic spectrum, from γ -rays to radio waves. AGNs are characterized by luminosities that generally exceed $10^{44} \text{ erg s}^{-1}$; having strong emission lines in the optical spectrum; rapid variation in the luminosity; and a much higher luminosity than a normal galaxy in at least one

of the x-ray, ultraviolet, infrared, or radio spectral regions.

1.2 Structure

It may be illustrative to the reader to refer to Figure 1.1 to understand the discussion of AGN structure in this section. Supermassive black holes are located at the heart of galaxies with masses ranging from $M_{BH} \sim 10^6 - 10^{10} M_{\odot}$. Material falls in toward the black hole forming the accretion disk that could possibly extend outward 0.1 parsecs [1 parsec (pc) = 3.26 light years]. The accretion disk, which is the power supply of the AGN since gravitational energy is converted to radiative energy, is embedded within a mixture of small, hot gas clouds, each a few astronomical units in size. This congregation of clouds, which may be 0.5-1 pc in radius, is orbiting the black hole at high speeds while emitting emission lines. Clouds closer to the accretion disk emit highly ionized emission lines, while those further out yield the lower ionization lines. Since the clouds have rapid random motions, the emission lines observed by an outsider are broadened; for this reason, this region is referred to as the broad line region (BLR).

A warm, geometrically thick dusty torus surrounds the central black hole, accretion disk, and BLR. This torus dust, formed from silicate minerals, emits in the infrared and spectral features at $10 \mu\text{m}$ and $18 \mu\text{m}$ have been detected. The size of the torus is a topic of discussion throughout this paper, though the inner radius is limited by the luminosity of the central source and the dust sublimation temperature, and can be as little as 0.4 pc for a $10^{45} \text{ erg s}^{-1}$ AGN. The torus obscures the BLR for certain lines of sight, namely those which view the torus edge on, and this obscuration gives rise to different source classifications, which will be discussed in the next section. Lastly, the torus is embedded within an assemblage of line-emitting gas clouds. Since these are further from the black hole as compared to the BLR clouds, their velocities are lower, and observed emission lines are therefore narrow. This region is known as the narrow line region (NLR).

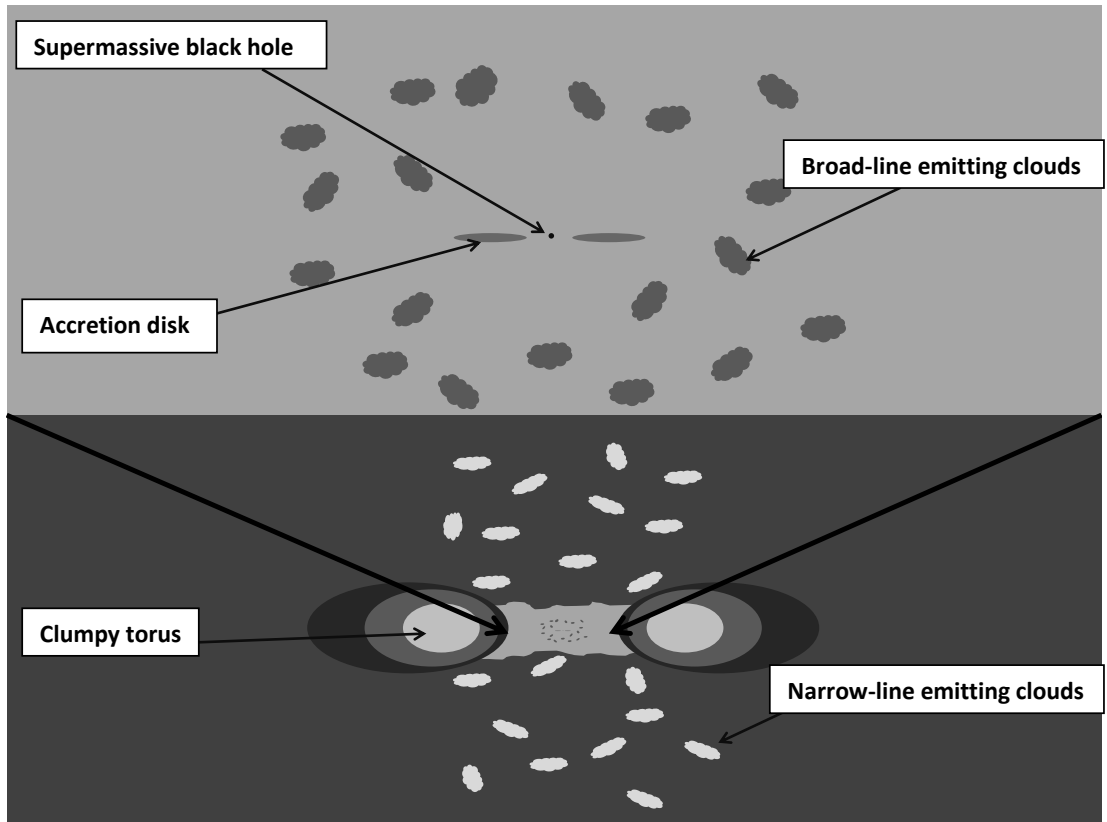


Figure 1.1 In the framework of active galactic nuclei, the central regions of a galaxy contain a supermassive black hole surrounded by an accretion disk (top). The infall of material and the transfer of gravitational energy into radiation produces the intense luminosities of the objects. Outside of the accretion disk is a region of high velocity clouds (BLR), that when observed emit optical broad-lines. Expanding our view (bottom) shows that the BLR is encased by a geometrically and optically thick, dusty torus, which inhibits view of the BLR region from angles along the equator of the system. Slower velocity, narrow-line emitting clouds are positioned in the polar regions.

1.3 AGN Classifications

A multitude of AGN classes has been defined based on both inherent physical differences and external observational factors. The classifications can be organized according to differences in spectra, variability, and polarization properties, but observational parameters, such as the orientation of the source to the observer, can often lead to class assignments. Though there is a tangle of classifications, in this section we

will emphasize two classes that will be discussed throughout this work, quasars and Seyfert galaxies.

1.3.1 Quasars and QSOs

Quasars form the most luminous class of AGNs. They are very distant (800 million – 13 billion light years) compact objects whose optical spectrum contains strong emission lines superimposed on a non-thermal continuum and may be the most luminous objects in the universe. These objects are typically 100 times brighter than the most luminous classical galaxies with $L > 10^{47}$ erg s⁻¹ and are associated with very massive black holes, $M_{BH} > 10^9 M_{\odot}$, accreting vast amounts of material. Due to their distance, quasars appeared as spatially unresolved sources due to the extreme luminosities of their nuclei compared to that of the host galaxy, and therefore were dubbed quasi-stellar objects, or QSOs. Quasars and QSOs are often treated as synonyms, but QSOs are radio-quiet and quasars are radio-loud.

1.3.2 Seyfert Galaxies

Seyfert galaxies establish a lower luminosity class of AGNs. These are often orders of magnitude less luminous than quasars with luminosities near $L \sim 10^{45}$ erg s⁻¹, and therefore require massive black holes, $M_{BH} \sim 10^7 - 10^8 M_{\odot}$. Seeing that the spectra of Seyfert galaxies and quasars are similar, it is believed that there may be a continuous progression in luminosity and spectral properties between the two classes. The luminosity difference is the primary distinction between Seyfert galaxies and quasars since the observational classification depends on whether the host galaxy is detectable against the bright central nucleus. The optical luminosity of a Seyfert galaxy's nucleus is comparable to that of the host galaxy, whereas the nuclear luminosity of a quasar overwhelms that of the entire galaxy.

Most Seyfert galaxies are spirals and can be subdivided into two classes based on optical emission lines. Seyfert 1 galaxies have both broad and narrow emission lines in their optical spectra, and Seyfert 2 galaxies show only narrow line emission. The broad lines, with line widths corresponding to velocities up to 10,000 km s⁻¹, are

emitted by clouds in the broad line region, and the narrow lines with line widths up to 1000 km s^{-1} originate from the narrow line region. Sub-classes of Seyferts, such as class 1.5 or 1.8, are distinguished on the basis of the relative strengths of the broad and narrow components of the $\text{H}\beta$ line. Furthermore, narrow-line Seyfert 1 galaxies are a subclass of Seyfert 1s and have their broad emission lines less than 2000 km s^{-1} (as compared to the $10,000 \text{ km s}^{-1}$ for typical Seyfert 1s), but the ratio of the strengths of the $[\text{O III}] 500.7$ and $\text{H I } 486.1$ spectral lines is lower than in Seyfert 2s.

1.4 Project Overview

In this dissertation we discuss the arrangement of dust within the tori of AGNs. To fully understand the process of determining this arrangement, we must first cover the basics of radiative transfer and light propagation in Chapter 2. Since this dissertation is based on dust, we describe the dust and its properties in Chapter 3 and integrate this into the models we use to describe the dust distribution (Chapter 4). Previous studies focusing on the tori of AGNs are examined in Chapter 5, and we reach the first results of the study in Chapter 6, namely, that the torus has a clumpy geometry. Chapters 7 and 8 consist of fitting clumpy torus model SEDs to MIR observations, and we find from these studies that the tori are extremely compact. Finally we summarize our results and in the Appendix we present several figures.

Chapter 2

Radiative Transfer and Polarization

Astronomy is a subject that is based entirely on the study of electromagnetic radiation and its propagation. If light cannot be collected, then observations of even the closest stars, let alone distant galaxies, are meaningless. On Earth, when humans observe the light from the Sun, we realize that something is happening as it is not always the same; the Sun appears yellow overhead yet red or orange in the evenings, and what about the differences between clear and cloudy days? These observed changes are due to interactions of the medium through which light is traveling, and to understand how light changes as it propagates, we examine in this chapter the basics of radiative transfer and polarization.

2.1 Equation of Radiative Transfer

For this discussion, we neglect scattering and assume only absorption and emission affect the intensity of the radiation. Let us consider a beam of radiation with intensity I_λ entering an assemblage of material, where s is the pathlength in the direction of propagation. As radiation propagates through a medium, the intensity of light changes according to the equation of radiative transfer

$$\frac{dI_\lambda}{ds} = j_\lambda - \kappa_\lambda I_\lambda, \quad (2.1)$$

where the first term concerns emission and the second term deals with the absorption. j_λ and κ_λ are respectively the emission and absorption coefficient at wavelength λ , where the former is a measure of emission per unit volume and the latter is absorption per unit length. Both absorption and emission processes occur within the medium such that the emergent radiation is different from the incident radiation (See Figure 2.1).

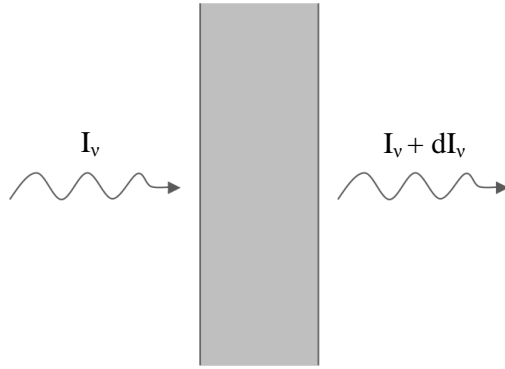


Figure 2.1 Incident radiation I_λ falls upon obscuring material in a slab geometry, and absorption and emission processes within the medium result in emergent intensity $I_\lambda + dI_\lambda$.

To measure how opaque a medium is compared to the radiation propagating through it, we introduce optical depth τ_λ which describes how much absorption occurs over a pathlength s :

$$d\tau_\lambda \equiv \kappa_\lambda ds. \quad (2.2)$$

Furthermore, we denote the ratio of the emission and absorption coefficients by the source function S_λ , as this represents the source of radiation for the material:

$$S_\lambda \equiv \frac{j_\lambda}{\kappa_\lambda}. \quad (2.3)$$

We rewrite the equation of radiative transfer in terms of τ_λ and S_λ as

$$\frac{dI_\lambda}{d\tau_\lambda} = S_\lambda - I_\lambda, \quad (2.4)$$

and integrating will result in the formal solution of the equation of radiative transfer:

$$I_\lambda(\tau_\lambda) = I_\lambda(0)e^{-\tau_\lambda} + \int_0^{\tau_\lambda} e^{\tau_\lambda - \tau'} S_\lambda d\tau'. \quad (2.5)$$

This solution has a simple physical interpretation: the intensity I_λ at optical depth τ_λ is just the initial intensity $I_\lambda(0)$ attenuated by a factor $e^{-\tau_\lambda}$ in the medium, plus the emission in the medium, represented by the second term.

2.2 Constant Temperature Medium

When the medium is in equilibrium, the emitted and absorbed energies are equal such that $dI_\lambda/d\tau_\lambda = 0$ and

$$I_\lambda = \frac{j_\lambda}{\kappa_\lambda} = S_\lambda. \quad (2.6)$$

Considering a dusty medium, the source function shows terms for both scattering and emission. Denoting $\omega_\lambda = \frac{\kappa_{S\lambda}}{\kappa_\lambda}$, where $\kappa_\lambda = \kappa_{A\lambda} + \kappa_{S\lambda}$ and $\kappa_{A\lambda}$ and $\kappa_{S\lambda}$ are respectively the absorption and scattering extinction coefficients, B_λ is the Planck function, and $g(\Omega', \Omega)$ is the angular phase function for coherent scattering from direction Ω' to Ω (Ivezić & Elitzur, 1997, and references therein), the dust source function is written as:

$$S_\lambda = (1 - \omega_\lambda)B_\lambda(T) + \omega_\lambda \int I_\lambda(\Omega')g(\Omega', \Omega) \frac{d\Omega'}{4\pi}. \quad (2.7)$$

Temporarily referring to the context of AGNs, mid-infrared (MIR) observations of obscuring tori (See Section 1.2.) led to modeling the emission by spherical dust grains with size distributions from Mathis et al. (1977) and whose composition has a standard Galactic mix of 53% silicates and 47% graphite (See Chapter 3.). Figure 2.2 shows the total, absorption, and scattering cross sections for the above dust composition using the optical dust properties of Ossenkopf et al. (1992) and Draine (2003a,b) for the silicates and graphite, respectively, scaled to the cross section at $0.55 \mu\text{m}$. The dust is responsible for the underlying continuum as well as the prominent spectral features at 10 and $18 \mu\text{m}$, which is attributed to the silicate dust, and Figure 2.2 clearly shows that we can neglect the effect of scattering beyond 1 or $2 \mu\text{m}$. As we progress through the remainder of this chapter, we consider only the dominating emission term in the source function, neglecting scattering.

Within the context of thermodynamic equilibrium, the radiation of the medium is blackbody radiation, and the source function obeys Kirchhoff's law and is given by Planck's law:

$$S_\lambda = B_\lambda(T) = \frac{2hc^2}{\lambda^5} \frac{1}{e^{hc/\lambda kT} - 1}. \quad (2.8)$$

We can finally describe the intensity of a constant temperature medium by

$$I_\lambda(\tau_\lambda) = I_\lambda(0)e^{-\tau_\lambda} + B_\lambda(T)(1 - e^{-\tau_\lambda}). \quad (2.9)$$

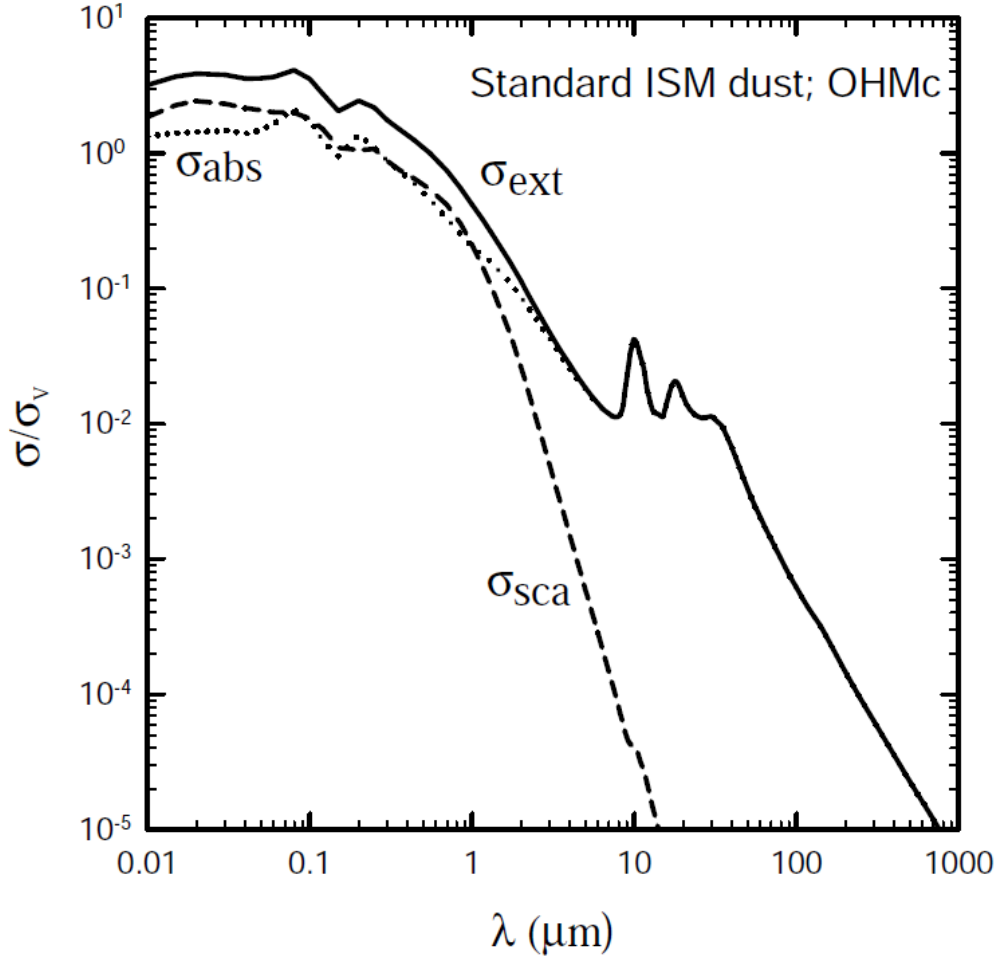


Figure 2.2 Total (solid), absorption (dotted), and scattering (dashed) cross sections for a dust composed of 53% silicates and 47% graphite. Scattering is negligible at wavelengths beyond 1 or 2 μm . The dust is responsible for both the underlying continuum and the prominent spectral features at 10 and 18 μm , which are attributable to the silicates.

If we ignore the incident radiation and concentrate on the emission from the medium, we must consider two limiting cases, when the region is optically thin ($\tau_\lambda \ll 1$) or when it is optically thick ($\tau_\lambda \gg 1$). When $\tau_\lambda \ll 1$, the two leading terms of the exponential expansion dominate, and the emergent intensity is a product of a blackbody and optical depth. Equation 2.9 then becomes

$$I_\lambda(\tau_\lambda) = B_\lambda(T)\tau_\lambda. \quad (\tau_\lambda \ll 1) \quad (2.10)$$

When the cloud is optically thick, the intensity goes as

$$I_{\lambda}(\tau_{\lambda}) = B_{\lambda}(T). \quad (\tau_{\lambda} \gg 1) \quad (2.11)$$

The emission and absorption processes within the cloud are in equilibrium, and the intensity emerging from the cloud would be that of a blackbody. Therefore a single-temperature region can never produce a dust feature, either in emission or absorption.

2.3 Emission of a Variable Temperature Medium

To describe the emission of a dusty region with temperature stratification requires numerical calculations because both the source function and the intensity must be solved for simultaneously. However, since the emission of a variable temperature cloud is an important concept – and one which is realistic –, it must be considered.

We saw in the last section that an optically-thick, uniform temperature dust will never produce an emission or absorption feature; the intensity goes as a Planck function lacking characteristics of the dust. A temperature gradient is essential for an absorption feature, with deep absorption requiring a dust geometry conducive to large gradients. If we consider a cloud illuminated from an outside light source whose dimension is much smaller than the distance to the source, then the incident heating flux across the cloud is constant. The temperature is uniform throughout this cloud if radiative transfer effects are ignored. However, if the dust is arranged in a geometrically thick shell such that the light source is in the center, a temperature gradient exists because of spatial dilution of the flux with radial distance (i.e. $F = L/4\pi D^2$, where L is the luminosity of the light source and D is the distance between the source and the observer.)

In the optically thick case, radiative transfer affects both the slab-like and shell geometries similarly; the external radiation is absorbed within a short distance from the illuminated face. This causes a large temperature gradient to exist close to the surface but only moderate gradients deeper in the cloud because the surface layer absorbs the heating radiation, and the propagation to subsequent layers degrades the photons to longer wavelengths. Therefore, in the externally illuminated slab

geometry, absorption depth is limited. However, in the centrally illuminated shell, both spatial dilution of flux and radiative transfer effects cause a deep absorption feature. As radiation propagates from hot regions toward the observer, it passes through cooler regions where where it suffers absorption that cannot be balanced by the emission from the cooler regions. The net effect is that absorption of the dust features sets in.

We will compare in Section 6.4 MIR observations to models of dusty tori and will further find how the dust features behave in regard to their environments.

2.4 Polarization

Light, or electromagnetic radiation, can be represented as a transverse wave consisting of mutually perpendicular, fluctuating electric and magnetic fields. Figure 2.3 shows in the left panel the electric field \mathbf{E} in the XY plane, the magnetic field \mathbf{B} in the XZ plane, and the propagation of the wave in the X direction. For the discussion of polarization, let us only consider the electric field vector (right panel) as it propagates to simplify the viewing representation and since \mathbf{B} acts similarly. Natural light is unpolarized, which means it has no preferred direction for the electric field vector; the waves come in with the vector oriented in a random direction. Polarized light, on the other hand, has a preferred direction for the electric field vector in the wave; \mathbf{E} field oscillates at all times in the plane of polarization.

2.4.1 Types of Polarization

There are three main types of polarization: linear, circular, and elliptical, and are shown in Figure 2.4. Light in the form of a plane wave is linearly polarized. Linearly polarized light is produced by in-phase (their peaks and troughs are in conjunction) waves, and does not require the waves to be oriented in any particular plane. At left in Figure 2.4, two in-phase light waves are superimposed in the XY plane, creating linearly polarized light whose vector sum is in the same plane, or whose \mathbf{E} field has only one spatial orientation. Alternatively, the initial waves can be oriented in

different planes, such as one in the YZ plane and the other in the XY. Provided these are in phase, the resultant light will be linearly polarized with the vector sum at 45° with respect to either plane.

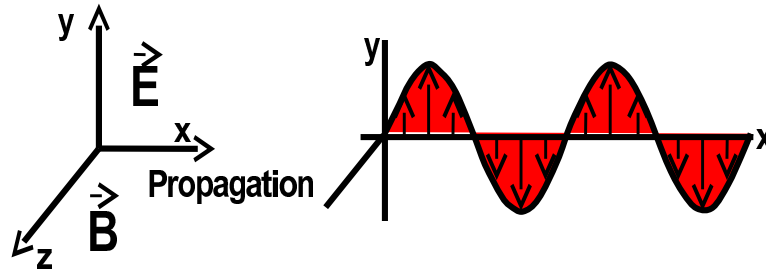


Figure 2.3 Electromagnetic wave composed of \mathbf{E} in the XY plane, \mathbf{B} in the XZ plane, and the direction of propagation in the X direction. Right panel shows only the propagation of \mathbf{E} .

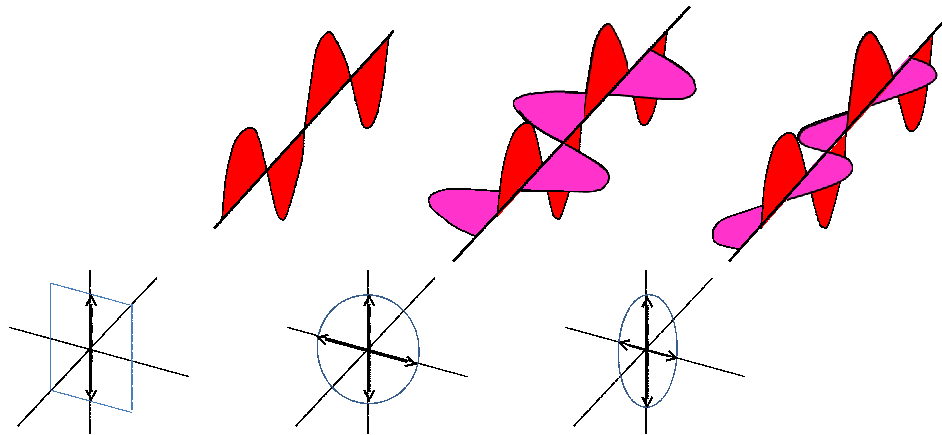


Figure 2.4 Only the \mathbf{E} vector is shown for waves whose combination produce different polarization classes. Linearly polarized (left), circularly polarized (middle), and elliptically polarized light (right) is created by in-phase waves, 90° out-of-phase waves whose amplitudes are equal, and by 90° out-of-phase waves whose amplitudes are not equal, respectively.

Circularly polarized light consists of the superposition of two electromagnetic plane waves (linearly polarized) of equal amplitude but whose phase difference is 90° (middle diagram of Figure 2.4). The phase difference of 90° means that as waves are

propagating in the X direction, at a certain position, the peak of one wave corresponds to the zero-point of the other wave. This causes the final electric field vector to rotate around the origin as the wave propagates. If one were to observe the light as it approached, the constant in magnitude electric field vector \mathbf{E} would appear to be moving in a circle, rotating counterclockwise – right-circularly polarized light.

Elliptically polarized light is the most general case and occurs when light waves of unequal amplitude are out of phase by 90° . Similar to circularly polarized light, \mathbf{E} rotates about the direction of propagation, but since the wave amplitudes are not equal, the vector sum of \mathbf{E} sweeps out an elliptical pattern. See right schematic of Figure 2.4.

2.4.2 Methods of Producing Polarization

Light can be polarized in several ways, three of which are by reflection, absorption, and scattering. Light reflecting off a surface becomes partially polarized with the direction of polarization (that is, the direction in which the \mathbf{E} field vector points) being parallel to the plane of the interface. The degree of polarization depends on the angle of incidence, with complete polarization occurring if the reflected and refracted beams are orthogonal. Consider a light wave striking an interface such that there is a 90° angle between the reflected and refracted beams; this results in the reflected beam being linearly polarized with the direction of polarization parallel to the plane of the interface.

Light can also be polarized by selectively absorbing light with electric field vectors pointing in a certain direction. Polarizers such as polarizing sunglasses are created by dichroic materials that absorb light polarized in one direction but do not absorb the light polarized in the perpendicular direction. If unpolarized light is passed through a polarizer, only half of the initial intensity is transmitted. If linearly polarized light passes through a polarizer, the intensity of the light transmitted is given by Malus' law $I = I_0 \cos^2 \theta$, where θ is the angle between the direction of polarization of the incident light and the polarization axis of the polarizer.

The third method to polarize light, and of which we are interested, is by scat-

tering. Light scattering consists of electrons within atoms absorbing photons and re-radiating a new photon in a random direction. The scattered light is unpolarized if it continues to travel in the same direction as the incident photon. However, if unpolarized light scatters off atoms and molecules, the \mathbf{E} field vibrates in a plane perpendicular to the direction of motion and results in linearly polarized light. Furthermore, if scattering occurs at angles other than 0 or 90°, then the light is partially polarized. If a free electron intercepts a photon of light, Thomson scattering may occur, which like above, results in outgoing linearly polarized light whose \mathbf{E} vector is perpendicular to the plane of incoming radiation. This latter scattering method, namely Thomson scattering by free electrons, is the type of which we are concerned and will discuss further in Section 7.1.1.

Chapter 3

Astronomical Dust and Its Properties

In this chapter we turn our attention to astronomical dust and its properties. While dust may be considered a hindrance on Earth be it the collection on photo frames to massive dust storms, astronomical dust and its effects provide valuable information that aid in our understanding of astrophysical objects. Trumpler (1930) first found that light from distant stars was more dim than expected from using the inverse square law ($F = L/4\pi D^2$), and he concluded that interstellar space must contain cosmic dust particles which attenuate star light. While dust was originally recognized for its obscuring effects, it is becoming increasingly important as a diagnostic with its mid-infrared emission spectrum providing an indication of the physical conditions in which the dust resides.

3.1 Dust Formation

It may be best to understand dust by first looking into its formation. Once the hydrogen fuel in the core of a star is exhausted by nuclear fusing processes, the star continues its evolution to become a giant with an enormous radius. In the Asymptotic Giant Branch phase, the giant star pulsates in size dredging up to the outer envelope newly created heavy elements such as carbon and oxygen from the central regions. As the stellar radius fluctuates, gaseous shells are ejected into the outer atmospheres of the star. As this gas travels outward, carbon and silicates often condense as dust grains as the temperature of the local environment lowers. Infrared measurements show that many cool giant and supergiant stars have dust shells around them, which is observational evidence that this process is occurring. The region surrounding these giant stars are predominantly molecular with H_2 and CO the most common molecular species. The type of dust that is formed around stars is dependent on the star's composition. If the abundance of oxygen is greater than carbon in the outer layers of

the star, then nearly all carbon will be trapped in the CO , leaving the excess oxygen to form other molecules, which will eventually form silicate dust grains. Graphite is formed by a similar process but in regions in which the abundance of carbon is greater than oxygen. The dust only exists in environments where the temperatures are sufficiently cool, $T < 1000$ K, otherwise the outer layers will evaporate and the grain will be destroyed by sublimation.

3.2 Grain Size and Composition

Analyzing the interaction of light with astronomical dust remains the most direct way to study the dust and its properties. Observed effects on dust grains such as ‘reddening’ or extinction (See Section 3.3) give clues to the nature of the particles involved, with possible grain candidates to be carbon solids (graphite, amorphous carbon, and diamonds), silicate particles, or large complex molecular hydrocarbons called polycyclic aromatic hydrocarbons or PAHs. Observations of ultraviolet extinction and optical scattering of dust grains have provided a broad size distribution from sizes as small as $0.01 \mu\text{m}$ to $0.1 \mu\text{m}$ for the silicate and carbon dust grains. The PAHs typically contain only 20-100 carbon atoms, so they are much smaller, but their lattice-like structure makes them extremely stable and durable against temperatures up to 1000 K.

In the context of AGNs, MIR observations have yielded clues to dust composition, and models replicating the dust’s MIR emission utilize dust grain size distributions of Mathis et al. (1977) whose composition has a standard Galactic mix of 53% silicates and 47% graphite. Sirocky et al. (2008) demonstrated that the optical dust properties of the cold, oxygen-rich silicate dust of Ossenkopf et al. (1992) and the graphite properties of Draine (2003a,b) accurately describe observations. Additional details regarding silicate dust is found in Section 3.4.

3.3 Dust Extinction

The most obvious effect of astronomical dust is its extinction of the light emitted from distant objects by scattering and absorption processes. Radiation of wavelengths less than to about the size of the dust grain can be absorbed. The dust is heated by high-energy UV photons emitted by stars or AGNs, absorbing them, and cools by radiating longer, less-energetic infrared photons. Dust also attenuates light by scattering it. In the scattering process, photons are absorbed by atoms within the dust, but the atoms quickly de-excite emitting the same wavelength photon that was initially absorbed but in random directions. Therefore, photons may be redirected by interaction, but their energies remain unchanged. The intensity of the scattered light depends on both the wavelength of the photon and the dust size. When light is scattered by objects much smaller than its wavelength, the intensity of the scattered radiation obeys the Rayleigh scattering law: $I_{scatter} \propto \lambda^{-4}$, which means that more blue light is scattered out of incident light than red. When the wavelength of the light and the dust size are similar, the scattering law becomes $I_{scatter} \propto \lambda^{-1}$, and scattering is independent of wavelength when the grains are much larger than the incident photon's wavelength. It is worth noting that electrons can scatter photons by either Thomson or Compton mechanisms, the former occurring in the low-energy regime and the latter in the highly-energetic 'hard' photon realm.

Astronomers study the reddening or extinction of star light by dust by assuming that we know the intensity of the light as though there was no dust. The reduction in the amount of light from a source shining through dust goes as $I_\lambda = I_\lambda(0)e^{-\tau_\lambda}$ where $I_\lambda(0)$ is the intensity that would be received in the absence of dust along the line of sight, I_λ is the intensity actually received, and τ_λ is the optical depth at the wavelength observed. The extinction is specified by the values of τ_λ in the direction to the object. Characterizing the attenuating effects of dust by extinction as A_λ measured in magnitudes at wavelength λ , we define

$$\frac{A_\lambda}{mag} = 2.5 \log_{10} \left(\frac{F_\lambda(0)}{F_\lambda} \right), \quad (3.1)$$

where F_λ is the observed flux, $F_\lambda(0)$ is the flux that would be observed if the only

attenuation resulted from the inverse square law. This formula is related to optical depth via

$$\frac{A_\lambda}{mag} = 2.5 \log_{10} \left(\frac{F_\lambda(0)}{F_\lambda} \right) = 2.5 \log_{10}(e^{\tau_\lambda}) = 1.086\tau_\lambda. \quad (3.2)$$

Extinction A_λ as a function of wavelength shows a rapid rise in extinction from red to blue, such that light reaching us will be ‘reddened’ owing to greater attenuation of blue light. Astronomers often describe reddening by using the color excess $E(B - V) = A_B - A_V$, which is the difference in extinction between two wavelength filters B and V, which are centered at ~ 4400 nm and 5500 nm respectively. Also the ratio of total to selective extinction, $R_V = A_V/E(B - V)$ compares the extinction and reddening properties of dust grains, both of which are sensitive to grain composition, size, and shape. The diffuse interstellar medium and the Milky Way Galaxy have $R_V \approx 3.1$. Furthermore, the amount of visual extinction along a line of sight is strongly correlated with the total column density of hydrogen, with typical values of $A_V/N(H) = 5.3 \times 10^{-22}$ mag cm², though the ratio depends on both dust grain properties and the dust-to-gas ratio. In the context of AGNs, dust encountered along the line of sight to these distant galaxies can be large, with extinction $A_V = 1000$ for some sources (Ramos Almeida et al., 2011).

3.4 Silicate Dust

Several grain models have been initiated in a quest to replicate the infrared emission of AGNs, many with varying compositions, but also many consisting of carbonaceous grains and amorphous silicates (Sirocky et al., 2008; Draine & Li, 2007). Regardless of model, the regions surrounding AGNs are believed to consist of silicates because silicate minerals generally have strong absorption resonances due to the Si-O stretching mode near 10 μm and an 18 μm feature attributable to the Si-O-Si bending mode in amorphous silicates, features that have been observed in starburst galaxies and AGNs for decades (e.g., Gillett et al., 1975; Rieke & Low, 1975a,b; Kleinmann et al., 1976). These features are generally assigned to silicates because 10 μm emission is observed in the outflows of oxygen-rich stars (which would condense silicate dust)

but not in the outflows of carbon-rich stars (See Section 3.1).

Silicate dust reprocessing dominates the MIR spectra, and it is responsible for the continuum emission as well as the 10 and 18 μm features. The MIR continuum emission depends only weakly on the dust chemistry, but comparison of the two features provides one of the few diagnostics of dust composition. Sirocky et al. (2008) considers the optical properties of three different models of dust chemistry: cool, oxygen-rich silicates typical of the diffuse ISM; warm, oxygen-deficient silicates that may be typical of circumstellar regions; and “astronomical silicate” from Draine (2003a,b), whereas the first two are from Ossenkopf et al. (1992). The models consisted of grains of 53% silicate and 47% graphite, where the optical properties of Draine (2003a,b) were used in the former constituent. The feature strengths depend physically on the mineral composition of the dust, and Sirocky et al. (2008) shows in their comparisons of the total dust cross sections of the three models that the 18 μm feature is relatively stronger in the cold dust of Ossenkopf et al. (1992). Furthermore, this difference is large enough that it accurately describes observations of ultraluminous infrared galaxies (ULIRGs) whereas the models of differing dust chemistries could not.

We have seen in Figure 2.2 and show in Figure 3.1 a zoom-in of the total dust absorption cross section of the Ossenkopf et al. (1992) cool dust that is incorporated into the CLUMPY models of Chapter 4. The cross section as a function of wavelength is plotted in black with the two prominent features at 10 μm and 18 μm standing out. The 10 μm feature is more pronounced than the 18 μm feature with $\tau_{sil,18}/\tau_{sil,10} = 0.49$. To measure the strengths of the features, a spline interpolation of the total cross section is performed at the intervals of 5-7 μm , 14 μm , and 27-31 μm . This fit, in red, represents the featureless dust. In other words, it would be the cross section if silicate dust contained no features in the MIR, and therefore also can be considered as the continuum emission from the dust. Performing a similar spline fit to MIR spectroscopic observations allow us to measure the strengths of the silicate features as

$$S_{Sil} = \ln \frac{F_{obs}(\lambda)}{F_{cont}(\lambda)}, \quad (3.3)$$

where negative values mean the feature is in absorption and positive values convey emission. In the context of AGNs, silicate emission was not universally observed in type 1 galaxies until recently, and type 2s show only weak absorption (See Chapter 6). Since silicate dust absorbs the high-energy photons of the AGN and reprocesses the light to be re-emitted in the infrared, we are able to ascertain from the emission as well as the strengths of the two features the geometry of the dust (See Sections 6.3.2 and 6.4).

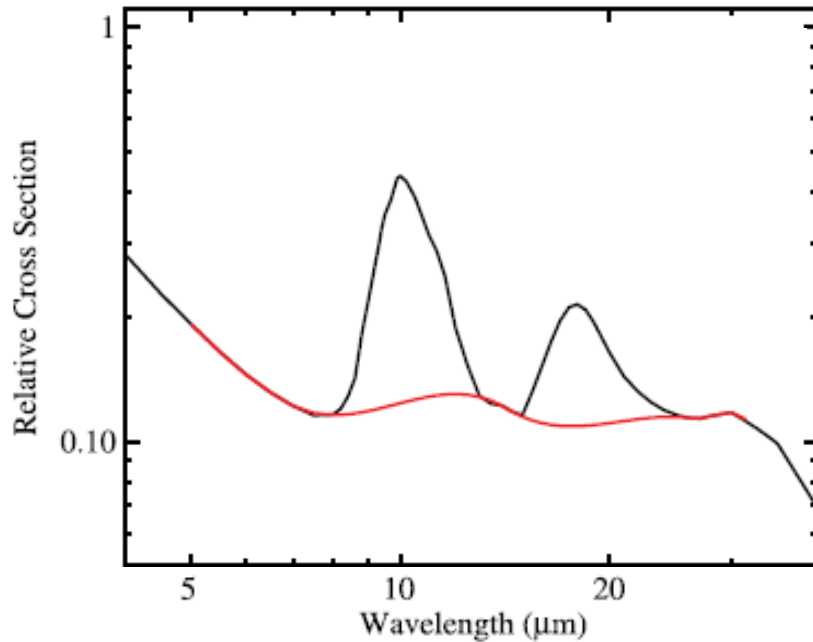


Figure 3.1 Total cross section of the cool, oxygen-rich silicate dust of Ossenkopf et al. (1992) as a function of wavelength (black). A spline interpolation is fit at 5-7 μm , 14 μm , and 27-31 μm intervals (red) and represents the continuum emission from the dust as though the prominent 10 μm and 18 μm features were not present.

3.5 Polycyclic Aromatic Hydrocarbons

The infrared emission spectra of polycyclic aromatic hydrocarbon (PAH) molecules contain broad features at 3.3, 6.2, 7.7, 11.3, and 12.7 μm , all attributable to vibrational transitions. These molecules are planar structures consisting of 20-100 carbon

atoms organized in a lattice-type structure with hydrogen atoms attached at the boundaries. These large molecules are excited by ultraviolet and optical radiation, and then decay to excited vibrational levels which emit photons in the aforementioned bands. The integrated emission from dusty spiral galaxies shows that the PAH emission features can account for as much as 20% of the total infrared luminosity of a star-forming galaxy (Smith et al., 2007). A 17 μm emission complex is correlated with the 6.2, 7.7, and 11.3 μm features, and is thus attributable also to PAHs.

In this dissertation focused on AGNs, we consider PAH emission to be a hindrance because they are attributable to star formation, as are several emission lines that are present in the mid-infrared (Genzel et al., 1998). We examine in Chapter 6.3.3 PAH emission and low-ionization emission lines to evaluate the energetic contribution of star formation, and how it compares to that of AGNs.

Chapter 4

CLUMPY Models

The past decades have seen much progress in the understanding of the properties of the molecular dusty torus. Originally, torus models consisted of smooth density distributions (e.g., Pier & Krolik, 1992; Granato & Danese, 1994; Efstathiou & Rowan-Robinson, 1995) but have since been replaced with more complex clumpy dust distributions (e.g., Nenkova et al., 2002; Hönic et al., 2006, 2008; Nenkova et al., 2008a,b; Schartmann et al., 2008; Hönic & Kishimoto, 2010) since high-resolution observations indicate that the obscuring torus has a clumpy geometry (Jaffe et al., 2004; Tristram et al., 2007; Beckert et al., 2008). The clumpy models reproduce and describe well the near-infrared and mid-infrared emission of AGNs (e.g., Mason et al., 2006, 2009; Nenkova et al., 2008b; Schartmann et al., 2008; Mor et al., 2009; Thompson et al., 2009; Nikutta et al., 2009; Ramos Almeida et al., 2009, 2011; Hönic & Kishimoto, 2010), whereas smooth torus models have difficulty in fitting infrared data of AGNs (Alonso-Herrero et al., 2001, 2003). In our analysis of AGN tori, we use the clumpy torus models of Nenkova et al. (2002, 2008a,b) to describe the distribution of dust in our sample of Seyfert 1s, Seyfert 2s, and quasars.

4.1 CLUMPY Torus Parameters

The clumpy torus is described by six free parameters in the context of the CLUMPY models of Nenkova et al. (2002, 2008a,b). An AGN with bolometric luminosity L_{bol} is surrounded by a torus of dusty clouds, all of which have the same optical depth τ_{avg} , which is defined in the optical V band ($0.55 \mu\text{m}$). The individual clouds are distributed according to Poisson statistics, with an average number of clouds along an equatorial ray N_0 . The radial distribution of the clouds follows a declining power law with index q ($\propto r^{-q}$), from the inner radius of the torus R_d to the outer radius R_o , where we define the radial thickness as $Y = R_o/R_d$. The inner radius of the torus

Table 4.1. Parameters of the CLUMPY Torus Models.

Parameter	Symbol	Interval
Number of clouds along an equatorial ray	N_0	[1,15]
Torus radial thickness	Y	[5,100]
Index of the radial density profile	q	[0,3]
Torus angular width	σ	[15°,70°]
Optical depth per single cloud	τ_{avg}	[10,300]
Viewing angle	i	[0°,90°]

Note. — Torus radial thickness: $Y = R_o/R_d$, where R_o is the outer radius and R_d is the inner radius. The cloud distribution between R_d and R_o is parameterized as r^{-q} .

is set by the the dust sublimation temperature ($T_{sub} \approx 1500K$):

$$R_d \simeq 0.4 \left(\frac{L_{bol}}{10^{45} \text{ergs}^{-1}} \right)^{1/2} \left(\frac{1500K}{T_{sub}} \right)^{2.6} \text{ parsecs.} \quad (4.1)$$

The angular distribution of the clouds is described as a Gaussian with width parameter σ where the boundary is assumed smooth. The torus is viewed from an inclination angle i as measured from the pole, so the average number of clouds along the line of sight is

$$N(i) = N_0 e^{-(90-i)^2/\sigma^2}. \quad (4.2)$$

We show in Figure 4.1 a schematic of the AGN with its model parameters and list in Table 4.1 these parameters and the interval of values considered in the models.

4.2 General Background

The radiative transfer equations (See Section 2.1) are solved for each cloud using the DUSTY code (Ivezić et al., 1999), which performs an exact solution of a slab. The dust grains are spherical with their size distribution according to Mathis et al. (1977). The composition has a standard Galactic mix of 53% silicates and 47% graphite, where the optical properties for graphite are from Draine (2003a,b) and those for silicate are from the Ossenkopf et al. (1992) oxygen-rich cold dust. The CLUMPY models integrate these results of individual clouds into a scheme were

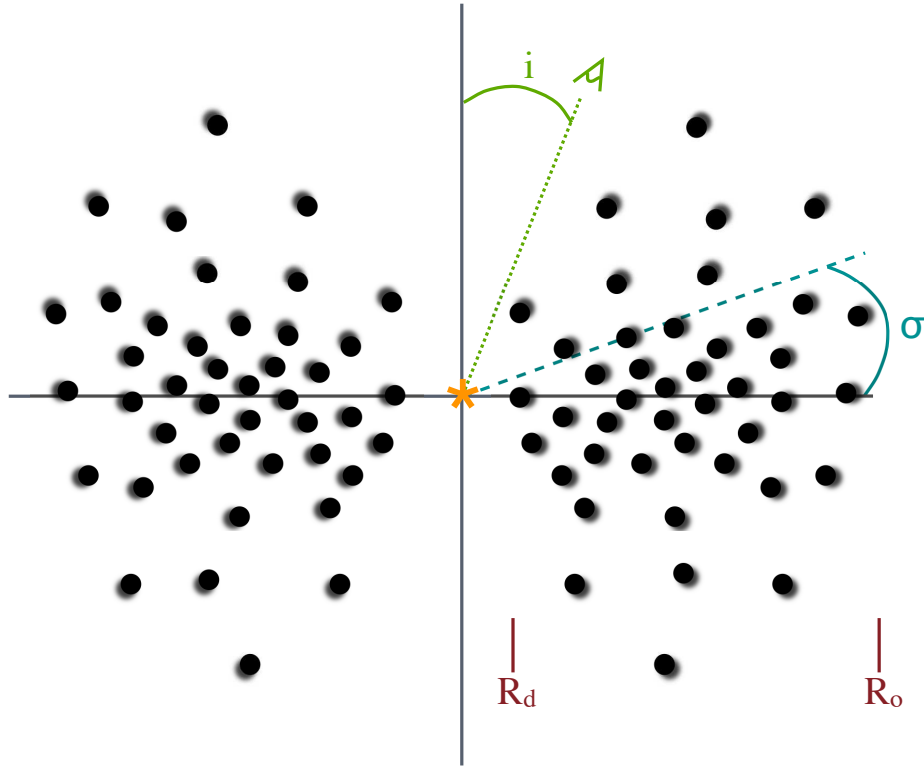


Figure 4.1 Schematic of the clumpy torus. Emission and obscuration of the central engine are functions of viewing angle, i . Dusty clouds are distributed from the dust sublimation radius, R_d , to the outer radius, R_o , according to a radial power law r^{-q} . The average number of clouds along an equatorial ray is N_0 . The angular width of the distribution is σ , with the average number of clouds $N(i) = N_0 \exp(-(90 - i)^2/\sigma^2)$ along a radial ray at angle i measured from the pole.

clouds are distributed in a clumpy toroidal geometry. Determined by their location with respect to the AGN and and observer, clouds may have cool dark sides or hot bright faces, the final emission determined by the viewing geometry, which we will discuss further below. The solutions to the CLUMPY models are dependent on the location of each cloud, its optical depth, and the dust composition.

The total torus emission is calculated by integrating the source function of all clouds convolved with the radiation propagation probability along the torus (Nenkova et al., 2002). That is to say, emission from clouds with a direct view of the torus can be well described, but clouds whose line of sight to the AGN is blocked by

another cloud will be heated only indirectly by the diffuse radiation. The emission received from the torus is thus the contribution of clouds that display a variety of characteristics – bright faces, dark faces, directly illuminated, indirectly illuminated. It is the clumpy geometry that allows a large range of dust temperatures to coexist at the same distance from the AGN, as opposed to the monotonic temperature decline with distance that is characteristic of smooth models. A cloud situated near the AGN has both a bright face, illuminated directly by the central engine, and a dark side facing opposite the AGN. If we assume the clouds are compact, isolated volumes of dust, then very different temperatures occur at approximately the same distance from the AGN. Furthermore, this clumpiness allows for views typically associated with type 2 inclinations (large i) to see emission from the hot faces (See Section 7.5 for the importance of this.).

There is an option to include contribution of the direct AGN emission into the models, as if describing type 1 sources whose view toward the central continuum is unimpeded. This AGN continuum emission is characterized with a piecewise power-law distribution (Nenkova et al., 2008b) and is dominates the emission at $\lambda < 3 \mu\text{m}$. As will be discussed in later chapters, our IR observations that will be modeled cover the wavelength range from 5-30 μm . Since the data provides no handle on as to whether this AGN emission component is needed, we do not employ its use and will no longer discuss this component in the remainder of this work.

4.3 CLUMPY Model Fitting

Implementing the six free parameters used to describe a torus, N_0 , Y , q , σ , τ_{avg} , and i , with a range of possible values for each (See Table 4.1), there exists a CLUMPY model database consisting of 1.2 million models. Each model SED is provided in terms of spectral shape with the total flux of the AGN (F_{AGN}) acting as a scale factor, so if we denote the torus flux as λF_λ , the spectral shape is $\lambda F_\lambda / F_{AGN}$. In the most general sense of fitting, that is comparing MIR spectroscopic observations to these model SEDs, each model is scaled to the data such that an overall goodness-of-fit measure is minimized. The measure we utilize is the reduced chi-squared value,

$$\chi_R^2 = \frac{1}{n_{\text{dof}}} \sum \frac{(\text{data} - \text{model})^2}{(\text{data error})^2} \quad (4.3)$$

where n_{dof} is the degrees of freedom, error is the observational error, and where values closer to zero signify more agreement between the data and model. Therefore, comparing each of the 1.2 million clumpy torus model SEDs to MIR data allows one to determine the best fit model, i.e. that model with the lowest χ_R^2 .

Observational evidence (Mor et al., 2009, See Section 7.4) shows IR emission shortward of the 10 μm silicate feature of which the CLUMPY models cannot account. In their study to explain the MIR emission of type 1 quasars, Mor et al. (2009) used a three-component model and found it necessary to include, as one of the components, a warm blackbody to explain the 2–7 μm emission, which they attributed to hot graphite dust located inside R_d of the torus. The CLUMPY models explain the MIR emission of the torus, where the torus has a sharply defined inner edge due to dust’s sublimation temperature. Physically, it is more likely that the inner boundary of the torus does not end abruptly. The probable scenario includes a progression of larger dust grains of varying species close to the central engine into smaller dust grains with chemistries similar to those found within the torus, until these mix with dust of the torus near the sublimation radius. The different grain sizes and/or species of dust can withstand warmer temperatures within the the dust sublimation radius of the torus. These warm grains such as graphite may explain this ‘hot’ component, and since they are not part of the torus, a component in addition to the torus would be required to fit the MIR emission. Since no multi-dust grain radiative transfer solution exists to include a gradual change in dust chemistry into the torus, we characterize the emission with a hot blackbody. Therefore, we introduce a 2-component (torus and blackbody) model to fit the data, where the blackbody temperature is allowed to vary between 800-1800 K. A description of the 2-component fitting is detailed in Nikutta et al. (2012, in prep.).

4.4 Bayesian Analysis

In regards to fitting model SEDs to observations, the χ_R^2 value of an individual model measures the goodness-of-fit of that model to the data as a whole. However, in this method we do not get any associated estimates of how well the parameter values fit and describe the data. While a single best fit model provides meaningful results, distributions for each free parameter showing the likelihood or probability that certain parameter values reflect the characteristics of the data is most beneficial. That is to say, if only a limited region of parameter space yielded good fits (low χ_R^2 for example), then the parameter is constrained and those values of the parameter signify what is occurring within the data.

The CLUMPY database has a discrete size, limited by the grid chosen for the parameters. However, it can be interpolated into a continuous distribution such that intermediate SEDs not originally in the database are now considered in the fit. The fitting procedure has been modified from simply finding the best-fit, lowest- χ_R^2 model since we now use a continuous grid of model SEDs. For the purpose of analyzing how accurately a model describes observations, we introduce the statistical procedure of Bayesian analysis, which is widely used to estimate parameters of an underlying distribution based on observation. Within this setting we have a data set D , and a model M that is proposed to explain the data. The model itself consists of parameters θ , each with a physical meaning, and our aim is to obtain information about these parameters from our observations. We first consider if there is any prior knowledge regarding these model parameters, but there often is none. So we instill a uniform distribution over the entire range of values, or in other words, we make each parameter value as likely as any other to describe the observations. Given a set of background assumptions (uniform prior) we can find the probability that a given set of parameters is compatible with the observations, and this probability is known as the posterior distribution $p(\theta|D)$. Statistically meaningful information concerning a single parameter is obtained if we integrate out or marginalize the other parameters. In this way, each parameter's marginalized posterior distribution provides information

solely about its distribution. We can obtain these posterior distributions by using Bayes' theorem, which relates the posterior distribution, $p(\theta|D)$ with prior knowledge and information introduced by the data:

$$p(\theta|D) = \frac{p(D|\theta)}{p(D)} p(\theta), \quad (4.4)$$

where $p(D)$ is the *evidence*, $p(\theta)$ is the *prior* distribution, and $p(D|\theta)$ is the *likelihood* function. The evidence which is equal to the integral of the posterior distribution over parameter space has no analytical expression due the high dimensionality of parameter space, and is thus often calculated numerically, e.g. via Monte Carlo methods (Asensio Ramos & Ramos Almeida, 2009). The prior distribution contains any relevant prior information concerning the model parameters. Outside observations may lead to a restriction of parameters (See Section 7.5, but often the priors are set to be uniform. It is the likelihood function $p(D|\theta)$ that gives the probability that a set of parameters provides a model SED that is compatible with the observations. In our case, the likelihood function behaves as the exponential of the χ^2 value (See discussion within Asensio Ramos & Ramos Almeida (2009); Nikutta et al. (2012)).

Since the posterior distributions heavily rely on the likelihood distribution, it is required to robustly find it. Recall that the models have been interpolated such that the model selection comes from a continuous database, so in comparing models to observations, we obtain a 6-dimensional (6 CLUMPY parameters) likelihood function. As described in Nikutta et al. (2012), a Markov-Chain Monte Carlo technique searches this 6-dimensional likelihood space finding maxima or peaks. These peaks correspond to those within the posterior distributions and therefore indicate that these parameter values have a high probability in describing our observations.

Using CLUMPY models, we perform this fitting procedure and Bayesian analysis in Chapter 7 on a large sample of AGNs to determine the arrangement of dust in the clumpy torus.

Chapter 5

Previous Studies Concerning AGN

The topic of active galactic nuclei and their inner structure has been a hot area of research for decades. Since the discovery of broad line emission in polarized light of Seyfert 2 NGC 1068 (Antonucci & Miller, 1985), the unification scheme relating different types of AGNs has emerged. The premise of unification is that Seyfert 1 and 2 AGNs are intrinsically the same class of object just viewed at different angles, and any differences in the observed emission are due to orientation effects. Vital in this context is the molecular dusty torus that surrounds the central engine as this torus provides the obscuration of the broad line region at edge-on-like views, leading to the classification of type 2 AGNs. In this chapter, we will look at some of the previous studies of AGNs and relate them to what we want to accomplish.

5.1 Smooth Torus

Since dusty tori of AGNs are compact objects millions of parsecs (pc) away, it is very difficult to get a grasp of their true nature. However, dust is efficient in processing high-energy radiation into lower-energy infrared light. Since the continuum source responsible for the AGN luminosity emits ‘hard’ photons, the dusty torus absorbs this light, reprocesses it, and emits infrared emission which by analysis can reveal the torus’ composition and geometry (See Sections 3.4 and 6.4).

Since this MIR emission is crucial in understanding the properties of the torus, many dusty torus models were derived that attempted to explain the emission. Originally, radiative transfer calculations modeled a smooth, uniform torus (Pier & Krolik, 1992; Granato & Danese, 1994; Efstathiou & Rowan-Robinson, 1995; Granato et al., 1997; Siebenmorgen et al., 2004; Fritz et al., 2006) even though Krolik & Begelman (1988) proposed a clumpy distribution some time before. Smooth density models could not replicate the MIR emission seen in observations, namely the dust features.

These models should show strong emission from type 1 orientations, since the direct views of the hot optically thin region would provide emission features, but observations typically lack *strong* emission (Hao et al., 2005, 2007; Siebenmorgen et al., 2005; Sturm et al., 2005; Thompson et al., 2009; Wu et al., 2009). Furthermore, a view through a cold screen shows dust features in absorption, so observing the torus in type 2 views should result in deep absorption. However, Seyfert 2 galaxies typically only show weak absorption (Mason et al., 2006; Shi et al., 2006; Hao et al., 2007, See Chapter 8). Lastly, smooth torus models which expect cool, far-infrared emitting material far from the nucleus on 100 pc scales, disagree with high-resolution Very Large Telescope Interferometer (*VLTI*) observations, which indicate that the obscuring torus is spatially compact (Jaffe et al., 2004; Tristram et al., 2007; Beckert et al., 2008). These observations also show the dusty torus has a clumpy geometry, allowing a large dust temperature gradient to exist at the same distance from the central heating source, a condition not consistent with a smooth torus description.

5.2 Clumpy Torus

As clumpy models emerged, it was necessary to find that they reproduced the MIR emission and feature characteristics found in observations. Concerning the CLUMPY models, Levenson et al. (2007) and Sirocky et al. (2008) found that using the strengths of the silicate features together reveals the distribution of dust with the tori. Comparing the feature strengths, Sirocky et al. (2008) found that ULIRGs that contain an active galactic nuclei are described by a clumpy distribution. Additionally Thompson et al. (2009) (See Chapter 6.) found from a large sample of Seyfert 1s and type 1 quasars that the torus is best described by a compact clumpy distribution.

It is clear then that clumpy models are sufficient in replicating the MIR emission of observations, so focus shifted toward actually comprehending what the models and their parameters provide when they reproduce the observations. Since the main goal is to understand the emission from the torus so that its properties and geometry can be found, it is imperative that only the torus emission is observed. Space-based observatories such as the *Infrared Astronomical Satellite (IRAS)*, the *Infrared Space*

Observatory (ISO), and the *Spitzer Space Telescope*, all provided low-resolution observations due to relatively small primary mirrors of diameters 60, 60, and 85 centimeters respectively, and therefore captured contribution of nearly the entire host galaxy, contaminating the torus emission. Thus, focus was turned to 8-10 meter-class ground based observatories that with diffraction limits in the MIR near 0.4 arc-seconds could almost resolve the torus.

High spatial resolution observations taken at 10 μm , a wavelength in which the torus emits strongly, indicate that tori could be very small. The outer diameter of the MIR-emitting dust associated with the torus was found to be no greater than a few parsecs in type 2s NGC 1068 and the Circinus galaxy (Jaffe et al., 2004; Packham et al., 2005), and ≤ 35 parsecs in type 1 NGC 4151 (Radomski et al., 2003). Mason et al. (2006) used N-band (8-13 μm) imaging and spectroscopy for the nucleus of NGC 1068, and comparing their MIR spectra to CLUMPY torus models and found that their observations constrained the radius of the torus to at most 15 parsecs, a value in agreement with the compact (~ 3 parsec) size determined by interferometry.

Additional high resolution observations of nearby active galactic nuclei have been made with the *Gemini Telescopes* and the *MID-infrared Interferometric Instrument* at the *VLTI*, and the tori of these sources have been shown to be compact. The torus emission of the Circinus galaxy was found to extend out to 2 pc or perhaps just 1 pc (Packham et al., 2005; Tristram et al., 2007, *Gemini* and *VLTI*, respectively), and the torus radius of Centaurus A was found to be 1.6 pc (Radomski et al., 2008, *Gemini*) or 0.3 pc (Meisenheimer et al., 2007, *VLTI*). Furthermore (Jaffe et al., 2004; Raban et al., 2009) measured the torus extent of NGC 1068 to 1.7-2 pc.

5.3 Torus Models and Observations

Many of the studies in the last section determined tori sizes by using imaging techniques without clumpy torus modeling. Observational evidence that the torus is compact is highly beneficial in understanding its true nature and also in the context of models. MIR spectroscopic observations can be directly compared to or fit with the clumpy torus models (See Section 4.3), which describe the torus in terms of several

parameters. If for example the MIR spectrum of NGC 1068 was best fit by a model whose parameters describe a large torus where the clouds are loosely distributed, then a red flag rises, and we must investigate both the data and models to confirm their robustness. In some situations, the observations cannot be fit well by the models, and we believe that in these cases, the data was not dominated by the emission of the torus (i.e., there was additional emission contaminating the spectrum).

Several recent studies have been performed with the goal of obtaining the distribution of the torus' dust. Mason et al. (2006) was one of the first that implemented a fitting of models to observations which yielded results consistent with observations, and Mason et al. (2009) continue to place tight limits on the size of the silicate emitting region. The models are created to show the torus emission regardless of what classification the object in question is. Nikutta et al. (2009) investigated type 2 QSOs are detected the $10\ \mu\text{m}$ silicate feature in emission in some sources and a complete absence of any deeply absorbed features. These two observations cannot be explained with smooth density torus models, yet torus models, whose clumpy nature allows for the chance to view the AGN directly, can explain the observations, describing the type 2 quasar with silicate emission as having few clouds (N_0) in the torus. Mor et al. (2009) analyze a large sample of QSOs with a three-component model which integrates the clumpy torus models of (Nenkova et al., 2002, 2008a,b) and find for type 1 QSOs a compact (1-35 pc) torus whose distribution clearly allows for a 'type 1 view' – low inclination angles combined with low torus scale heights with few clouds on average along an equatorial ray.

Asensio Ramos & Ramos Almeida (2009) first implemented the CLUMPY models into the Bayesian framework, and recent papers have used their technique in retrieving the posterior distributions of each model parameter (e.g. Ramos Almeida et al., 2009, 2011; Alonso-Herrero et al., 2011). These studies all consisted of fitting IR photometric points, including observations at $10\ \mu\text{m}$ and $18\ \mu\text{m}$, to characterize the torus emission. Based solely on the fittings, Ramos Almeida et al. (2009) found their type 1 and 2 AGNs had tori whose radii were generally smaller than 5 pc, and Ramos Almeida et al. (2011) continued further and compared the model parameter values

of the two classifications. They found that the tori of Seyfert 1s, as compared to Seyfert 2s, were more compact with shallower opening angles (σ) with fewer clouds which happened to be considerable more compact. Since the immediate dusty surroundings of Seyfert 1 and 2 nuclei are intrinsically different, the authors suggest the unification may not hold. While these last papers used only photometry in the fittings, Alonso-Herrero et al. (2011) pursued the analysis using high-spatial resolution ground-based spectroscopy, in addition to the photometric data, as means to place tighter constraints on the torus model parameters. They too found that Seyferts contain compact tori and that viewing orientation is not the only difference between type 1 and type 2 AGNs.

Chapter 6

Dust Emission from Unobscured Active Galactic Nuclei

This chapter consists of the published work of Thompson et al. (2009). In the time since submitting this paper to *The Astrophysical Journal*, we have performed additional analysis on the sources mentioned in this chapter, and we present these results in Chapter 8.

6.1 Introduction

Accretion onto central supermassive (10^6 - $10^{10} M_{\odot}$) black holes powers active galactic nuclei (AGNs). AGNs exhibit a great variety of observational characteristics, notably the presence or absence of spectrally broad emission lines, which determine their classification as type 1 or type 2, respectively. Unified AGN models (Antonucci, 1993) account for these differences in terms of viewing geometry, with an optically and geometrically thick dusty torus that blocks the broad line region and central engine from some (type 2) lines of sight.

The presence of the dusty torus can be detected not only in absorption but also in emission, with the bulk of the reprocessed AGN continuum emerging at infrared wavelengths. The exact spectral energy distribution (SED) is a function of dust geometry, and initial radiative transfer calculations modeled a smooth, uniform torus, which is consistent with basic requirements of unification (Pier & Krolik, 1992; Granato & Danese, 1994; Efstathiou & Rowan-Robinson, 1995). However, recent high-resolution observations indicate that the obscuring torus has a clumpy geometry (Jaffe et al., 2004; Tristram et al., 2007; Beckert et al., 2008). These data require a large range of dust temperatures to coexist at the same distance from the central heating source, whereas the temperature of a smooth torus declines with distance. New models that place the dust in a clumpy toroidal distribution account for these observations while remaining consistent with unification schemes (Nenkova et al., 2002; Hönig et al.,

2006; Schartmann et al., 2008).

Silicate dust specifically dominates the mid-infrared (MIR) spectra of galaxies, and it can produce both the continuum and prominent spectral features at 10 and 18 μm . The stronger 10 μm feature originates from a SiO stretching mode and the 18 μm feature from a SiO bending mode (Knacke & Thomson, 1973). A view of a hot, optically thin surface produces the features in emission, and a view through a cold screen shows the features in absorption. A smooth torus therefore exhibits strong emission from type 1 orientations (which view the hot inner throat of the torus directly), and deep absorption in type 2 AGNs (viewed through the torus). However, observations of AGNs do not conform to these expectations. Silicate emission is not universally observed in type 1 galaxies, and only recently has it been detected, primarily in high-luminosity AGNs (Hao et al., 2005, 2007; Siebenmorgen et al., 2005; Sturm et al., 2005). Current observations of samples of the lower-luminosity Seyfert 1 galaxies even show silicate absorption on average (Hao et al., 2007), and Seyfert 2 galaxies typically show only weak absorption (Mason et al., 2006; Shi et al., 2006; Hao et al., 2007).

Here we use MIR spectroscopy of unobscured AGNs to diagnose their native dusty environments. Even more informative than the behavior of one silicate feature alone, the combination of both silicate features together reveals the geometry of the reprocessing dust around the AGNs, discriminating between smooth and clumpy distributions (Sirocky et al., 2008). We also use the spectra to evaluate the energetic contribution of star formation, which is evident in low-ionization emission lines and polycyclic aromatic hydrocarbon (PAH) emission, and which accounts for a significant fraction of the long-wavelength continuum flux.

6.2 Sample and Data Reduction

We select Seyfert 1 galaxies from the Rush et al. (1993) 12 μm survey, using 31 with archival low-resolution spectra from the *Spitzer Space Telescope Infrared Spectrograph (IRS)* in this study (Werner et al., 2004; Houck et al., 2004). The hot dust continuum of AGNs dominates the MIR emission in this flux-limited sample. We restrict

the Seyfert 1s to those galaxies with optical classification between 1 and 1.5. As a comparison sample, we use 21 nearby ($z < 0.4$) type 1 quasars having archival *IRS* spectra. We classify all sources with monochromatic luminosity (νL_ν) at $14\ \mu\text{m}$ $L_{14} \geq 7 \times 10^{10} L_\odot$ as quasars. We list the galaxies, their basic properties, and observational details in Table 6.1.

These *IRS* observations cover the MIR bandpass from 5.2 to $38\ \mu\text{m}$. We used standard *Spitzer* Science Center pipeline version S15.3.0 data and extracted the spectra with the *Spitzer IRS* Custom Extraction (SPICE) package. The observations were performed in either staring or mapping mode. We used two nodded positions of the same order to background subtract the staring mode observations, in which the nucleus is always centered in the slit. Differencing exposures in first and second orders provided background subtraction of mapping mode data. For these mapping mode observations, in addition to the central spectrum obtained with the slit centered on the nucleus, we included contributions from the two adjacent off-center spectra. We compared the galaxies' FWHM to that of a calibration star to identify extended sources, finding eight: ESO 12-G21, MCG -5-13-17, NGC 7469, IC 4329A, NGC 1566, UGC 5101, NGC 3227, and MCG -6-30-15. We used default SPICE extraction for point sources and extracted only the central 4 pixels (which corresponds to $7.2''$ and $20.4''$ in the short- and long-wavelength orders, respectively) from extended spectra. We robustly averaged individual spectra from each order to remove bad data. We scaled short wavelength spectra to match the flux of the long-wavelength order "Long Low 1," which has the widest slit and is less sensitive to pointing errors.

6.3 Results

6.3.1 Broadband Spectral Characteristics

The Seyfert 1 sample and the comparison quasars reveal the typical MIR characteristics of unobscured AGNs alone, which are evident in their average spectra (Figures 6.1 and 6.2). The individual spectra are normalized at $14\ \mu\text{m}$, which represents the dust continuum, and weighted according to their signal-to-noise in each average spectrum.

Table 6.1. Observations and Galaxy Data

Galaxy	R.A. (J2000.0)	Decl. (J2000.0)	z	Scale (pc arcsec ⁻¹)	AOR
<u>Seyfert 1s</u>					
ESO 12-G21	00 40 46.2	-79 14 24	0.030	610	12465920
Mrk 335	01 22 40.8	+26 52 06	0.026	530	12450560
Mrk 1034NE	02 23 20.4	+32 11 34	0.034	700	20320512
NGC 931	02 28 14.5	+31 18 42	0.017	340	12460032
IRAS F03450+0055	03 47 40.2	+01 05 14	0.031	630	4674816
NGC 1566	04 20 00.4	-54 56 16	0.005	100	9490688
3C120	04 33 11.1	+05 21 16	0.033	670	4847360
MCG -5-13-17	05 19 35.8	-32 39 28	0.012	260	12468480
Mrk 6	06 52 12.3	+74 25 38	0.019	390	12483584
Mrk 9	07 36 57.0	+58 46 13	0.040	800	12483072
Mrk 79	07 42 32.8	+49 48 35	0.022	450	12453632
Mrk 704	09 18 26.0	+16 18 19	0.029	590	12444416
UGC 5101	09 35 51.7	+61 21 11	0.039	790	4973056
Mrk 1239	09 52 19.1	-01 36 44	0.020	410	12453120
NGC 3227	10 23 30.6	+19 51 54	0.004	80	4934656
NGC 3511	11 03 23.8	-23 05 12	0.004	77	12473600
NGC 3516	11 06 47.5	+72 34 07	0.009	180	12473344
NGC 4051	12 03 09.6	+44 31 53	0.002	48	12451072
NGC 4151	12 10 32.6	+39 24 21	0.003	69	3754496
Mrk 766	12 18 26.5	+29 48 46	0.013	270	12465408
NGC 4593	12 39 39.4	-05 20 39	0.009	190	12457216
MCG -2-33-34	12 52 12.5	-13 24 53	0.017	340	12481280
MCG -6-30-15	13 35 53.8	-34 17 44	0.008	160	4849920
IC 4329A	13 49 19.2	-30 18 34	0.016	330	4848640
NGC 5548	14 17 59.5	+25 08 12	0.017	350	4855296
Mrk 817	14 36 22.1	+58 47 39	0.032	640	12461056
NGC 6860	20 08 46.9	-61 06 01	0.015	310	12462592
Mrk 509	20 44 09.7	-10 43 25	0.034	700	4850432
NGC 7213	22 09 16.3	-47 10 00	0.006	120	4856320
NGC 7469	23 03 15.6	+08 52 26	0.016	330	3755008
NGC 7603	23 18 56.6	+00 14 38	0.030	600	10870784
<u>Quasars</u>					
PG0052+251	00 54 52.1	+25 25 38	0.155	3500	4675072
3C048	01 37 41.3	+33 09 35	0.367	9300	4670720
IRAS F07599+6508	08 04 33.1	+64 59 49	0.148	3300	17103104
PG0947+396	09 50 48.4	+39 26 51	0.206	4800	14190592
PG0953+414	09 56 52.4	+41 15 22	0.234	5500	4675328
3C234	10 01 49.6	+28 47 09	0.185	4200	11305728
PG1048+342	10 51 43.9	+33 59 27	0.167	3800	14192128
PG1116+215	11 19 08.6	+21 19 18	0.177	4000	4734464
PG1121+422	11 24 39.2	+42 01 45	0.225	5300	14193664
3C273	12 29 06.7	+02 03 09	0.158	3600	4978176
Mrk 231	12 56 14.2	+56 52 25	0.042	880	4978688
PG1307+085	13 09 47.0	+08 19 49	0.155	3500	4735488
PG1309+355	13 12 17.8	+35 15 21	0.184	4200	4736000
PG1322+659	13 23 49.5	+65 41 48	0.168	3800	14196224
IRAS F13349+2438	13 37 18.7	+24 23 03	0.108	2400	4373760
PG1352+183	13 54 35.6	+18 05 17	0.152	3400	4736512
PG1354+213	13 56 32.7	+21 03 52	0.300	7400	14196992
PG1402+261	14 05 16.2	+25 55 35	0.164	3700	4675584
PG1427+480	14 29 43.1	+47 47 26	0.221	5200	14198528
PG2130+099	21 32 27.8	+10 08 20	0.063	1400	3761408
PG2233+134	22 36 07.7	+13 43 55	0.326	8100	4734208

Note. — Units of right ascension are hours, minutes, and seconds, and units of declination are degrees, arcminutes, and arcseconds.

Both the Seyfert and quasar spectra show prominent $10\ \mu\text{m}$ silicate emission, which reveals the geometry of the dust distribution, high-ionization emission lines, which are predominantly the result of ionization by the AGN continuum, and polycyclic aromatic hydrocarbon (PAH) emission, which is associated with star formation.

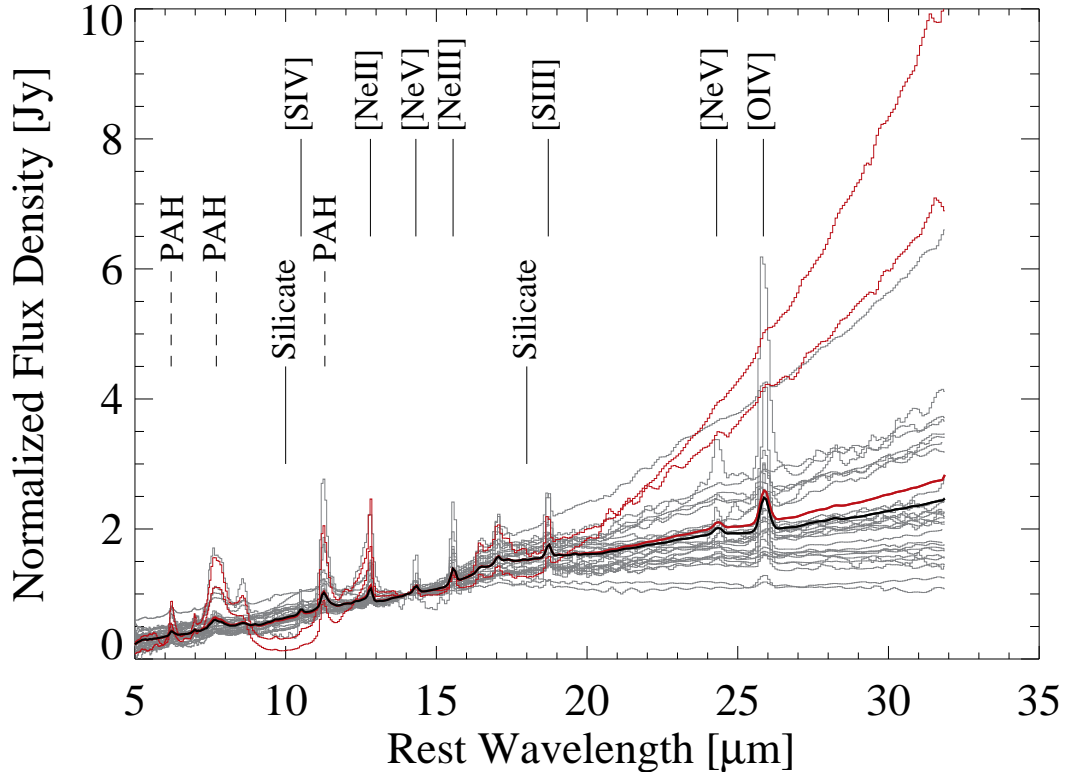


Figure 6.1 Average Seyfert 1 spectra (smooth heavy lines) show 10 and $18\ \mu\text{m}$ silicate emission. The bold black line best isolates the AGNs alone and is the average of 29 individual sources (grey histograms, normalized at $14\ \mu\text{m}$) excluding LIRGs UGC 5101 and Mrk 1034 (red histograms). The bold red line is the average spectrum of all sources. In addition to the silicates, emission features that are characteristic of both AGNs and star formation are labeled.

A few sample members are luminous or ultraluminous infrared galaxies (LIRGs or ULIRGs), having $L_{IR} > 10^{11}L_{\odot}$ or $> 10^{12}L_{\odot}$, respectively. These galaxies (plotted as red histograms) are preferentially mergers (Sanders & Mirabel, 1996), and they often exhibit extended MIR emission (Soifer et al., 2000; Alonso-Herrero et al., 2006), which is not directly attributable to the AGN. We show the average Seyfert

Table 6.2. Average Type 1 AGN Spectra

Rest Wavelength (μm) (1)	Seyfert 1 Scaled Flux Density (Jy) (2)	Quasar Scaled Flux Density (Jy) (3)
5.000	0.226	0.441
5.030	0.237	0.446
5.060	0.247	0.449
5.090	0.257	0.453
5.120	0.266	0.450
5.150	0.271	0.449
5.180	0.277	0.453
5.210	0.287	0.458

Note. — Table 6.2 is published in its entirety in the electronic edition of the *Astrophysical Journal*. A portion is shown here for guidance regarding its form and content. Col. (1): Rest wavelength. The wavelength scale is non-uniform and based on the original resolution, which decreases toward longer wavelengths. Col. (2): Average Seyfert 1 spectrum normalized at 14 μm . Col. (3): Average quasar spectrum normalized at 14 μm .

1 and quasar spectra, both including (red) and excluding (black) these (U)LIRGs. The IR-luminous galaxies' spectra are different from the others', showing silicate absorption and relatively strong long-wavelength emission. However, because only two of 31 Seyfert 1 galaxies and one of 21 quasars are also (U)LIRGs, the resulting average spectra are not significantly different in each case. We base the subsequent analysis on the (U)LIRG-free average spectra, which better isolate the AGN contribution. Table 6.2 contains the normalized average spectra of the Seyfert 1 galaxies and quasars.

Figure 6.2 further shows both the average Seyfert spectrum (green) and the average quasar spectrum (black) together. Overall, these spectra are very similar in shape and emission features. The 5 to 14 μm flux density ratios, F_5/F_{14} , are slightly but not significantly different, with $F_5/F_{14} = 0.25 \pm 0.12$ in the Seyfert 1s and $F_5/F_{14} = 0.45 \pm 0.16$ in the quasars. We can describe the MIR spectra as a power law $F_\nu \propto \nu^\alpha$, where $\alpha < 0$ is characteristic of AGNs (Elvis et al., 1994; Klaas et al., 2001; Alonso-Herrero et al., 2006). The power law indices range from -0.5 to -2.8 in the Seyfert 1 sample and -0.3 to -1.6 in the quasars, with $\alpha = -1.3$ and -0.8 in the average Seyfert 1 and quasar spectra, respectively. These results agree with those of Alonso-Herrero et al. (2006), who found $-2.8 < \alpha < -0.5$ over the wavelength range

of 3.6–8 μm in AGN-dominated galaxies.

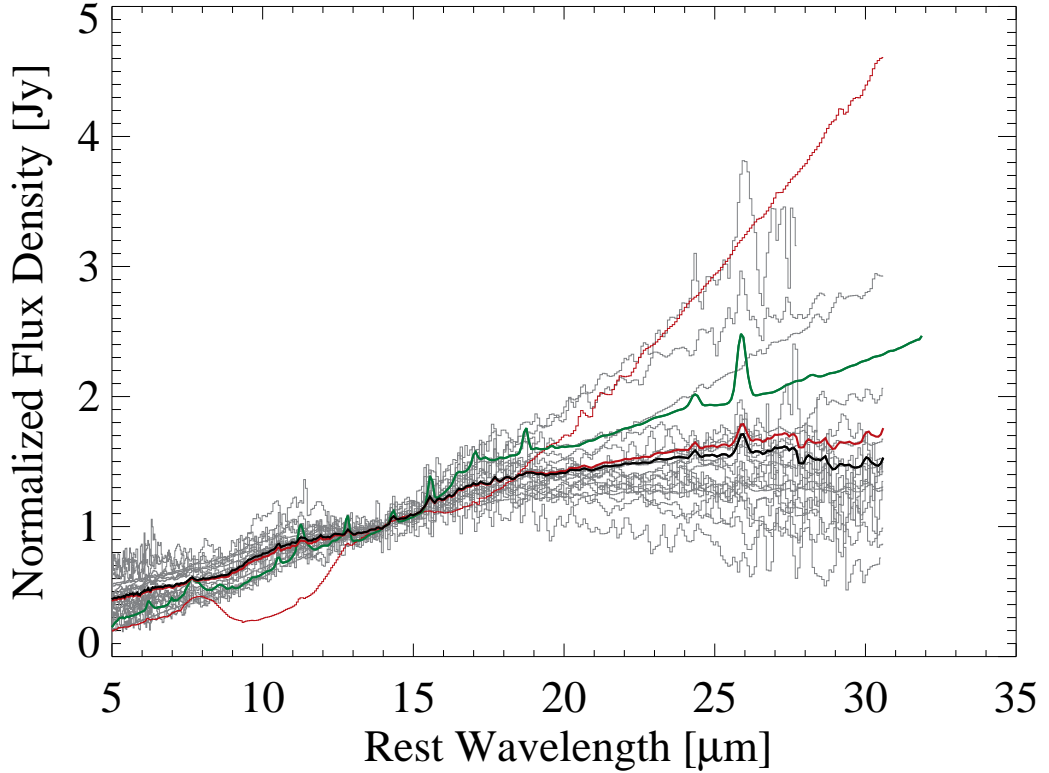


Figure 6.2 Average quasar spectra (smooth heavy lines) show 10 and 18 μm silicate emission. The spectrum plotted in black best isolates the MIR emission of these luminous AGNs and excludes the ULIRG Mrk 231 (red histogram), which contributes to the average plotted in red. As a comparison, the average Seyfert 1 spectrum is overplotted in green. The equivalent widths of both AGN-originating emission lines, such as [O IV], and star formation indicators, such as PAHs and [Ne II], are larger in the average Seyfert 1 spectrum.

We also measured the equivalent widths (EWs) of strong emission lines in the average spectra. We find the line EWs to be larger in the Seyfert galaxy spectra than in the quasar spectra, considering both strong high excitation lines, such as [O IV] and [Ne V], which are attributable to AGNs (Lutz et al., 2003), and the low ionization lines [Ne II] and [S III], which originate in star formation. Specifically, the [O IV] EW is 0.09 μm in the average Seyfert spectrum and 0.03 μm in the average quasar spectrum. These results agree with previous MIR work by Hönig et al. (2008) and Keremedjiev et al. (2008). Meléndez et al. (2008) find $L_{[\text{OIV}]} \propto L_{2-10\text{keV}}^{0.7}$, which

similarly indicates smaller EW in the higher luminosity AGNs, if we consider the 2–10 keV X-ray luminosity as a proxy for intrinsic AGN luminosity. Finally, while the quasar comparison sample was not selected robustly, we note the resulting average spectrum is extremely similar to that of Netzer et al. (2007), showing a comparable spectral shape, broad silicate emission, and PAH emission.

6.3.2 Type 1 AGN Silicate Emission

Dust produces both the MIR continuum and the silicate features. We model the spectra assuming the same dust produces both, as opposed to invoking physically separate line- and continuum-producing regions (c.f. Schweitzer et al., 2008). In the *IRS* spectra, we measure the continuum over a short-wavelength region (typically 5–7 μm), an intermediate point (around 14 μm), and a long-wavelength region (typically 26.5–31.5 μm), and we fit a spline to define the full continuum, utilizing the method of Sirocky et al. (2008). The silicate features are evident in the dust absorption cross section, and the local minimum around 14 μm produces the pseudo-continuum of the observed spectra at this wavelength. The resulting continuum fits agree well with the radiative transfer model calculations of the emission from synthetic dust that lacks the silicate features (Sirocky et al., 2008). Figure 6.3 shows an example of the continuum fit to Mrk 766. The procedure slightly varies depending on the spectral characteristics, with “continuum-dominated spectra” containing AGN emission lines and weak PAHs, “PAH-dominated spectra” exhibiting strong PAH emission, and “absorption-dominated spectra” showing strong ice and hydrocarbon absorption below 14 μm (Spoon et al., 2005; Sirocky et al., 2008). Most of these spectra are continuum-dominated, which provide more reliable 10 μm silicate measurements, while the silicate strength measurements of PAH-dominated and absorption-dominated spectra are more uncertain.

We measure the silicate feature strength

$$S_{Sil} = \ln \frac{F_{obs}(\lambda)}{F_{cont}(\lambda)}$$

at the wavelength of the strength extremum around 10 and 18 μm , where F_{obs} is the

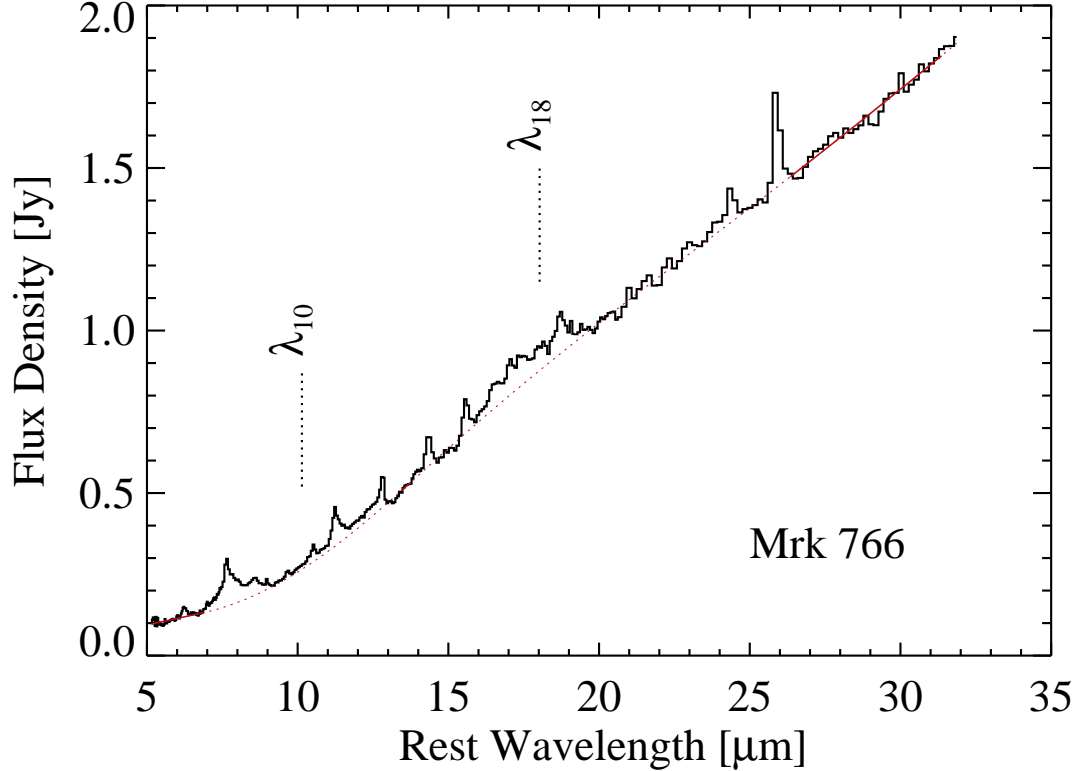


Figure 6.3 Spectrum of the typical Seyfert 1 galaxy Mrk 766 illustrates the continuum fitting technique. The resulting continuum (dotted red) is a spline fit to measurements over a short-wavelength region, an intermediate point around $14 \mu\text{m}$, and a long-wavelength region (solid red). Vertical lines mark the measured peak wavelengths of the 10 and $18 \mu\text{m}$ silicate features, which both appear in emission here, although the $10 \mu\text{m}$ emission is very weak.

observed flux density and F_{cont} is the fitted continuum flux density, as in Levenson et al. (2007). Table 6.3 lists these silicate strengths (S_{10} and S_{18}) and peak wavelengths (λ_{10} and λ_{18}). The average values of λ_{10} and λ_{18} are $10.0 \pm 0.1 \mu\text{m}$ and $18.1 \pm 0.2 \mu\text{m}$ in Seyfert 1 AGNs and $10.1 \pm 0.2 \mu\text{m}$ and $18.0 \pm 0.2 \mu\text{m}$ in quasars. These values are consistent with the dust cross sections of Ossenkopf et al. (1992) and characteristic of the interstellar medium, although radiative transfer effects can result in small ($\sim 0.3 \mu\text{m}$) wavelength shifts. In contrast, we note that Sturm et al. (2005) attribute the large wavelength shifts they measure (λ_{10} up to $11.5 \mu\text{m}$) to unusual grain size distributions.

Table 6.3. Spectral Measurements

Galaxy	S_{10}	λ_{10} (μm)	S_{18}	λ_{18} (μm)	Integrated Flux			F_5 (Jy)	F_{14} (Jy)	F_{30} (Jy)
					[Ne II] ($\text{erg s}^{-1} \text{cm}^{-2}$)	6.2 μm PAH ($\text{erg s}^{-1} \text{cm}^{-2}$)				
<u>Seyfert 1s</u>										
ESO 12-G21	0.15	10.1	0.08	18.2	2.1E-13	5.9E-13	0.05	0.15	0.34	
Mrk 335	0.15	10.0	0.10	18.3	0.11	0.22	0.35	
Mrk 1034	-0.65	10.0	0.12	18.3	6.9E-13	1.5E-12	0.02	0.17	1.00	
NGC 931	0.05	10.1	0.08	18.2	8.6E-14	9.6E-14	0.16	0.54	1.10	
IRAS F03450+0055	0.14	9.9	0.06	18.0	0.09	0.31	0.49	
NGC 1566	0.02	10.0	0.16	18.2	2.2E-13	7.5E-13	0.05	0.15	0.43	
3C120	0.26	10.2	0.15	17.8	6.3E-14	1.0E-13	0.09	0.31	0.63	
MCG -5-13-17	0.09	9.8	0.10	18.2	1.6E-13	2.3E-13	0.03	0.21	0.64	
Mrk 6	0.24	10.2	0.18	18.1	2.4E-13	2.0E-13	0.11	0.32	0.70	
Mrk 9	0.04	9.7	0.14	17.8	7.8E-14	...	0.09	0.24	0.52	
Mrk 79	0.07	10.1	0.10	18.0	7.0E-14	...	0.15	0.48	1.07	
Mrk 704	0.07	10.2	0.05	18.2	2.9E-15	...	0.16	0.44	0.47	
UGC 5101	-1.52	9.9	-0.19	18.3	6.4E-13	1.4E-13	0.09	0.27	2.24	
Mrk 1239	0.13	10.1	0.11	18.3	1.5E-14	2.5E-13	0.36	0.82	1.37	
NGC 3227	0.01	10.0	0.06	18.2	1.1E-12	1.6E-12	0.13	0.63	1.91	
NGC 3511	0.07	10.2	0.07	18.2	3.2E-13	3.8E-13	0.004	0.06	0.22	
NGC 3516	0.03	10.0	0.10	17.7	9.9E-15	9.3E-14	0.12	0.39	0.92	
NGC 4051	0.07	10.0	0.06	18.0	3.1E-13	7.2E-13	0.14	0.64	1.43	
NGC 4151	0.14	10.0	0.15	18.4	1.3E-12	6.2E-13	0.56	2.45	4.06	
Mrk 766	0.05	10.1	0.08	18.0	3.3E-13	3.5E-13	0.11	0.57	1.75	
NGC 4593	0.11	10.0	0.08	18.1	6.8E-14	1.6E-13	0.16	0.46	0.97	
MCG -2-33-34	0.04	9.8	0.15	17.8	1.2E-13	2.1E-13	0.02	0.12	0.39	
MCG -6-30-15	0.02	10.2	0.10	18.3	1.7E-14	1.0E-13	0.13	0.45	0.79	
IC 4329A	0.04	9.9	0.04	18.1	2.4E-13	...	0.25	1.36	2.05	
NGC 5548	0.14	10.1	0.08	18.1	1.2E-13	7.9E-14	0.05	0.29	0.59	
Mrk 817	0.08	10.1	0.07	18.0	2.4E-14	1.5E-13	0.10	0.40	1.36	
NGC 6860	0.06	10.1	0.10	18.0	6.9E-14	...	0.11	0.25	0.36	
Mrk 509	0.12	10.1	0.19	18.0	1.6E-13	3.0E-13	0.13	0.35	0.66	
NGC 7213	0.60	10.1	0.16	17.9	2.8E-13	7.0E-14	0.09	0.28	0.46	
NGC 7469	0.05	9.8	0.11	17.8	2.8E-12	4.6E-12	0.15	1.41	7.96	
NGC 7603	0.12	10.2	0.13	17.7	1.9E-13	4.7E-13	0.17	0.27	0.33	
<u>Quasars</u>										
PG0052+251	0.30	10.2	0.15	17.9	2.1E-14	7.6E-14	0.02	0.06	0.05	
3C048	0.16	10.3	0.07	18.3	6.7E-15	...	0.02	0.10	0.39	
IRAS F07599+6508	0.07	10.0	0.01	17.8	2.3E-14	8.6E-14	0.16	0.30	0.84	
PG0947+396	0.09	10.3	0.10	17.9	1.2E-14	...	0.02	0.03	0.05	
PG0953+414	0.25	9.8	0.19	17.9	1.7E-14	1.1E-13	0.02	0.04	0.04	
3C234	0.01	10.0	0.06	17.9	1.4E-14	1.2E-15	0.04	0.20	0.27	
PG1048+342	0.22	10.2	0.21	18.4	1.2E-14	...	0.01	0.02	0.02	
PG1116+215	0.22	10.2	0.09	18.2	0.06	0.09	0.11	
PG1121+422	0.12	10.0	0.09	18.2	0.01	0.01	0.01	
3C273	0.12	10.1	0.05	18.1	3.8E-14	3.2E-14	0.21	0.38	0.55	
Mrk 231	-0.62	9.8	-0.23	17.9	5.8E-13	5.9E-13	0.63	2.98	13.17	
PG1307+085	0.34	9.8	0.21	17.7	0.01	0.05	0.06	
PG1309+355	0.57	10.0	0.18	17.7	3.5E-14	...	0.02	0.07	0.10	
PG1322+659	0.14	10.0	0.11	18.2	6.5E-15	1.7E-14	0.01	0.03	0.05	
IRAS F13349+2438	0.06	10.1	0.05	17.8	2.7E-14	...	0.26	0.56	0.72	
PG1352+183	0.08	10.3	0.21	18.2	0.02	0.02	0.03	
PG1354+213	0.12	9.9	0.13	17.9	0.01	0.02	0.04	
PG1402+261	0.22	10.0	0.05	17.9	1.4E-14	...	0.04	0.08	0.16	
PG1427+480	0.14	10.3	0.09	17.7	1.6E-14	...	0.01	0.02	0.07	
PG2130+099	0.02	10.0	0.05	18.3	1.5E-14	4.3E-14	0.08	0.22	0.35	
PG2233+134	0.29	9.8	0.13	17.7	0.02	0.04	0.07	

The silicate strengths reveal features in emission ($S_{sil} > 0$) in 49 of 52 AGNs in the combined sample (Figure 6.4), although the emission is generally weak. The only type 1 AGNs that show $10\ \mu\text{m}$ silicate absorption are also LIRGs or ULIRGs. The corresponding average Seyfert 1 spectrum shows the $10\ \mu\text{m}$ silicate feature in obvious emission ($S_{10} = 0.11$), whereas the average Seyfert 1 spectrum of Hao et al. (2007) shows weak silicate absorption. The homogeneous sample selection we employ and the exclusion of (U)LIRGs better isolates the AGN and its immediate environment in the MIR spectra. In contrast, the heterogeneous Seyfert 1 sample of Hao et al. (2007) includes LIRGs and ULIRGs. Most of the red 2MASS sources, for example, are indeed LIRGs and ULIRGS based on their IR luminosities. The dusty star-forming regions of these (U)LIRGs contribute significantly to their *IRS* spectra and alter the appearance of the silicate features. We conclude that the average Seyfert 1 spectrum of Figure 6.1, which shows $10\ \mu\text{m}$ silicate emission, best characterizes the AGN and its immediate surroundings in the MIR. The higher luminosity quasars similarly show $10\ \mu\text{m}$ emission, with $S_{10} = 0.18$ on average. Silicate emission in AGNs was first discovered in high luminosity galaxies (Hao et al., 2005; Siebenmorgen et al., 2005; Sturm et al., 2005), and although the quasar sample shows stronger $10\ \mu\text{m}$ silicate strength than the Seyfert sample, we find no significant correlation of silicate strength with AGN luminosity. Finally, we find no trends with λ_{10} or λ_{18} , indicating that the chemical composition of the dust does not vary significantly with AGN luminosity or silicate strength.

6.3.3 AGN-Star Formation Connection

Indicators of star formation, including [Ne II] $12.8\ \mu\text{m}$ and several PAH bands (Genzel et al., 1998, and references therein), are present in the majority of the spectra. We measure the integrated luminosities of the [Ne II] and $6.2\ \mu\text{m}$ PAH emission to quantify the star formation contribution, fitting a local continuum and a Gaussian for the line emission. The $5\ \mu\text{m}$ monochromatic continuum luminosity scales with the AGN luminosity, without the ambiguity of a star formation contribution to the continuum luminosity that is present at longer wavelengths. These AGN and star formation

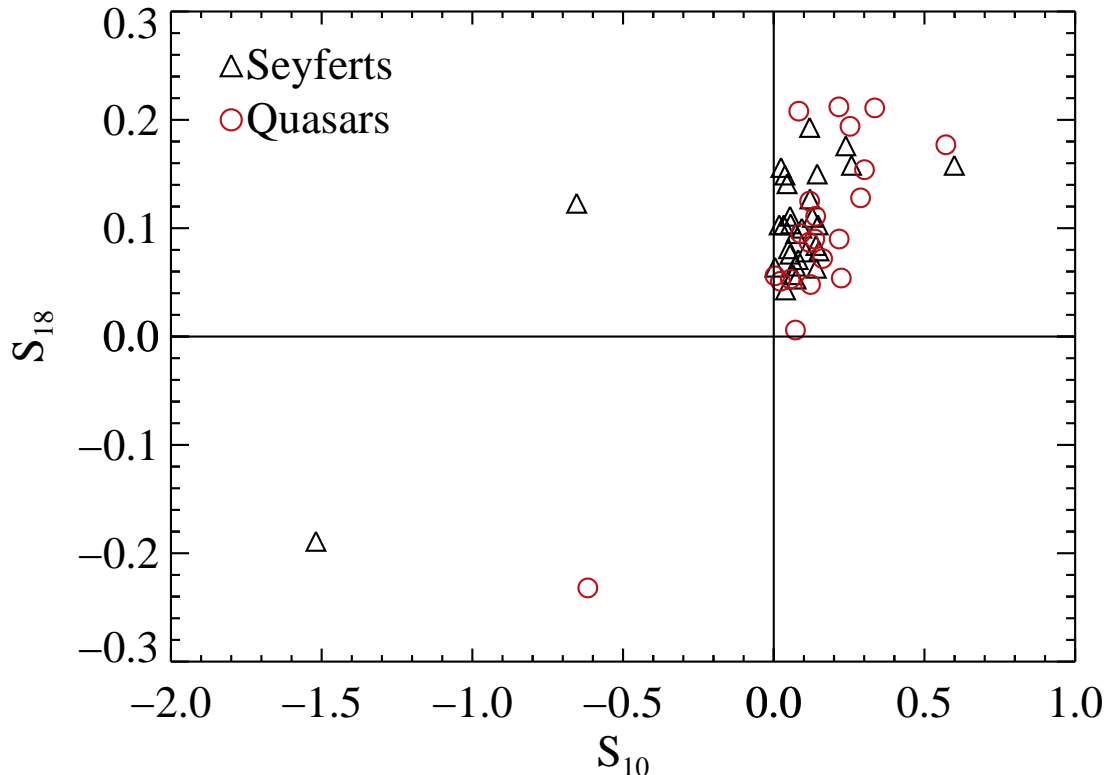


Figure 6.4 Feature strengths at 10 and 18 μm (S_{10} and S_{18}). Positive strengths show silicate emission in 49 of the 52 type 1 AGNs. The only type 1 AGNs that do not show 10 μm silicate emission are also LIRGs or ULIRGs. Vertical and horizontal lines at zero strength separate the regions of emission ($S > 0$) and absorption ($S < 0$). Triangles identify Seyfert 1 AGNs, and circles mark quasars.

luminosities are indeed positively correlated over both Seyfert 1 and quasar luminosities (Figure 6.5). We certainly measure [Ne II] in all but two Seyfert galaxies, and the resulting robust [Ne II]-5 μm correlation (dashed line) is consistent with the less complete quasar measurements. The [Ne II] non-detections are a consequence of poor signal-to-noise. Combining the spectra without detections, we successfully measure the line. We plot these sources (green) at this average [Ne II]-5 μm ratio, considering the Seyfert 1 galaxies and quasars separately. The solid line shows the subsequent correlation over all galaxies, including those in which [Ne II] is not detected directly, which agrees with the Seyfert 1 result using individual detections alone.

The PAH measurements indicate similar trends of star formation increasing with

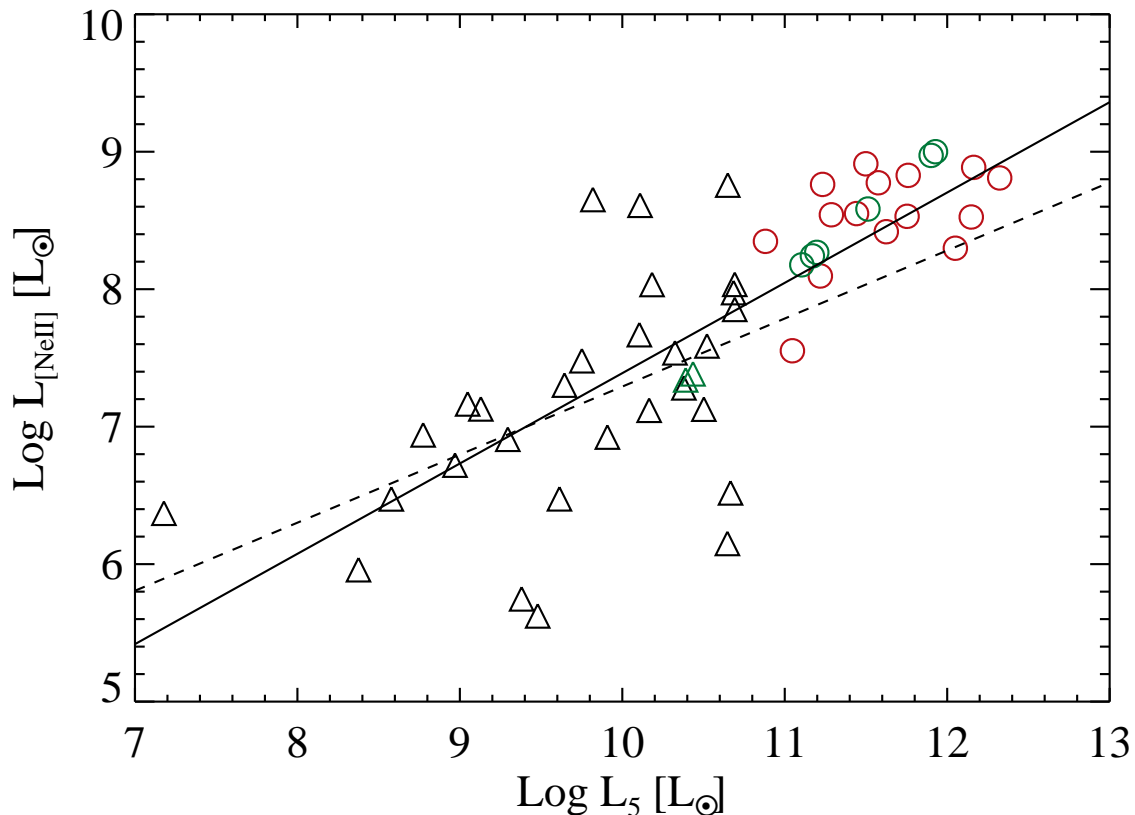


Figure 6.5 AGN and star formation luminosities, which the $5 \mu\text{m}$ monochromatic continuum luminosity and the $[\text{Ne II}] 12.8 \mu\text{m}$ integrated luminosity indicate, are positively correlated, although star formation becomes proportionally less important with increasing AGN luminosity. We certainly measure $[\text{Ne II}]$ in all but two Seyfert 1s and six quasars. Considering the Seyferts and quasars separately and averaging spectra without detections, we estimate $[\text{Ne II}]$ in these cases (green). The solid line shows the correlation over all galaxies, which agrees with the Seyfert 1 result using certain measurements alone (dashed). Other symbols as in Figure 6.4.

AGN luminosity, but these results are less robust. We directly detect the PAH emission in fewer individual spectra (24 of 31 Seyfert 1s and 8 of 21 quasars). While we recover the PAH emission in the average “PAH-less” Seyfert 1 spectrum, we do not certainly detect PAH emission in the average “PAH-less” quasar spectrum. Overall, this work agrees with that of Schweitzer et al. (2006) who find a similar correlation between AGN and starburst luminosity, measuring $6 \mu\text{m}$ continuum luminosity and PAHs in quasars.

While luminosity due to star formation and accretion are correlated, the relative

contribution of star formation decreases with increasing AGN luminosity. The slopes of the linear fits are 0.50 ± 0.16 and 0.66 ± 0.07 for the well-measured Seyferts and all sources, respectively. Using equation 1 of Ho & Keto (2007), we calculate the luminosity contribution of the starburst component from the [Ne II] integrated luminosity, treating the infrared luminosity as an approximation of bolometric luminosity. Similarly, using the median SED and bolometric corrections of Elvis et al. (1994), we obtain the bolometric scale factor for 5 μm continuum, $L_{bol} = 10.1L_5$. For weaker AGN contributors (e.g., $L_5 = 10^{8.5}L_\odot$), the star formation luminosity is as much as 80% of the AGN contribution, whereas the star formation luminosity of strong quasars ($L_5 = 10^{12}L_\odot$) is around 5% of their AGN luminosity. The contribution of star formation to the continuum flux increases with wavelength. Comparing the AGN-dominated 14 μm flux density with that at 30 μm , at which dust-reprocessed stellar light becomes significant, we find the average $F_{14}/F_{30} = 0.44 \pm 0.18$ for the Seyfert 1s and $F_{14}/F_{30} = 0.68 \pm 0.27$ for the quasars. Similar to the conclusions based on [Ne II] and PAH emission, these results also suggest that the relative luminosity of star formation is greater in the Seyfert 1 galaxies than in the quasars.

6.4 Dust Geometry from Silicate Features

The strengths of the 10 and 18 μm silicate features together are sensitive to the distribution of dust surrounding any heating source, including stars as well as AGNs. Smooth and clumpy distributions occupy distinct regions of the “feature-feature diagram” (Sirocky et al., 2008), which shows S_{18} vs. S_{10} (Figure 6.6). We compare these radiative transfer calculations with the observations to discern the dusty environment of the AGNs we observed. While the two strength measurements in an individual galaxy cannot constrain all the free parameters of any of the models, the type 1 AGNs are located in an area of the diagram that only clumpy models occupy.

Schweitzer et al. (2008) alternatively model MIR spectra of AGNs with multiple independent emission components. Combinations of blackbodies represent the continuum, due to hot dust close to the nucleus. The more distant, cooler, optically-thin narrow line region, located at 100–200 dust sublimation radii produces the silicate

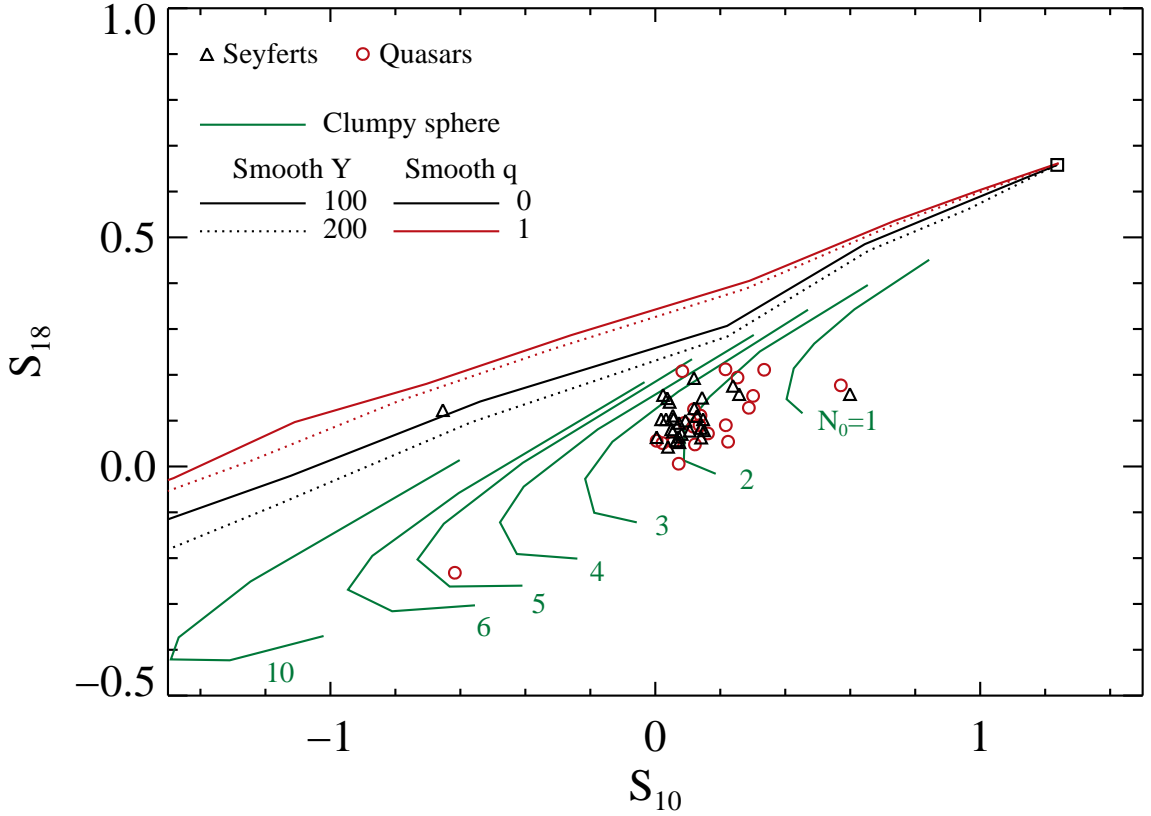


Figure 6.6 Together, 10 and 18 μm silicate feature strengths are sensitive to the dust geometry, and the AGN observations reveal clumpy surroundings. Independent of geometry, all optically thin configurations are located at the same point in the diagram (square), and tracks of increasing optical depth move toward weaker emission and eventually show absorption. All tracks of smooth spherical dust distributions (black and red), have similar slopes and lie separate from the data, for a range of spatial extent, Y , and radial density distribution ($\propto r^{-q}$). Models of clumpy environments (green) occupy regions of this “feature-feature diagram” that are inaccessible to the smooth models. Each clumpy sphere track is a function of the average number of clouds along radial rays, N_0 , with $q = 1$ and $Y = 30$. Clumpy models of $N_0 \sim 2$ generally agree with the data.

features. A disadvantage of this approach is that it allows silicate only in emission. It never produces silicate absorption, which is typical of type 2 AGNs (Hao et al., 2007). Indeed, assuming AGN unification, these models would instead predict silicate emission from type 2 AGNs in general. Moreover, the hot inner edge of the disk Schweitzer et al. (2008) describe would also produce strong silicate emission that would be observed directly in unobscured AGNs but is absent from their model. The

key difference between the description of Schweitzer et al. (2008) and ours is the location of the silicate-emitting region. Unfortunately, no current observations provide the spatial resolution to discriminate between them directly. Thus, we pursue here models in which a common dust distribution simultaneously accounts for the MIR continuum and spectral features. This technique has the advantage that it may be consistently and directly applicable to obscured AGNs, in agreement with unified AGN schemes, although we acknowledge that additional separate emission regions may be present in some galactic centers.

Independent of geometry, all optically thin configurations exhibit silicate emission and are located at the same point in the diagram, which corresponds to the feature strength in the optical cross section. Tracks of increasing optical depth move toward weaker emission. Only smooth dust distributions can exhibit large negative feature strengths, producing the temperature gradient that is essential for deep absorption. All smooth spherical distributions show similar slopes in the diagram, independent of the density distribution and total dust extent, which the dust’s optical properties determine (Sirocky et al., 2008). We plot several characteristic examples in Figure 6.6. Spherical distributions of clumps occupy a distinct region of the feature-feature diagram, never showing deep absorption, even for comparable total optical depth. The reason for this behavior is that both dark (absorbed) and bright (illuminated) cloud faces are observed in the clumpy distribution. The silicate emission from the bright sides fills in the absorption trough, reducing its depth (Nenkova et al., 2002).

We consider whether changes to the dust composition could provide smooth distributions that describe the observations on the feature-feature diagram. The dust’s optical properties determine both the location of the optically thin point and the slopes of the smooth model tracks on the diagram (Sirocky et al., 2008). Compared to the dust we employ here (Ossenkopf et al., 1992), the “astronomical silicate” of Draine (2003a,b), for example, shows a reduced 18 μm feature relative to the 10 μm feature, so the silicate features of these smooth models (Figure 9 of Sirocky et al. 2008) are more similar to those of the observations. However, the specific models that lie close to the data are optically thick, with $\tau_V \gg 10$, which is inconsistent with

the small optical depths measured in type 1 AGNs. This resulting optical thickness is a general problem for smooth models of any dust that exhibits the MIR silicate features. Only a contrived dust having extremely weak intrinsic silicate features could remain optically thin in the observed region of the diagram, yet even such a forced solution could not then produce the observed range of strength ratios. We conclude that the data lie below the smooth model tracks for reasonable dust properties, a region that only clumpy models occupy.

While the smooth spherical models offer a valuable contrast, they are inappropriate in these cases, failing to allow direct views of the central engine and the resulting spectrally broad emission lines. Nevertheless, the smooth spherical geometries do usefully indicate some of the realm of the smooth torus of classical AGN unification schemes, which provide unobscured views along select lines of sight. Specifically, the obscured type 2 view through the torus is analogous to the spherical geometry, admitting no view of directly-illuminated hot dust. Strictly unobscured (type 1) lines of sight to the central engine view the silicate emission from the optically thin illuminated surface of the torus directly. The net result is silicate emission, located near the optically thin point of the feature-feature diagram, independent of the total dust optical depth in the torus, with only a weak absorption contribution from the cooler torus interior within the observing beam (Granato & Danese, 1994; Efstathiou & Rowan-Robinson, 1995; Van Bemmell & Dullemond, 2003). In type 1 views, the silicate strength is sensitive to the shape of the inner edge of the dusty torus. The models of Pier & Krolik (1992), for example, do not typically exhibit strong silicate emission. However, several independent lines of evidence argue against smooth dust distributions generally. First, the MIR emission of AGNs is observed to be effectively isotropic (Lutz et al., 2004; Buchanan et al., 2006; Horst et al., 2006), whereas all smooth torus models predict type 1 AGNs to be significantly brighter than type 2 AGNs in the MIR, for a fixed intrinsic luminosity. Second, all optically thick smooth descriptions produce very deep absorption in obscured nuclei, which is not generally observed (Hao et al., 2007).

Thus, we pursue clumpy dust distributions, which Krolik & Begelman (1988)

originally proposed. The clumpy geometry allows a large range of dust temperatures to coexist at the same distance, as opposed to the monotonic temperature decline with distance that is characteristic of smooth models. Interferometric observations of NGC 1068 with the *VLTI*, for example, resolve the 10 μm emission and indicate cool dust located close to the nucleus (Jaffe et al., 2004). Similarly, *VLTI* observations of the Circinus galaxy and NGC 3783 provide further evidence of a clumpy dust structure (Tristram et al., 2007; Beckert et al., 2008).

Initially, we minimize the number of model free parameters and consider a spherical distribution of clumps. Although this geometry does not generally provide any clear lines of sight to the central engine, the simplified spherical models are powerful, and they capture the essence of the MIR spectra. Fundamentally, the total population of clouds produces the observed MIR emission, and the SEDs are insensitive to viewing orientation effects in any case, even when the dust distribution is not spherically symmetric. (We explicitly demonstrate this result below, presenting calculations for toroidal distributions of clouds.) We follow the formalism of Sirocky et al. (2008), which is based on the radiative transfer code of Nenkova et al. (2008a). In the computations, the individual clouds are distributed according to Poisson statistics, with an average number of clouds along a radial ray, N_0 . The clumps are radially distributed according to a power law, $\propto r^{-q}$, from the dust sublimation radius, R_d to an outer radius R_o , which we parameterize with $Y = R_o/R_d$. The bolometric luminosity of the central source sets R_d , with $R_d \simeq 0.4(L_{bol}/10^{45}\text{erg s}^{-1})^{1/2}$ for the AGN heating spectrum and dust sublimation temperature of 1500 K. The optical depth of each cloud in the V band is τ_V , so the total average optical depth through all clouds is $N_0\tau_V$. The dust includes both silicates and graphite, and we use the Ossenkopf et al. (1992) cool silicate optical properties. The model results we present are applicable to any heating source, not restricted to AGNs, because the dust erases all signatures of the incident spectrum from the emergent MIR emission.

We initially leave the model parameters unconstrained in order to show the effects different parameters have on the model curves in the feature-feature diagram. The plotted simulations therefore do not all represent best- (or even “good-”) fitting mod-

els. In exploring these parameter variations, we will identify the parameter values that produce models that generally agree with the observations on the feature-feature diagram.

Figure 6.6 shows the silicate strengths of the clumpy sphere models for a range of N_0 , with $Y = 30$ and $q = 1$. The optical depth per cloud increases along each track of fixed N_0 , from $\tau_V = 10$ (at the upper right) to 80. Overall, increasing N_0 results in diminished silicate emission, with silicate absorption emerging for $N_0 > 3$. Having more clouds increases the chance that bright faces are obscured, and views of dark, absorbed faces occupy more lines of sight. As the optical depth per cloud increases along the constant N_0 track, silicate strength initially decreases. Around $\tau_V = 60$, which corresponds to $\tau_{10} \approx 3$, optical depth effects within individual clouds become important, and the $10 \mu\text{m}$ silicate strength increases as the optical depth per cloud increases further. The $18 \mu\text{m}$ strength generally continues to decrease, with $\tau_{18} < 2$ per cloud when $\tau_V = 80$. These clumpy models describe the type 1 AGN data well, typically with a small number of clouds ($N_0 \sim 2$).

The MIR-emitting region is compact, and clouds located far from the AGN do not significantly affect the silicate feature strengths. We demonstrate this result first considering the radial density profile $q = 2$ models over a range of outer size, Y (Figure 6.7). Having steep radial density profiles, these distributions are inherently compact and therefore are not sensitive to the outer extent. For example, 80% of clouds are located within $3.6R_d$ and $4.8R_d$ for $Y = 10$ and $Y = 100$, respectively. However, the shallower radial distributions are sensitive to the total size because the number of *nearby* clouds is a function of both Y and N_0 . In these cases, replicating the MIR behavior of the small- N_0 compact distributions requires increasing N_0 as the total size increases.

Small numbers of clouds along radial rays in spherical clumpy models best match the silicate strengths of type 1 data, with $N_0 \sim 2$. We find little variation in silicate strength as a function of other parameters when N_0 is small, so the conclusion that the immediate surroundings of these AGNs contain few clouds along radial rays is robust. However, for larger values of N_0 , the silicate strengths depend sensitively on

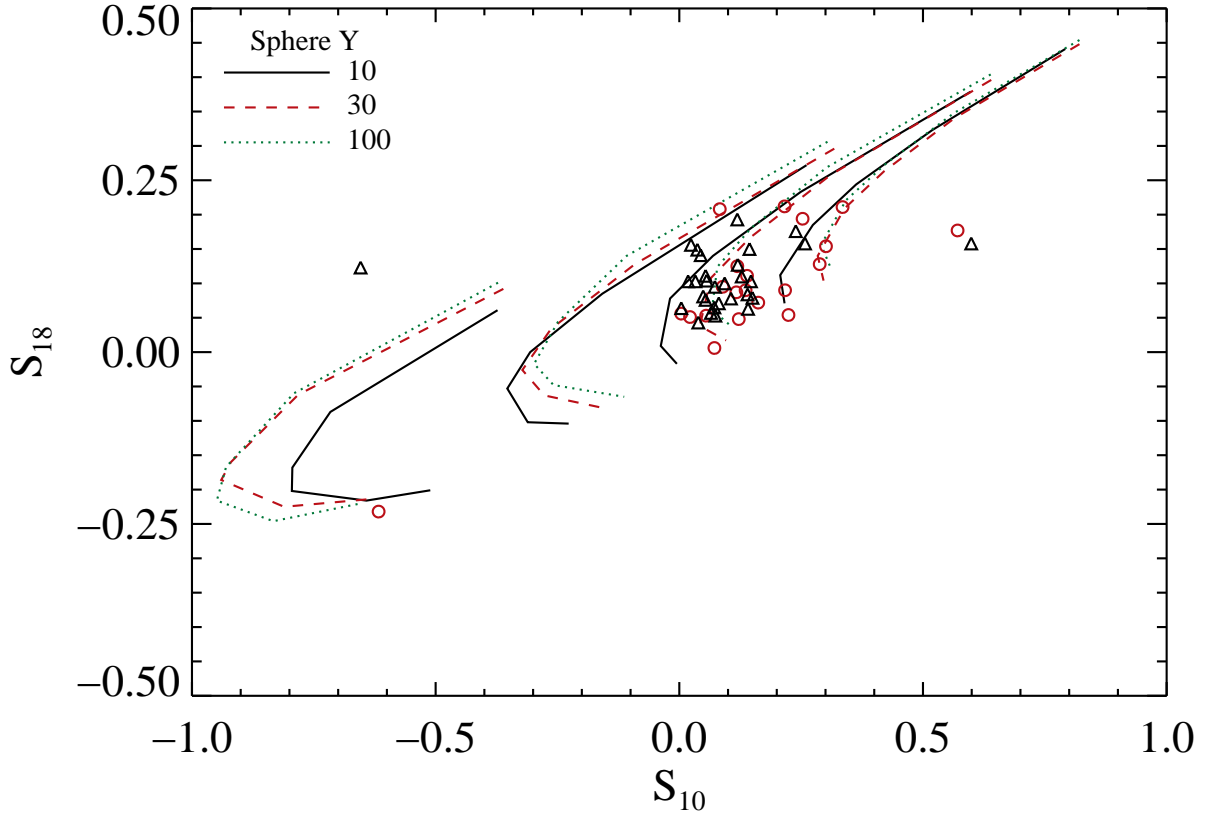


Figure 6.7 Clumpy spherical distributions as a function of radial extent, Y , for $q = 2$. For $Y = 10, 30$, and 100 , we plot curves of $N_0 = 1, 2, 4$, and 10 . Because the clouds closest to the AGN determine the MIR behavior, this inherently compact steep ($q = 2$) distribution is insensitive to the outer radius.

the combination of all parameters, including q and Y , as well.

While the clumpy sphere captures the essence of the MIR emission from these AGNs, general support for unified AGN models, especially the requirement of unobscured lines of sight to the central engine, favors a toroidal distribution. We use the clumpy toroidal models of Nenkova et al. (2002, 2008a,b), which allow variation of the viewing inclination angle, i , and torus scale height, σ , in addition to the parameters of the spherical model. Figure 6.8 illustrates the clumpy torus. The quantity N_0 now represents the average number of clouds through an equatorial ray of the torus, and we consider Gaussian distributions, where the average number of clouds $N_{los}(\beta) = N_0 \exp(-\beta^2/\sigma^2)$ along angle β measured from the equator. (The

inclination angle is measured from the symmetry axis of the torus, so $\beta = 90^\circ - i$.) Unobscured views are more likely for small values of i , with the photon escape probability $P_{esc} = \exp(-N_{los}(\beta))$ describing the likelihood of an unobscured view of the central engine (Nenkova et al., 2008b).

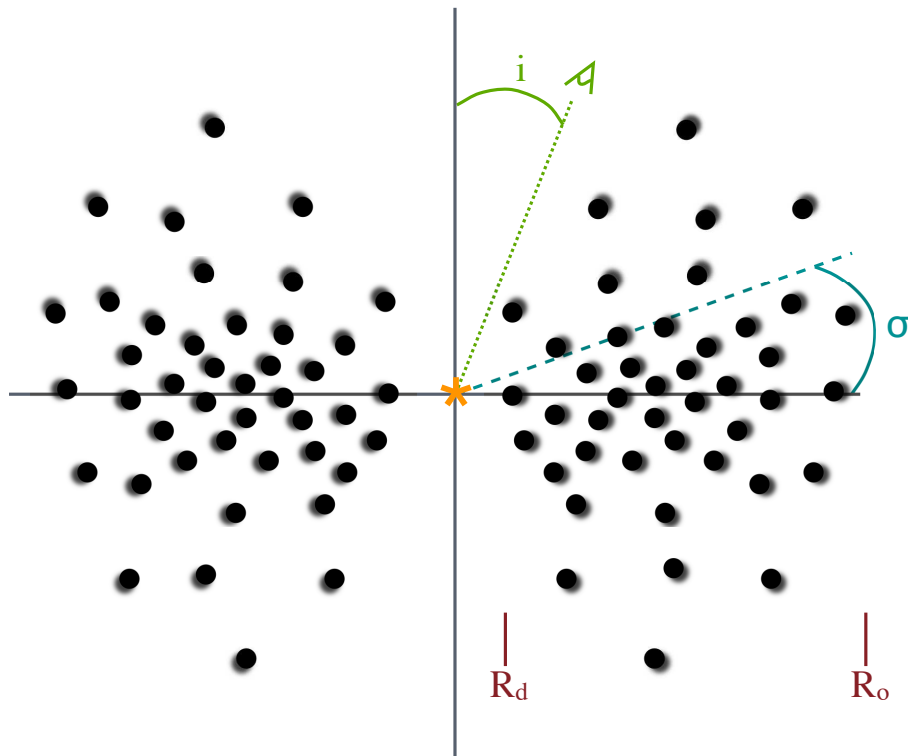


Figure 6.8 Cartoon of the clumpy torus. Emission and obscuration of the central engine are functions of viewing angle, i . Clouds are distributed from the dust sublimation radius, R_d , to the outer radius, R_o , according to a radial power law. The average number of clouds along an equatorial ray is N_0 . The scale height of the distribution is σ , with the average number of clouds $N_{los}(\beta) = N_0 \exp(-\beta^2/\sigma^2)$ along a radial ray at angle β measured from the equator.

The clumpy nature of the dust is fundamental, and as a result, the toroidal distributions occupy a region of the feature-feature diagram similar to that of the spherical arrangements. The toroidal calculations uphold the general conclusion that the MIR-emitting region is small. For example, these inherently compact $q = 2$ results are

insensitive to the total outer extent of the torus, similar to the spherical calculations above. The flat ($q = 0$) radial density profile, however, is a strong function of outer radius (Figure 6.9). In this case, the most compact tori (having $Y = 10$) generally describe the data well, with $N_0 \sim 4$. The clouds are spread over a large volume in the extended ($Y = 100$ or $Y = 30$) tori when $q = 0$. With this radial distribution few clouds are located close to the nucleus, even when the total number of clouds is large. For example, using model parameters $Y = 100$, $q = 0$, and $N_0 = 10$, an average of only two clouds are located within $20R_d$ along equatorial rays. As a result, this particular combination of parameters describes many of the observations. However, a significant fraction of observations lie above these models (having greater S_{18}), even for large values of N_0 . No change in other parameters can shift the $q = 0$, $Y = 100$ model tracks up to account for the stronger S_{18} measurements. Thus, this combination of parameter values is not generally characteristic of the observed sample, although it may describe particular galaxies.

Computations of varying q for fixed Y again show that the nearby clouds determine the silicate feature strengths. In Figure 6.10, we plot the strengths for models in which q ranges from 0 to 2, with $Y = 30$, $i = 30^\circ$, $\sigma = 45^\circ$, and $N_0 = 1, 2, 4$, and 10. Models having steeper density distributions require fewer clouds along radial rays to match the silicate strength of comparable models having shallower radial distributions. Furthermore, as q increases, a larger fraction of the clouds are located closer to the AGN. For example, with $Y = 30$, in a $q = 0$ distribution, 80% of all clouds are located within $24R_d$ whereas the same fraction of clouds are confined to $4.4R_d$ in the $q = 2$ density profile. The shallowest density profile ($q = 0$) does not follow the general trend of decreasing strength with increasing N_0 as rapidly as the steeper distributions do. Considering the observations, few clouds (~ 6) along radial rays within a compact torus (size $\sim 15R_d$) accounts for the MIR silicate features of unobscured AGNs.

Increasing the torus scale height reduces the silicate strength for a given N_0 , as Figure 6.11 shows. The total cloud distribution determines the behavior of the MIR emission, and an increase in σ results in more clouds overall for a given N_0 .

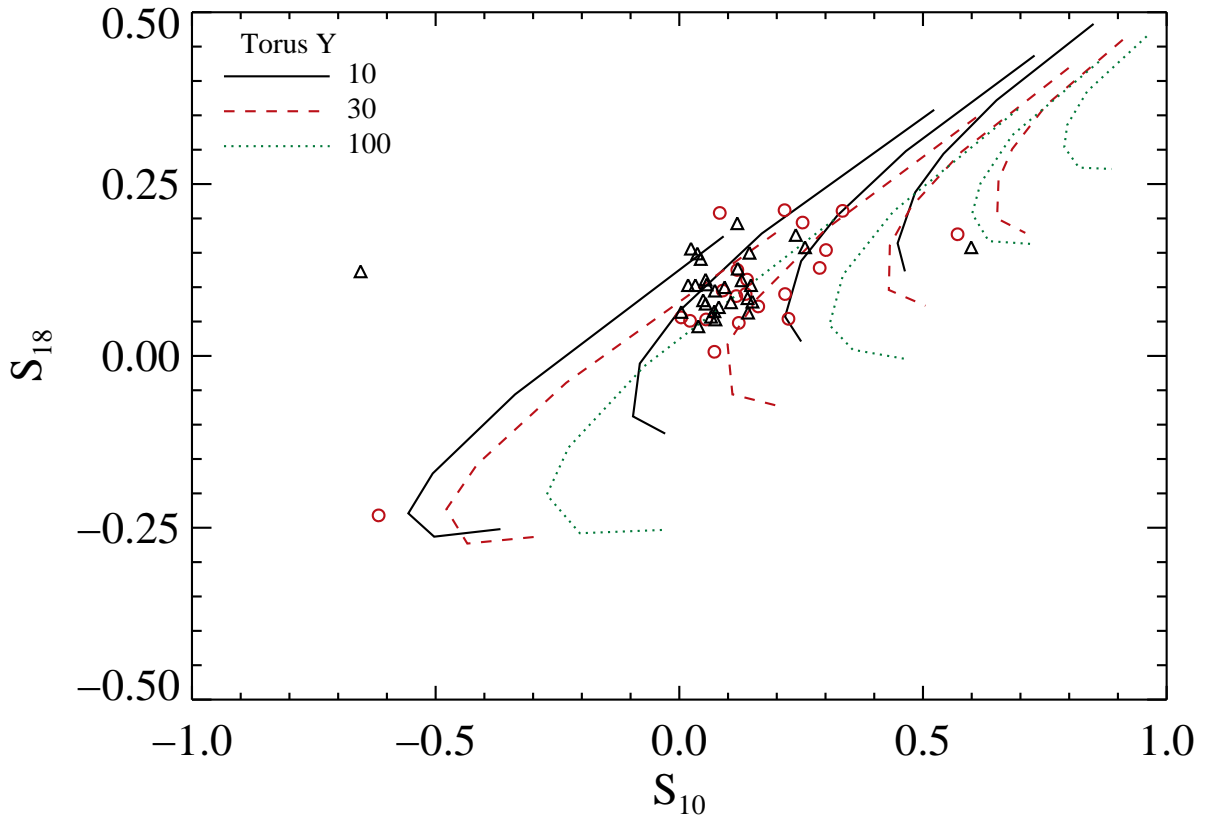


Figure 6.9 Clumpy torus models as a function of Y , for $q = 0$. For $Y = 10, 30$, and 100 , we plot curves of $N_0 = 1, 2, 4$, and 10 , fixing $\sigma = 45^\circ$ and $i = 30^\circ$. In this distribution that is constant with radius, the size of the torus and N_0 are related, with increasing values of both Y and N_0 together producing results similar to models having smaller size and cloud number. The clouds close to the AGN govern the MIR emission, so in a large torus, N_0 must increase to provide enough clouds at small radius to match the features of a smaller torus having fewer clouds that are all confined to the small scale.

Formally, N_0 sets only the average number of clouds along equatorial rays, and σ determines how rapidly the radial number declines with altitude. Again, with more clouds present, the bright cloud faces are more likely to be obscured, which reduces the net silicate emission and produces absorption in some cases. Here, the increased total number of clouds (N_{tot}) is a consequence of increasing σ rather than increasing N_0 alone. However, even for $N_0 = 10$, the $\sigma = 15^\circ$ model shows emission, because N_{tot} is small in this narrow torus. Few high-altitude clouds are present to block views of the directly-heated cloud surfaces that exhibit silicate emission.

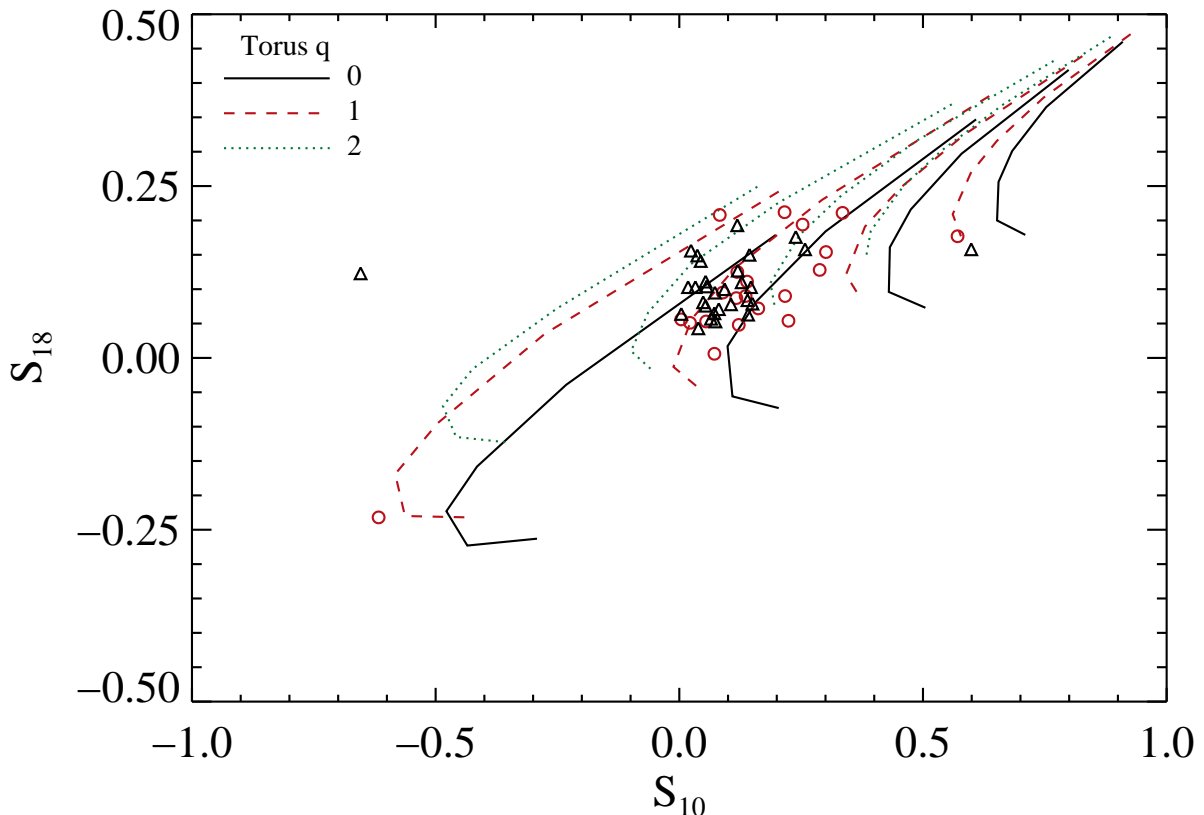


Figure 6.10 Clumpy torus models as a function of radial density profile, q . We plot curves for $N_0 = 1, 2, 4$, and 10 , fixing $Y = 30$ and $i = 30^\circ$. Increasing q places more clouds close to the AGN for a given value of N_0 . Thus, the models having steeper density distributions require fewer clouds to match the silicate emission of the bulk of the data. The shallowest density profile ($q = 0$) does not follow the general trend of decreasing strength as rapidly as the steeper distributions with increasing N_0 . A compact torus (effective size $\sim 15R_d$) having few clouds along radial rays (~ 6 along the equator) accounts for the MIR silicate features of unobscured AGNs.

The dominant direct view of a hot optically thin surface produces strong silicate emission in general, which is typical of smooth torus models of type 1 AGNs. The small- σ case approaches a two-dimensional dust distribution and explicitly demonstrates the failure of this simplification (in a clumpy or smooth arrangement), given the observed weak silicate features. Instead, the mixture of contributions from hot and cold cloud faces is the essence of the MIR emission. Thus, despite the defect of the spherical models in not providing unobscured lines of sight to the AGN in general, they better approximate the MIR results than a two-dimensional geometry does, and

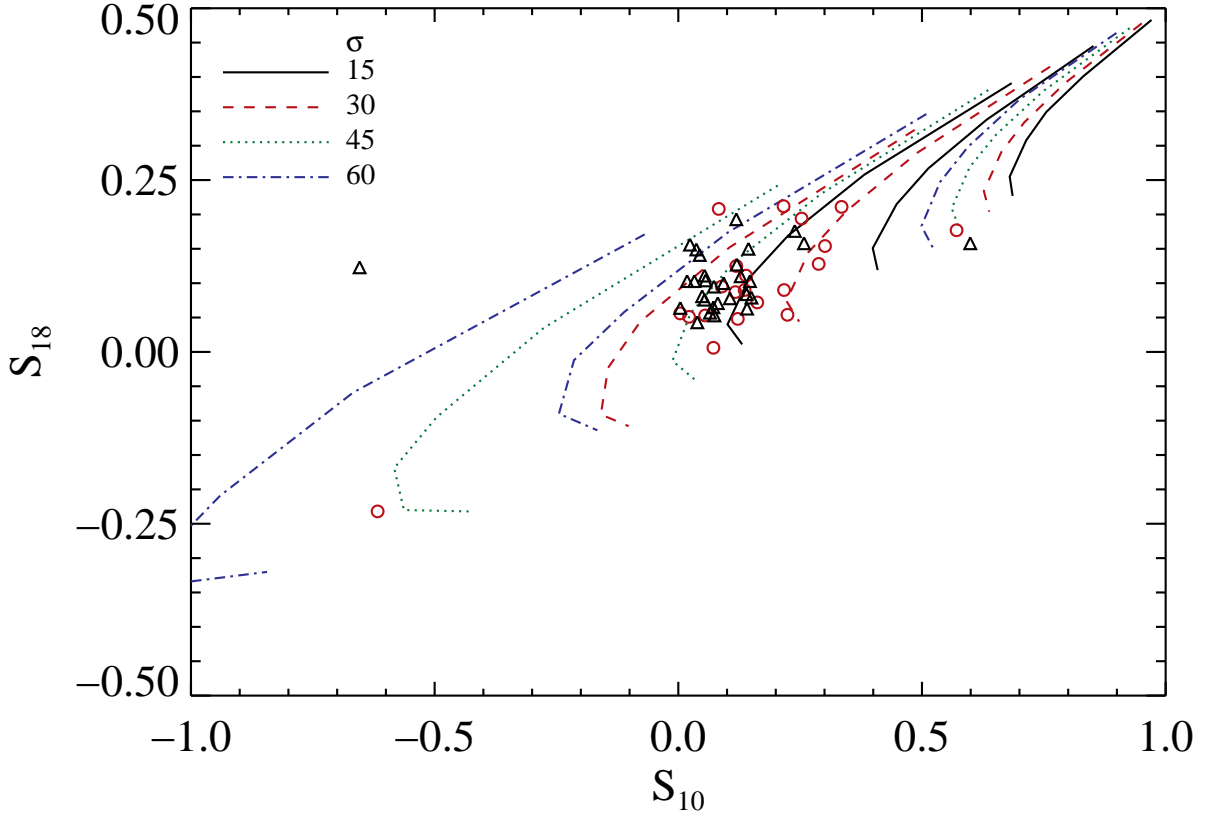


Figure 6.11 Clumpy torus models as a function of σ . We plot curves of $N_0 = 1, 4,$ and $10,$ fixing $Y = 30, q = 1,$ and $i = 30^\circ.$ Increasing the torus scale height reduces the silicate strength for a given $N_0,$ obeying the general trend of decreasing strength with increasing total cloud number. However, even for $N_0 = 10,$ the $\sigma = 15^\circ$ model shows emission, because this thin torus contains fewer clouds to block direct views of bright cloud faces. We measure the same effect for other values of Y and $q.$

the development to the toroidal configuration ultimately corrects this problem.

We consider several inclination angles for fixed N_0 and σ and find no significant differences in the models' silicate strengths for small i typical of type 1 views ($i \leq 40^\circ$). Thus, the silicate features do not usefully diagnose the viewing angle, and we adopt $i = 30^\circ$ in the comparisons below. According to unification schemes, the only difference between type 1 and type 2 AGNs is the viewing angle, whereby direct views of the central engines of type 2 AGNs are obscured, although the dusty AGN surroundings are inherently the same in both cases. A smooth torus strictly separates the different types at a particular viewing angle, distinguishing lines of sight through

the dusty torus material from unobscured views near the symmetry axis. The clumpy formalism presents no strict dividing line, however. Instead, type 1 or type 2 views may arise from any angle, but lines of sight near the equatorial plane are more likely to be obscured, and those near the symmetry axis are more likely to remain clear. The escape probability, P_{esc} , describes the likelihood of a type 1 view, and it is a function of i , σ , and N_0 .

We compare clumpy torus properties that describe the type 1 observations well to predict the silicate characteristics of their type 2 counterparts, viewed at higher inclination, which are obscured. We find that these type 2 AGNs show less silicate emission than type 1 views of the same dust distribution. Specifically, we calculate the silicate strengths for combinations of model parameters that describe the type 1 measurements well: $N_0 = 2-4$, $\tau_V = 30-60$, $\sigma = 30-60^\circ$, with $Y = 10-30$ for $q = 1$, and $Y = 10-100$ for $q = 2$. The corresponding type 2 views ($i = 70^\circ$) yield $-0.4 < S_{10} < 0.15$ and $-0.15 < S_{18} < 0.18$, a wider range of silicate strength than the $i = 30^\circ$ views exhibit. Overall, the silicate is generally weakly absorbed in the obscured AGNs, which agrees with previous observations (Hao et al., 2007; Levenson et al., 2009). Another way to test unified AGN schemes is to model the characteristic clumpy distribution of observed type 2 AGNs and compare this result with the type 1 distributions. The peak of the $10 \mu\text{m}$ silicate strength distribution of the Hao et al. (2007) Seyfert 2s ranges over $-0.4 \leq S_{10} \leq -0.1$, which corresponds to $N_0 \simeq 3-4$ in the $i = 70^\circ$ clumpy torus models using the same parameter combinations as above. Changing inclination to $i = 30^\circ$ and holding all other parameters constant, the silicate strengths of the $N_0 = 3$ or 4 models match those of the type 1 observations. These results are again consistent with standard AGN unification, whereby the central engine and its immediate environment are the same in all AGNs, and variations in viewing geometry alone produce observable differences. One further consequence of the clumpy geometry is that it *can* produce silicate emission even when the AGN is obscured, which has been observed (Sturm et al., 2006; Teplitz et al., 2006; Hao et al., 2007), unlike a smooth distribution, in which type 2 AGNs always exhibit silicate absorption. Even when the AGN and broad line region are hidden, direct view of

some hot cloud faces can result in measurable silicate emission.

Despite the model degeneracies, we identify several ranges of “standard” parameters that describe the data well and do not impose severe restrictions on other parameters. In particular, we favor $Y = 30$, $q = 1$, $\sigma = 45^\circ$, $i = 30^\circ$, $\tau_V = 30\text{--}60$, and $N_0 \leq 6$. Because the clouds close to the AGN determine the MIR emission, confining the total extent of the torus ($Y = 10$ or 30) generally produces models that describe the data well. Recent observations also show a compact MIR torus, with sizes of $3\text{--}5R_d$ and $10R_d$, in Mason et al. (2006) and Tristram et al. (2007), respectively. The extended ($Y = 100$) torus is successful only when the clouds are concentrated (with radial density profile $q = 2$). Similarly, in the constant density distribution ($q = 0$), only $Y = 10$ yields acceptable results.

The MIR measurements alone do not strongly constrain the torus scale height. Instead, relative numbers of type 1 and 2 Seyfert galaxies indicate $\sigma \simeq 30$ to 45° (Schmitt et al., 2001; Hao et al., 2005), and consideration of the SED and $10\ \mu\text{m}$ silicate feature favors $\sigma = 30^\circ$ (Nenkova et al., 2008b). However, the $\sigma = 30^\circ$ models underpredict S_{18} at lower values of S_{10} , even with large numbers of clouds ($N_0 > 10$). Thus, we adopt $\sigma = 45^\circ$ as the standard value and consider the range $30^\circ < \sigma < 60^\circ$ to be applicable to various individual galaxies. A disk-like geometry suggested by Schweitzer et al. (2008) with a clumpy distribution could be identified as a small- σ torus, but low σ values disagree with the observations. Because varying inclination angle does not significantly change the strength measurements provided that $i < 40^\circ$, we discount directly face-on views and identify $20^\circ < i < 40^\circ$ to be typical of these type 1 AGNs. Furthermore, models of $\tau_V = 30\text{--}60$ produce silicate strengths that are similar to those of the observations.

The physical characteristics of clumpy dust distributions are fundamentally different from those of smooth distributions. Both spherical and toroidal clumpy models cover the same regions of the feature-feature diagram, which remain inaccessible to all smooth descriptions. The behavior of the silicate features in the simplified clumpy spherical models yields results that are directly applicable to the more realistic clumpy torus models. To account for the MIR observations, the small-scale dust distribu-

tion is relevant, and both geometries show how the total torus extent and radial distribution together govern the effective compactness. In addition, small numbers of clouds within the small sphere or torus agree with the observations of type 1 AGNs. However, the N_0 parameter is not constant across all models that describe the data: it increases from the sphere to the torus generally, and it increases with decreasing torus scale height. We therefore conclude that the total number of clouds available to reprocess the intrinsic AGN flux, N_{tot} (not N_0), and their distribution ultimately determine the behavior of the emergent MIR emission.

Figure 6.12 demonstrates that for the same inputs of Y and q , fitting the data requires larger values of N_0 in the torus than in the sphere. In general, translating from any torus to sphere model requires $N_0(torus) > N_0(sphere)$. The parameter N_0 describes only the number of clouds along the equatorial ray of the torus, and the number of clouds diminishes with altitude. For a given N_0 , the spherical model contains more clouds in total than the toroidal model does. Thus, in order to achieve the same N_{tot} in both geometries, N_0 must be greater in the torus. The spherical models yield robust conclusions about the nature of the dust distribution around AGNs, confirming that few clouds within a small radius account for the observed MIR emission. However, because the spherical geometries generally fail to provide an unobscured view of the central engine, which these type 1 AGNs demand, we conclude that a clumpy, dusty torus characterizes the immediate surroundings of AGNs.

6.5 Conclusions

Dust reprocesses the AGN continuum to emerge at MIR wavelengths, and we model both the resulting continuum and spectral features at 10 and 18 μm due to a common dusty region. Isolating unobscured AGNs, we find these features in emission, both in Seyfert 1 galaxies and in quasars. The emission is weak, however, with average emission strength $S_{10} = 0.11$ and 0.18 in the Seyferts and quasars, respectively. In contrast, an optically thin medium, such as the directly-viewed hot interior of a smooth torus, would yield stronger emission ($S_{10} = 1.2$). We conclude that the observable but weak emission is a consequence of clumpy AGN surroundings. We measure the

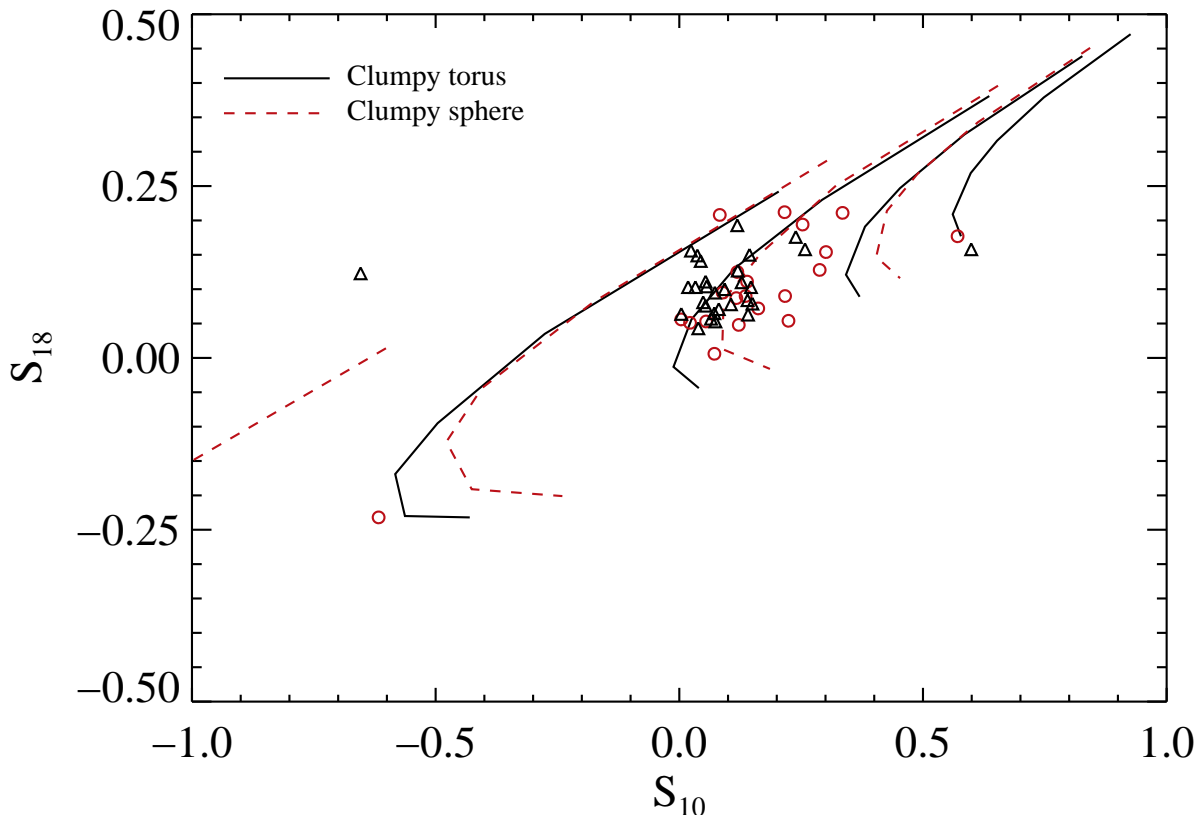


Figure 6.12 Clumpy torus and clumpy sphere models. We plot curves of $N_0 = 1, 2, 4,$ and $10,$ fixing $Y = 30$ and $q = 1$ in both cases, and $i=30^\circ$ and $\sigma = 45^\circ$ in the torus models. The sphere and torus results are extremely similar for different values of $N_0,$ with larger N_0 in the torus. Because all clouds reprocess the AGN light and contribute to the MIR emission, the larger value of the parameter N_0 in the toroidal distribution is required to have the same total number of clouds as the spherical distribution with smaller $N_0.$

peak wavelength $\lambda_{10} = 10.0 \pm 0.1$ and $10.1 \pm 0.2 \mu\text{m}$ in the Seyfert 1s and quasars, respectively. These values are consistent with radiative transfer computations using the optical properties of silicates that Ossenkopf et al. (1992) model. In agreement with earlier work, we find that star formation increases with AGN luminosity, using $[\text{Ne II}]$ and $6.2 \mu\text{m}$ PAH to quantify the star formation contribution and the 5 and $14 \mu\text{m}$ continua as proxies for the AGN luminosity. The fractional contribution of star formation to the total bolometric luminosity of these galactic centers decreases with AGN luminosity. Furthermore, considering the flux ratio $F_5/F_{14},$ we can describe the type 1 AGN spectra as a power law, with power law indices ranging from -0.5 to -2.8

in the Seyfert 1s and -0.3 to -1.6 in the quasars.

The strengths of the 10 and 18 μm silicate features together are sensitive to the distribution of dust surrounding any heating source, including stars as well as AGNs. We interpret the silicate strength measurements of these isolated AGNs as a consequence of a native AGN environment that is clumpy. The dust that determines the MIR behavior is confined to small scales. In radiative transfer calculations, either limiting the total radial extent of the dust or concentrating the cloud distribution effectively produces the compact distributions that describe the observations.

A toroidal distribution of clouds is consistent with unified AGN schemes, offering unobscured lines of sight to the central engine from some viewing angles. The total cloud distribution, not only the clouds located along the line of sight, determines the MIR emission. As a consequence, the MIR output is effectively isotropic, as observations of all types of AGNs show (e.g., Horst et al., 2006). We thus account for the model results in general: properties such as torus scale height and the number of clouds along radial rays that determine the total cloud distribution govern the MIR behavior. Although spherical distributions do not generally provide the unobscured views these type 1 AGNs require, they do usefully capture the essence of the total cloud distribution while minimizing the number of free parameters. While two silicate strength measurements cannot constrain all the free parameters of any of the models, we find that the type 1 AGNs are located in an area of the feature-feature diagram that only clumpy models occupy. Few clouds are located along radial rays within the compact torus, which is consistent with column density variability observed in some AGNs (Elvis et al., 2004; Risaliti et al., 2007). The MIR observations are not sensitive to the more distant cloud population, and we conclude the arrangement of dust immediately surrounding the AGN central engine is a clumpy torus that contains few clouds (~ 6) along radial rays within a small radius ($\sim 15R_d$).

Chapter 7

Determining the AGN Viewing Angle with Spectropolarimetry and MIR Emission

In this chapter, we will further examine a key ingredient of AGNs, the obscuring dusty torus. Despite much work, the intricate structure and characteristics of the torus remain unconstrained. We implement two independent methods that allow for the determination of the torus viewing angle – optical spectropolarimetry and clumpy torus model fittings of mid-IR spectra. Our goal in this study is to not only quantify the inclination angle of the torus, but to also enable a more detailed examination of the relationship between optical polarizations and MIR emission.

7.1 Spectropolarimetry

Spectropolarimetry is an important tool in understanding AGNs as it provides a view into the central regions of active nuclei via scattered polarized light and allows us to probe the structure of the emission source and of the polarizing material. Spectropolarimetry is the use of spectroscopy on polarized light, or moreover, the measure of the polarization of light at different frequencies or wavelengths. The location of the light-scattering material can be identified by using both the polarization position angle (θ) and the degree of polarization, the latter calculated by comparing the polarized and total flux densities. Section 7.1.5 explains this method in detail.

7.1.1 Spectropolarimetry in the Realm of AGNs

Although a large array of AGN classifications exist, the discovery in polarized light of broad-line emission from Seyfert 2 NGC 1068 (Antonucci & Miller, 1985) initiated the emergence and development of a unification scheme for Seyfert galaxies, which simply suggests that Seyfert 1 and 2 nuclei are intrinsically the same class of object viewed at different orientations. In the context of Seyfert 2 galaxies, our direct view

of the central continuum source and the broad line emitting region is obscured by an optically and geometrically thick torus of molecular gas and dust, co-planar with the accretion disk. While the torus inhibits radiation from escaping equatorially, radiation is free to escape in conical beams aligned with the poles of the torus. Previous authors (Antonucci & Miller, 1985; Miller et al., 1991; Young et al., 1995) postulated that scattering by free electrons above the poles of the torus could explain the optical polarization properties of NGC 1068 and other type 2 AGNs. Others such as Bailey et al. (1988), however, favored dust scattering as the polarization source, though for distant AGNs, the electron- and dust-scattering regions cannot be resolved (Smith et al., 2004). Light emitted from nuclear regions of AGNs cannot be directly observed from generic Seyfert 2 orientations, leaving Seyfert 2s with a lack of broad-line emission. However, light can be scattered in the observer’s direction likely by a mixture of free electrons and dust, and in polarized light, broad-line emission can reveal the presence of hidden type 1 cores.

The discovery of polarized broad-lines has motivated many spectropolarimetric studies of Seyfert 2 galaxies (Inglis et al., 1993, 1995; Young et al., 1996; Tran, 2003, and references therein), and an obscured broad line region has been confirmed in nearly 50% of the local Seyfert 2s (Gu & Huang, 2002). In contrast with the Seyfert 2s, the optical polarization properties of the Seyfert 1s received relatively little attention, in spite of evidence suggesting that scattered light emerging from Seyfert 1s follows a different path than that in Seyfert 2s (Antonucci, 1983; Brindle et al., 1990; Goodrich & Miller, 1994). Later sections describe a spectropolarimetric study that examined both Seyfert classes and offers an explanation of the cause of different polarization properties between the two.

7.1.2 Type 2 Scattering Geometry

The optical polarization characteristics of Seyfert 2 galaxies prompts an explanation as to the geometry of the scattering region. As seen in Section 7.1.1, a torus of molecular gas and dust surrounds the central engine of an AGN. Obscuring the BLR and hot gas and dust near the center, the torus allows radiation to escape only in

the direction of the toroidal poles. For an observer viewing an AGN at angles nearly equatorially or edge-on, the torus halts observation of broad-line emission. However, polarized broad lines in Seyfert 2 galaxies exist, and their presence is due to scattering of light from the AGN hidden within the circumnuclear torus.

Geometrically, light from the BLR and central continuum source emanate out of the torus illuminating the NLR. Dust and free electrons scatter some of the light into our line-of-sight causing it to be polarized (See Section 2.4). The scattered light has a polarization PA perpendicular to the incident light’s direction, and thus requires that the ‘pre-scattered’ photons originated in a direction parallel to the AGN’s principal axis of rotation. If this principal axis is defined by the rotation axis of the accretion disk, and provided that the axes of the torus and radio source are co-aligned, then the scattered light will be polarized with its \mathbf{E} perpendicular to the projection of the radio source axis and to the axis of the torus. In fact, Antonucci (1983) and Brindle et al. (1990) found that the optical polarization PA is almost always perpendicular to the radio source axis in Seyfert 2s. This picture would explain why some Seyfert 2 galaxies have type 1-like spectra in polarized light and also accounts for the observed perpendicular orientation of the polarization \mathbf{E} vector relative to the radio source (Smith et al., 2004).

7.1.3 Type 1 Scattering Geometry

Seyfert 1 galaxies do not have the same optical polarization properties as Seyfert 2s, which in turn implies that the simplest unification geometry including only a single polar scattering region is incomplete. The same general torus description as mentioned for the type 2 AGNs applies for type 1s, but the unification scheme specifies that Seyfert 1s are observed at more pole-on inclination angles. This orientation prohibits the torus from obscuring the nuclear source continuum and the BLR, thus yielding broad line emission to be observed in type 1 AGNs. Regarding the polarization properties of Seyfert 1s, if only the polar scattering region is present, type 1 galaxies should still be polarized perpendicular to the projected radio source axis. However, the optical polarization \mathbf{E} vector is more often aligned with this axis (An-

tonucci, 1983, 1984). This implies that the scattered light emerging from type 1 nuclei follows a path different from that of type 2 galaxies (Antonucci, 1983; Brindle et al., 1990; Goodrich & Miller, 1994). Scattering locations in addition to the polar scattering region are needed to explain both the alignment of the polarized light \mathbf{E} vector with the radio axis and the polarization properties.

Young et al. (1999); Smith et al. (2002, 2004, 2005) identified the different scattering paths that explain the observed polarization characteristics of Seyfert 1 nuclei and find the properties vary progressively with orientation. The optical polarization in the majority of Seyfert 1s is dominated by scattering in a compact region that lies in the equatorial plane of the circumnuclear torus (and is thus obscured in Seyfert 2s). Since scattering occurs in the plane of the torus, the scattered light has its \mathbf{E} vector parallel to the radio source axis.

Seyfert 1s exhibit a much wider range of optical polarization characteristics than Seyfert 2s. Though a majority of the polarization properties of Seyfert 1s are explained in accordance with this equatorial scattering region, about 20% exhibit null polarization, while 5 – 25% show characteristics of Seyfert 2-like polar scattering (Smith et al., 2004) The latter cases are likely explained by having the line-of-sight to the nucleus passing through the upper layers of the torus, producing enough extinction to suppress light from the equatorial scattering region, but without completely obscuring the much stronger direct emission from the BLR.

7.1.4 Interpretation of the Different Scattering Regions

Seyfert 1 and 2 polarization properties require a refinement of the unified model which can accommodate the diversity in observed optical polarization properties of Seyfert nuclei. Smith et al. (2002) proposed that these properties of Seyfert nuclei could be explained by a model in which both the broad Balmer line emission and equatorial scattering originate in co-planar rotating disks. Goodrich & Miller (1994) found the maximum degree of polarization expected from scattering comes from disks, so Smith et al. (2002, 2004, 2005) base their polarimetric results on both broad-line emitting and scattering disks, though it was understood that other complicated configurations

such as warped disks or discrete clouds of scatterers may be possible. In this new picture, the broad Balmer line emission is scattered by two distinct scattering regions that produce orthogonally polarized light:

- 1) a compact scattering region co-planar with the line-emitting disk and situated within the equatorial plane of the torus – the ‘equatorial’ scattering region;
- 2) a scattering region situated outside the torus but aligned with the torus/emission disk-axis – the well-established ‘polar’ scattering region.

The inclination of the torus’ axis to the observer’s line-of-sight determines which scattering region is responsible for the polarization characteristics. This is to say that both scattering regions are active, but only one, which is determined by the viewing angle, is dominant and governs the observed polarization properties. Regarding unobscured views towards the central regions (i.e. type 1 AGNs), both scattering regions are detectable, but the equatorial scattering region governs the polarization characteristics in these sources, and Smith et al. (2004) find that the observed polarization appears to be dominated by equatorial scattering in most Seyfert 1 galaxies. Furthermore, if Seyfert 1s are viewed in such a way that toroidal extinction hides the equatorial scattering region (See Section 7.1.3), then properties of the polar scattering region dominate the emission. There also exists the opportunity to view the galaxy face-on, with an inclination angle of 0° , and this orientation leads to null or intrinsically weak polarization because both scattering regions exhibit circular symmetry and cancel. The polar scattering region dominates the polarization characteristics in Seyfert 2 galaxies, or in systems with large inclinations ($i > 45^\circ$), because the equatorial scattering region and the BLR is hidden by the torus.

7.1.5 Polarization Properties

In the context of spectropolarimetry, identifying and understanding behaviors of polarization properties is required to classify their origin. The following briefly explains the techniques of Smith et al. (2002, 2004, 2005) to ascertain the scattering region

by analyzing various polarization parameters. These authors utilize the polarization position angle (θ), the polarized flux density, the percentage of polarization, and the total flux density. Generally speaking, the polarization properties of Seyfert 1 galaxies (namely those whose polarization is governed by the equatorial scattering region) behave differently than those of Seyfert 2s. There exists only in Seyfert 1s both a swing in position angle across the broad $H\alpha$ profile and a dip in polarization in the core of the profile, which is joined by flanking polarization peaks in the wings, as explained below.

The position angle identifies the direction in space that the polarized radiation's \mathbf{E} vector points. In the 'polar' scattered frame, the PA is perpendicular to the principal axis of the system, whereas in the 'equatorial' scattering dominated case, θ is aligned with this axis. Employing optical spectropolarimetry on type 1 nuclei, Goodrich & Miller (1994) studied the polarization of the broad $H\alpha$ line and found a diversity of characteristics, including PA rotations across the line profile. These authors additionally found that scattering in an optically thin disk in the equatorial plane of the system could produce optical polarization PAs aligned with the radio axis. This swing in θ from blue to red can only be produced if broad $H\alpha$ originates in a rotating disk and is scattered in the compact region, which itself must closely surround the disk (Smith et al., 2005). These PA rotations are absent in Seyfert 2 galaxies and in some Seyfert 1 galaxies. In the latter, it is believed that the torus obscures the equatorial scattering region, allowing the polar scattering properties to dominate.

Observing in an optical band containing the $H\alpha$ line, Smith et al. (2002, 2004, 2005) calculate the percentage of polarization using the measured polarized and total flux densities. Attributable to the rotating ring surrounding the disk responsible for the $H\alpha$ emission, a dip in this degree of polarization occurs at the peak of the $H\alpha$ profile. In addition to this dip, the degree of polarization shows peaks on the flanks of the profile, in the wings (see Figure 7.1). This swing does not occur in Seyfert 2 data, and occasionally the percentage of polarization is too weak or undetectable, leading to a categorization of no – or null – polarization.

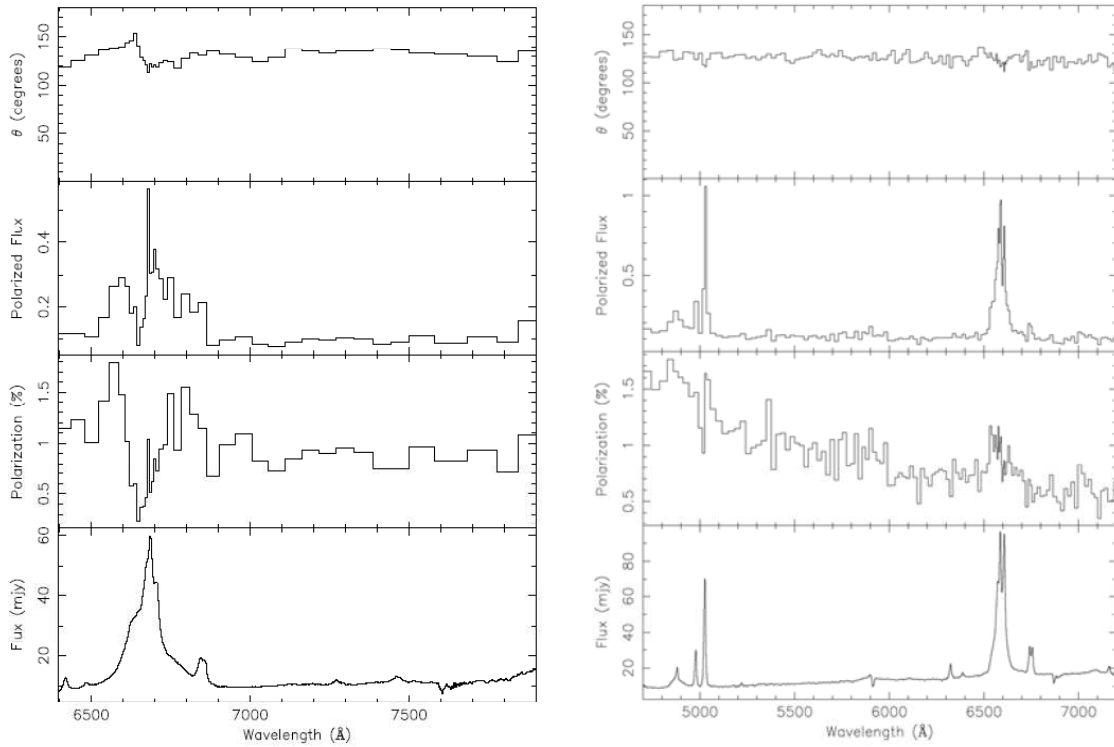


Figure 7.1 Polarization spectra of the Seyfert 1 galaxies Mrk 6 (left) and NGC 3227 (right). From top to bottom: polarization position angle θ ; polarized flux density; percentage polarization; and total flux density. The polarization data are binned to an error of 0.1 percent. Mrk 6 is a Seyfert 1 where equatorial scattering dominates the observed polarization, while NGC 3227 is an example in which polar scattering is dominant (from Smith et al. (2002)). Note the blue to red swing in θ and the peak-trough-peak variation in the degree of polarization over the $H\alpha$ profile are seen only in the equatorially scattered (left) source.

To reiterate, the equatorial scattering region is responsible for the polarization properties for Seyfert 1 sources that have an unobstructed view to this region. These objects exhibit distinctive polarization structure across the broad $H\alpha$ emission-line profile, namely a blue to red swing in θ coupled with a peak-trough-peak variation in degree of polarization. This is naturally produced only if broad $H\alpha$ originates in a rotating disk and is scattered in the compact region, which must closely surround the disk. These structures are absent if the equatorially scattering region is obscured, be it Seyfert 2s or Seyfert 1s whose view still allows for direct sight of the BLR.

7.1.6 Polarization Classes

Four orientation classes are predicted, broadly conforming to the observed range in optical polarization properties among Seyferts (See Figure 7.2). Increasing the inclination angle, i , from pole-on to edge-on yields null polarization Seyfert 1s; then Seyfert 1s showing broad polarization signatures of a compact scattering region located within the torus and whose θ is aligned with the radio source axis; then Seyfert 1s with polarization properties attributed to a scattering cone outside the torus but aligned with the torus disk axis (polar scattering region); and lastly with Seyfert 2s exhibiting polarized broad lines due to the polar scattering region.

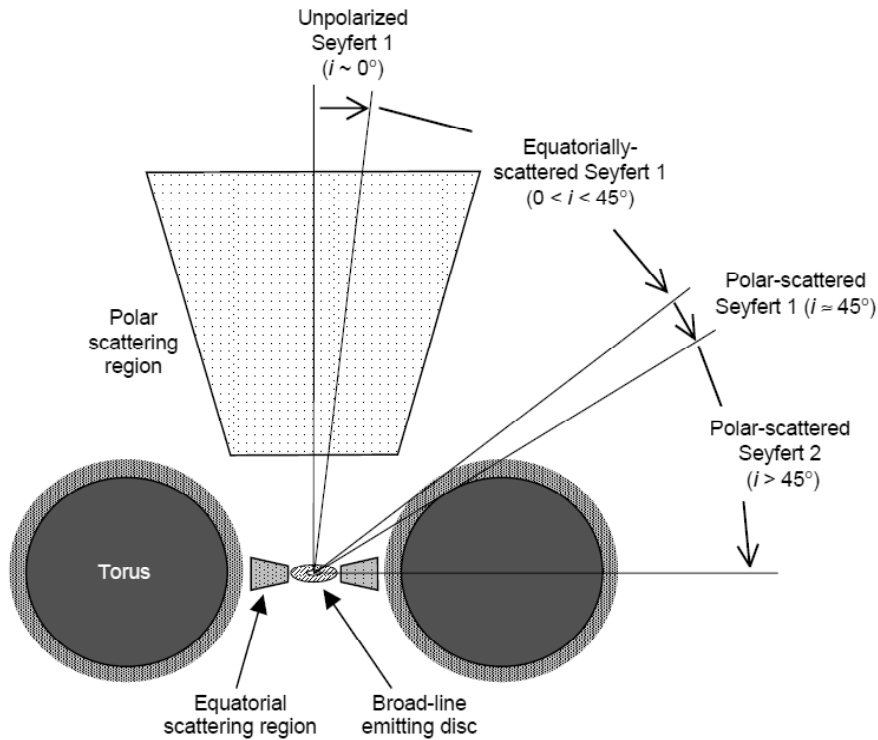


Figure 7.2 Relation between polarization class and orientation in the generic scattering geometry that broadly explains the optical polarization spectra of Seyfert galaxies (from Smith et al. (2004)).

Smith et al. (2002, 2004, 2005) performed analysis of polarization properties (Section 7.1.5) on a sample of ‘representative’ low- z broad-line AGNs, which cover a wide range in luminosity. The sample selection requires broad-line sources (Seyfert types

1 - 1.9 or QSO) to have $z < 0.3$ for the observed $H\alpha$ to line in the optical regime. Furthermore, to achieve polarization measurements to $< 1\%$, the sources chosen must have apparent magnitudes < 16 . The authors calculate the scattering region responsible for the observed polarization signatures for each of their type 1 and 2 Seyferts. The complete sample contains 41 Seyfert 1 galaxies and 20 type 2 AGNs and offers a good coverage of all four polarization classes. It contains 12 null polarization Seyfert 1s, 17 equatorially scattered Seyfert 1s, 12 polar scattered Seyfert 1s, and 20 polar scattered Seyfert 2s. Table 7.1 lists the scattering regions for each source.

Each scattering region can be loosely assigned a range of viewing angles which allow for certain polarization properties (See Figure 7.2). As discussed in Section 7.1.5, when a galaxy is viewed almost face-on ($i \sim 0^\circ$), both scattering regions have circular symmetry leading to null or weak polarization caused by cancellation. Inclinations in the range of $0 < i < 45^\circ$ allow direct lines of sight to both scattering regions, and equatorial scattering generally dominates the observed polarization. Once the inclination angle is comparable to the torus opening angle (σ), the line of sight to the nuclear regions is subject to extinction by the upper layers of the torus. This leads to Seyfert 1s (as the BLR is still observable) having polar scattering properties govern the polarization since the torus obscures the equatorial scattering region. Lastly, at large inclinations ($i > 45^\circ$), both the BLR and the equatorial scattering region are blocked by the torus and any observable broad-lines are only visible in polarized light scattered from the polar scattering region, and this results in a Seyfert 2 with polarized broad lines.

7.1.7 Conclusions

This spectropolarimetric study has determined, via polarization measurements across the structure of the $H\alpha$ emission line profile, two scattering regions responsible for different polarization signatures – the polar and equatorial scattering regions. Polarization properties attributable to the equatorial scattering regions include a blue to red swing in θ coupled with a peak-trough-peak variation in degree of polarization. These are produced only if the $H\alpha$ emission originates in a compact rotating disk.

Table 7.1. Polarization Classes.

Source Name	Type	Polarization	Source Name	Type	Polarization
Ark 120	S1	EQUATORIAL	NGC 4593	S1	POLAR
Fairall 51	S1.5	POLAR	NGC 5548	S1.5	EQUATORIAL
IC 3599	S1n	NULL	NGC 7213	S1	NULL
IC 4329A	S1.2	POLAR	NGC 7469	S1.5	NULL
IZW1	S1n	EQUATORIAL	PG 1211+143	S1n	NULL
KUV 18217+6419	S1.2	EQUATORIAL	PG 1612+261	S1.5	NULL
MCG -6-30-15	S1.5	POLAR	PG 1700+518	S1	EQUATORIAL
Mrk 1040	S1	POLAR	PG 2214+139	S1	EQUATORIAL
Mrk 1048	S1.5	EQUATORIAL	PHL 1811	S1n	EQUATORIAL
Mrk 1239	S1n	POLAR	UGC 7064	S1.9	POLAR
Mrk 231	S1	POLAR	3C321	S2	POLAR
Mrk 279	S1	EQUATORIAL	3C234	S2	POLAR
Mrk 335	S1n	EQUATORIAL	IRAS F04385-0828	S2	POLAR
Mrk 478	S1n	NULL	IRAS F15480-0344	S2	POLAR
Mrk 486	S1	POLAR	IC 5063	S2	POLAR
Mrk 507	S1n	POLAR	IRAS 05189-2524	S2	POLAR
Mrk 509	S1.5	EQUATORIAL	IRAS 18325-5926	S2	POLAR
Mrk 590	S1	NULL	IRAS 20210+1121	S2	POLAR
Mrk 6	S1.5	EQUATORIAL	IRAS 20460+1925	S2	POLAR
Mrk 705	S1.2	NULL	MCG -05-23-016	S2	POLAR
Mrk 766	S1n	POLAR	Mrk 463E	S2	POLAR
Mrk 841	S1.5	EQUATORIAL	NGC 1068	S2	POLAR
Mrk 876	S1	EQUATORIAL	NGC 2992	S2	POLAR
Mrk 896	S1n	NULL	NGC 4388	S2	POLAR
Mrk 915	S1.8	NULL	NGC 5252	S2	POLAR
Mrk 926	S1.5	NULL	NGC 5506	S2	POLAR
NGC 3227	S1.5	POLAR	NGC 5728	S2	POLAR
NGC 3516	S1.5	NULL	NGC 7582	S2	POLAR
NGC 3783	S1.5	EQUATORIAL	NGC 7674	S2	POLAR
NGC 4051	S1n	EQUATORIAL	TOL 1238-364	S2	POLAR
NGC 4151	S1.5	EQUATORIAL			

Note. — Seyfert Type classifications includes Seyfert 1n (narrow line Seyfert 1); where Seyfert is abbreviated as S. The observed polarization is classified according to the scheme outlined in Figure 7.2.

Additionally, the \mathbf{E} field vector is parallel to the radio source, whereas the vector is perpendicular to the system axis in the polar scattered case. Concerning the latter, the polarization structures of θ and the degree of polarization are absent. This can be described by a geometry that has sufficiently large inclination angles such that the equatorially scattering region is obscured. Furthermore, the study applied this last concept of relating polarization classes and inclination angles and assigned these classifications to a large sample of Seyfert galaxies. The upcoming sections will compare the inclination angle results of spectropolarimetry to those of fitting MIR emission with clumpy torus models.

7.2 Utilizing the Mid-Infrared

Active galactic nuclei show either a presence or absence of spectrally broad lines, classifying them as type 1 or type 2, respectively. Unified AGN models (Antonucci, 1993) account for differences, such as this, in terms of viewing geometry, with an optically and geometrically thick dusty torus blocking the view of the broad line region and central engine from some (type 2) lines of sight. While several means of observation have inferred the existence of the torus, its properties remain unconstrained.

Toroidal silicate dust reprocesses the high energy radiation from the central engine into MIR radiation. The behavior of MIR spectra depends on the arrangement of this dust, and though initial radiative transfer calculations of smooth, uniform tori could not explain the behavior, models using a clumpy toroidal dust distribution can (See Chapter 5). To further quantify the toroidal distribution of dust, we will implement the radiative transfer code of Nenkova et al. (2002, 2008a,b), CLUMPY (See Section 4), for our clumpy toroidal models. Studies of AGNs which use the aforementioned clumpy models found spatial scales of tori to be a few tens of parsecs, a compactness consistent with interferometric observations (Mason et al., 2006, 2009; Ramos Almeida et al., 2009; Levenson et al., 2009; Alonso-Herrero et al., 2011; Ramos Almeida et al., 2011).

In this section, we will examine the sample of AGNs studied within the context of spectropolarimetry by fitting each source's 5-30 μm *Spitzer IRS* spectrum with

synthetic torus models generated by CLUMPY, all in order to further understand the environment of the dust close to the central engine. Additionally, we will determine if the two methods of determining the torus viewing angle – spectropolarimetry and clumpy torus model fittings of mid-IR spectra – produce consistent results.

7.2.1 Sample and Data Reduction

This project examines whether spectropolarimetry and model fittings of MIR spectra yield similar results regarding the torus inclination angle, and it therefore must follow that both methods use the same sample. Hence, we adopt the sample of 61 Seyfert galaxies from Smith et al. (2002, 2004) for which polarization classifications have been assigned (See Section 7.1.6 and Table 7.1). The source selection is part of the study by Buchanan et al. (2006) who considered all Seyfert galaxies from the extended 12 μm sample of Rush et al. (1993) that have $cz < 10,000 \text{ km s}^{-1}$. The spectropolarimetry approach placed additional selection requirements, namely the necessity to have $z < 0.3$ such that the observed $\text{H}\alpha$ line lies within the optical band. Also, to achieve polarization measurements to within 1%, sources must have apparent magnitudes < 16 , so there exists the possibility that the sample selection is biased by polarization requirements. Table 7.2 lists measured quantities of our sample.

For the 41 Seyfert 1 and 20 Seyfert 2 sources, we obtained archival low-resolution spectra from the *Spitzer Space Telescope Infrared Spectrograph (IRS)* (Werner et al. 2004; Houck et al. 2004). Like the *Spitzer* observations of Section 6, we used the standard *Spitzer* Science Center pipeline and extracted the spectra with the *Spitzer IRS* Custom Extraction (SPICE) package. The observations were performed in either staring or mapping mode. We used two nodded positions of the same order to background subtract the staring mode observations, in which the nucleus is always centered in the slit. Differencing exposures in first and second orders provided background subtraction of mapping mode data. In addition to the central spectrum obtained with the slit centered on the nucleus, we included contributions from two adjacent off-center spectra for the mapping mode observations. We scaled short wavelength spectra to match the flux of the long-wavelength order “Long Low,” which has the widest slit

Table 7.2. Observations and Galaxy Data for Seyfert 1s

Source Name	R.A. (J2000.0)	Decl. (J2000.0)	z	Scale (pc arcsec ⁻¹)	AOR
Ark 120	05 16 11.4	-00 08 59	0.033	677	18941440
Fairall 51	18 44 54.0	-62 21 53	0.014	289	26489088
IC 3599	12 37 41.2	+26 42 28	0.022	442	18852608
IC 4329A	13 49 19.3	-30 18 34	0.016	328	18506496
IZW1	00 53 34.9	+12 41 36	0.059	1244	3761920
KUV 18217+6419	18 21 57.3	+64 20 36	0.297	7282	4676096
MCG -06-30-015	13 35 53.8	-34 17 44	0.008	157	4849920
Mrk 1040	02 28 14.5	+31 18 42	0.017	341	12460032
Mrk 1048	02 34 37.8	-08 47 15	0.043	900	13022720
Mrk 1239	09 52 19.1	-01 36 43	0.020	409	12453120
Mrk 231	12 56 14.2	+56 52 25	0.042	880	34294016
Mrk 279	13 53 03.4	+69 18 30	0.031	629	7616512
Mrk 335	00 06 19.5	+20 12 10	0.026	531	12476416
Mrk 478	14 42 07.5	+35 26 23	0.079	1694	10452224[SL] 14199040[LL]
Mrk 486	15 36 38.4	+54 33 33	0.039	810	10949632
Mrk 507	17 48 38.4	+68 42 16	0.056	1178	14450688
Mrk 509	20 44 09.7	-10 43 25	0.034	713	18508288
Mrk 590	02 14 33.6	-00 46 00	0.026	544	18508544
Mrk 6	06 52 12.3	+74 25 37	0.019	385	12483584
Mrk 705	09 26 03.3	+12 44 04	0.029	602	14203392
Mrk 766	12 18 26.5	+29 48 46	0.013	264	12465408
Mrk 841	15 04 01.2	+10 26 16	0.036	756	3761664
Mrk 876	16 13 57.2	+65 43 10	0.129	2861	10452480[SL] 14201344[LL]
Mrk 896	20 46 20.9	-02 48 45	0.026	544	14448640
Mrk 915	22 36 46.5	-12 32 43	0.024	496	26495488
Mrk 926	23 04 43.5	-08 41 09	0.047	981	4856832
NGC 3227	10 23 30.6	+19 51 54	0.004	78	4934656
NGC 3516	11 06 47.5	+72 34 07	0.009	179	12473344
NGC 3783	11 39 01.7	-37 44 19	0.010	198	18510592
NGC 4051	12 03 09.6	+44 31 53	0.002	47	12451072
NGC 4151	12 10 32.6	+39 24 21	0.003	67	3754496
NGC 4593	12 39 39.4	-05 20 39	0.009	183	12457216
NGC 5548	14 17 59.5	+25 08 12	0.017	352	18513152
NGC 7213	22 09 16.3	-47 10 00	0.006	118	18514176
NGC 7469	23 03 15.6	+08 52 26	0.016	334	3755008
PG 1211+143	12 14 17.7	+14 03 13	0.081	1736	3760896
PG 1612+261	16 14 13.2	+26 04 16	0.131	2907	14201088
PG 1700+518	17 01 24.8	+51 49 20	0.292	7140	4675840
PG 2214+139	22 17 12.3	+14 14 21	0.066	1396	10453504[SL] 14202368[LL]
PHL 1811	21 55 01.5	-09 22 24	0.190	4381	18223360
UGC 7064	12 04 43.3	+31 10 38	0.025	514	10870272

Note. — Units of right ascension are hours, minutes, and seconds, and units of declination are degrees, arcminutes, and arcseconds. Spatial scale based on $H_0 = 72$.

and is less sensitive to point errors. Lastly the data was redshift-corrected to rest wavelength using redshift values obtained from the NASA Extragalactic Database (NED).

7.2.2 Star Formation and Emission Line Removal

Our aim is to understand the MIR behavior of the torus, so it is of utmost importance that when we analyze the *Spitzer* observations, we examine only the emission from the central regions of galaxies. The large 7.2'' aperture of *Spitzer* clearly gathers more than just the emission from the torus, undeniably gathering thermal emission from the host galaxy. In order to isolate the torus from star formation contamination, we removed the ISO-SWS spectrum of M82 as a star formation template (Sturm et al., 2000), similar to the approach of Schweitzer et al. (2006) and Mor et al. (2009).

The process of removing star formation contribution is outlined below with Figure 7.3 accompanying the explanation. Polycyclic aromatic hydrocarbons (PAHs) are prominent indicators of star formation with several broad features occurring in the *Spitzer* bandpass, including those at 6.2, 7.7, 11.3, and 17 μm . With the star formation template interpolated onto the *Spitzer* wavelength grid of the data, we subtract from the data the template in varying amounts until the strong 7.7 μm PAH vanishes. The validity of the subtraction can be judged from any residual emission or absorption in the wavelengths corresponding to the PAH features. Figure 7.3 shows the restframe *Spitzer* spectrum of Mrk 1048 in red, the scaled M82 template in blue, and the resultant ‘star formation-less’ spectrum in black. While the removal of the broad PAH features rids the spectrum of star formation indicators, the more ‘big picture’ result of subtracting the template is the change in long wavelength emission. Netzer et al. (2007) show that after subtracting a starburst spectrum, QSOs with strong FIR emission and those with weak FIR emission have nearly the same ‘intrinsic’ AGN SED. Subtracting an increased fraction of star formation reduces the emission at long wavelengths, and this is shown in green in Figure 7.3. While other authors (Smith et al. (2007)) decompose their *Spitzer* spectra of star formation using multiple PAH and emission line components, we believe subtracting the M82 template sufficiently

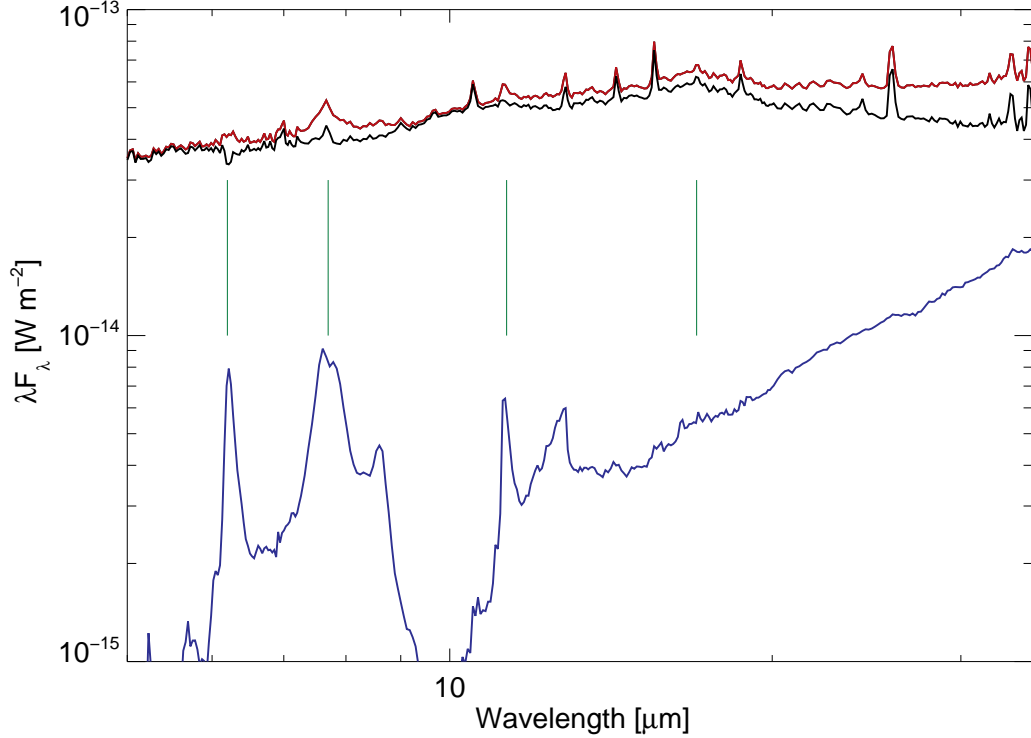


Figure 7.3 Seyfert 1 Mrk 1048 undergoing star formation removal. The black line is the spectrum after the scaled M82 star formation template (blue) is removed from the unaltered rest wavelength *Spitzer* spectrum (red). Vertical green lines represent the locations of the 6.2, 7.7, 11.3, and 17 μm PAH features.

removes features of star formation, though it may distort the resultant spectrum in other ways, leading to an adjustment that is discussed in Section 7.4.

Spitzer spectra, post star formation removal, contain emission lines attributable to both the AGN and star formation. The clumpy torus models produce SEDs that explain torus emission and do so using only the properties of the dust. Therefore, since the models exclude emission lines, we apply an emission line removal technique such that the final spectrum we fit with CLUMPY models is smooth and represents the emission intrinsic to the AGN. For each individual line present in the spectrum, a spline is fit over a limited wavelength range that includes the line. The wavelengths associated to the line (as lines do have width) are replaced by the values of the spline

resulting in a spectrum whose shape is defined by the dust of the torus.

7.3 Constraining the MIR Sample with Ground-Based Observations

It is our aim to fully comprehend the distribution of dust that makes up the tori of the unified theory of AGNs, and to do so, we must exploit all available resources. While we have in hand the reduced low-resolution observations taken by the large aperture *Spitzer Space Telescope*, there exists the option to observe AGNs with higher spatial resolution, allowing us to probe deeper into the central regions of galaxies focusing primarily on the emission of the torus and AGNs. In this section, we examine 6 galaxies observed in the MIR by the ground-based *Gemini* Telescopes and provide insight into the characteristics of the dusty environments that surround the central engine of AGNs. The results of this brief ground-based study will place additional constraints on the Seyfert sample.

To accurately compare the predictions of any torus models with observations, it is imperative to isolate the small-scale torus emission. Large aperture observations such as that of *Spitzer* is strongly contaminated with emission from the host galaxy, as many authors find starburst emission is a large component of IR flux (Netzer et al., 2007; Barmby et al., 2006; Polletta et al., 2007; Ramos Almeida et al., 2009). Furthermore, even ground-based observations of NGC 1068 show that apertures larger than $0.5''$ have different spectral shapes in the MIR, that is likely attributed to nearby dust outside the torus (Mason et al., 2006). These authors found that the torus contributes less than 30% of the $10 \mu\text{m}$ flux within apertures larger than $1''$ with the majority of this flux coming from the dust in the ionization cone.

Ground-based MIR observations of nearby Seyferts have revealed that the torus size is likely restricted to a few parsecs, a feat space-based observations cannot achieve. Using the *Gemini* telescopes, Packham et al. (2005) and Radomski et al. (2008) established upper limits of 2 and 1.6 pc for the outer radii of the Circinus galaxy and Centaurus A tori, respectively. Additionally, interferometric observations at the *VLTI* of Circinus, NGC 1068, and Centaurus A suggest the tori extend to $R=1$ pc (Tristram et al., 2007), $R = 1.7\text{-}2$ pc (Jaffe et al., 2004; Raban et al., 2009), and $R =$

Table 7.3. Observations and Galaxy Data for Ground-Based Sources

Source Name	Instrument	Instrument Scale (arcsec pix ⁻¹)	Distance (Mpc)	Scale (pc arcsec ⁻¹)	Observation Epoch	On-source Time (s)
IC 5063	T-ReCS	0.089	47.7	231	2005 Jul	909
NGC 1068	T-ReCS	0.089	15.8	77	2005 Jan	680
NGC 2992	Michelle	0.201	32.3	157	2006 May	710
NGC 4388	Michelle	0.201	35.3	171	2006 May	710
NGC 5506	T-ReCS	0.089	25.9	126	2004 May	927
NGC 4151	Michelle	0.201	13.9	67	2007 Mar	427

0.3 pc (Meisenheimer et al., 2007), respectively. These observations further affirmed that the distribution of dust is in the geometry of a torus, which further confirm the approach of our models.

7.3.1 Sample and Data Reduction

We have obtained ground-based MIR high-angular resolution archival observations of 6 nearby active galaxies, with the sample consisting of 5 Seyfert 2s and a single Seyfert 1 source that were a part of the sample in Section 7.2.1. We list in Table 7.3 properties of the sources and their observations. For each of the sources, we get high-angular resolution N-band (8-13 μm) spectroscopy that can only be attained from the ground using 8-10 meter-class telescopes (diffraction limit $\sim 0.3'' - 0.4''$ at 10 μm).

Observations were performed using either the MIR camera/spectrograph T-ReCS (Thermal-Region Camera Spectrograph; Telesco et al. (1998)) on the *Gemini*-South Telescope or the MIR camera/spectrograph Michelle (Glasse et al., 1997) on the *Gemini*-North Telescope. T-ReCS uses a Raytheon 320 x 240 pixel Si:As IBC array, providing a plate scale of 0.089''/pixel, corresponding to a field of view of 28.5'' x 21.4'' with a resolution at 10.4 μm near 0.5''. The Michelle detector is a Si:As IBC array with a format of 320 x 240 pixels, a 0.201''/pixel plate scale for spectroscopy, and has resolution of 0.4'' at 11.3 μm . The plate scale translates into a field of view of 32'' x 24'' .

For the observations, be it from T-ReCS or Michelle, a standard chopping-nodding technique was used to remove the time-variable sky background, the telescope thermal emission, and the $1/f$ detector noise. The data was reduced using in-house-developed IDL routines in addition to *Gemini-IRAF*. The resulting spectra were extracted in various apertures, wavelength-calibrated using telluric lines, divided by the standard star, and multiplied by a blackbody spectrum. A further examination into the background subtraction technique is required, but until this is addressed, the ground-based spectra will be scaled to photometric measurements from the literature.

7.3.2 2-D Spectrum

We initiate our analysis using the seldom-used 2-dimensional spectro-spatial profile, which is the initial result of passing the light that was captured in the telescopic slit through a diffraction grating. We show on the left of Figure 7.4 the Michelle $10.5 \mu\text{m}$ image ($6.2'' \times 6.2''$) of NGC 2992 where the gray lines represent the alignment of the Michelle $0.4''$ spectroscopy slit. The panel below the image shows the 2-D spectrum with wavelength extending from 8 to $13 \mu\text{m}$ in the x-direction and the spatial direction on the y-axis, where the vertical line represents the spatial distance of 157 pc. To clarify, the 2-D profile shows slices perpendicular to the slit, so in the figure, up and down in the profile represents left and right in the image. The right side of Figure 7.4 shows the *Spitzer* spectrum of NGC 2992 (black) and the *Gemini*/Michelle $0.5''$ (dark gray) and diffraction limited $0.3''$ (light gray) spectra. The *Spitzer* aperture gathers all the extended emission evident in the top left image providing clearly seen star formation indicators such as PAHs at 7.7 and $11.3 \mu\text{m}$. *Gemini* observations with lower aperture extractions provide an uncontaminated view of the AGN emission.

For each source we obtain and analyze the features of these 2-D spectra (Figures 7.5-7.8). We immediately notice fainter emission near $9 \mu\text{m}$; this is the residual of the difficult-to-remove telluric ozone absorption feature still present in the data. Additionally, since for these figures a single pixel in the vertical direction corresponds to a certain spatial size in parsecs, tracing the bright nuclear emission can quickly

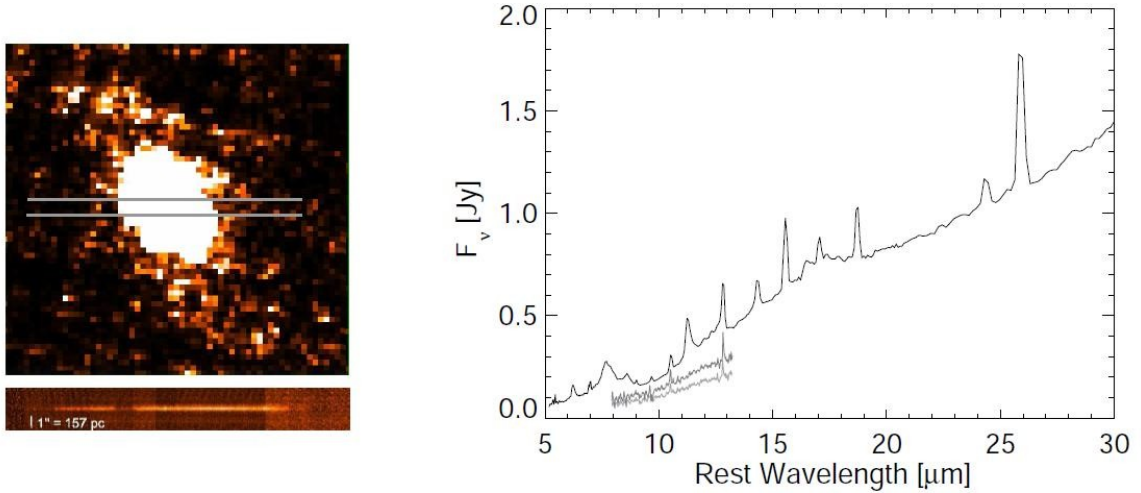


Figure 7.4 The Michelle $10.5 \mu\text{m}$ image ($6.2'' \times 6.2''$) of NGC 2992 is shown at left where the gray lines indicate the alignment of the $0.4''$ spectroscopic slit. The lower panel is the spectro-spatial profile which is the result of vertical spectral slices in the MIR image and shows wavelength on the x-axis and spatial extent in the y-direction where the vertical line represents a spatial distance of 157 pc. At right is the *Spitzer* (black), Michelle $0.5''$ (dark gray), and Michelle $0.3''$ (light gray) spectra for NGC 2992. *Gemini* provides an uncontaminated view of the torus whereas the *Spitzer* aperture gathers extended emission such as star formation, as seen from the PAH features.

point to the full spatial extent of the torus. However, this is always an upper limit since even for the nearest Seyfert, these observations cannot resolve the torus.

From each of these spectra, we can immediately see that we have a constraint on size scale. The black vertical line represents $0.4''$, and for these sources an extraction using an aperture of this size would gather MIR emission only from regions within spatial scales of no more than 90 pc. The nearby Seyfert 1 NGC 4151 is the closest source for which we have these observations, and its $0.4''$ aperture corresponds to a compact 27 pc. We are limited by the telescope as to how deep we can probe the structure, and if finding that the spatial shapes of the large aperture *Spitzer* spectrum is in accordance with this small *Gemini* aperture, then we have confirmed that the torus and/or the material confined to these compact regions is responsible for the overall emission (See Section 7.3.4).

It is difficult to decipher any extended emission in the sources shown as we see

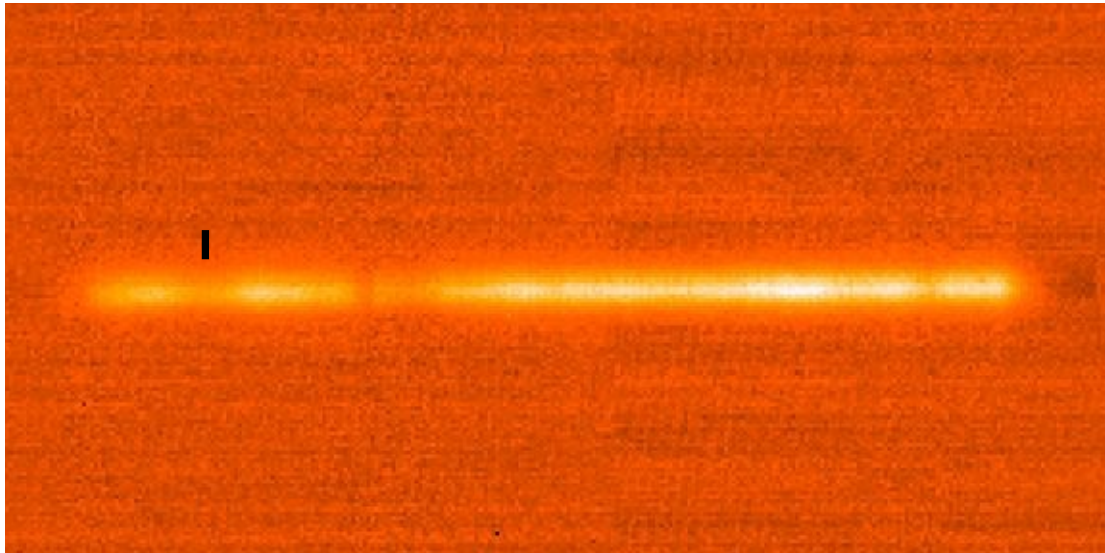


Figure 7.5 The 2-D profile of IC 5063 shows wavelength from 8-13 μm on the x-axis and spatial direction in the y-axis. The vertical black line represents an aperture of $0.4''$ or ~ 90 pc. The bright band passing horizontally is the nucleus of the AGN, and faint and bright areas represent where the intensity within the spectrum is weak or strong, respectively. The fainter area towards the middle-left is the telluric absorption feature near $9.5 \mu\text{m}$.

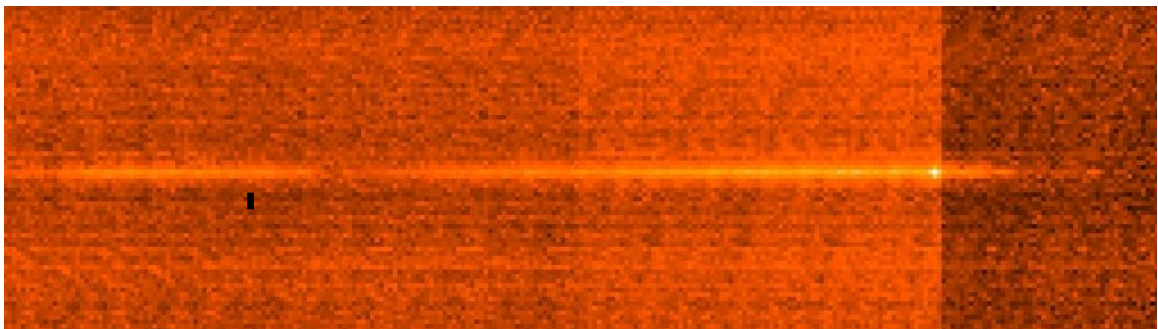


Figure 7.6 Same as Figure 7.5 but for NGC 4388. The vertical black line of $0.4''$ equals ~ 68 pc for this source.

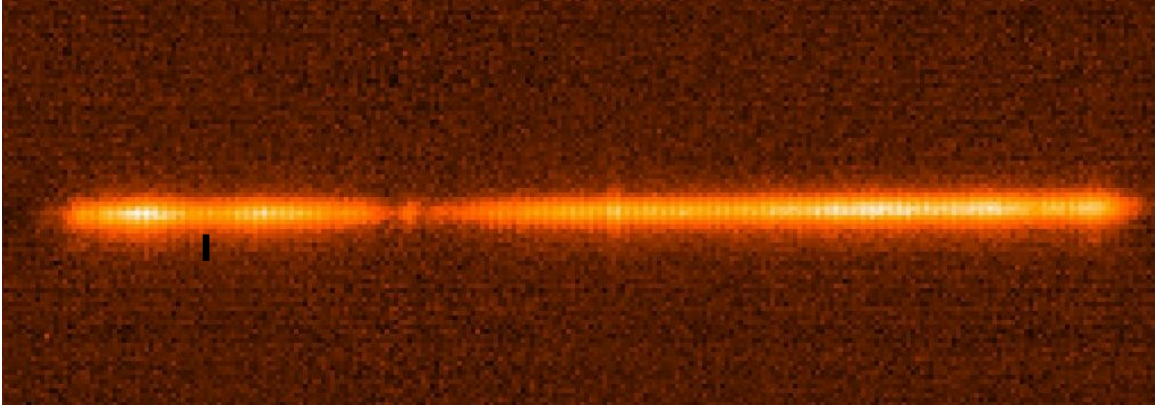


Figure 7.7 Same as Figure 7.5 but for NGC 5506. The vertical black line of $0.4''$ equals ~ 60 pc for this source.

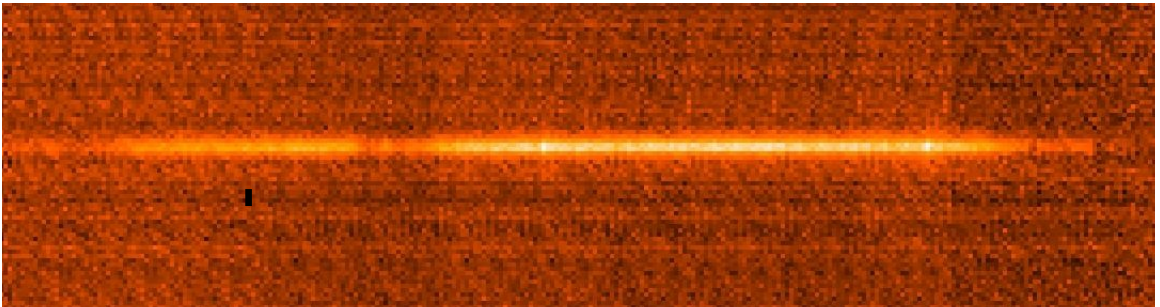


Figure 7.8 Same as Figure 7.5 but for NGC 4151. The vertical black line of $0.4''$ equals ~ 27 pc for this source.

little extension from the central peak, other than the point spread function of the telescope that gives the broadened effect. NGC 5506 in Figure 7.7, however, shows some extended emission, though not intense. It is clear to see in this source the $10.5 \mu\text{m}$ [SIV] emission line towards the center of the profile spatially extending above and below the nuclear band. The relatively high ionization potential (34.8 eV) of this line may be interpreted as a signature of AGNs or very young starbursts where ionization is dominated by young hot stars (Roche et al., 2001; Verma et al., 2003). We discuss this source further in Section 7.3.4 as its spectra are not representative of AGNs.

7.3.3 Spectral Extractions

Extracting horizontal strips (rows) from the 2-D spectrum, we can obtain the spectra of certain spatial regions observed during the observations. Though a single observation was taken, one can isolate certain spatial regions in which the spectrum can provide meaningful results. That is to say, you can isolate only the central regions of the galaxy by extracting the central few pixels or you can study off-source emission by extracting an aperture of a given size centered off the peak of emission. Apertures of different sizes can also be centered on the torus and grown to show how much emission the torus contributes over larger and larger spatial scales.

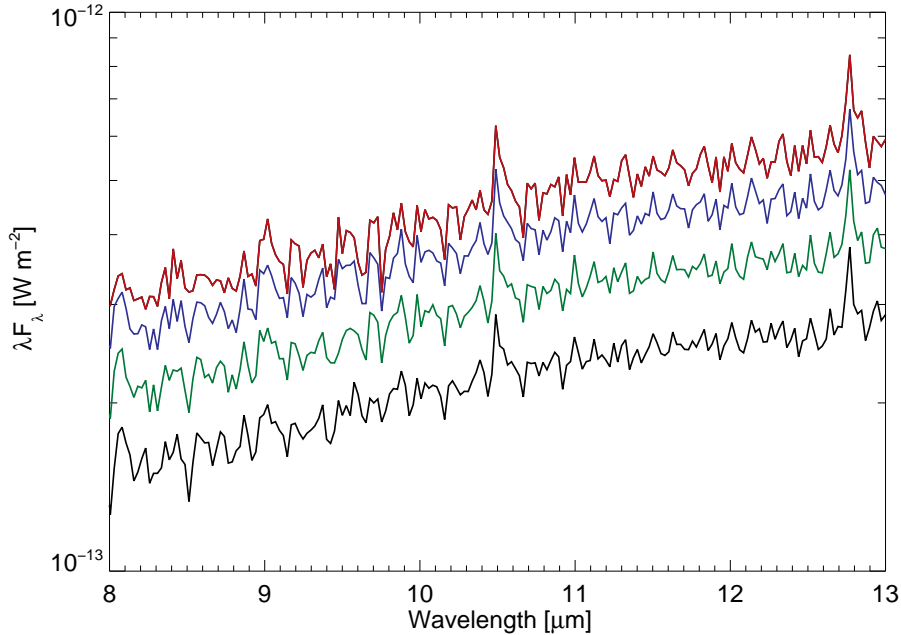


Figure 7.9 N-band spectra of Seyfert 1 NGC 4151 were extracted using nucleus-centered apertures of 0.4 (black), 0.7 (green), 1.0 (blue), and 1.7'' (red). There is little if any change in the spectral shapes over the different extractions, and for each, the 10.5 μm [S IV] and 12.8 μm [Ne II] emission lines are present indicating regions responsible for their emission are confined to within 27 pc.

Four extractions centered on the nucleus of NGC 4151 were performed, and their resultant spectra are shown in Figure 7.9. The smallest aperture extracted was 0.4'' in

diameter, which when taking the distance of this source into account equals roughly 27 parsecs. If this spectrum reflects the MIR emission of the torus, then we have isolated the torus to a radius of 13 pc, spatial scales in agreement with Radomski et al. (2003). Extractions using larger apertures were performed to identify any extended emission since, as mentioned in Section 7.3.2, determining its presence in the 2D spectra is not always easy. For NGC 4151, apertures of 0.7, 1.0, and 1.7'', relating to spatial sizes of 47, 67, and 114 pc respectively, were extracted with their spectra showing virtually the exact shape and characteristics of the 0.4'' spectrum. Within each spectrum, the 10.5 μm [S IV] and 12.8 μm [Ne II] emission lines stand out, and note that these are evident as bright points in the 2D spectrum of Figure 7.8. The [S IV] emission line can be attributed to either the AGN or star formation whereas the lower ionization [Ne II] emission line typically indicates star formation (See Section 6.3.3.). If a vast amount of star formation is present within the aperture, the 11.3 μm PAH feature is bound to stand out, and it is not present in any of the spectra, not even that of the largest aperture extraction. For this source, we propose the torus is the dominant source of emission coming from the extracted region. We will see in the next section that the *Spitzer* spectrum contains the same shape, again indicating the AGN dominates the MIR emission even on scales of 500 pc sampled by *Spitzer*.

Performing the same analysis on the other sources yielded similar results – increasing the aperture increased the flux but maintained the shape. Even NGC 5506, the source with apparent extended emission in its 2D spectrum, shows little difference in different aperture diameters ranging from 50 to 160 pc. Therefore, from the ground-based spectra of these sources, we find that compact regions observed with high-resolution ground based telescopes dominates the MIR emission.

7.3.4 *Spitzer* vs *Gemini* Observations

Having reduced and analyzed the ground-based observations, we can now directly compare the low-resolution *Spitzer* spectra to the high-resolution *Gemini* observations to see if they are in agreement, namely by comparing their spectral shapes. In each of the Figures 7.10-7.15, we show the *Spitzer IRS* spectrum spanning 5-30 μm in

black with its associated error and a N-band 0.4'' aperture extraction from *Gemini* plotted in red. The N-band *Gemini* spectra were scaled to ground-based photometric measurements of Ramos Almeida et al. (2009), and we plot for the sources in green the ground-based photometry from the same author at the N- (10 μm) and Q-bands (18 μm). Ground-based observations of NGC 1068 are those found in Alonso-Herrero et al. (2011) and consist only of N- and Q-band spectroscopy, so photometry is ignored for this source.

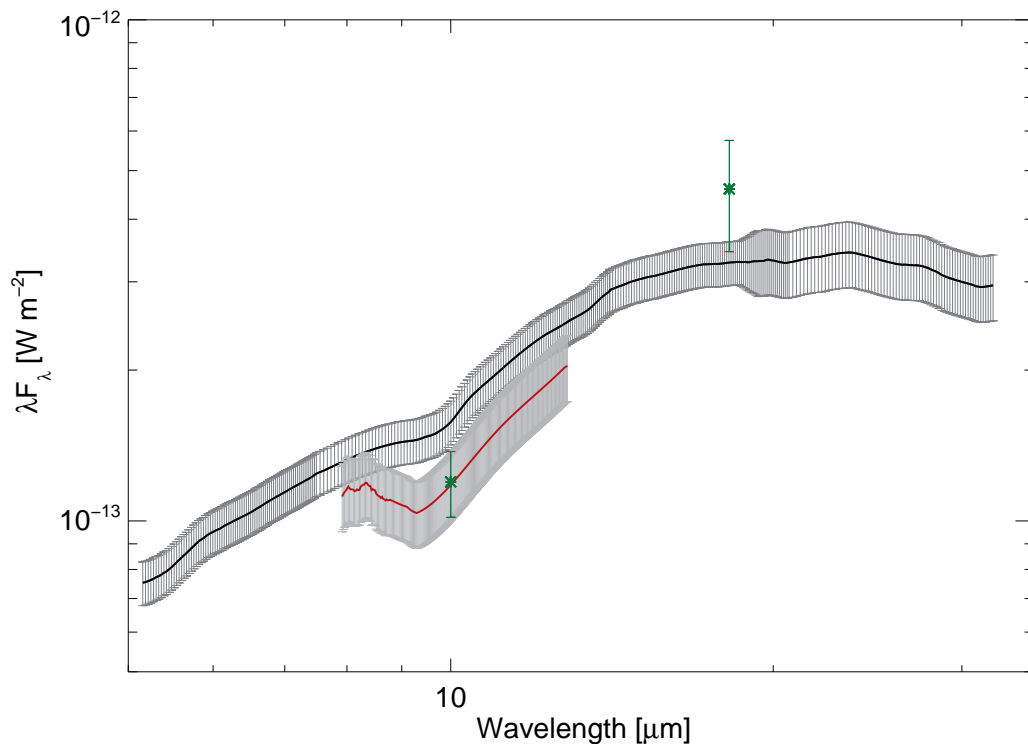


Figure 7.10 The *Spitzer IRS* spectrum of IC 5063 is shown in black and is compared to a 0.4'' *Gemini* aperture (red). N- and Q-band photometric point from Ramos Almeida et al. (2009) are plotted in green for comparison.

The two spectra of IC 5063 shown in Figure 7.10 have similar shapes in the ranges of 8-8.5 μm and $> 10 \mu\text{m}$. The trough within the *Gemini* spectrum is likely the effect of a mixture of both silicate absorption, as 10 μm absorption is present in the *Spitzer* spectrum, and telluric absorption, as it appears to be centered near 9.5 μm . The photometry agrees within error with the large aperture *Spitzer* spectrum, so in

quantifying the relation between the *Spitzer* and *Gemini* observations, we believe the two are in relative agreement. This suggests that the source responsible for producing the MIR emission in the small aperture is also the dominant contributor in the large aperture, so it is therefore reasonable IC 5063 can be fit by the torus models.

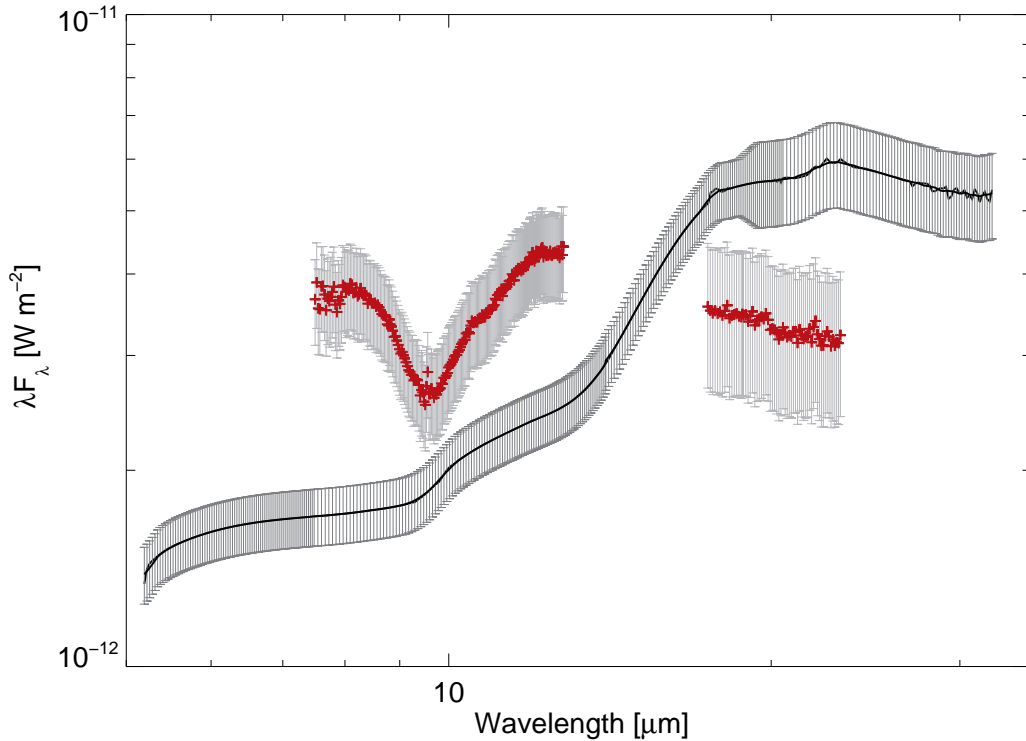


Figure 7.11 Same as Figure 7.10 but for NGC 1068. The red ground-based observations were taken from Alonso-Herrero et al. (2011) and were unaltered to emphasize the difference between *Gemini* and *Spitzer* observations.

Seyfert 2 NGC 1068, the source that has been studied several times in understanding the torus structure (Jaffe et al., 2004; Mason et al., 2006; Raban et al., 2009; Alonso-Herrero et al., 2011), shows completely different spectral structure in Figure 7.11 between the observations. Mason et al. (2006) did find that apertures exceeding $0.5''$ had different spectral shapes, with the torus responsible for not even 30% of the $10 \mu\text{m}$ flux within $1''$ apertures. In comparing the *Spitzer* and *Gemini* spectra, where the unaltered ground-based observations were taken from Alonso-Herrero et al. (2011), the N-band shapes are completely different with the ground-based data

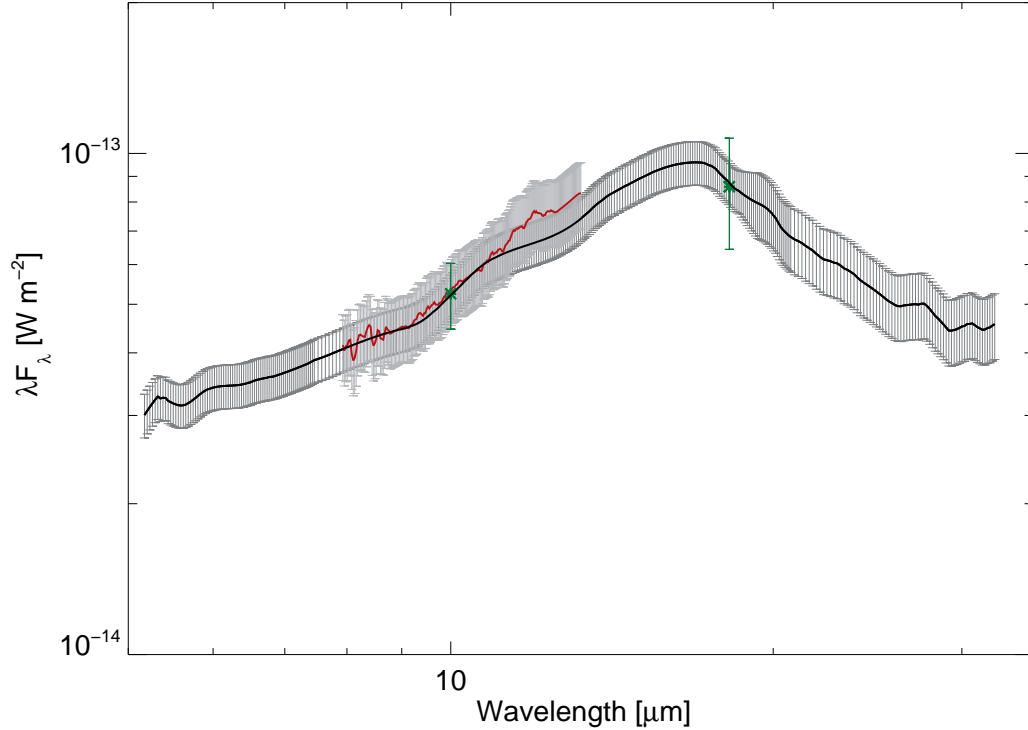


Figure 7.12 Same as Figure 7.10 but for NGC 2992.

again showing deep absorption, whereas this absorption lacks in the *Spitzer* observations. Perhaps the most startling difference is in the long wavelengths. The Q-band spectrum is much lower in the ground observations. Since this $0.4''$ aperture attempts to isolate the torus, though the findings of Mason et al. (2006) say otherwise, any extended emission is minimized, where in the case of *Spitzer*, additional emission is collected within the large aperture. If we were to only compare spectral shapes in the N-band, while in this source they are not in agreement, Figure 7.11 shows that without including additional information and only utilizing the N-band, we would be flawed in our technique. We would simply be analyzing data that we would assume was torus-dominated, but is in fact emission not attributed to the torus. Since the ground- and space-based observations are not in agreement, NGC 1068 is removed from our overall sample in which we will determine the distribution of dust.

We compare in Figure 7.12 *Spitzer* and *Gemini* spectra of NGC 2992 and find

they are quite similar. The 8-13 μm spectral regions have virtually the same shape, and the photometry falls completely in-line with *Spitzer*. Seeing that the torus is isolated within the ground-based observations, it can be assumed that the torus is the dominant source of emission in *Spitzer*. Since there is not complete wavelength coverage between 14-18 μm , we do not know if the spectral bump near 17 μm is matched in the high-resolution data. It is possible that this bump may be attributed to the broad PAH complex found at these wavelengths, though the complete star formation removal technique was conducted thoroughly.

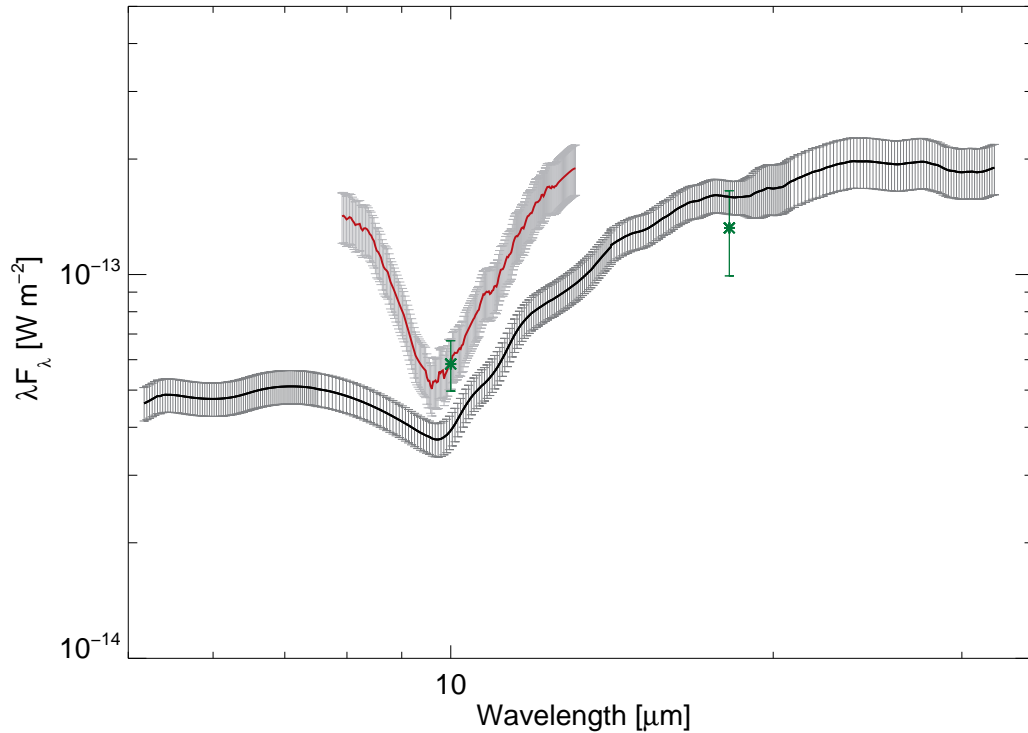


Figure 7.13 Same as Figure 7.10 but for NGC 4388.

The *Spitzer* and *Gemini* spectra of NGC 4388 in Figure 7.13 may display torus dominated emission but contain strong 10 μm silicate absorption features. They are quite similar in the bands of 8-8.5 μm and 10-13 μm , but telluric effects tend to slightly enhance the absorption feature near 9.5 μm in the ground-based observations. Sirocky et al. (2008) measure in their sample of ULIRGs strong 10 μm silicate absorption,

but they also find quite prevalent $18 \mu\text{m}$ absorption. This source, however, is not an ULIRG and shows virtually no feature at $18 \mu\text{m}$, yet it has the strong trough at $10 \mu\text{m}$. Since this feature is found in both large aperture and small $0.4''$ aperture observations, we attribute the absorption to foreground extinction. Ramos Almeida et al. (2011) fit photometry of this source with BayesCLUMPY (Asensio Ramos & Ramos Almeida, 2009) and found the extinction to this source can be as much as $A_V = 270$. However, since the spectral shapes of the two observations are different from one another, we have steep reservations as to whether the torus truly dominates the emission.

The spectra of Seyfert 2 NGC 5506 (Figure 7.14) have nearly the same spectral shape over the N-band, though the N-band photometry is in disagreement. This source, while showing strong $10 \mu\text{m}$ absorption, lacks the spectral shape AGNs are known to have. We believe this source lacks torus dominated emission, and for that reason we remove it from the sample.

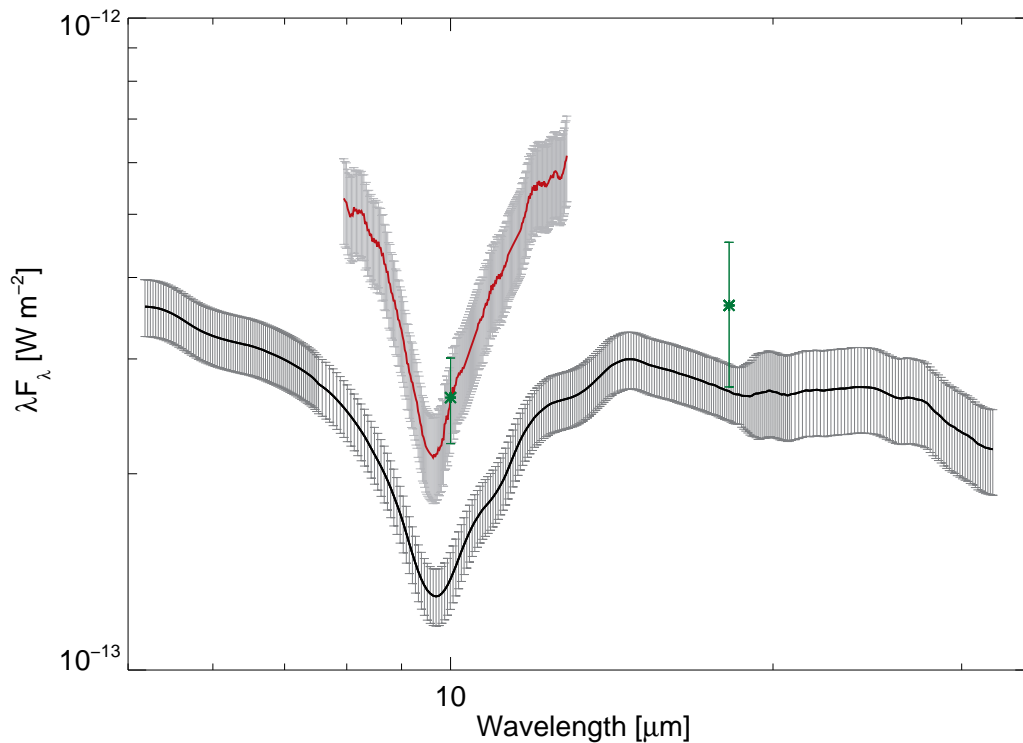


Figure 7.14 Same as Figure 7.10 but for NGC 5506.

Our final figure (Figure 7.15) shows the *Spitzer* and *Gemini* spectra of our only Seyfert 1, NGC 4151. The spectral shapes of both observations are similar, indicating both spectra are dominated by emission from the same source. Additionally, the photometry is in agreement with space-based observations, though the Q-band point is a bit lower. Like NGC 2992, a 17-18 μm bump occurs in the *Spitzer* spectrum which again could be the PAH complex emission, as this would explain the increased flux as compared to the photometry.

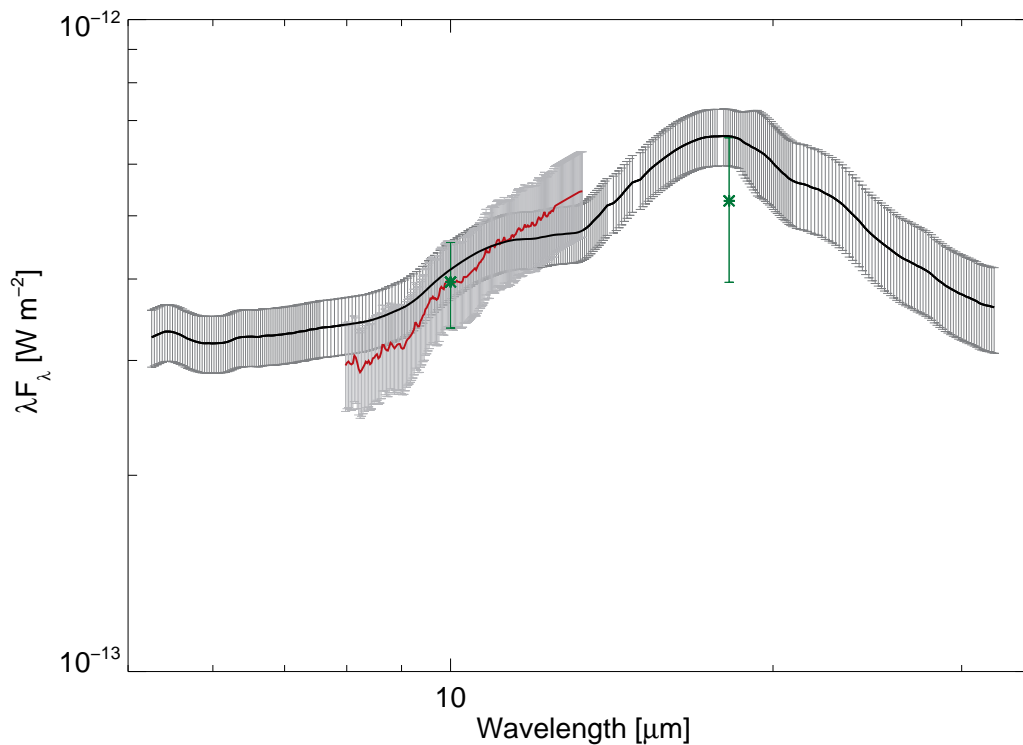


Figure 7.15 Same as Figure 7.10 but for NGC 4151.

7.3.5 Conclusions

As with any modeling, the more data you have to fit, the better grasp of the results you have. For this reason, the observations we have of the N-band spectroscopy will not yield any useful results if we fit them alone as they have insufficient wavelength coverage. This notion is quite evident in Figure 7.11, in which a fit would likely be

completely different if we excluded additional data such as the $18\ \mu\text{m}$ observations. With a very limited wavelength range as compared to the entire wavelength range of the models, there is little reliability in the best fit model as there are no outside pivot points to constrain the models at other wavelengths to control the shape. Analyses that include photometry alone or in combination with N-band spectroscopy have been carried out with CLUMPY torus models (Ramos Almeida et al., 2009, 2011; Alonso-Herrero et al., 2011) with results important to our understanding of the torus. Since these studies include data over a spread of wavelengths, any fitting results should be reliable as long as the measured flux represents the emission of the torus. In the last paragraphs where we compared *Spitzer* observations to $0.4''$ aperture *Gemini* data, we found that as long as their spectral shapes are similar, then those observations of *Spitzer*, even though they are large aperture, are dominated by the AGN. Since there is a large wavelength range for these observations, any fitting results we obtain should be reliable.

The ground-based N-band observations are cherished as they provide very valuable information at high spatial resolution, but as observations that stand by themselves, any fits would be unreliable. However, several avenues exist in gathering additional beneficial scientific results from the ground-based observations. In addition to extractions of different spatial scales as in Figure 7.9, extractions across the nucleus offer a glimpse as to how the spectrum changes over different spatial regions, including, but not limited to, strength and spatial variations of the $10\ \mu\text{m}$ silicate feature. Also, examining the fine-structure lines present in the narrow wavelength band can provide additional details regarding the nuclear regions of AGNs. At this stage however, we use the ground-based observations as a check to the validity of the *Spitzer* observations; is the MIR emission captured by *Spitzer* truly that of the torus? From the above comparisons, we found that the *Spitzer* spectra of NGC 1068 and NGC 5506 are not dominated by the torus or AGN emission, so it is of really no use to fit them with the clumpy torus models. In assigning a measure of confidence in how well we believe the *Spitzer* observations represent the torus emission, as determined by comparing them to *Gemini*, we are confident that the *Spitzer* spectrum of NGC 2992

contains the torus emission; the spectrum of NGC 4151 is very acceptable; IC 5063 is marginally acceptable; and we believe NGC 4388 is somewhat acceptable but we have reservations concerning the foreground extinction. Additional details about the clumpy torus model fits to the *Spitzer* spectra of these sources are found in the appendix. Ideally, a larger percentage of the initial sample would contain ground-based observations so that we could confirm *Spitzer's* emission is that of the torus, but until these observations are taken, we must continue with the *Spitzer* analysis under the uncertainty that some sources may or may not contain non-torus dominant emission.

7.4 CLUMPY Model Fitting of MIR Emission

To further understand the environment of the dust close to the central engine, we examine the sample of AGNs studied within the context of spectropolarimetry by fitting each 5–30 μm *Spitzer* spectrum with synthetic torus models generated by CLUMPY. We utilize a Bayesian Markov-Chain Monte Carlo fitting procedure (see Section 4.4) which provides a variety of fit options. The basic method fits observations by a continuous set of CLUMPY models, or more precisely, the entire model database. Additional fitting configurations allow the user to specify parameter value ranges, an option that provides a ‘prior’ in the context of Bayesian analysis. Furthermore, an additional component, namely a blackbody restricted to values between 800–1800 K, is available to be introduced into the fitting procedure to complement the 6 CLUMPY parameters (See Table 4.1). The blackbody is an additional component that serves to better fit the data in hand, and it is at the user’s discretion and responsibility to implement and identify the scientific results it signifies.

It is important to reiterate the scope of this study. The viewing angle of AGNs is the single most critical component of the unification scheme, since it is the observer’s orientation that causes the differences in observed properties. Though there are no direct means to measure the viewing angle, we suggest MIR emission can allow for the possibility of determining it, namely by a method which encompasses detailed fits of MIR spectral energy distributions of torus models to AGN spectra. However, an additional aspect of this research calls for the comparison of the results gained

from both the spectropolarimetric and MIR emission methods in determining the inclination angle. The following paragraphs outline the steps necessary to fulfill both goals.

Regarding the type 1 AGNs of the spectropolarimetric sample, all spectra were fit in four combinations, by : (1) only CLUMPY torus models; (2) a 2-component model, which includes the CLUMPY torus and a blackbody (See Sections 7.4.1 and 7.4.2; (3) a subset of all the CLUMPY models in which spectropolarimetric observations provide prior knowledge on the i parameter; and (4) a combination of (2) and (3) (See Sections 7.5.1 and 7.5.2). In cases (1) and (2), the analysis was performed independently from the polarization results, whereas cases (3) and (4) used the results of polarization as input into the models.

Prior to individual source analysis, a general examination of the different fitting techniques was performed. Looking only at cases (1) and (2), where the difference lay solely in the addition of the blackbody, we found that the type 1 sources are more well fit by the CLUMPY + blackbody models. We quantify the fits with a goodness-of-fit measurement, the reduced chi-squared value specified in Equation 4.3. On average, including the blackbody component in the fitting resulted in improved χ_R^2 values, from 0.50 in the torus-only fits to 0.08 in the torus+blackbody composite. Understanding that more degrees of freedom for any fit typically yields better results, we argue that the blackbody component is required, not only for the better fit, but also to offer a physical explanation of the dusty environment. The CLUMPY models explain the MIR emission of the torus, where the torus has a sharply defined inner edge at the dust's sublimation temperature, i.e. the torus sublimation radius. In reality, the inner boundary of the torus does not end abruptly. Rather, there is likely a progression of larger dust grains of varying species close to the central engine to smaller dust grains with chemistries similar to those found within the torus, until these mix with dust of the torus near the sublimation radius. The different grain sizes and/or species of dust can withstand warmer temperatures within the the dust sublimation radius of the torus. Evidence shows IR emission shortward of the 10 μm silicate feature for which an extra 'hot' component could account (See Figure 7.16). Additionally, in

their study to explain the MIR emission of type 1 quasars, Mor et al. (2009) used a three-component (clumpy torus, NLR clouds, and a blackbody) model and found it necessary to include a warm blackbody to explain the 2–7 μm emission, which they attribute to hot graphite dust located within the silicate sublimation radius. We too believe this ‘hot’ component is not part of the torus, but rather dust which resides within the torus’ dust sublimation radius, so we introduce the blackbody into the fitting to more adequately describe the MIR emission. In this scenario, both the torus and the hot component are taken into account in the model fitting, the former responsible for the majority of the MIR emission (Section 7.4.1 discusses this issue further). For the remainder of this examination, we will only consider cases (2) and (4), in which two-component (torus and blackbody) models are fit to MIR observations.

7.4.1 Seyfert 1 Analysis

Within the paradigm in which our data is best described by a torus + blackbody composite, we assess the results of the Bayesian Markov-Chain Monte Carlo fitting technique for each source. Figure 7.16 shows the MIR *Spitzer* spectrum of Seyfert 1 source Mrk 1239, fit by a torus + blackbody synthetic model, where the solid line reflects the composite model, the dotted line refers to the blackbody, and the dashed line is the torus component. The best-fit values of the CLUMPY parameters are $N_0 = 7$, $Y = 20$, $q = 1.9$, $\sigma = 35^\circ$, $\tau_{avg} = 99$, and $i = 0^\circ$. Encountering a single cloud while viewing an AGN would obscure the central regions, and this type 1 source is described by a model whose torus has 7 clouds along an equatorial ray, on average. However, N_0 is not describing the number of clouds the observer encounters along a certain viewing angle. This is reserved for the quantity

$$N(i) = N_0 \exp\left(-\frac{(90^\circ - i)^2}{\sigma^2}\right)$$

(Equation 4.2) as it is the average number of clouds along a radial ray at angle i measured from the pole, and for Mrk 1239, the number of clouds encountered is

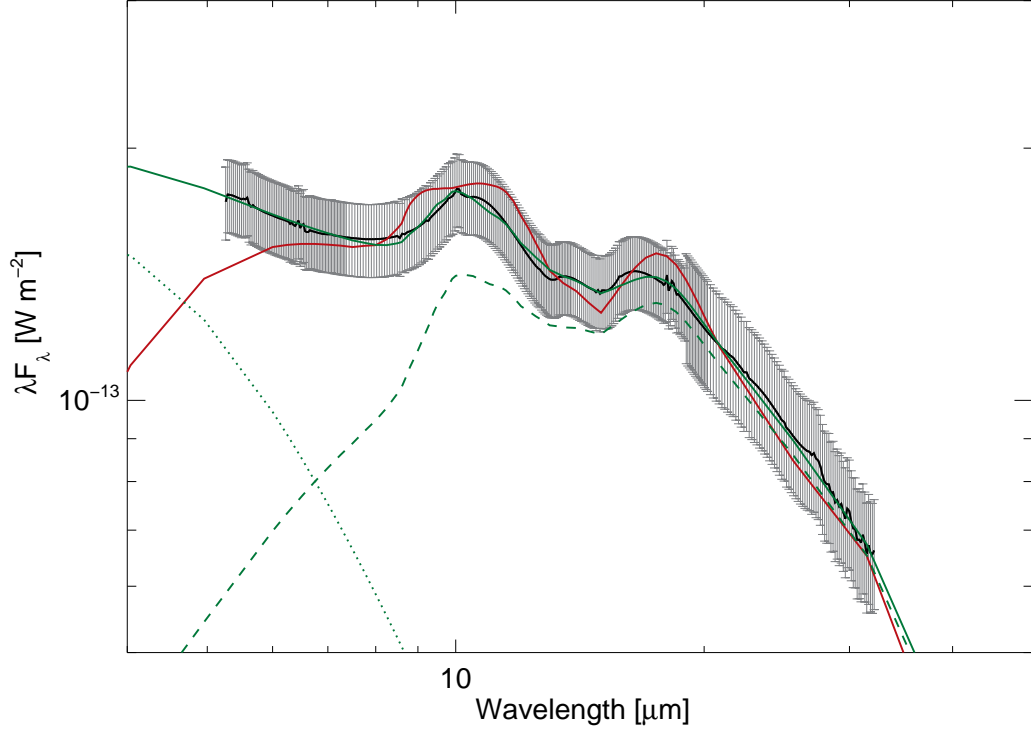


Figure 7.16 The *Spitzer* spectrum of Seyfert 1 Mrk 1239 (black with gray error bars) is fit by single-component (CLUMPY torus only) and 2-component (torus and blackbody) models. The model without the blackbody that most accurately describes the data is plotted in red and has a $\chi_R^2 = 0.36$. The blackbody-inclusive model (solid green) more accurately describes the spectrum and has $\chi_R^2 = 0.01$. The dashed and dotted green lines respectively represent the individual torus and blackbody components necessary to produce such a fit, and the CLUMPY parameter values of the best-fit model are $N_0 = 7$, $Y = 20$, $q = 1.9$, $\sigma = 35^\circ$, $\tau_{avg} = 99$, and $i = 0^\circ$.

~ 0.01 . It is clear then that N_0 alone does not govern the obscuration possibility but rather a combination of N_0 , σ , and i .

Though a model that best describes the observations can be determined (the best-fit model), we must examine the marginalized posterior distributions of the parameters. Within the Bayesian approach, prior information concerning parameters is combined with the observations to create updated or posterior beliefs about the parameters. The resulting posterior distributions then summarize the current state

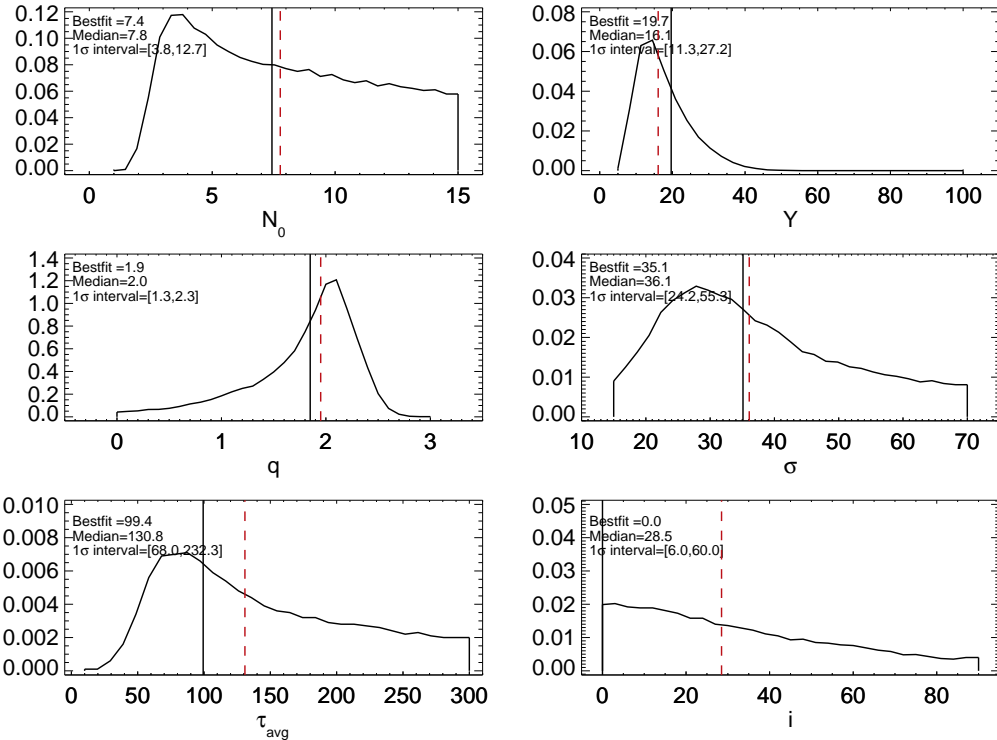


Figure 7.17 The marginalized posterior distributions of the 6 CLUMPY parameters are plotted for Mrk 1239, and printed in each panel is the best-fit (vertical black line) and median value (red dashed line) associated with the fit as well as a 1-sigma interval.

of knowledge about all the uncertain quantities and display the results in probability distributions for each parameter. In our setting, all parameters are given uniform priors, which allows any parameter value to be as likely as any other in describing the data, or to say it differently, no one parameter value is weighted more over the others. Furthermore, the *marginalized* posterior distributions refine the general posterior distributions by integrating out all parameters but the one in question. This marginalization will leave statistically relevant information since the integration of unimportant parameters will rid the posteriors of ambiguities and degeneracies (Asensio Ramos & Ramos Almeida, 2009).

The marginalized posterior distributions of each CLUMPY parameter are plotted

in Figure 7.17 for Mrk 1239. It is evident that the best-fit value need not necessarily be toward the peak of the distribution, though there is the tendency. We chose to quantify the distribution of each posterior by its median value and its 1-sigma interval range since the median tends to hover around peaks of the distribution. To understand the nature of the posteriors, a well-defined peak in a distribution means that particular parameter is well constrained. For example, the Y parameter of Mrk 1239 in Figure 7.17 is constrained to values near 15. Alternately, more flat posteriors indicate the parameter is not constrained and that we cannot gain any valuable information about or from the parameter. Occasionally, posteriors rise toward one edge of parameter space in a ramp-like fashion, and we believe in these cases that the data prefers values outside the allowed parameter interval. In these cases, we regard the fits to be unreliable, but still provide the lower/upper 1-sigma limit, depending on which edge of parameter space the ramp prefers.

We performed the 2-component model fitting technique on all 41 Seyfert 1s of the original spectropolarimetric sample. In any fitting method, there is a requirement to both measure how well data is fit and to define a value at which the fits are no longer acceptable. Implementing the goodness-of-fit quantity, χ_R^2 , we impose an upper limit, such that models with $\chi_R^2 \leq 0.25$ are considered ‘well-fit’ and those whose best-fit model exceeds this threshold value of χ_R^2 are deemed not well-fit. For the latter sources, the models do not accurately describe the observations, either over the entire wavelength range or over limited wavelength intervals whose accuracy is important, namely the 10 and 18 μm sub-intervals.

Of the original 41 type 1 AGNs, 36 sources satisfy the ‘well-fit’ specifications of χ_R^2 , and we will examine the 5 sources that were not well described by the models in detail in Appendix A.3 Poorly Fit Sources. Our final sample of 36 type 1 sources is well-fit by the torus+blackbody composite models, with the torus responsible for 86% of the emitted flux and the blackbody component assuming the remaining 14%, on average. This reiterates the reality that the sample is AGN-dominated and is best described by models created to produce the MIR flux of the torus. It is important to note however, that from the original *Spitzer* spectra to the fitting, the data had been

modified with the removal of a star formation template. Taking this into consideration, the original spectroscopic data can now be described by a three component composite model, consisting of a torus, a blackbody representing hot dust, and a star formation template. As described in Section 7.2.2, we subtract from all source spectra a generic star formation template to remove any residual emission not attributable to the AGN. Only then do we perform the fitting of clumpy torus SEDs to the resulting star formation-less spectra. In the standing type 1 sample, the fractional contribution of total flux for each component is on average 73% torus, 16% star formation template, and 11% blackbody (See Table 7.4). This reaffirms that our sample consists of AGN-dominated sources. We additionally calculated the blackbody's fractional contribution of the total non-torus flux. Determining that the non-torus emission is nearly split equally between the blackbody and the star formation indicates that the IR emission of these components are isolated from each other. As suggested earlier, we believe the blackbody emission explains, in the context of Seyfert 1s, the hot dust within the sublimation radius of the torus, and we find the component is generally required to well describe the observations.

Upon performing the clumpy torus model fittings to the Seyfert 1 observations, the best-fit model and the marginalized posterior distributions as in Figure 7.17 were examined for each source individually as well as for the type 1 sample overall. The best-fit model parameter values and the median values of the posterior distribution are not in exact agreement, which they are not required to be, but when deciphering the arrangement of dust in the clumpy tori, the differences are significant. The best-fit values refer to the parameters describing the one CLUMPY model that best fits the observations, whereas the posteriors provide an indication as to which values of the parameter describe the observations and with what degree. Since the latter truly is a probability distribution, we characterize it by the median value, which depending on the actual distribution may or may not reflect the character of the posterior. Consider, for example, two distributions, one which is sharply peaked that has a shallow wing toward lower values such as q in Figure 7.17, and another which is broad but still favors certain values, τ_{avg} for example. The first distribution would

Table 7.4. Fractional Contribution of Total Flux per Component in Seyfert 1s

Seyfert 1 Sources	Torus	SF Template	Blackbody	$\frac{BB}{SF+BB}$
Ark 120	70.6%	16.0%	13.4%	45.6%
Fairall 51	63.1%	24.7%	12.2%	33.2%
IC 3599	61.1%	38.9%	0%	0%
IC 4329A	73.7%	5.5%	20.8%	79.1%
IZW1	80.8%	10.3%	8.9%	46.2%
KUV 18217+6419	74.1%	3.9%	22.0%	84.9%
MCG -06-30-015	71.1%	13.0%	15.9%	54.9%
Mrk 1040	80.5%	12.9%	6.7%	34.1%
Mrk 1048	77.1%	18.3%	4.6%	20.2%
Mrk 1239	67.3%	20.7%	12.0%	36.8%
Mrk 231	99.2%	0.8%
Mrk 279	72.9%	12.4%	14.7%	54.1%
Mrk 335	74.1%	12.4%	13.5%	52.2%
Mrk 478	62.4%	28.3%	9.4%	24.9%
Mrk 486	68.7%	20.2%	11.1%	35.6%
Mrk 507	99.2%	0.8%
Mrk 509	88.3%	11.7%
Mrk 590	86.1%	6.2%	7.7%	55.1%
Mrk 6	71.1%	12.0%	16.9%	58.6%
Mrk 705	60.0%	32.1%	7.9%	19.8%
Mrk 766	66.3%	30.5%	3.2%	9.6%
Mrk 841	81.4%	7.4%	11.2%	60.4%
Mrk 876	59.8%	23.6%	16.6%	41.2%
Mrk 896	71.4%	15.5%	13.1%	46.0%
Mrk 915	62.6%	32.7%	4.7%	12.5%
Mrk 926	73.6%	5.0%	21.4%	81.1%
NGC 3227	95.0%	5.0%
NGC 3516	78.5%	9.9%	11.6%	53.8%
NGC 3783	84.0%	7.9%	8.1%	50.3%
NGC 4051	62.2%	36.5%	1.3%	3.5%
NGC 4151	79.9%	5.8%	14.3%	71.1%
NGC 4593	75.1%	12.9%	12.0%	48.2%
NGC 5548	73.0%	20.9%	6.1%	22.4%
NGC 7213	83.6%	16.4%
NGC 7469	95.3%	1.5%	3.2%	68.6%
PG 1211+143	71.9%	5.8%	22.3%	79.3%
PG 1612+261	84.6%	9.9%	5.5%	35.9%
PG 1700+518	83.0%	4.3%	12.7%	74.5%
PG 2214+139	72.2%	0%	27.8%	100%
PHL 1811	74.6%	5.4%	20.0%	78.6%
UGC 7064	51.2%	44.3%	4.5%	9.3%
Average Values	72.6%	15.8%	11.6%	46.7%

Note. — MIR emission of our data can be described by a clumpy torus, a star formation template, and a blackbody signifying the emission of hot gas and dust that lies within the torus. We only list the star formation and general torus emission contributions for sources whose fits were poor. Column 5 specifies the fractional contribution of the blackbody regarding the non-torus components.

provide a median value that nearly falls in line with the distribution's peak, perhaps at slightly lower values. Recall that the median is statistically the middle value of an ascending distribution, so when most of the data hovers around a localized region, the middle value is not too far from that peak. The median for the second distribution would lie more toward the middle of the distribution's range than at the peak. The more broad or uniform a distribution is, the more the median value tends toward the center of the distribution's interval. This then explains, in the case of the broad τ_{avg} posterior at least, why the median is more toward the central value of $\tau_{avg} = 150$ than the peak ~ 75 . When examining the posterior distributions, N_0 does not have localized peaks but rather general rising or ramp-like shapes toward large values, and the best fit models pick large values of N_0 . The difference in techniques carries to the figure in the sense that the median value would be skewed toward lower values due to the non-localized distribution, and the best-fit truly shows those values. We therefore focus on the best-fit results since they show better the behavior of the parameter but still present the median results. We continue with the analysis of the Seyfert 1s and show for each CLUMPY torus parameter in Figure 7.18 a histogram created from best-fit values in black.

From the best-fit distributions in Figure 7.18, we collectively find the tori of Seyfert 1s to be compact with relatively large scale heights and several optically thick clouds along equatorial rays. As a sample, the dust distribution of Seyfert 1s tends to be reminiscent or similar to the distributions Alonso-Herrero et al. (2011) found for Seyfert 2s. To investigate this type 2 appearance, we examine the the distribution of the average number of clouds encountered along the line of sight, $N(i)$. This value is one which determines if the observer's line of sight to the central engine and BLR is obscured or not. In the most general picture, if a cloud passes between an observer and an object which he is observing, the cloud blocks or obscures the view. Since Seyfert 1s have optically broad emission lines whose origin is the BLR, it is required that the models describing the type 1 observations allow for unobscured views into the central regions of AGNs. A model predicting complete BLR obscuration for a type 1 source would be complete nonsense. Surveying the distribution of $N(i)$, we see

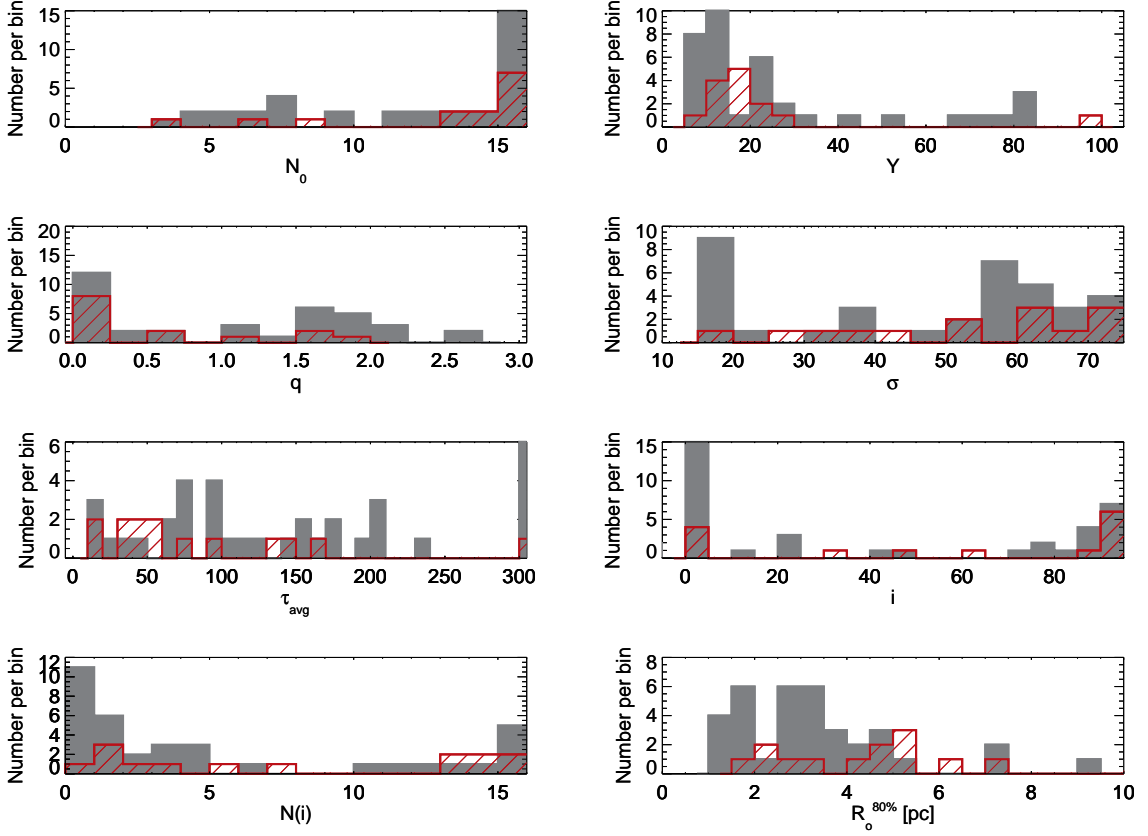


Figure 7.18 Shown for all 36 well-fit Seyfert 1s (black) and 14 well-fit Seyfert 2s (red) are histograms of the best-fit values for the 6 CLUMPY parameters, as well as the average number of clouds encountered along direction i , $N(i)$, and the outer extent of the torus for which 80% of the clouds have been accounted, $R_o^{80\%}$.

that a majority of the Seyfert 1s have few clouds along the line of sight. The enhanced opening angles of the torus in conjunction with several clouds along equatorial rays lead to increased probabilities of obscuration and may explain the high $N(i)$ values. The reason type 1 AGNs are described by models that allow for this obscuration may be due to the limited power the MIR has in constraining certain torus parameters, and we will continue to discuss and examine this issue in Section 7.5.

As discussed in Section 4.3, CLUMPY models are provided in terms of spectral shape with the total flux of the AGN (F_{AGN}) acting as a scale factor, so if we denote the torus flux as λF_λ , the spectral shape is $\lambda F_\lambda / F_{AGN}$. Since F_{AGN} serves as the

scaling factor between the model SEDs and MIR observations, once a source is fit, we obtain the bolometric luminosity of the AGN via $L_{bol} = 4\pi D^2 F_{AGN}$, where D is the distance to the source. In the context of a CLUMPY model torus, the inner radius R_d is set by both the luminosity of the AGN and the temperature at which silicate dust sublimates by Equation 4.1. Inserting the values of L we obtain from the fits into Equation 4.1, we obtain the inner radius of the torus. We can further utilize CLUMPY parameter Y to determine in spatial scales how large the torus is since $Y = R_o/R_d$, where R_o is the outer extent of the torus. Even better, using the q parameter in combination with Y to understand the radial distribution of the clouds of the torus, we determine the extent at which 80% of all clouds lie and denote this outer radius as $R_o^{80\%}$. Using for each source the best-fit values for Y and q , in addition to the AGN luminosity we obtained from the scale factor, we computed $R_o^{80\%}$ and plotted its distribution found for Seyfert 1s in Figure 7.18. The tori of Seyfert 1 galaxies are preferentially compact with the majority of the clouds within 5 parsecs of the central engine. This is consistent with both MIR imaging observations, which found the torus of Circinus to be ≤ 4 pc (Packham et al., 2005), and with interferometric observations which assert that the torus is relatively compact (Jaffe et al., 2004; Tristram et al., 2007, 2009; Burtscher et al., 2009; Raban et al., 2009).

7.4.2 Seyfert 2 Analysis

In similar fashion to the analysis on the Seyfert 1 sources, we performed both a single- and 2-component model fitting technique on all 18 Seyfert 2s of the original spectropolarimetric sample (NGC 1068 and NGC 5506 were removed). As in the case of Seyfert 1s, we find the 2-component model fitting technique performs better in terms of χ_R^2 ; on average $\chi_R^2 = 0.77$ and 0.12, respectively for the single- and double-component fitting. Unlike the Seyfert 1s, the additional blackbody component cannot be explained by the ‘hot’ dust within the torus sublimation temperature since these Seyfert 2 sources have obscured views toward the central regions.

We can explain the necessity of the blackbody component for Seyfert 2s in terms of galaxy emission. In type 2 AGNs, the central engine is obscured by the torus, allowing

the emission from the host galaxy to become a larger fraction of total emission. We assume the emission of the host galaxy is in addition to that described by the star formation template. This would mean the blackbody could be a refinement to the star formation template in the sense that if we want to isolate the AGN emission, we must remove any contribution from the host galaxy, including star formation. The three-component model which includes the torus, the star formation template, and a blackbody would still be valid but under the conditions that a modified star formation / host galaxy template is formed from the sum of the blackbody and star formation template components. The differences between the original star formation template and the new template are expected to be small, on the order of a few percent and being no larger than 20%. Tables 7.5 and 7.6 provide observational details of the sources and show that, on average, the host galaxy (blackbody) contribution is 7% overall and is responsible for about 18% of all non-torus MIR emission. Since the blackbody is not a major component of the entire flux, the blackbody is not assumed to be an independent source of emission, but rather serves as an addendum to the star formation. Comparing the fractional contribution of total flux of the torus and star formation components of Seyfert 2s to those of Seyfert 1s (See Tables 7.4 and 7.6), we find the torus contribution to be comparable whereas the star formation template is a stronger component in Seyfert 2 sources. Since traditional views of Seyfert 2 galaxies are edge-on, it only makes sense that increased star formation emission is gathered along the line of sight to the central engine.

We proceed with the torus+blackbody composite models and determine that 14 of our 18 type 2 AGNs satisfy the $\chi_R^2 \leq 0.25$ requirements. In 2 of the 4 ‘not well-fit’ sources, the torus is not the dominant component in MIR emission. Since we are focused on modeling the intrinsic AGN properties with torus models, star formation-driven MIR emission will not be fit well by the models. We will explain why each of the 4 sources cannot be well fit in Appendix A.3 Poorly Fit Sources.

Performing the same analysis we applied on Seyfert 1s for the best-fit values of the parameters, we plot in Figure 7.18 the distributions of the parameter values for 14 Seyfert 2 AGNs in red. We immediately find that Seyfert 2 tori are compact with

Table 7.5. Observations and Galaxy Data for Seyfert 2s

Source Name	R.A. (J2000.0)	Decl. (J2000.0)	z	Scale (pc arcsec ⁻¹)	AOR
3C234	10 01 49.5	+28 47 09	0.185	4251	11305728
3C321	15 31 43.5	+24 04 19	0.096	2084	10828544
IRAS F04385-0828	04 40 55.0	-08 22 22	0.015	308	12447232
IRAS F15480-0344	15 50 41.5	-03 53 18	0.030	626	12480256
IC 5063	20 52 02.3	-57 04 08	0.011	231	18506752
IRAS 05189-2524	05 21 01.4	-25 21 45	0.043	888	32513792
IRAS 18325-5926	18 36 58.3	-59 24 09	0.020	411	18507520
IRAS 20210+1121	20 23 25.4	+11 31 35	0.056	1189	14872064
IRAS 20460+1925	20 48 17.3	+19 36 54	0.181	4144	16210176
MCG -05-23-016	09 47 40.1	-30 56 56	0.008	173	26484992
Mrk 463E	13 56 02.9	+18 22 19	0.050	1049	4980736
NGC 2992	09 45 42.1	-14 19 35	0.008	157	4934144
NGC 4388	12 25 46.7	+12 39 44	0.008	171	18510848
NGC 5252	13 38 16.0	+04 32 33	0.023	472	18946304
NGC 5728	14 42 23.9	-17 15 11	0.009	190	18945536
NGC 7582	23 18 23.5	-42 22 14	0.005	107	3855616
NGC 7674	23 27 56.7	+08 46 45	0.029	597	12468736
TOL 1238-364	12 40 52.9	-36 45 21	0.011	223	12466432

Note. — Units of right ascension are hours, minutes, and seconds, and units of declination are degrees, arcminutes, and arcseconds. Spatial scale based on $H_0 = 72$.

many clouds along equatorial rays distributed uniformly. Using the MIR emission to quantify the viewing angles towards these tori results in a bi-modality at the extremes of parameter space, with more preference toward edge-on views. Since observations of type 2 AGNs lack broad-line emission, we expect clouds to lie within our line-of-sight toward the central regions. The distribution of $N(i)$ agree with this expectation by showing that Seyfert 2s typically have more than one cloud along the line with nearly 50% of them encountering 13 or more clouds. Lastly, we found the outer extent of 80% of all clouds of the torus to be generally less than 5 parsecs.

We found in our MIR analyses of Seyfert 1s and 2s that the tori of both classes are spatially compact with sizes on the order of a few parsecs, with the tori of type 1s being generally smaller than those of type 2s. Comparing Seyfert 1s and 2s in Figure 7.18, we discover a similarity in some parameter distributions between the two classes, specifically N_0 , Y , q , and σ . Though Y and q are very similar between

Table 7.6. Fractional Contribution of Total Flux per Component in Seyfert 2s

Seyfert 2 Sources	Torus	SF Template	Blackbody	$\frac{BB}{SF+BB}$
3C234	98.0%	0%	2.0%	100%*
3C321	76.4%	23.6%
IRAS F04385-0828	65.8%	29.9%	4.3%	12.7%
IRAS F15480-0344	76.4%	19.2%	4.4%	18.5%
IC 5063	83.9%	15.7%	0.4%	2.5%
IRAS 05189-2524	74.4%	22.4%	3.2%	12.5%
IRAS 18325-5926	56.9%	36.6%	6.5%	15.2%
IRAS 20210+1121	82.1%	15.3%	2.6%	14.6%
IRAS 20460+1925	80.4%	10.2%	9.4%	48.1%
MCG -05-23-016	71.0%	21.1%	7.9%	27.1%
Mrk 463E	69.2%	24.2%	6.6%	21.5%
NGC 2992	44.8%	55.2%
NGC 4388	66.9%	29.6%	3.5%	10.6%
NGC 5252	70.9%	0%	29.1%	100%*
NGC 5728	35.2%	64.8%
NGC 7582	87.8%	12.2%
NGC 7674	65.8%	25.5%	8.7%	25.5%
TOL 1238-364	70.3%	27.2%	2.5%	8.4%
Average Values	73.7%	19.8%	6.5%	18.1%

Note. — Like Table 7.4 for Seyfert 2s. Sources with an * did not require the removal of the star formation template, thus the fractional contributions of the blackbody in column 5 for these sources are 100%. Since these are unique, we exclude them in the average, as the values would greatly skew the result.

the Seyfert classes, type 1s have an increased chance to be described by deeper radial distributions with smaller Y , which explains why this class has smaller tori. An interesting find is that both classes favor many clouds along an equatorial ray, essentially the maximum number limited by the models. If many clouds were limited to lie in the equatorial plane, type 1s with their typical face-on or shallow inclination angles would easily detect the broad-line emission, whereas type 2s would not since their large viewing angles nearly edge-on would obscure the BLR. However, the clouds are not constrained to just the equatorial plane, but are rather distributed according to a Gaussian centered on the equator (Nenkova et al., 2008b). Therefore, introducing σ into the discussion, it is of little surprise σ is generally flat with a slight favor toward larger values for type 2 viewing (See Figure 16 of Nenkova et al. (2008b)); however, for more than half of the type 1 sources σ is large, a result we do not expect. If a torus

had a large scale height, an observer really only has the chance to observe the central continuum emission if the inclination angle of the system is nearly face-on. By the values of $N(i)$, it appears that several of the type 1 AGNs confirmed this description. The average optical depth of each cloud τ_{avg} is nearly twice as high on average for the Seyfert 1s than for Seyfert 2s. In comparing these results to those of Ramos Almeida et al. (2011), who focused on a limited ground-based data set, there is some overlap in conclusions, mainly in that Seyfert 1s and 2s are intrinsically different; unification does not stand because the inclination angle is not the only parameter leading to differences in the MIR emission. The two studies found compact tori for both Seyfert classes though we found q tended to be larger in type 1s whereas Ramos Almeida et al. (2011) favor very large q for Seyfert 2s. In addition, the other authors found few clouds ($N_0 \sim 4$) for Seyfert 1s where we barely had any sources having that value.

7.5 Comparing the Analyses of Mid-Infrared Emission and Polarization

Despite much work in the area of AGN research, the intricate structure and characteristics of the torus remain unconstrained. The motivation of both the optical spectropolarimetry study and this MIR SED fitting examination is to determine the torus viewing angles. The polarimetric study has already quantified inclination angle estimates for a fairly large AGN sample. Our MIR assessment is structured to be completely independent of the polarimetry and has been up to this point. It is expected that if both techniques yield similar results, then there exists a first confirmation that the alluding torus inclination angle has been constrained. Thus far, we have concluded that fits of the torus+blackbody composite resulted in lower χ_R^2 values than those models consisting of only the torus component. However, the introduction of a ‘prior’ restriction on any parameter has yet to be analyzed. Any parameter, prior to fitting, can be restricted; that is, users of the fitting procedure have the option to limit the range of parameter values. This, in turn, creates a subset of the entire model database from which models are chosen to fit the data. For example, if a user has evidence that the torus has a small scale height, this person may force the fitting procedure to only use models that have tori with small opening angles. In

our situation, we have outside observations that may provide valuable prior information, that of spectropolarimetry. As witnessed in Section 7.1, the spectropolarimetric study examines the polarization structure over the broad H α emission line profile to conclude the geometry of the scattering dust. In the case of type 1 observations, the dust responsible for scattering was attributed to either a region co-planar and within the torus that quickly revolves around the black hole, or a scattering region above the rotation axis of the AGN. Each scattering region can then yield estimates of viewing or inclination angles. In order to obtain a more detailed examination of the relationships between optical polarizations and MIR emission, we implement the ‘prior’ knowledge of the i parameter from the polarization and compare the results to those of non-restricted fits. On average, the differences between restricting i and not doing so were minimal, $\chi_R^2 = 0.09$ and 0.08 , respectively, but much more can and will be discussed in the following sections.

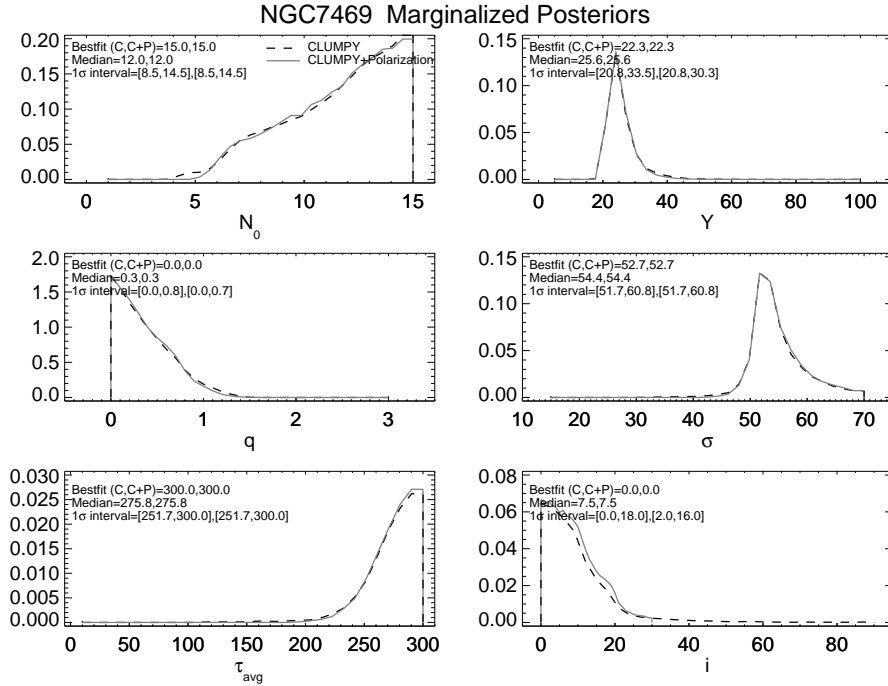
7.5.1 Seyfert 1 Analysis

The sample of 36 type 1 Seyferts can be divided into the three classes of polarization, ‘Null’, ‘Equatorial’, and ‘Polar’. While Smith et al. (2004) give inclination angle approximations for each scattering region as ‘Null’ – $i \sim 0^\circ$, ‘Equatorial’ – $0 < i < 45^\circ$, and ‘Polar’ – $i > 45^\circ$, we allow a slightly larger range for each classification. We adopt the ‘Null’ or unpolarized type 1 source to be viewed with angles $0 < i < 30^\circ$, the equatorial scattered type 1 with $i < 50^\circ$, and the polar scattered type 1 AGNs with $30^\circ < i < 60^\circ$, and thus place these restrictions on i when we implement the ‘prior’ knowledge of the polarization. Our sample thus consists of 11 unpolarized, 9 polar-scattered, and 16 equatorially-scattered Seyfert 1 sources.

Concerning the agreement of the non-restricted and restricted fits, we performed an evaluation utilizing the marginalized posterior distributions of each CLUMPY parameter and the best-fit value. We examined for each source individually, the consistency between the non- and restricted fits, which we now label for convenience as ‘C’ and ‘C+P’, respectively, where the convention comes from ‘C’LUMPY models only and ‘C’LUMPY+‘P’olarization restrictions. Please note that both C and C+P

include the blackbody component in the fitting and that Section 7.4.1 represents the results of C. Like Figures 7.16 and 7.17, we show in Figure 7.19 for NGC 7469 the marginalized posterior distributions of the 6 CLUMPY parameters. The difference between the figures is that we now plot the posteriors of both C and C+P, or (2) and (4) from the convention in Section 7.4. The dashed lines correspond to the posteriors of the CLUMPY (or C) fittings, whereas the solid line produces the distribution of the C+P fits. The bottom right panel, corresponding to the i parameter, allows for quick realization of the parameter restriction as the solid line is clearly constrained within an interval. Also printed in each panel is the best-fit and median value associated with the fit. The best-fit value need not be equal to the median value of the posterior, but we use this value as a means to assess how well the CLUMPY database fits the data (see below). Lastly, a 1-sigma interval is printed in each panel specifying the range of parameter values that are most likely or in which we have more confidence. The bottom panel for each source plots the *Spitzer IRS* spectrum in black with gray error bars, overplotted by both the best-fit model determined by C (solid red) and by the best-fit model yielded by C+P (solid blue). Since each model consists of a torus (dash) and blackbody component (dot), we plot each to show their respective contribution to the fit. The lower panel legend lists the best-fit parameter values in addition to the reduced chi-squared values each model results in, and we see that the C+P χ_R^2 are greater than or equal to that of the C fit.

The two fitting techniques, C and C+P, were performed such that the full database of clumpy torus models fits the data and provides the best-fit and posteriors for the C method, and a subset of the database, determined by the polarization restrictions on i , fits the data for the C+P method. In this manner, C fits show the capabilities of the MIR in determining the inclination angle, whereas the C+P method requires the final models that describe the data to have i values in agreement with the polarization estimates. Therefore, overplotting their respective best-fit values and posterior distributions allows for quick inspection as to whether the MIR assessment is in agreement with the polarization predictions. That is to say, if the posteriors and the best-fit models completely agree between the C and C+P fits, then the inclination angles



Data with CLUMPY and CLUMPY+Polarization Bestfits

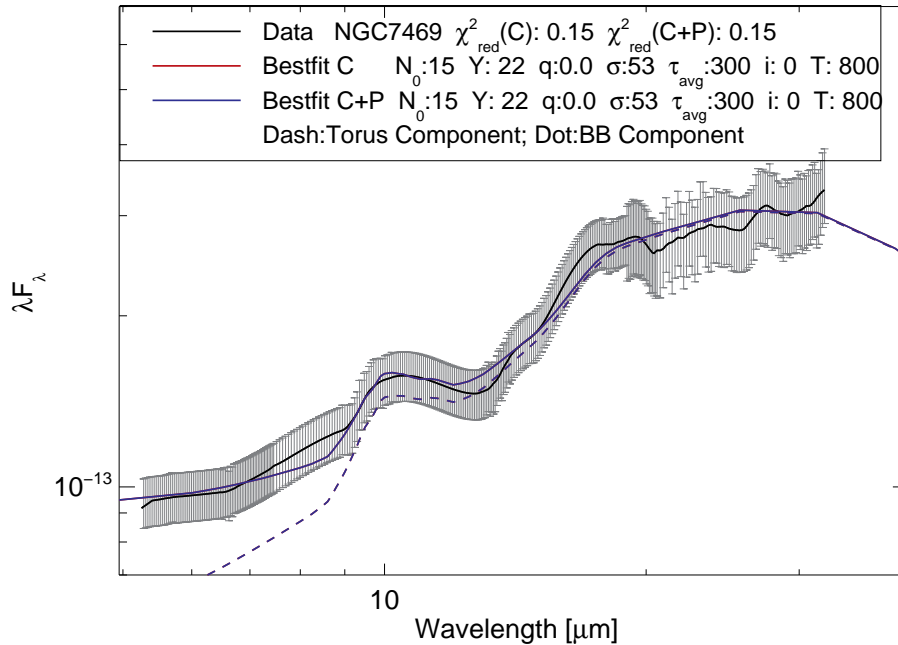


Figure 7.19 Bottom: The *Spitzer IRS* spectrum of Seyfert 1 NGC 7469 (black with gray error bars) is fit by the best-fit model (solid red), which is composed of the torus (dashed) and a blackbody (dotted). best-fit values are listed in the figure as well as the χ^2_R value. Top: The marginalized posterior distributions of the 6 CLUMPY parameters with the dashed lines corresponding to the posteriors of the CLUMPY+blackbody fittings, whereas the solid line produces the distribution of the torus+blackbody+polarization priors fits. Printed in each panel is the best-fit and median value associated with the fit as well as a 1-sigma interval.

determined solely by MIR emission are in accordance with the predictions of polarization. For the Seyfert 1 sample, 15 of 36 sources had their fits behave like this, and for reference, let us refer to this subsample as ‘First Class’. Of these, 10 sources were classified with equatorial scattering, 4 as null polarization, and 1 as polar scattering which shows the strong preference for lower i values. The majority of the Seyfert 1s classified as polar scattered sources – those that supposedly have views glancing the torus – are in the ‘Second Class’ which require i to be restricted to ‘match’ polarization.

Alternately, if observations are described only by MIR emission (i.e., C fitting) with fitting results indicating large viewing angles, for example, and polarization suggests lower values of i , the posteriors clearly show that there is disagreement between the two techniques. This does not mean the MIR emission cannot support the predictions of polarization. Rather, a different route of analysis must be explored to determine if any models with inclination angles preferred by polarization successfully describe the observations. As long as the clumpy models describe the data within the viewing orientation predictions of polarization *and* have χ_R^2 values less than the threshold value, then it can be stated that MIR emission supports and agrees with the polarization predictions of inclination angles. Let us call these 21 type 1s, ‘Second Class’ sources.

Figure 7.19 as well as Figures A.1a-A.1ii contain the marginalized posterior distributions and SEDs of 36 Seyfert 1 sources, and as discussed in the previous paragraph, the posteriors of the C and C+P fittings are overplotted. We expect the C and C+P posteriors to overlap for the i parameter and thus calculate the area of overlap between the two fitting methods. A larger overlapping area suggests that the C and C+P fit are in agreement and that MIR emission confirms the viewing angle estimates of spectropolarimetry, whereas little overlap means the two fitting methods do not pick the same models (which one would expect since i is restricted). Figure 7.19 and Figures A.1a-A.1ii are arranged as ‘First Class’ and ‘Second Class’ sources with each subset ordered in decreasing percentage of overlapping area between the C and C+P fits in the i posterior distributions. As might be expected, the sources with

large overlapping areas are fit by the same best-fit model and are described by the same posterior distributions. Progressing through the figures, as the overlapping area between the two i posteriors decreases, we find that the both the best fit models and the parameter posteriors deviate from each other.

To collectively analyze the results of Figure 7.19 and Figures A.1a-A.1ii, the fits without restrictions on i – those that are completely independent of the polarization study – are in general agreement with those fits with restrictions. This exhibits that the MIR emission confirms the polarization predictions. We base this on first the First Class objects of which fits with and without i restrictions were identical. Secondly, all sources when fit with the restricted database were found to be described well ($\chi_R^2 \leq 0.25$) by models with smaller inclination angles, even if the best fit model from the full database preferred large i values. Additionally, minimal fluctuations were seen between the C and C+P posteriors and the best-fit models in general. As we progress through the figures, C fits start to prefer inclination angles that lie outside the C+P restricted range. This leads to not only differences in the best-fit models, but also causes the posteriors between the two techniques to change. These cases can be explained in two ways: (1) the i posterior for both C and C+P is flat. If the posterior is flat, we can say nothing about the behavior of the parameter; there is no constraint on the parameter. Therefore, there is no favoring one value of i over another, and it becomes evident that the models inherently contain a degeneracy. This is clearly seen in Figure A.1o for NGC 4051, and in this circumstance, we must confess that our models are insensitive to viewing angle for the data in question. This does not mean we do not understand the distribution of dust for this source, but rather that we lack the ability to place a constraint on i , for all the other parameters are fairly well constrained. (2) The other explanation for the differing behavior of the posteriors between the C and C+P methods is that the non-restricted fit favors viewing angles much outside the range limited by the polarization estimates. In these situations, the C+P fit favors the upper/lower limit of i in such a manner to match the results sans restrictions. If the limiting range was extended, the best-fit value would reflect the alteration and still favor the upper boundary value. As the procedure is designed to

discover the best fit model and distribution of parameters, it is of significant reporting in these later cases that as i is impeded from reaching larger values in C+P, other parameters alter in such a way to compensate for the larger i values that cannot be obtained. For example, IC 4329A has an $30 < i < 60^\circ$ restriction; however the best-fit model (and the i posterior) for C tends toward $i = 90^\circ$. Since i cannot reach 90° , it chooses the maximum value of 60° , and for the model with lowest χ_R^2 to be chosen (which should resemble the best-fit model for C), the parameter σ compensates with increased values. This can be understood with the comparison of a small scale height torus with views close to edge-on to a slightly larger scale height torus with decreased viewing angles. In both cases, the views would be similar, nearly glancing the limit of the torus scale height.

Tables 7.7a and 7.7b list the median and best fit values for the i -restricted fits. The 15 First Class sources kept their parameter values constant with and without polarization priors, whereas those of Second Class sources shifted. Similar to the histograms of Figure 7.18, we plot the distribution of best-fit parameter values for First and Second Class Seyfert 1 sources in black in Figures 7.20 and 7.21. The two ‘classes’ consist of different distributions, but we must recall that the ‘Second Class’ sources had their resultant best-fit model altered by the i restraint, whereas the ‘First Class’ sources maintained their best-fit parameters. The large majority of First Class sources favored small i values, which is expected from the polarization since their polarization classes were mostly equatorial and null – the two classes with small i . The majority of Second Class sources were polar scattered, in which the constraint on i kept all values below 60° and above 30° which is what we see. Since the polar scattered objects have small angles now, the σ values increased, spiking at large values, whereas First Class sources have σ nearly unconstrained. Both classes prefer a compact torus (< 4 pc) with similar Y and q values as well as several highly optically thick clouds. First Class sources intercept fewer clouds along direction i than Second Class sources, where this can be explained by their differing values of σ and i .

The appendix contains a detailed analysis for each source describing the behavior

Table 7.7a. Fitted Torus Model Parameters for Seyfert 1s

Seyfert 1s	N_0		Y		q	
	Median	Best-Fit	Median	Best-Fit	Median	Best-Fit
<u>'First Class'</u>						
NGC 7469	$12.0_{3.5}^{2.5}$	15.0	26_5^4	22	$0.3_{0.3}^{0.4}$	0.0
PHL 1811	$9.6_{3.9}^{4.0}$	7.0	54_{14}^{11}	67	$1.8_{0.3}^{0.1}$	1.8
Mrk 1048	$11.0_{3.9}^{3.1}$	15.0	26_{11}^{17}	22	$1.4_{0.8}^{0.6}$	1.2
PG 1700+518	$9.6_{3.9}^{4.0}$	14.5	57_{20}^{18}	83	$1.5_{0.3}^{0.2}$	1.5
Mrk 876	$9.2_{4.0}^{4.4}$	7.0	29_{11}^{17}	34	$1.9_{0.8}^{0.2}$	2.2
IZW1	$8.7_{3.5}^{4.0}$	12.8	67_{18}^{11}	74	$1.5_{0.1}^{0.2}$	1.7
Mrk 335	$8.7_{4.4}^{4.4}$	6.2	29_{11}^{14}	20	$1.6_{0.6}^{0.4}$	0.7
PG 2214+139	$5.4_{2.5}^{3.5}$	10.0	26_{11}^{17}	15	$1.6_{0.8}^{0.3}$	0.6
NGC 3783	$11.5_{3.0}^{2.6}$	15.0	16_5^5	12	$0.9_{0.6}^{0.8}$	0.0
Mrk 896	$13.4_{2.1}^{1.6}$	15.0	57_{11}^{15}	50	$0.2_{0.2}^{0.2}$	0.0
NGC 5548	$10.6_{3.1}^{3.0}$	15.0	16_8^8	10	$1.6_{1.1}^{0.6}$	0.0
Mrk 279	$10.1_{3.5}^{3.5}$	15.0	13_5^8	8	$1.5_{0.9}^{0.7}$	0.0
Mrk 766	$10.6_{2.6}^{3.0}$	10.1	32_{11}^8	43	$2.0_{0.3}^{0.2}$	2.1
Mrk 915	$12.4_{2.1}^{2.1}$	15.0	10_2^5	11	$0.2_{0.2}^{0.4}$	0.0
Mrk 590	$12.4_{2.5}^{2.1}$	15.0	10_2^1	9	$0.6_{0.5}^{0.5}$	0.0
<u>'Second Class'</u>						
NGC 4051	$7.8_{3.1}^{4.4}$	4.9	26_8^8	23	$1.8_{0.6}^{0.3}$	1.5
Mrk 478	$8.7_{3.5}^{4.0}$	4.0	45_{18}^{20}	82	$1.5_{0.3}^{0.4}$	1.5
Ark 120	$7.8_{4.5}^{4.4}$	2.4	13_5^5	10	$1.2_{0.6}^{0.7}$	0.4
KUV 18217+6419	$12.0_{3.1}^{2.5}$	14.3	10_2^5	11	$1.5_{0.8}^{0.6}$	2.1
MCG -06-30-015	$9.6_{3.5}^{4.0}$	8.0	13_5^8	9	$1.6_{0.8}^{0.6}$	0.7
Fairall 51	$7.3_{2.6}^{4.4}$	6.9	29_8^{11}	29	$1.9_{0.5}^{0.2}$	2.1
Mrk 1239	$7.3_{3.5}^{5.4}$	4.8	16_5^{11}	19	$2.0_{0.7}^{0.3}$	1.8
Mrk 1040	$7.3_{3.0}^{4.9}$	4.9	57_{17}^{18}	80	$1.5_{0.2}^{0.3}$	1.6
Mrk 486	$5.9_{2.6}^{4.9}$	3.6	10_5^5	10	$1.9_{0.8}^{0.7}$	1.4
IC 4329A	$10.1_{3.5}^{3.5}$	15.0	13_5^7	10	$1.9_{0.9}^{0.4}$	2.1
NGC 4593	$9.6_{4.9}^{4.5}$	12.8	70_{14}^8	75	$1.6_{0.1}^{0.2}$	1.7
UGC 7064	$9.2_{2.6}^{3.5}$	10.4	16_5^5	19	$1.6_{0.5}^{0.5}$	2.1
Mrk 926	$13.4_{2.1}^{1.6}$	15.0	10_2^1	9	$0.2_{0.2}^{0.5}$	0.0
Mrk 6	$13.8_{1.6}^{1.2}$	15.0	10_2^1	9	$0.2_{0.2}^{0.4}$	0.0
IC 3599	$7.3_{2.6}^{4.9}$	4.1	29_8^5	20	$1.5_{0.2}^{0.2}$	1.1
NGC 4151	$12.4_{3.0}^{2.1}$	15.0	10_2^5	8	$0.6_{0.5}^{1.3}$	0.0
PG 1211+143	$11.5_{4.4}^{2.6}$	13.9	10_2^5	9	$2.0_{0.7}^{0.5}$	2.3
Mrk 841	$12.0_{3.5}^{2.1}$	15.0	10_2^8	11	$1.5_{1.1}^{0.6}$	1.9
NGC 3516	$9.2_{2.6}^{3.9}$	6.1	26_8^{14}	25	$1.4_{0.8}^{0.4}$	1.3
PG 1612+261	$12.0_{2.1}^{2.1}$	12.9	29_5^5	30	$0.6_{0.4}^{0.3}$	0.7
Mrk 705	$12.4_{2.5}^{2.1}$	12.9	13_5^2	10	$2.5_{0.3}^{0.2}$	2.5

Note. — Median values with $\pm 1\sigma$ and best-fit values are listed for the C+P fitting technique for three of the six torus model parameters. The remaining three parameters follow in Table 7.7b.

Table 7.7b. Fitted Torus Model Parameters for Seyfert 1s (cont.)

Seyfert 1s	σ		τ_{avg}		i	
	Median	Best-Fit	Median	Best-Fit	Median	Best-Fit
<u>'First Class'</u>						
NGC 7469	54_2^7	53	276_{24}^{26}	300	8_6^8	0
PHL 1811	29_8^{14}	36	228_{92}^{53}	300	19_{14}^{18}	0
Mrk 1048	43_8^{11}	37	102_{24}^{24}	99	16_{13}^{17}	0
PG 1700+518	31_9^{13}	19	141_{63}^{101}	70	18_{13}^{19}	50
Mrk 876	42_{10}^{17}	68	199_{72}^{72}	300	18_{13}^{17}	0
IZW1	25_8^{14}	20	237_{73}^{53}	300	26_{18}^{16}	41
Mrk 335	31_{10}^{15}	36	150_{63}^{102}	79	21_{14}^{19}	0
PG 2214+139	27_{10}^{19}	15	83_{34}^{53}	69	23_{16}^{17}	0
NGC 3783	62_8^6	58	189_{34}^{34}	209	24_{17}^{18}	0
Mrk 896	56_8^7	56	15_5^5	11	18_{11}^8	20
NGC 5548	60_8^8	53	160_{34}^{43}	206	31_{14}^{23}	0
Mrk 279	58_{10}^8	57	141_{32}^{33}	180	29_{21}^{16}	5
Mrk 766	56_{10}^{10}	69	150_{14}^{24}	148	43_{10}^{11}	30
Mrk 915	64_5^4	61	160_{15}^{14}	157	12_9^{11}	0
Mrk 590	64_5^6	62	218_{34}^{34}	196	18_{13}^9	25
<u>'Second Class'</u>						
NGC 4051	45_{10}^{16}	44	112_{34}^{33}	92	23_{16}^{19}	47
Mrk 478	47_{12}^{14}	62	112_{44}^{101}	73	15_{11}^{10}	30
Ark 120	29_{12}^{21}	53	54_{25}^{43}	51	21_{16}^{21}	50
KUV 18217+6419	62_8^6	70	247_{44}^{43}	252	33_{20}^{14}	38
MCG -06-30-015	56_{12}^{10}	70	121_{24}^{24}	156	47_{12}^9	30
Fairall 51	45_{10}^{16}	68	189_{63}^{63}	282	43_{10}^{11}	40
Mrk 1239	34_{12}^{19}	44	112_{44}^{110}	96	43_{10}^{11}	30
Mrk 1040	42_{10}^{18}	59	73_{24}^{24}	71	43_{10}^{11}	30
Mrk 486	49_{16}^{16}	48	73_{34}^{82}	54	48_{12}^9	60
IC 4329A	60_{12}^8	70	102_{24}^{24}	108	51_{12}^7	60
NGC 4593	31_7^{13}	30	112_{34}^{24}	112	40_8^{11}	30
UGC 7064	62_{10}^6	70	121_{14}^{24}	113	53_{12}^5	60
Mrk 926	67_4^3	70	218_{34}^{43}	195	20_8^{13}	30
Mrk 6	67_6^3	70	276_{34}^{24}	300	44_{11}^6	50
IC 3599	53_{10}^{12}	67	54_{25}^{18}	53	20_{13}^8	29
NGC 4151	65_8^5	68	150_{34}^{24}	153	36_{24}^8	0
PG 1211+143	62_{10}^6	70	266_{53}^{34}	300	19_{13}^8	30
Mrk 841	64_7^6	70	102_{15}^{24}	103	43_{18}^7	50
NGC 3516	62_8^6	70	131_{24}^{34}	134	19_{13}^9	30
PG 1612+261	58_8^7	50	15_5^5	15	26_8^3	30
Mrk 705	67_6^3	70	102_{15}^{14}	104	24_{12}^5	30

Note. — Continued from Table 7.7a

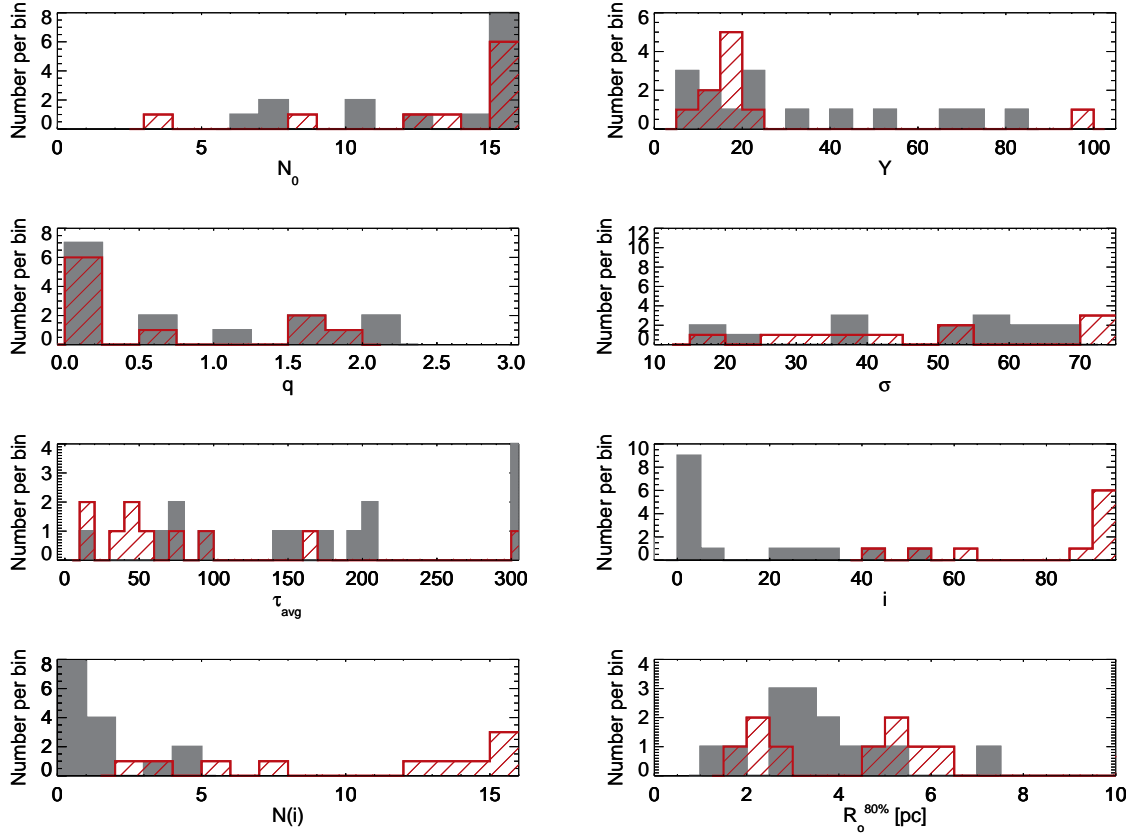


Figure 7.20 Shown for the ‘First Class’ sources, 15 Seyfert 1s (black) and 10 Seyfert 2s (red), are histograms of the best-fit values of the 6 CLUMPY parameters derived from the C+P fitting technique, as well as the average number of clouds encountered along direction i , $N(i)$, and the outer extent of the torus for which 80% of the clouds have been accounted, $R_o^{80\%}$.

of each fit and the agreement between polarimetry and MIR emission. Sources are listed in order of the percentage of overlapping area between the C and C+P posterior distributions for the i parameter, and accompanying figures can also be found there.

7.5.2 Seyfert 2 Analysis

We perform the same analysis on Seyfert 2s as we did on type 1s in Section 7.4.1, though only one polarization class exists for type 2s. Objects lacking broad emission

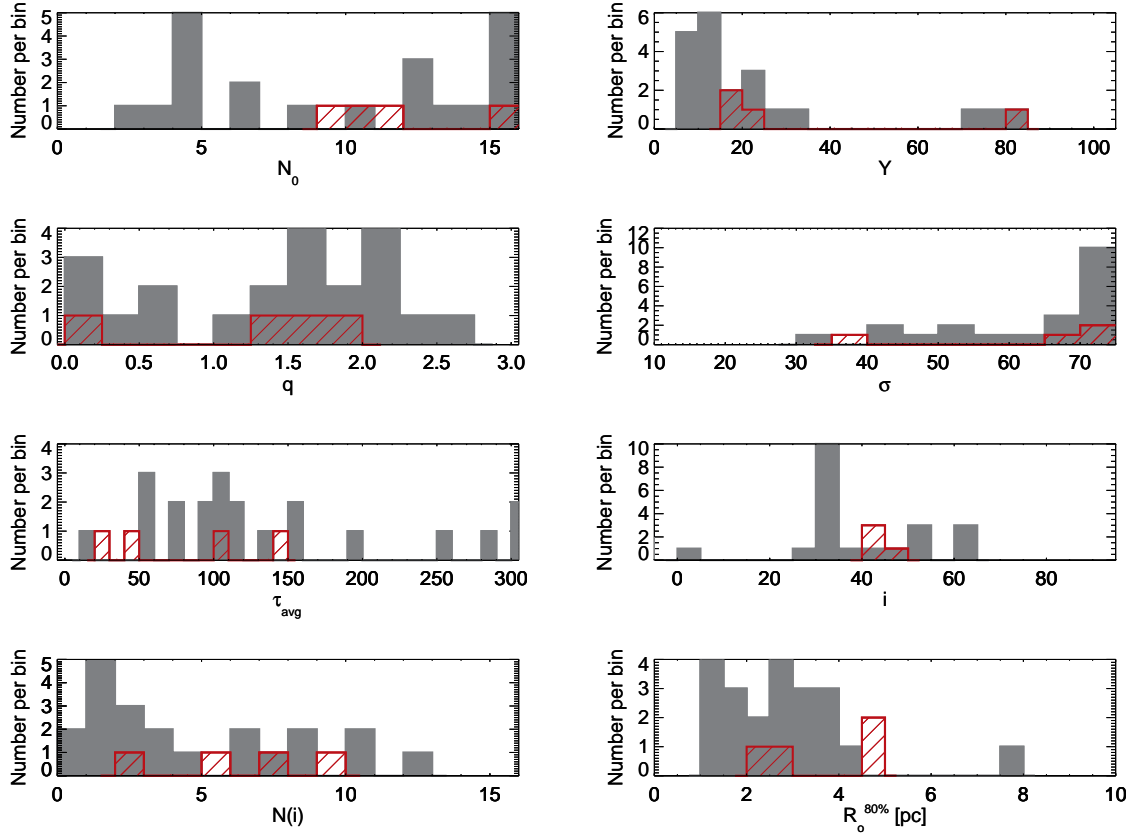


Figure 7.21 Same as Figure 7.20 but for ‘Second Class’ sources: 21 Seyfert 1s (black) and 4 Seyfert 2s (red).

lines are classified as type 2 AGNs, yet broad lines have been observed in polarized light for these sources (Smith et al., 2002, 2004). The polar scattering region explains (See Section 7.1.2.) the polarization properties, and Smith et al. (2004) provide inclination angle approximations for the polar scattering region of $i > 45^\circ$. This is generally accepted since orientation angles greater than 45° typically have views toward the central engine obscured by the torus. However, in our fitting, we implement the ‘prior’ knowledge of the polarization by placing the restrictions $i > 40^\circ$.

To confirm the two fitting methods (with and without $i > 40^\circ$ restrictions set by polarization) are consistent, we compared, on a source-by-source basis, the marginal-

ized posterior distributions and best-fit values found by both procedures, identical to the method in Section 7.4.1. Like Figure 7.19, Figures A.2a-A.2n show the posterior distributions and best-fit SEDs of 14 Seyfert 2 sources. The non-restricted C posteriors are dashed lines while the C+P posteriors are solid, and any overlap between the two suggests that they may be used together as a proxy for inclination angles. The 14 sources are arranged first by their ‘First’ and ‘Second Class’ status and then in order of decreasing percentage of overlapping area between the C and C+P fits in the marginalized posterior distribution of i , where the Class status is as defined in Section 7.5.1. Seven of the sources have more than 80% overlap which suggests the two fits are similar, and the first 7 figures clearly show that the best-fit model and posterior distributions of all the parameters are virtually identical. These 7 sources in addition to three more sources that have the same best-fit models for the C and C+P fitting results are the First Class sources. Seyfert 2s are generally thought of having large inclination angles. Fitting without prior restrictions on i yields posteriors that favor high inclination values, and restricting the model database to only include models of high i made no difference since these were the preferred values anyway. However, five sources whose fits were independent of polarization predictions favored lower values of inclination, but these sources confirmed polarization in the sense that models utilizing the constrained values of i still successfully described the data. We present a brief overview for each source describing the degree of agreement between polarimetry and MIR emission in the appendix.

Table 7.8 lists the best-fit and median values of the posterior, and Figures 7.20 and 7.21 show, in red, histograms of the best-fit values for Seyfert 2s separating the sources into First and Second Classes respectively. The First Class sources strongly favored large inclinations whereas the Second Class sources liked low values and were thus limited by the restraint to $i = 40^\circ$. With a small sample, it is difficult to quantify any other parameter results, but as a Seyfert 2 sample, the models show that the tori are compact ($R_o^{80\%} < 0.5$ pc) with several clouds encountered along the line of sight.

Table 7.8. Fitted Torus Model Parameters for Seyfert 2s

Seyfert 2s	N_0		Y		q	
	Median	Best-Fit	Median	Best-Fit	Median	Best-Fit
<u>‘First Class’</u>						
MCG -05-23-016	$12.0_{3.1}^{2.5}$	15.0	13_{5}^5	14	$1.4_{0.9}^{0.4}$	1.7
Mrk 463E	$13.8_{1.1}^{1.2}$	15.0	19_{4}^2	19	$0.4_{0.2}^{0.3}$	0.5
NGC 4388	$12.9_{3.5}^{1.6}$	13.4	19_{1}^5	20	$0.2_{0.2}^{0.3}$	0.0
IRAS 05189-2524	$4.0_{0.7}^{0.2}$	3.5	98_{4}^2	99	$0.1_{0.1}^{0.0}$	0.0
NGC 5252	$8.7_{3.5}^{4.0}$	15.0	13_{5}^5	8	$1.2_{0.8}^{0.9}$	0.0
IRAS 20210+1121	$13.4_{2.6}^{1.1}$	15.0	16_{5}^5	19	$1.6_{0.6}^{0.4}$	2.0
IRAS 18325-5926	$9.2_{3.5}^{3.9}$	12.7	16_{5}^8	15	$1.5_{1.0}^{0.6}$	0.0
IC 5063	$12.0_{3.5}^{2.5}$	15.0	16_{1}^5	16	$0.6_{0.5}^{0.7}$	0.0
IRAS F15480-0344	$9.2_{2.6}^{3.5}$	8.2	22_{4}^8	20	$1.9_{0.5}^{0.2}$	1.7
IRAS 20460+1925	$12.9_{3.0}^{1.6}$	15.0	16_{5}^2	16	$0.3_{0.3}^{0.5}$	0.0
<u>‘Second Class’</u>						
NGC 7674	$10.6_{3.1}^{3.0}$	10.8	29_{11}^{11}	24	$1.8_{0.6}^{0.3}$	1.8
3C234	$7.8_{3.1}^{4.9}$	11.1	19_{8}^8	16	$1.8_{0.8}^{0.4}$	1.4
TOL 1238-364	$9.6_{2.1}^{3.1}$	9.0	16_{1}^5	15	$0.6_{0.5}^{0.6}$	0.0
IRAS F04385-0828	$13.4_{2.1}^{1.6}$	15.0	79_{7}^5	83	$1.5_{0.1}^{0.1}$	1.5
	σ		τ_{avg}		i	
	Median	Best-Fit	Median	Best-Fit	Median	Best-Fit
<u>‘First Class’</u>						
MCG -05-23-016	54_{11}^{12}	52	54_{15}^{14}	54	81_{11}^7	90
Mrk 463E	45_{4}^7	41	15_{5}^5	11	79_{11}^9	90
NGC 4388	54_{6}^{11}	53	34_{5}^{24}	32	81_{11}^7	90
IRAS 05189-2524	60_{6}^6	70	73_{15}^5	71	83_{8}^5	90
NGC 5252	29_{10}^{15}	18	266_{53}^{24}	300	81_{13}^7	90
IRAS 20210+1121	62_{10}^8	70	92_{14}^{15}	94	76_{18}^{11}	90
IRAS 18325-5926	43_{15}^{18}	29	44_{24}^{24}	15	71_{18}^{14}	90
IC 5063	40_{10}^{12}	33	73_{34}^{14}	44	58_{13}^{17}	62
IRAS F15480-0344	58_{14}^8	70	141_{15}^{24}	162	61_{16}^{19}	50
IRAS 20460+1925	38_{5}^5	37	63_{24}^{15}	48	44_{4}^6	40
<u>‘Second Class’</u>						
NGC 7674	58_{12}^{10}	70	102_{15}^{14}	106	61_{14}^{19}	50
3C234	40_{12}^{19}	38	54_{15}^{14}	49	59_{14}^{19}	40
TOL 1238-364	62_{10}^6	68	131_{14}^{14}	41	53_{11}^{20}	40
IRAS F04385-0828	64_{7}^6	70	25_{5}^4	23	58_{15}^{19}	40

Note. — Median values with $\pm 1\sigma$ and best-fit values are listed for the CLUMPY torus model parameters as derived from the C+P fitting technique for Seyfert 2 sources.

7.5.3 Overall Sample Analysis

We set out to find if techniques using polarization to determine torus inclination angles yielded results similar to those we achieve by fitting MIR emission with clumpy torus SEDs. Out of a sample of 50 well-fit Seyfert galaxies, 25 (15 type 1 and 10 type 2) confirmed that the two techniques provide similar inclination angles. This means that there is roughly a 50-50 chance that MIR emission and polarization will agree when determining torus viewing angles. If we look just at the parameter distributions of these sources which we have labeled as ‘First Class’ in Figure 7.20, we see that there is a fine distinction between type 1 and type 2 sources but surprisingly in only two parameters: i and τ_{avg} . Seyfert 2s consistently favor high i values and lower values of τ_{avg} (< 100), and Type 1s prefer low i and allow for larger cloud optical depths. Both Seyfert classes have their tori described by large scale heights with many clouds along an equatorial ray, but only Seyfert 1s provide high probabilities to see the central regions of the AGN since few clouds, on average, are seen.

These results are consistent with the analysis we performed in Section 7.4 when we took only the results of the MIR emission without polarization predictions. In fact, comparing the full Seyfert 1 results of both sections to each other and likewise for the type 2s, there is not a whole lot of change in the parameter distribution. As the i restrictions are imposed, the only Seyfert 2 parameter that noticeably changes is i from low values to required larger values, and this change influences $N(i)$ which too favors increased values when implementing the polarization conditions. Parameter i is also the prominent change for the type 1s, where a now low i allows $N(i)$ to decrease. These results completely follow the restrictions: make type 1 sources more like type 1 sources – low i – and type 2s like type 2s – high i . Does this signify that similar model parameter distributions come about when fitting observations with and without polarization priors? The only parameter distribution to change is i , and the other parameters maintain their general shape. If (1) i is restricted from prior information to make the models pick different i values, (2) the fits choose new models that sufficiently describe well the data, and (3) the other parameters don’t change

significantly between the two fits, then using the technique of fitting SEDs to MIR emission is not sufficient in determining the inclination angles of AGNs. It means i cannot be constrained using MIR emission; there are too many degeneracies involved with the models that make it difficult to determine i with certainty. This may explain why we found the 50-50 chance that MIR emission and polarization agree; it may truly be a toss-up, we either do find they agree or we do not. In addition to the degeneracies that exist within the model database, the technical capability of the fitting procedure has its limitations also. As will be discussed in Nikutta et al. (2012, in prep.), the fitting technique becomes less reliable and accurate as the error of the observation increases (more noisy data). Increasing the error bars allows for more models to describe the data ‘well’ since the observation error is part of the χ_R^2 , leading to the posterior distributions to flatten, which ultimately means a parameter cannot be constrained.

While i may not be a constrainable parameter as far as the model fitting is concerned, we regard Y as the most static parameter as it generally always gives the same result – $Y \sim 15 - 20$ for both Seyfert classes. The overall behavior of τ_{avg} is more understood than certain values: type 2 AGNs have lower cloud optical depths than type 1, where the former have typical values less than 100, while type 1s generally prefer values exceeding 100. Parameter q is consistent in the sense that it behaves bimodally, desiring values of 0.0 or 1.5 regardless of AGN type. The histograms show N_0 liking higher values, but since the favored value lingers on the edge of parameter space, we are cautious. Lastly, σ is definitely not constrained as it changes as much as i with sporadic fluctuations. Though $N(i)$ depends on the three parameters that are least constrained, the resultant values are promising. Type 1 sources generally have low values of $N(i)$, less than 2 most of the time, though there are times type 1s have large values. Since type 1 AGN are required to have direct lines of sight to the BLR, it is unreasonable to have several optically-thick clouds along the line of sight for the Seyfert 1s in the sample. This shows an inherent problem in the analysis, likely caused by the large degeneracies in the models. To rectify these enigmatic type 1 $N(i)$ values, we will fit type 1 sources only by models that provide at least a 50%

probability of seeing the central engine. This constraint will drastically reduce the size of the model database used in the fitting and should therefore provide a more robust conclusion regarding the dust distribution. Type 2s fancy the larger values, which would definitely obscure the BLR and central regions.

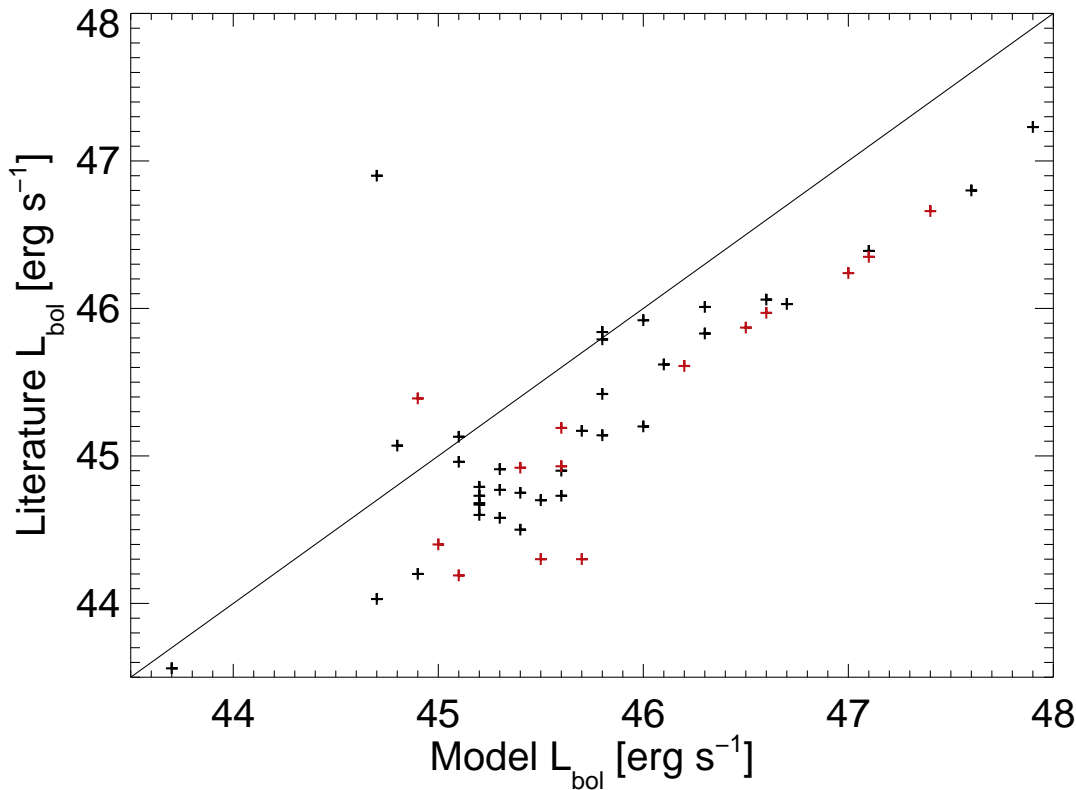


Figure 7.22 Comparison between the bolometric luminosities of the AGN as obtained from the best-fit models and the literature. Black and red points are Seyfert 1s and 2s respectively, and the solid line is a 1:1 relation. The luminosities are tabulated in Tables 7.9 and 7.10.

As we discussed in both Section 4.3 and Section 7.4.1, we can obtain the bolometric luminosity of the AGN from scaling the models to the observations. As a check of consistency for the models, we compare the bolometric luminosities of the models to published values found in the literature. Tables 7.9 and 7.10 list for Seyfert 1s and Seyfert 2s separately, the model luminosities, literature values of luminosity, the radius at which 80% of all the clouds are found, the number of clouds along direction

i , $N(i)$, and the covering factor of the torus. We used three different methods to obtain the bolometric luminosity from the literature: the 2-10 KeV X-ray luminosity using a bolometric correction of 20 (Nandra & Iwasawa, 2007; Risaliti & Elvis, 2004), the 5100 Angstrom luminosity with a correction factor of 10.3 (Richards et al., 2006), and the IR luminosity and a 3.2 bolometric correction (Risaliti & Elvis, 2004). We plot in Figure 7.22 a comparison between the AGN bolometric luminosities we obtained from fitting and bolometric luminosities from the literature for both Seyfert 1s (black) and Seyfert 2s (red). We use the upper limits of the literature values and find that a correlation exists, and the two data sets are within ~ 0.4 dex of the 1:1 relation (solid line). The difference may come from the bolometric corrections as a wide range of values are found; Vasudevan et al. (2010) found the 2-10 KeV X-ray bolometric corrections ranging from 10-30, for example. We used the bolometric luminosities provided by the fitting procedure and using Equation 4.1, calculated the dust sublimation radius of the torus. Employing the q distribution with Y , we determined at what radius 80% of all toroidal clouds lie within, and on average the radii of Seyfert 1 and 2 tori extend to 3.1 pc and 3.9 pc, respectively. These values using Spitzer observations in combination with MIR clumpy torus model SEDs are consistent with high-resolution observations that found clumpy tori are geometrically compact.

Table 7.9. Measurements of Seyfert 1s

Source Name	L_{bol}^{model}	L_{bol}^{lit}	References	$R_o^{80\%}$	$N(i)$	Covering factor
<u>‘First Class’</u>						
NGC 7469	46.0	44.35-45.92	1,2,3,4,6,7,8,9,11	7.3	0.8	0.99
PHL 1811	47.1	45.98-46.39	10,12	2.6	0.0	0.80
Mrk 1048	46.0	45-45.2	1,8	3.9	0.0	0.89
PG 1700+518	47.6	46.56-46.8	7,12	4.7	0.2	0.55
Mrk 876	46.6	45.66-46.06	7,10,12	1.5	1.2	0.98
IZW1	46.7	44.95-46.03	2,10,12	3.1	0.0	0.56
Mrk 335	45.4	44.69-44.75	2,7,10	5.4	0.0	0.79
PG 2214+139	45.8	45.42	10	4.3	0.0	0.42
NGC 3783	45.3	44.26-44.77	1,4,6,7,8,11,12	3.8	1.3	0.99
Mrk 896	45.1	44.96	10	16.0	3.1	0.99
NGC 5548	45.2	44.4-44.73	1,2,7,8,12	3.2	0.8	0.99
Mrk 279	45.6	44.07-44.9	1,8,10	2.7	1.6	0.99
Mrk 766	45.3	43.6-44.58	1,3,8,10	1.7	4.8	0.99
Mrk 915	45.2	44.67	12	3.4	1.7	0.99
Mrk 590	45.3	44.38-44.91	1,4,7,8,10,12	2.8	5.0	0.99
<u>‘Second Class’</u>						
NGC 4051	43.7	42.9-43.56	1,2,7,8,10,12	2.9	1.8	0.83
Mrk 478	46.1	45.22-45.62	10,12	4.3	1.6	0.91
Ark 120	45.7	45.1-45.17	1,7,12	3.1	1.4	0.75
KUV 18217+6419	47.9	47.23	12	1.5	8.2	0.99
MCG -06-30-015	44.7	43.58-46.9	1,4,8	2.6	3.8	0.99
Fairall 51	45.2	44.68	12	1.5	4.0	0.98
Mrk 1239	45.6	44.73	10	2.0	0.7	0.83
Mrk 1040	45.5	44.4-44.7	1,7,8	3.9	1.7	0.93
Mrk 486	45.2	44.6	10	2.1	2.4	0.81
IC 4329A	45.8	44.18-45.14	1,7,8,9,10,12	1.4	12.5	0.99
NGC 4593	44.9	43.63-44.2	1,2,4,7,8,10,11	3.2	0.2	0.78
UGC 7064	45.1	45.13	12	1.6	8.7	0.99
Mrk 926	45.8	45.5-45.79	13	2.9	7.2	0.99
Mrk 6	45.4	44.28-44.5	1,8	3.1	10.8	0.99
IC 3599	44.0	43.41	10	4.0	1.8	0.93
NGC 4151	44.7	43.26-44.03	1,2,3,7,9,12	2.7	2.6	0.99
PG 1211+143	46.3	45.81-46.01	7,10	1.2	6.7	0.99
Mrk 841	45.8	44.6-45.84	1,7,8	1.6	10.8	0.99
NGC 3516	44.8	43.7-45.07	7,8,12	4.0	2.9	0.98
PG 1612+261	46.3	45.83	12	7.6	3.1	0.97
Mrk 705	45.2	44.27-44.79	10,12	1.1	6.2	0.99

Note. — L_{bol}^{model} and R_o were derived from the best-fit model using Equation 4.1. Ranges of L_{bol}^{lit} were drawn from the references provided using $L_{2-10keV}$ X-ray L_{5100} , and L_{IR} luminosities and their respective bolometric corrections of 20 (Nandra & Iwasawa, 2007; Risaliti & Elvis, 2004), 10.3 (Richards et al., 2006), and 3.2 (Risaliti & Elvis, 2004). (1) Winter et al. (2012); (2) Brightman & Nandra (2011); (3) Singh et al. (2011); (4) Gandhi et al. (2009); (5) LaMassa et al. (2011); (6) Prieto et al. (2010); (7) Woo & Urry (2002); (8) Vasudevan et al. (2010); (9) Alonso-Herrero et al. (2011); (10) Sani et al. (2010); (11) Yuan et al. (2010); (12) Sargsyan et al. (2011)

Table 7.10. Measurements of Seyfert 2s

Source Name	L_{bol}^{model}	L_{bol}^{lit}	References	R_o	$N(i)$	Covering factor
<u>‘First Class’</u>						
MCG -05-23-016	45.0	44.4	9	2.0	15.0	0.98
Mrk 463E	46.5	45.87	5,12	5.5	15.0	0.93
NGC 4388	45.1	43.54-44.19	2,4,5,8	6.5	13.4	0.98
IRAS 05189-2524	47.0	45.47-46.24	2,5,11,12	32.5	3.5	0.91
NGC 5252	44.9	45.39	7	2.7	15.0	0.54
IRAS 20210+1121	46.6	45.97	12	1.7	15.0	0.99
IRAS 18325-5926	45.6	45.15-45.19	11,12	4.7	12.7	0.76
IC 5063	45.6	44.3-44.93	5,7,8,11,12	5.1	7.5	0.84
IRAS F15480-0344	45.7	44.3	2	2.3	5.9	0.99
IRAS 20460+1925	47.4	46.66	12	5.4	2.3	0.89
<u>‘Second Class’</u>						
NGC 7674	46.2	44.92-45.61	2,3,5,7,9,11	2.2	7.8	0.99
3C234	47.1	46.35	12	2.8	2.0	0.88
TOL 1238-364	45.4	44.76-44.92	4,5,11	4.9	5.3	0.99
IRAS F04385-0828	45.5	44.3	2	4.5	9.0	0.99

Note. — Same as Table 7.9 except for Seyfert 2s.

Chapter 8

Integrating Previous Two Studies

This section uses the techniques of the previous chapter to determine the dust distribution for the sample of Thompson et al. (2009). Several sources overlapped between the two studies, but we will only present here the results of the unanalyzed sources. We revisit the feature-feature (S_{18} vs S_{10}) diagram for the entire sample of AGNs: 48 Seyfert 1s, 14 Seyfert 2s, and 12 type 1 Quasars and confirm a clumpy torus distribution accurately describes the models.

8.1 Feature-Feature Diagram Revisited

Certain species of dust provide similar MIR emission features as found in observations (Sirocky et al., 2008). The specific properties of the dust we used to describe the dust of the torus are those of Ossenkopf et al. (1992), and it has prominent spectral features at $10\ \mu\text{m}$ and $18\ \mu\text{m}$. As discussed in Section 6.3.2, the ratio of the strength of these features provides an indication as to the dust’s geometry, and we found by using the ‘feature-feature diagram’ that smooth density distributions do not describe observations of type 1 AGNs.

The silicate strength measurements of Section 6.3.2 were performed on *Spitzer* data that contained ‘contamination’, namely star formation. Spectral cleansing procedures such as star formation and emission line removal (Section 7.2.2) were not carried out on these data. Since PAHs and emission lines may affect the determination of the underlying continuum, we re-present the feature-feature diagram with all 74 star formation-less AGNs in Figure 8.1. The majority of all 74 sources show $10\ \mu\text{m}$ silicate emission, where all Seyfert 1s do and a handful of Seyfert 2s. The removal of star formation and emission lines did increase the silicate strengths (toward positive values) for some sources, indicating that MIR contamination by star formation can strongly affect the continuum fitting. These AGNs are confined to a region of

silicate feature strengths only described the clumpy distributions, as the majority of the sources lie in the area similar to that of Figure 6.6, though with larger S_{10} values.

We present a large sample of 48 Seyfert 1 sources whose $10\ \mu\text{m}$ silicate feature is always in emission. This result is consistent with Thompson et al. (2009) though somewhat differing from Hao et al. (2007). The method in measuring the feature strengths, namely the spline interpolation using a $14\ \mu\text{m}$ pivot point, is the major difference as explained by both Sirocky et al. (2008) and Thompson et al. (2009). The quasars of our sample do not show overwhelmingly larger silicate strengths, but rather lie with the Seyfert 1s on the diagram. The 12 Seyfert 2s as a sample show $10\ \mu\text{m}$ silicate absorption though there seems to be little $18\ \mu\text{m}$ feature present in their spectra. The few type 2s that show emission can only be explained by a clumpy geometry that allows for views of hot cloud faces (providing emission) yet still obscuring the BLR, hence leading to the classification of type 2.

8.2 CLUMPY fits of Seyferts and Quasars

We perform the CLUMPY fitting analysis of Chapter 7 on 12 Seyfert 1s and 12 type 1 quasars from Chapter 6 that have not yet been analyzed besides their silicate strengths. From their strengths however, we expect them to be well described by clumpy torus models. The fits are conducted using the entire model database without any restrictions, as there was no previous information available to constrain any parameters beforehand. We present only the best-fit values and median values of the posteriors for these fits. The χ^2_R values ranged from 0.008 to 0.248 for all sources indicating that the data was well-described by the models. We plot in Figure 8.2 distributions of the best-fit values of the 6 CLUMPY parameters for Seyfert 1s in addition to the average number of clouds along the line of sight, $N(i)$, and the outer extent of the torus, where we quantify 80% of all clouds within the torus lie at $R_o^{80\%}$. The Seyfert sources are in complete agreement with those of Chapter 6 as this is evident in the comparison of Figure 8.2 with Figure 7.18.

What is more interesting is that the distributions of the quasars is also similar to the Seyfert 1s (green histograms in Figure 8.2). Mid- to larger values of N_0 describe

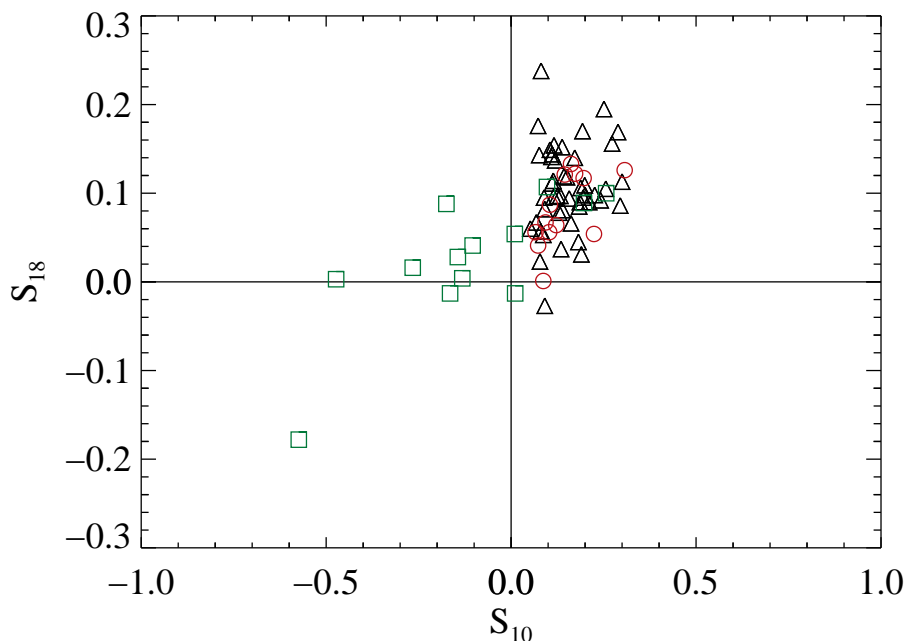


Figure 8.1 Updated version of the Feature-Feature diagram, we plot 48 Seyfert 1s as triangles, 12 type 1 quasars as circles, and 14 Seyfert 2s as squares. Positive strengths show silicate emission in 66 of the 74 AGNs, including Seyfert 2s.

the compact tori for these sources. Unlike Seyfert 2s, the optical depth per cloud is fairly large with a preference for few clouds along the line of sight. All histograms concerning type 1 AGNs show a peak for the inclination at $i = 0$ for nearly 30 – 40% of all the sources. This fits well explaining the typical type 1 views. However, the other 60% of the i values are spread randomly around parameter space. Lastly, this newer sample of Seyferts and quasars have very compact tori with 80% of all the clouds located within 4 pc. These results are consistent with interferometric and imaging observations (See Chapter 5.).

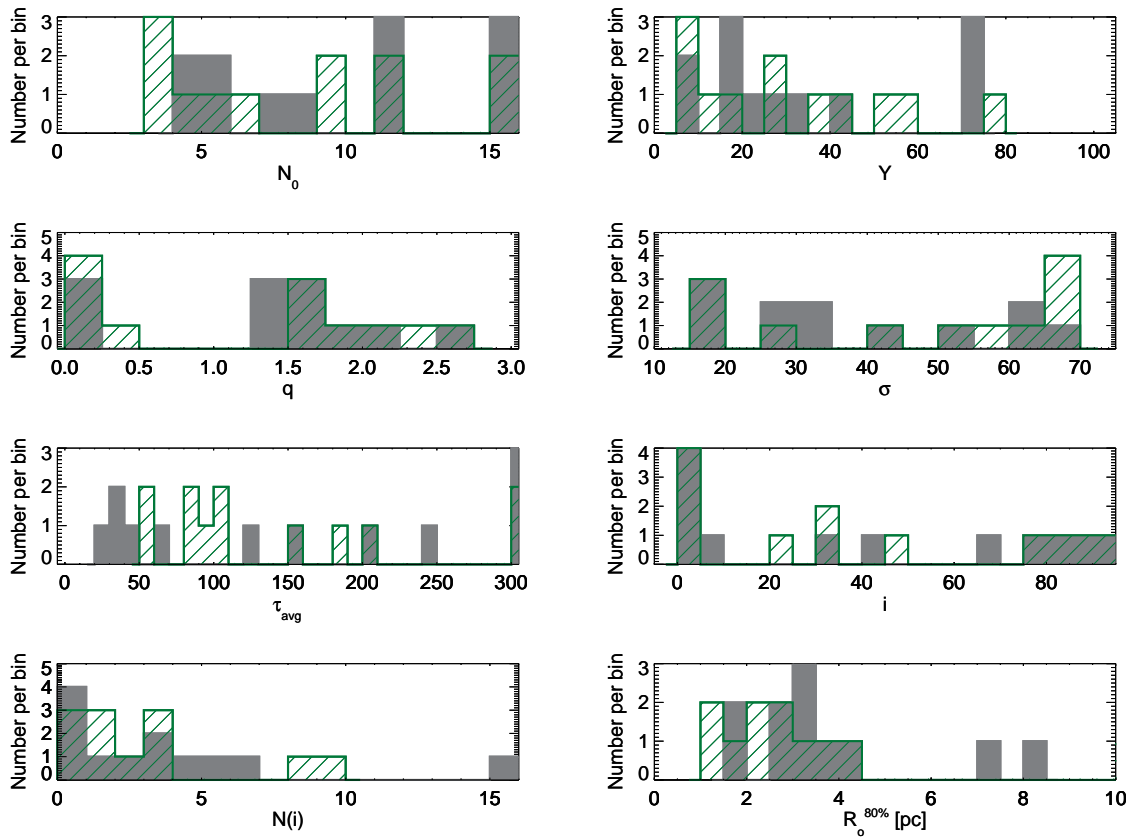


Figure 8.2 Shown for the ‘well-fit’ sources, 12 Seyfert 1s (black) and 12 type 1 quasars (green), are histograms of the best-fit values of the 6 CLUMPY parameters derived from the fitting technique, as well as the average number of clouds encountered along direction i , $N(i)$, and the outer extent of the torus for which 80% of the clouds have been accounted, $R_o^{80\%}$.

Chapter 9

Summary and Outlook

We have examined in detail the intricate structure and characteristics of the molecular torus surrounding the central engine of AGNs. Though a clumpy geometry was proposed for the torus some time ago, just in this last decade have observations confirmed the compact clumpy structure. To completely understand the distribution of the dust within the torus requires extensive modeling that can replicate the MIR emission of AGNs, and we employed use of the CLUMPY torus models, as they fulfill this obligation. Concentrating first on a large sample of Seyfert 1s and type 1 quasars, we found that tori are indeed arranged in a clumpy geometry, a result that confirmed the consistency between observation and model. To obtain this result, we used what was readily available, namely the dust and its properties. Silicate dust reprocessing dominates the MIR spectra with two prominent spectral features occurring at $10\ \mu\text{m}$ and $18\ \mu\text{m}$. The strengths of these two features together are sensitive to the dust distribution. Fitting a spline to observations to ascertain the underlying continuum is the crucial step in calculating the feature strength since the strength itself is a ratio of the flux and the continuum. Utilizing a spline fit that encompasses a pivot point at wavelengths between the dust features provides for a robust silicate strength measurement. Measuring both the $10\ \mu\text{m}$ and $18\ \mu\text{m}$ silicate feature strengths and comparing them provides an indication of the dust's geometry, and we determined that the dusty environment of the torus is clumpy. We also used the feature strengths and determined type 1 AGNs show $10\ \mu\text{m}$ silicate emission, a result that has just recently become popular. Based only on the analysis of the silicate feature strengths, we determined that the tori of the type 1 sample were described as being compact to within 15 parsecs with few clouds along radial rays, an impressive feat for using two parameters - the feature strengths. This feature-feature comparison was applied to a larger sample consisting of Seyfert 1s, Seyfert 2s, and type 1 quasars and we

found all type 1 AGNs had $10\ \mu\text{m}$ silicate emission. Additionally, several Seyfert 2 sources displayed silicate emission, which can only be explained in terms of a clumpy geometry. There is a chance to view hot sides of clouds even from type 2 viewing angles, and the dust may be arranged such that a hot face is visible but the BLR obscured, allowing for the type 2 classification.

The feature strengths can only partially describe the dust distribution. To fully depict the arrangement of material around the central engine requires detailed model fits to observations. The best-fit model and/or the marginalized posterior distributions can then provide an indication as to the layout of the dust since each CLUMPY model is based on 6 physical parameters. Performing this fitting routine for all sources, type 1 and type 2, we found that the parameters of the clumpy torus indicate that as over-all samples, type 1 AGNs are intrinsically different from type 2 AGNs, a piercing blow to the theory of unification that implies only the inclination angle is the cause for the different observed MIR emission from Seyfert 1s and 2s. Furthermore, regardless of AGN type, fitting MIR SEDs of clumpy torus models to observations shows that the majority of the clouds in the torus are within 3-4 parsecs of the central engine, size scales that are consistent with high-resolution interferometric observations.

While we primarily focused on space-based observations using spectroscopy from the large aperture *Spitzer Space Telescope*, we additionally retrieved high-resolution ground-based spectroscopic observations. These cannot spatially resolve the torus but can capture the MIR emission from small spatial scales of which we attribute to the AGN and torus. These can spatially sample regions down to 15 parsecs in diameter, and extracting several apertures of different diameters still shows that the emission from the central source is the dominant contributor of the MIR emission. We heavily rely on this ground-based data since its small aperture is intended to isolate the torus emission. When we utilize *Spitzer*, the large aperture captures extended emission from the host galaxy contaminating the MIR flux. We use ground-based observations to confirm *Spitzer's* MIR emission is that of the torus by comparing the spectral shapes of the two observations. Of a small sample of 6 AGNs of which we had ground-based observations, 2 showed a disagreement between *Spitzer* and *Gemini*

spectra indicating that the larger aperture observations were contaminated and not dominated by the AGN emission. This emphasizes the uncertainty in progressing with just the *Spitzer* sample alone; additional ground-based observations are thereby required to confirm the observed emission is that of the torus.

The ability to confidently deduce the inclination angle from MIR emission remains a challenge. Two independent techniques in determining inclination angles of tori were conducted, one through use of spectropolarimetry, the other fitting MIR emission with clumpy torus model SEDs. Of an AGN sample size of 50, only 25 sources had consistent results between the two methods, which leads to the conclusion that one of the methods, more likely the MIR emission, is not sufficient at determining the viewing angles. Applying polarization constraints to the fitting procedure emphasized both the inherent degeneracies within the model database and also the inability of MIR emission to harness all the CLUMPY parameters. Notable, i and σ are problematic in the procedure because their best fit values appear stochastic. This analysis shows the necessity to have any and all additional information. It is possible several of these *Spitzer* observations contained contamination hindering the ability of the fitting procedure to accurately assign a torus model SED to the data, but this can only be confirmed with additional ground-based observations. For this reason, in addition to others, ground-based observations are on standby to be conducted in the Fall 2012. From this data, we can proceed little by little in either confirming the above result or finding that MIR emission and spectropolarimetry techniques are compatible, though it is essential more high-resolution observation be taken.

Appendix A: CLUMPY Torus Model Fittings

A.1 Seyfert 1 Source Summaries

Following is a detailed analysis for each source describing the behavior of each fit and how and if there is agreement between polarimetry and MIR emission. Sources are arranged by ‘First Class’ then ‘Second Class’ and within each subset in order of the percentage of overlapping area between the C and C+P posterior distributions for the i parameter. We start with the Seyfert 1 sources and continue to the Seyfert 2s. We also show in this appendix figures (like that of Figure 7.19 that show the *Spitzer IRS* spectrum being fit by the best-fit model (solid red), which is composed of the torus (dashed) and a blackbody (dotted). Best-fit values are listed in the figure as well as the χ_R^2 value. We also show in these figures the marginalized posterior distributions of the 6 CLUMPY parameters with the dashed lines corresponding to the posteriors of the CLUMPY+blackbody fittings, whereas the solid line produces the distribution of the torus+blackbody+polarization priors fits. Printed in each panel is the best-fit and median value associated with the fit as well as a 1-sigma interval.

NGC 7469 – Classification: Seyfert 1.5; Polarization class: Null;

Percentage of overlapping area: 96%; See Figure 7.19

This source is firmly supportive of the polarization predictions of viewing angle; fitting with and without restrictions on i produce the exact same posterior distributions for all parameters in addition to the same best-fit models.

PHL 1811 – Classification: Narrow line Seyfert 1; Polarization class: Equatorial;

Percentage of overlapping area: 94%; See Figure A.1a

PHL 1811 is predicted by polarization to have low values of i , and fitting the MIR emission with torus models confirm the estimates.

Mrk 1048 – Classification: Seyfert 1.5; Polarization class: Equatorial;

Percentage of overlapping area: 93%; See Figure A.1b

A source that confirms the viewing angle predictions of polarization, Mrk 1048 contains a compact dusty torus and whose orientation leads observers to intercept virtually zero clouds along the line of sight.

PG 1700+518 – Classification: Seyfert 1; Polarization class: Equatorial;

Percentage of overlapping area: 92%; See Figure A.1c

The i posterior for the C fit prefers values less than 50° though the best-fit value is $i = 50^\circ$. Estimates from polarization place limits of $0 < i < 50^\circ$, allowing the chance that the exact model to be chosen in the C+P analysis, as it is. MIR emission and polarization predictions are in accordance for this source.

Mrk 876 – Classification: Seyfert 1; Polarization class: Equatorial;

Percentage of overlapping area: 90%; See Figure A.1d

This source is firmly supportive of the polarization predictions of viewing angle. Fitting with and without restrictions on i produce nearly the same posterior distributions for all parameters in addition to the same best-fit models.

IZW1 – Classification: Narrow line Seyfert 1; Polarization class: Equatorial;

Percentage of overlapping area: 89%; See Figure A.1e

The i posterior for the C fit strongly caters to values less than 50° which happen to coincide to the limits placed on i by the polarization estimates. Both best-fit models are identical and fall within this range. The two methods of identifying inclination angles are consistent for this source.

Mrk 335 – Classification: Narrow line Seyfert 1; Polarization class: Equatorial;

Percentage of overlapping area: 85%; See Figure A.1f

The MIR analysis with and without polarization clues yield similar results. Lower i values are preferred in a compact torus with a small scale height and zero clouds

encountered in the direction i .

PG 2214+139 – Classification: Seyfert 1; Polarization class: Equatorial;

Percentage of overlapping area: 74%; See Figure A.1g

Similar to Mrk 335, PG 2214 is described by the same torus geometry with and without restrictions on i . Lower inclination angles are preferred along with few clouds on average along an equatorial ray.

NGC 3783 – Classification: Seyfert 1.5; Polarization class: Equatorial;

Percentage of overlapping area: 59%; See Figure A.1h

The posteriors of this source change as i is restricted whereas the best-fit models are unaltered. The i posteriors are generally flat with and without limitations. The MIR models are insensitive to viewing angles for this source as we cannot constrain i . Limiting the allowed values for i causes the posteriors of the other parameters to fluctuate, albeit minimally, and these parameter combinations call for a compact torus with a large opening angle.

Mrk 896 – Classification: Narrow line Seyfert 1; Polarization class: Null;

Percentage of overlapping area: 43%; See Figure A.1i

This source has a limited spectral coverage from 5 μm to 18 μm , yet MIR emission and analysis can confirm polarization predictions of i . The best-fit models utilizing restrictions or not are the same, though the posteriors are somewhat altered. The C posterior of i prefers values less than 60° and contains a local maximum near 20° . Imposing restrictions of $i < 30^\circ$ allows only the maximum to stand out for the C+P fit. Since both methods agree, confirmation of the polarization predictions stand. Notice that imposing restrictions on i also led σ to favor higher values, which can be interpreted as a compensation (See text above.)

NGC 5548 – Classification: Seyfert 1.5; Polarization class: Equatorial;

Percentage of overlapping area: 43%; See Figure A.1j

The posteriors of the two methods are in general agreement though the posterior of i appears to favor larger values yet has a slight degree of flatness. The best-fit models are in agreement favoring face-on viewing, and this source may emphasize that the best fit model does not necessarily have to lie within the mass of the posterior.

Mrk 279 – Classification: Seyfert 1; Polarization class: Equatorial;

Percentage of overlapping area: 42%; See Figure A.1k

The i posterior of both fitting methods favor larger inclination angles, where that of C+P is simply a slice of the full range. Again, best-fit and posteriors are not aligned in their values of i as the best-fit models prefer lower values. However, since the method using prior information about i from polarization is in complete agreement with a method based only on MIR emission, the polarization assessment is confirmed by the MIR torus models.

Mrk 766 – Classification: Seyfert 1; Polarization class: Polar;

Percentage of overlapping area: 40%; See Figure A.1l

Though there is little overlap between the C and C+P posteriors of i , the best-fit values differ by a mere 7° . Allowing the restriction of i to include down to 20° instead of 30° corrects the difference, and the posteriors and best-fit models are identical. Cases like these where preferred values lay just outside the self-imposed limits of i are subject to criticism, thus we examine if different limits alter the results, which in this case, they did.

Mrk 915 – Classification: Seyfert 1.8; Polarization class: Null;

Percentage of overlapping area: 35%; See Figure A.1m

Polarization predictions are confirmed for this source since both the best-fit models and the i posteriors are in agreement. Imposing the restrictions on i allowed the posteriors of the other parameters to alter as the remaining models favored a slightly different distribution.

Mrk 590 – Classification: Seyfert 1; Polarization class: Null;

Percentage of overlapping area: 29%; See Figure A.1n

The posterior of i appears flat over the entire range with the restricted posterior indicating a slight incline to higher values. Though the best-fit values are in agreement, the flatness of the i posterior shows the insensitivity of the torus models to choose inclination angles for this source. While the inclination cannot be constrained, the torus is found to be compact with many clouds along an equatorial ray.

NGC 4051 – Classification: Narrow line Seyfert 1; Polarization class: Equatorial;

Percentage of overlapping area: 65%; See Figure A.1o

The C posterior of i contains a slight local maximum near 60° , which the C+P posterior attempts to recreate. With the restriction $i < 50^\circ$ imposed, the C+P fitting cannot use the best-fit values of the C fit. Therefore to compensate for the lower i values available, slightly larger σ values are introduced and appear in both the posteriors and best-fit model. This source, which contains an overlapping area of only 65%, does uphold the polarization estimates of i .

Mrk 478 – Classification: Narrow line Seyfert 1; Polarization class: Null;

Percentage of overlapping area: 52%; See Figure A.1p

In this source, a large swing in i occurs between the best-fit models. It is clear to see that the i posterior is somewhat flat over its entire range, and the restriction is simply a slice of the flatness. Therefore, we again admit that the MIR models are insensitive to viewing angles for this source as we cannot constrain the viewing angle. Though we cannot quantify a value for i , the fits describing the data are quite good and the posteriors fairly well constrained.

Ark 120 – Classification: Seyfert 1; Polarization class: Equatorial;

Percentage of overlapping area: 49%; See Figure A.1q

The i posterior of C shows a slight bi-modality at $i = 0$ or 65° , with a preference for the latter value. Introducing the polarization restriction of $i < 50^\circ$ makes it clear that

the posterior maintains its shape, but still prefers larger values. While the best-fit models differ, the posteriors of C and C+P are generally similar, and both methods have low χ_R^2 values, leading us to confirm the polarization predictions for this source.

KUV 18217+6419 – Classification: Seyfert 1.2; Polarization class: Equatorial;

Percentage of overlapping area: 40%; See Figure A.1r

The models describing the MIR emission favor large values of i , as is evident in both the posterior and best-fit model, and imposing restrictions of $i < 50^\circ$ exaggerate the shape. Though the best-fit models do not agree regarding parameter values, the result SED shapes are nearly identical. Also, the posteriors are similar between the two fitting methods. These two assessments, in addition to the low χ_R^2 values for the best-fit models, indicate that polarization is still confirmed.

MCG -06-30-015 – Classification: Seyfert 1.5; Polarization class: Polar;

Percentage of overlapping area: 35%; See Figure A.1s

Polarization predictions are confirmed for this source although the best-fit values of i differ between the C and C+P fittings, due to the restrictions. Posteriors are similar between the fits, with i and σ changing to accommodate each other.

Fairall 51 – Classification: Seyfert 1.5; Polarization class: Polar;

Percentage of overlapping area: 33%; See Figure A.1t

The i posterior of the C+P model is simply a slice of the C posterior. MIR emission favors lower inclinations and the restricted best-fit model chooses the limit $i = 30^\circ$. The best-fit model then lowers N_0 to compensate for the increased i in order to replicate or approach the unrestricted solution. The parameters are constrained however, and we see that the dust is arranged in a compact torus.

Mrk 1239 – Classification: Narrow line Seyfert 1; Polarization class: Polar;

Percentage of overlapping area: 31%; See Figure A.1u

Similar to Fairall 51, the posterior of i of C+P tends to be a slice of that of C, and

all other posteriors are identical. The best-fit models behave similarly as Fairall 51, in that lower values of N_0 are integrated to offset the increased i values.

Mrk 1040 – Classification: Seyfert 1; Polarization class: Polar;

Percentage of overlapping area: 29%; See Figure A.1v

Mrk 1040 is another source in which the i posteriors favor lower values and the C+P posterior is a slice of the whole range. The polarization prediction is still upheld for this source since the C+P is very well constrained even though the original non-restricted results favored even lower values of i .

Mrk 486 – Classification: Seyfert 1; Polarization class: Polar;

Percentage of overlapping area: 27%; See Figure A.1w

The C+P posterior of i is again a slice of the C posterior, both which indicate a preference toward larger values of i . Since the preferred value is outside the restricted range, the upper limit value is used in the C+P best-fit model while σ is increased. Examining the results if the restriction of i allows values up to 80° results in complete agreement with both the posteriors and best-fit model of the C fitting.

IC 4329A – Classification: Seyfert 1.2; Polarization class: Polar;

Percentage of overlapping area: 22%; See Figure A.1x

Like many sources we have already seen, the MIR fitting alone tends to like large i values. Increased N_0 and σ values compensate for the lower values of i for both the best-fit models and the posteriors. Implementing the polarization + MIR approach, we see that polarization is confirmed since the resulting fit, even though it is not identical to the non-restricted model, is acceptable.

NGC 4593 – Classification: Seyfert 1; Polarization class: Polar;

Percentage of overlapping area: 20%; See Figure A.1y

The inclination angles are restricted to $30^\circ < i < 60^\circ$, and for this source, the C+P posterior of i behaves as a slice of the C posterior. Since the latter posterior and

best-fit model favored lower values of i and we now force larger values to be used, the σ posterior and best-fit values decline to compensate. Though the models are not exactly the same, polarization is confirmed, and the distribution of dust describes a compact torus.

UGC 7064 – Classification: Seyfert 1.9; Polarization class: Polar;

Percentage of overlapping area: 19%; See Figure A.1z

The C and C+P fitting techniques yield different models and posteriors, but both describe the data within our set threshold. The torus of this source is compact with several clouds. The polar scattering class is placed on sources whose geometry allow for a possible or partial obscuration. The distribution of dust in this source clearly allows for this scenario.

Mrk 926 – Classification: Seyfert 1.5; Polarization class: Null;

Percentage of overlapping area: 6%; See Figure A.1aa

Both fitting methods describe the data with nearly the same parameter values, with the largest difference in the restricted i value. Although this source clearly favors to be described by a large inclination angle, lower values describe the data within our well-fit threshold.

Mrk 6 – Classification: Seyfert 1.5; Polarization class: Equatorial;

Percentage of overlapping area: 4%; See Figure A.1bb

Like Mrk 926, the difference between the C and C+P fitting techniques are values of i . Since both methods yield models that describe the data within $\chi_R^2 \leq 0.25$, the polarization prediction is upheld.

IC 3599 – Classification: Narrow line Seyfert 1; Polarization class: Null;

Percentage of overlapping area: 4%; See Figure A.1cc

MIR-only analysis of this source preferred large inclination angles and small torus scale heights. Introducing limits of low i , σ tended toward higher values to compen-

sate for the loss of high i values. With a $\chi_R^2 = 0.18$ for the C+P best-fit model, MIR emission confirms polarization.

NGC 4151 – Classification: Seyfert 1.5; Polarization class: Equatorial;

Percentage of overlapping area: 4%; See Figure A.1dd

Imposing the restriction of i for this source changed the posterior of q from high to lower values. The data clearly wants to be described by values of large i , and since it cannot attain those values, the models instead favor a less compact distribution with an increased preference for higher N_0 values, such that the chance of obscuration increases. However, the limits in how they currently stand still support the estimates of polarization since the best-fit model has $\chi_R^2 \leq 0.25$.

PG 1211+143 – Classification: Narrow line Seyfert 1; Polarization class: Null;

Percentage of overlapping area: 4%; See Figure A.1ee

The i posteriors resulting from the C and C+P fitting methods are similar in shape but cover different ranges of i , which is the reason there is little overlap between the two. Both show a preference for large values, but the C+P posterior does so to replicate that of the C fit. The σ and N_0 posteriors now lean toward larger values to offset the enforced lower i values. Though there is a difference in best-fit models, they both describe the data with lower values of χ_R^2 , and therefore asserts that MIR emission is in agreement with polarization predictions.

Mrk 841 – Classification: Seyfert 1.5; Polarization class: Equatorial;

Percentage of overlapping area: 2%; See Figure A.1ff

Like many sources previously discussed, the unrestricted fit prefers large values of i while the polarization limits i to lower values. This inherently creates a difference between the best-fit models, but this source still supports the polarization prediction, even with a 50 to 90° swing in i since the best-fit model contains $\chi_R^2 \leq 0.25$.

NGC 3516 – Classification: Seyfert 1.5; Polarization class: Null;

Percentage of overlapping area: 2%; See Figure A.1gg

This unpolarized source is expected by polarization to be represented by low i values. Placing the restrictions of $i < 30^\circ$ on the models, we find that posteriors between C and C+P change. However, using the polarization priors, the best fit model still has lower χ_R^2 values.

PG 1612+261 – Classification: Seyfert 1.5; Polarization class: Null;

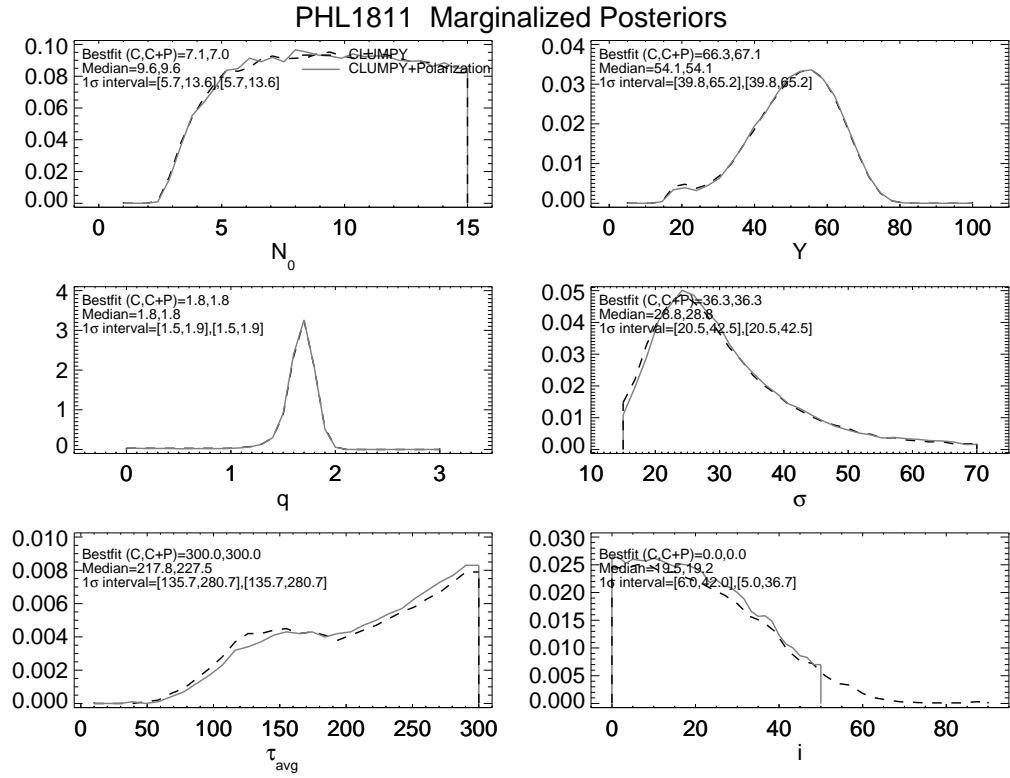
Percentage of overlapping area: 0%; See Figure A.1hh

This is another case where the restriction of i completely changes σ . Since i is low in the C+P case, in order to approach the results of the C case, σ must become large, as they do in both the posteriors and the best-fit model. The null polarization prediction should result in inclination angles near 0° , yet MIR emission favors larger values. The posteriors of the other parameters do not change significantly, and the restricted best-fit model describes the data well.

Mrk 705 – Classification: Seyfert 1.2; Polarization class: Null;

Percentage of overlapping area: 0%; See Figure A.1ii

While the i posteriors differ between the C and C+P fits with no overlap between the two, other parameter posteriors are consistent between the cases. Since i is restricted to lower values, σ compensates with much higher values, completely altering its posterior. The two best-fit models, while similar compared to the data, do have quite different parameter values creating them, namely in the i and σ parameters. For this source, the MIR emission would not have predicted similar inclination angles as did polarization. The null polarization would expect inclination angle values near zero. However, implementation of the polarization restrictions provides models that do describe the dust distribution and do so just within our goodness-of-fit threshold.



Data with CLUMPY and CLUMPY+Polarization Bestfits

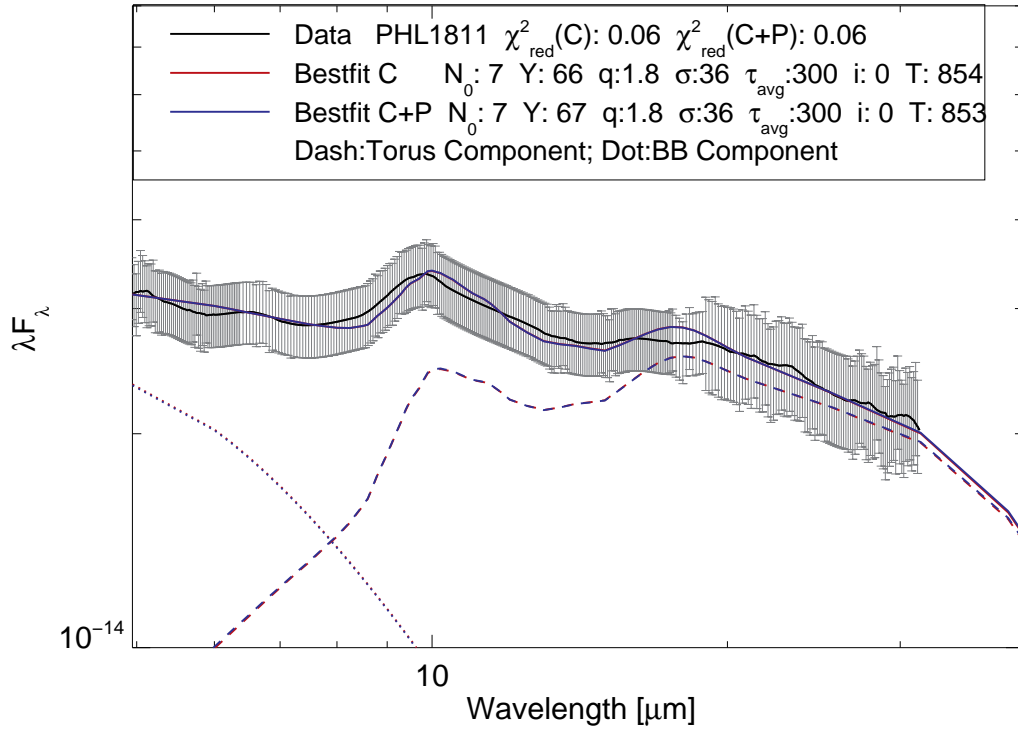
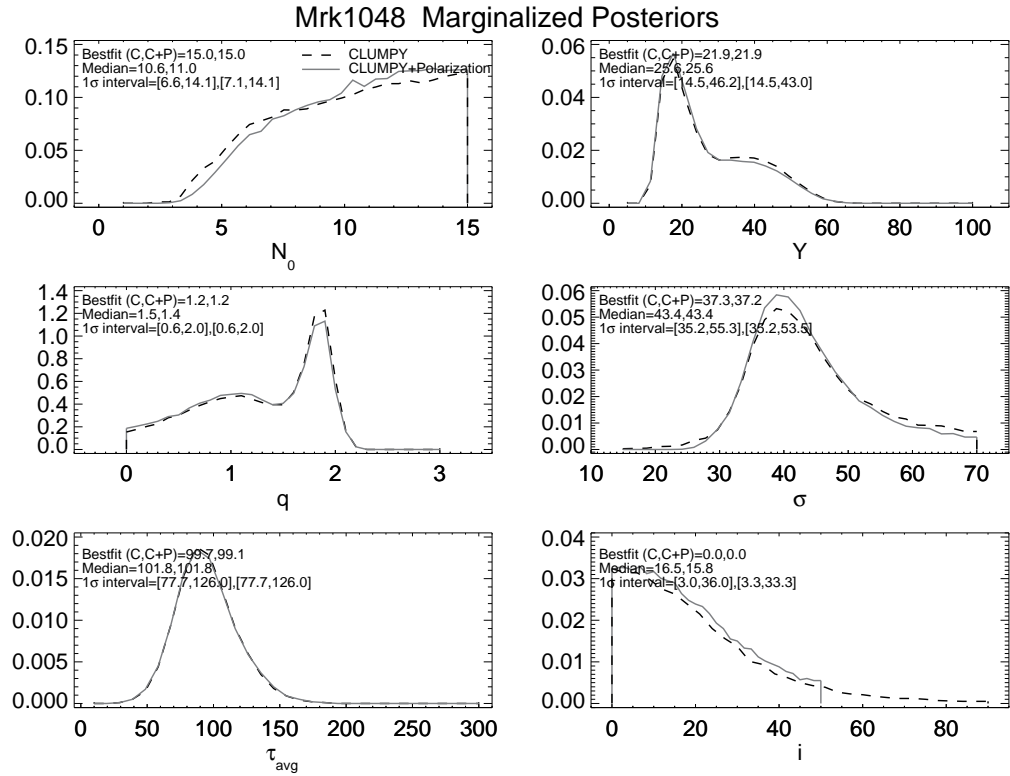


Figure A.1a Same as Figure 7.19 but for PHL 1811.



Data with CLUMPY and CLUMPY+Polarization Bestfits

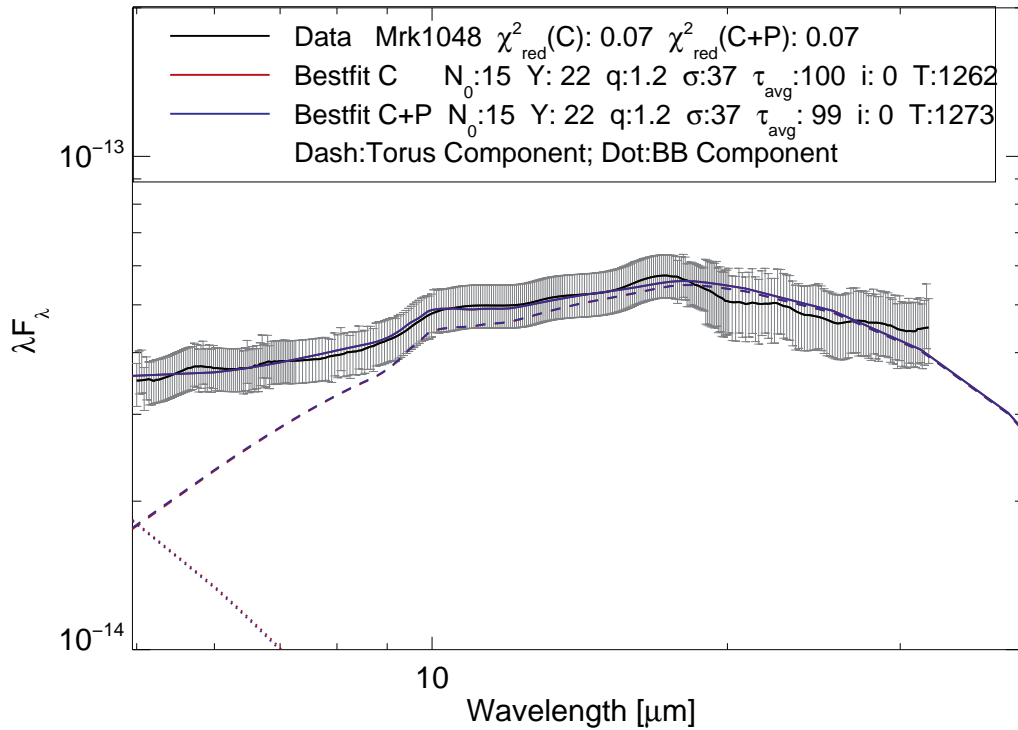


Figure A.1b Same as Figure 7.19 but for Mrk 1048.

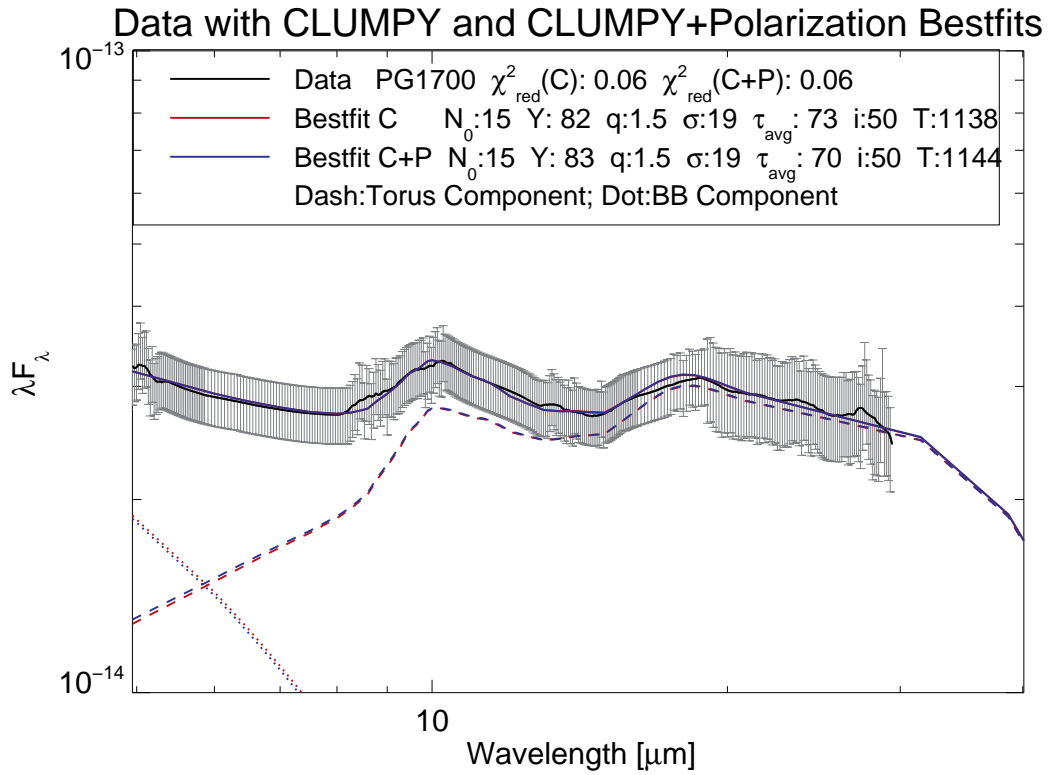
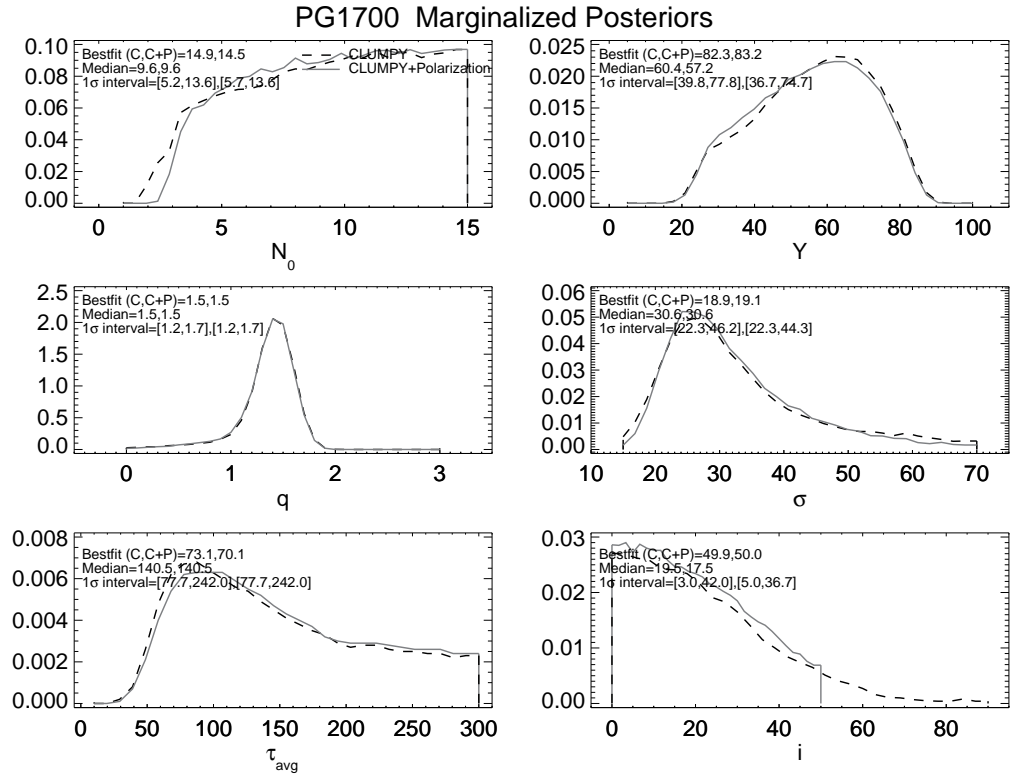
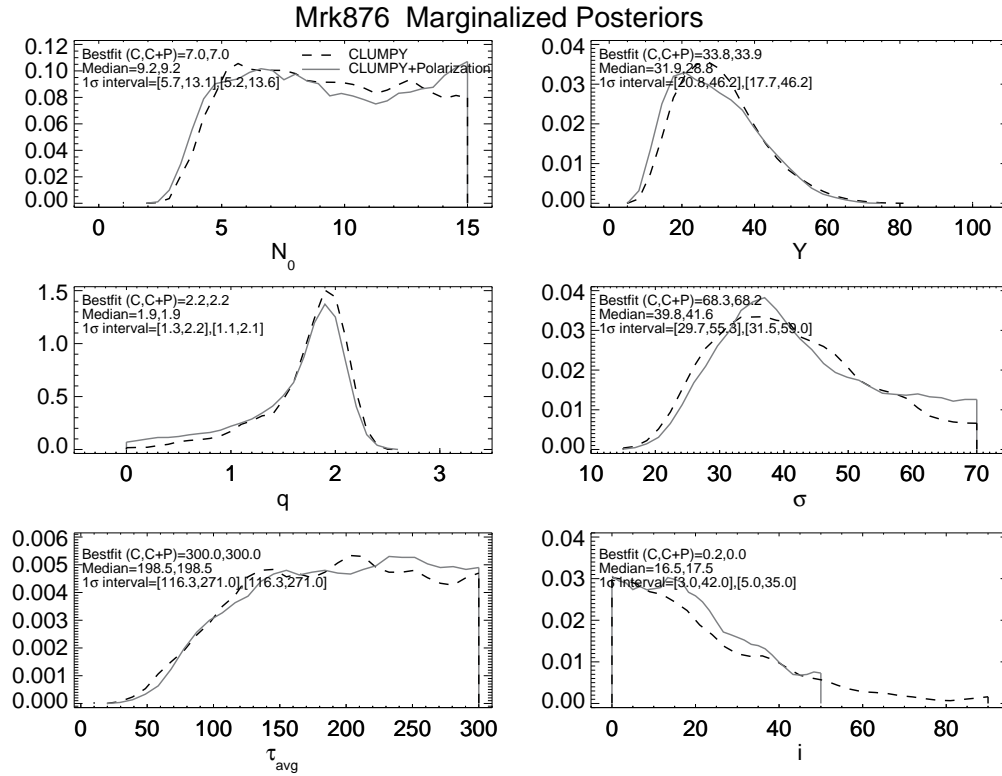


Figure A.1c Same as Figure 7.19 but for PG 1700+518.



Data with CLUMPY and CLUMPY+Polarization Bestfits

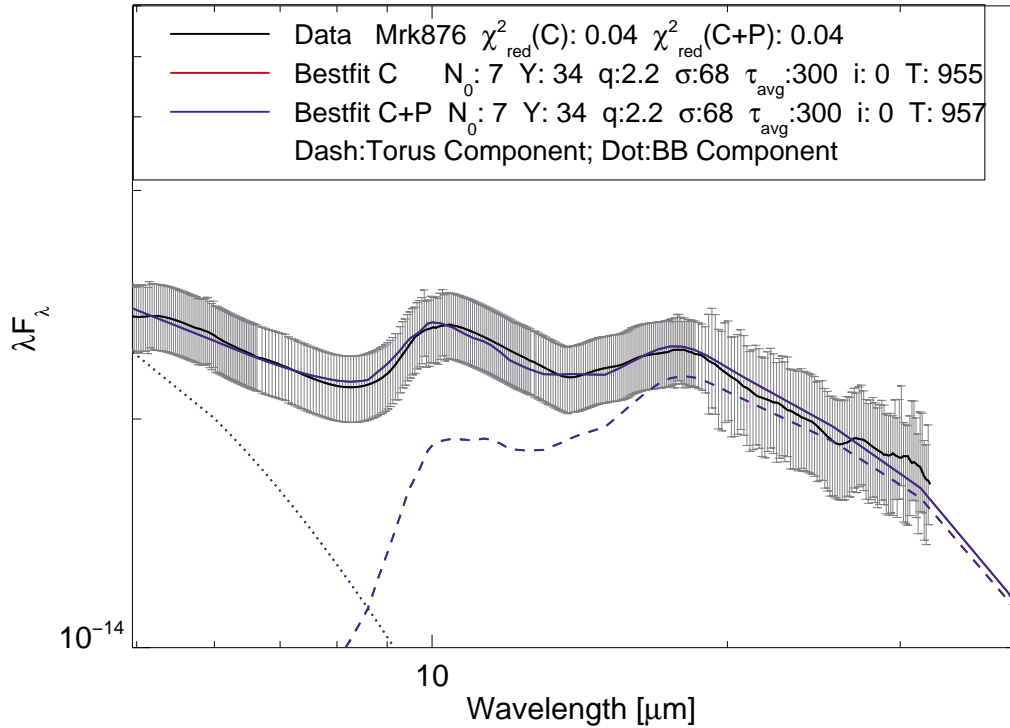
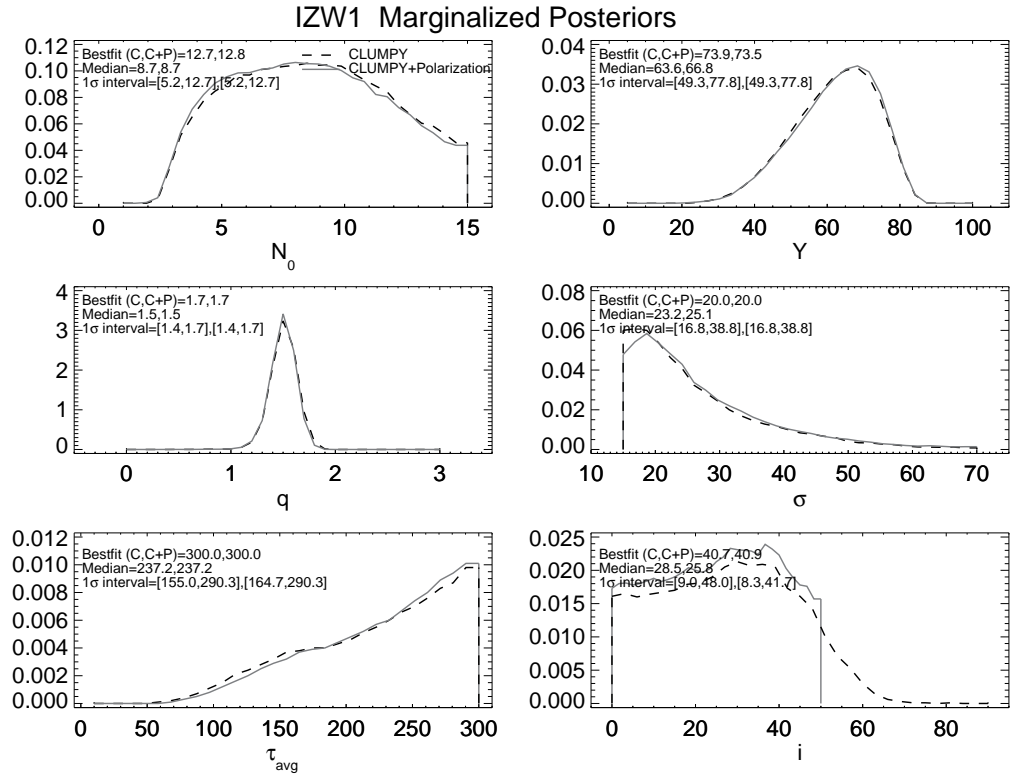


Figure A.1d Same as Figure 7.19 but for Mrk 876.



Data with CLUMPY and CLUMPY+Polarization Bestfits

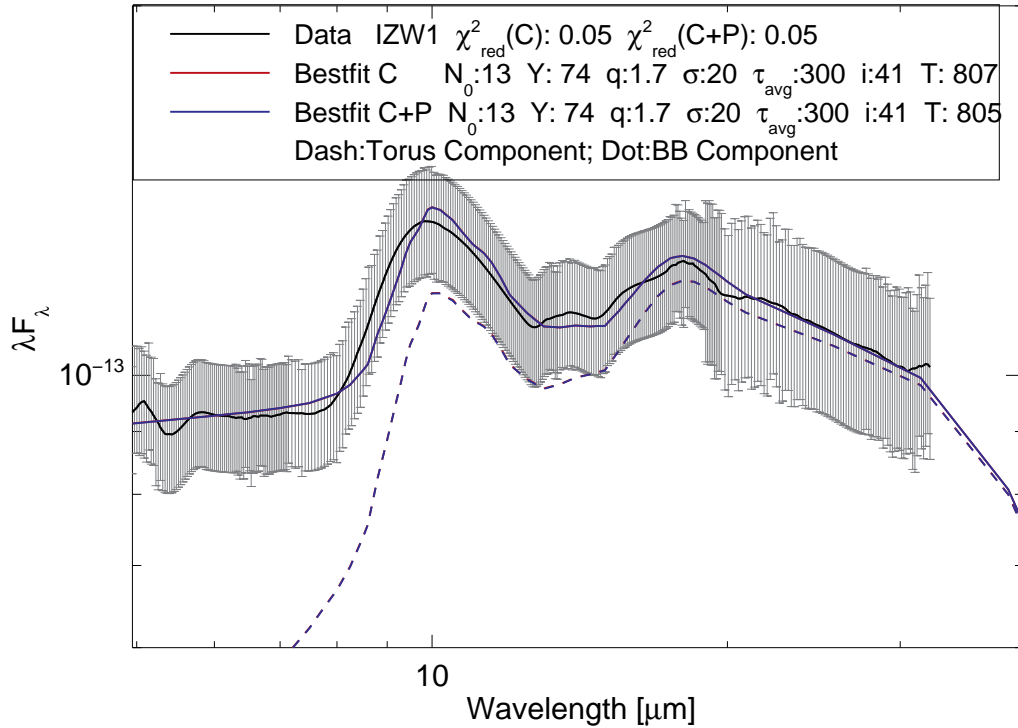


Figure A.1e Same as Figure 7.19 but for IZW1.

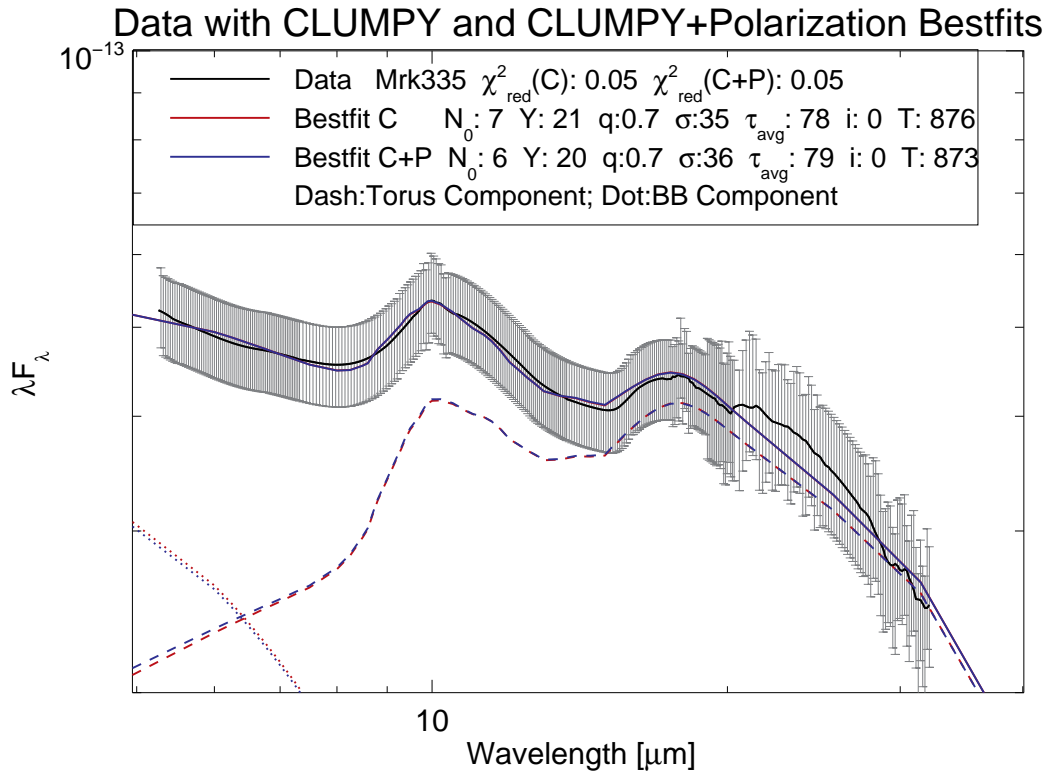
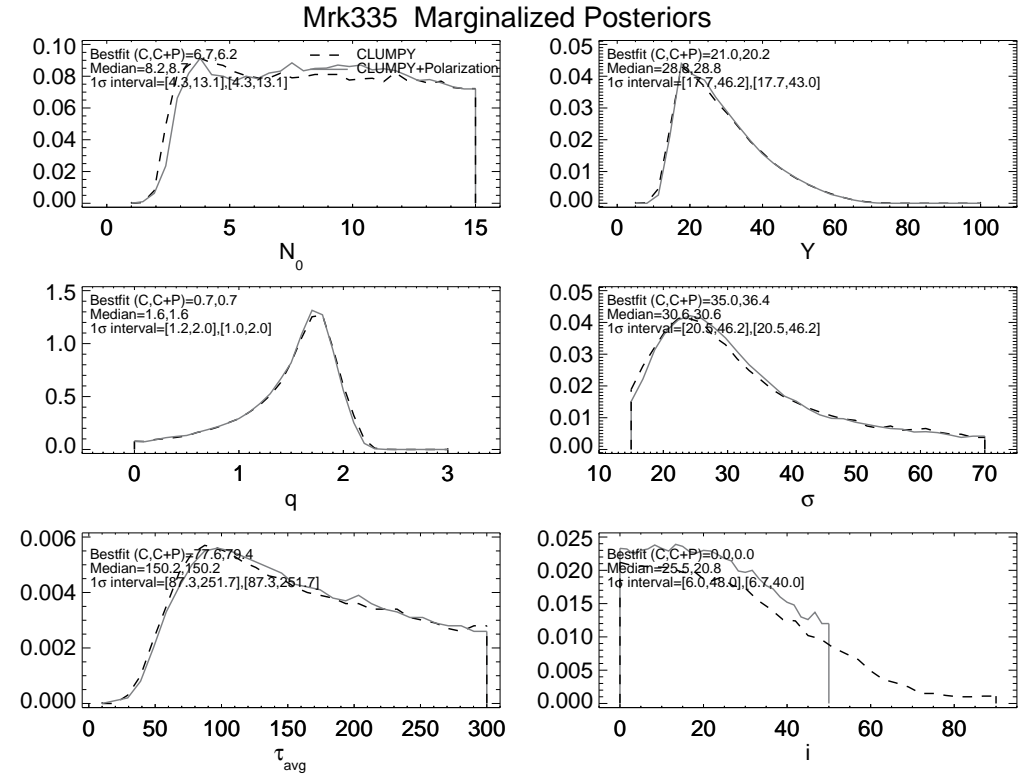
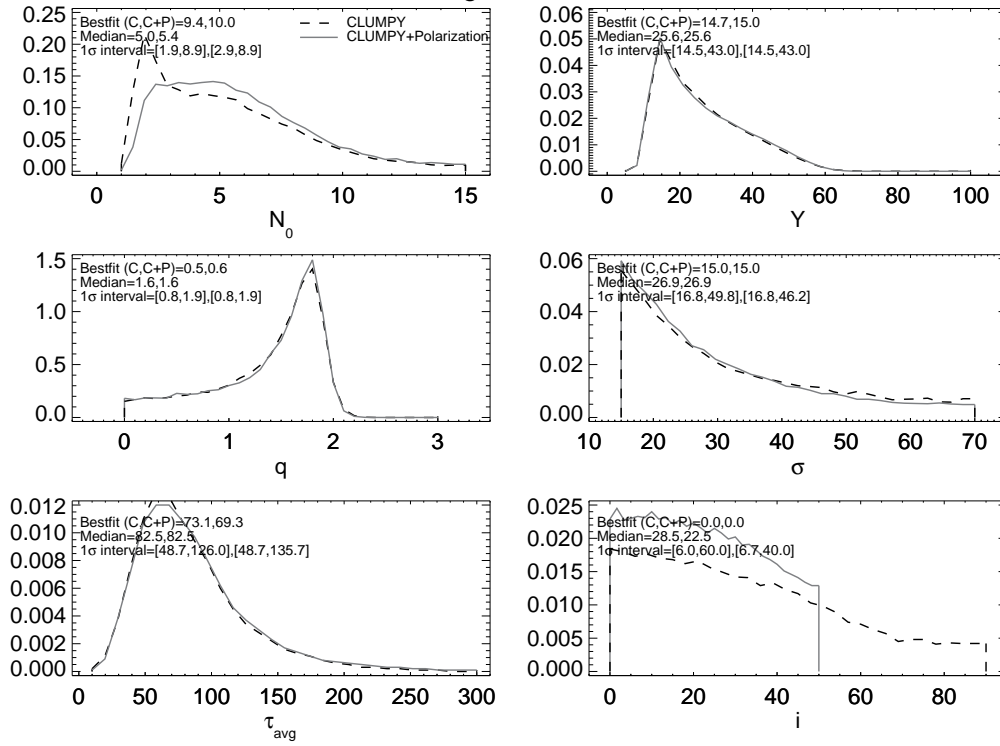


Figure A.1f Same as Figure 7.19 but for Mrk 335.

PG2214 Marginalized Posteriors



Data with CLUMPY and CLUMPY+Polarization Bestfits

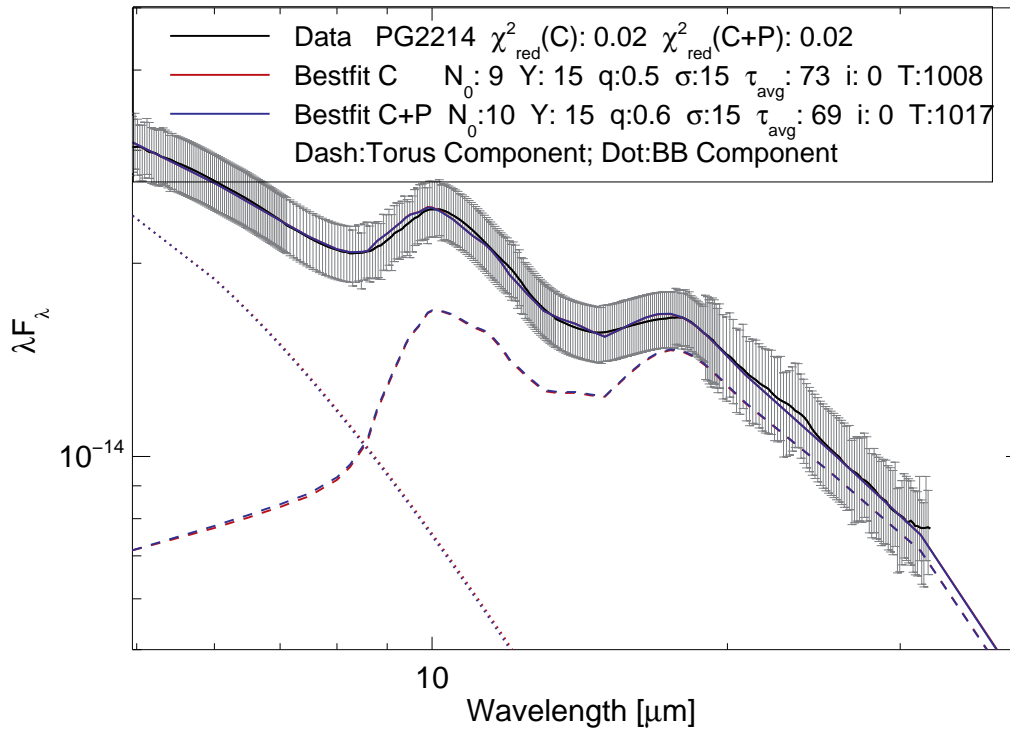
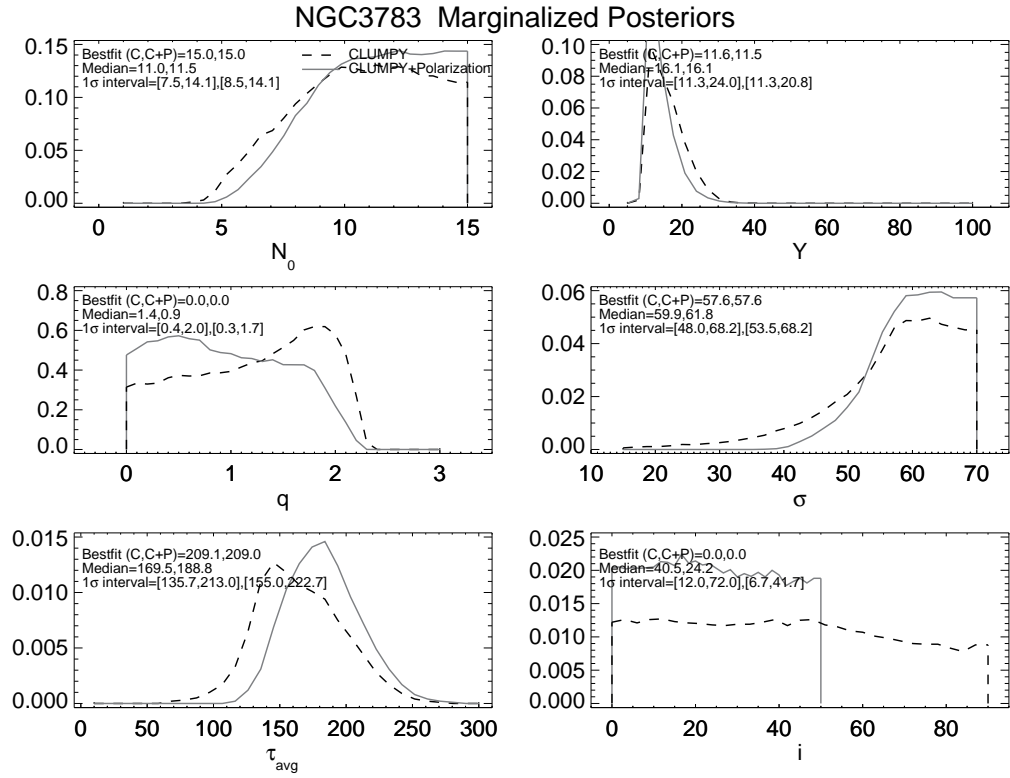


Figure A.1g Same as Figure 7.19 but for PG 2214+139.



Data with CLUMPY and CLUMPY+Polarization Bestfits

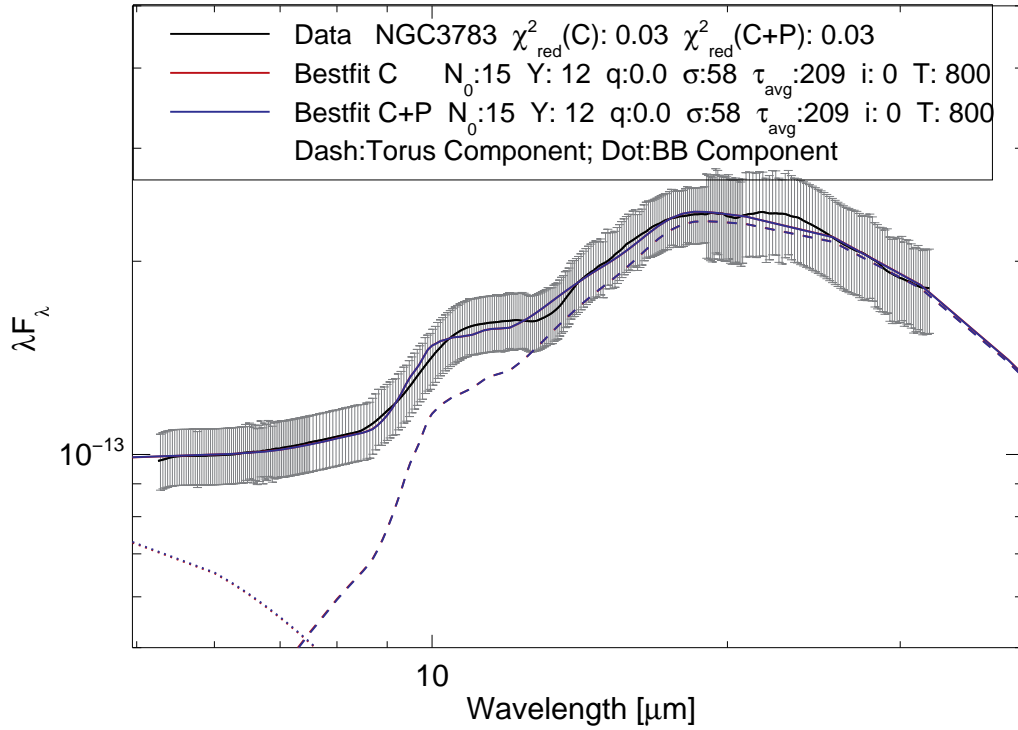
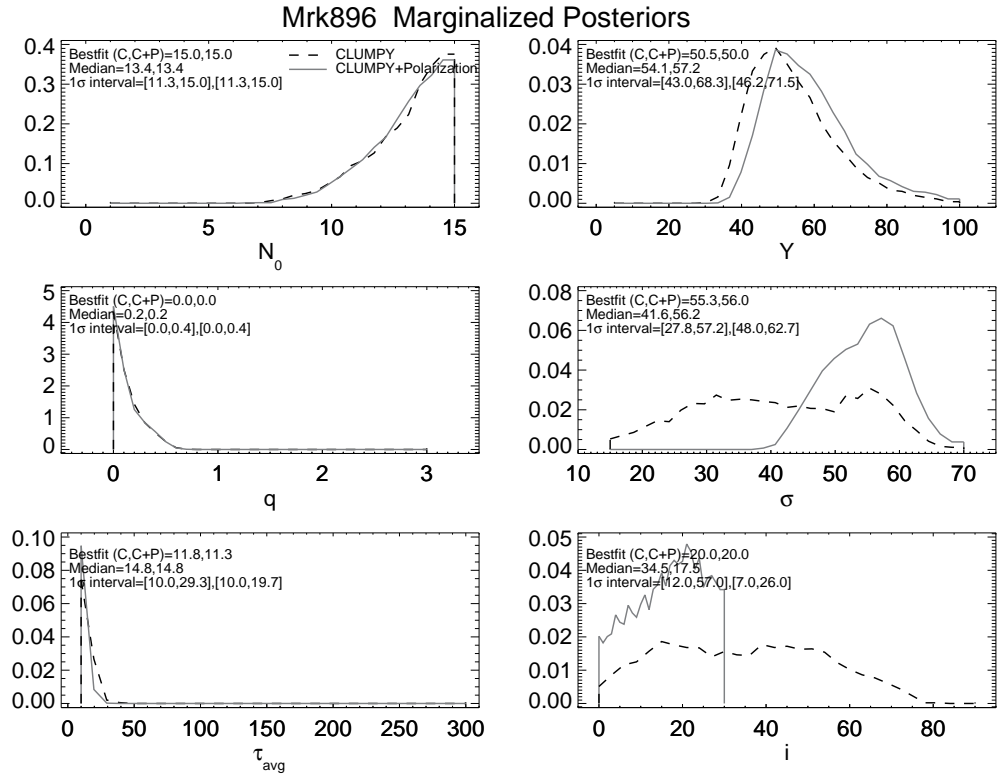


Figure A.1h Same as Figure 7.19 but for NGC 3783.



Data with CLUMPY and CLUMPY+Polarization Bestfits

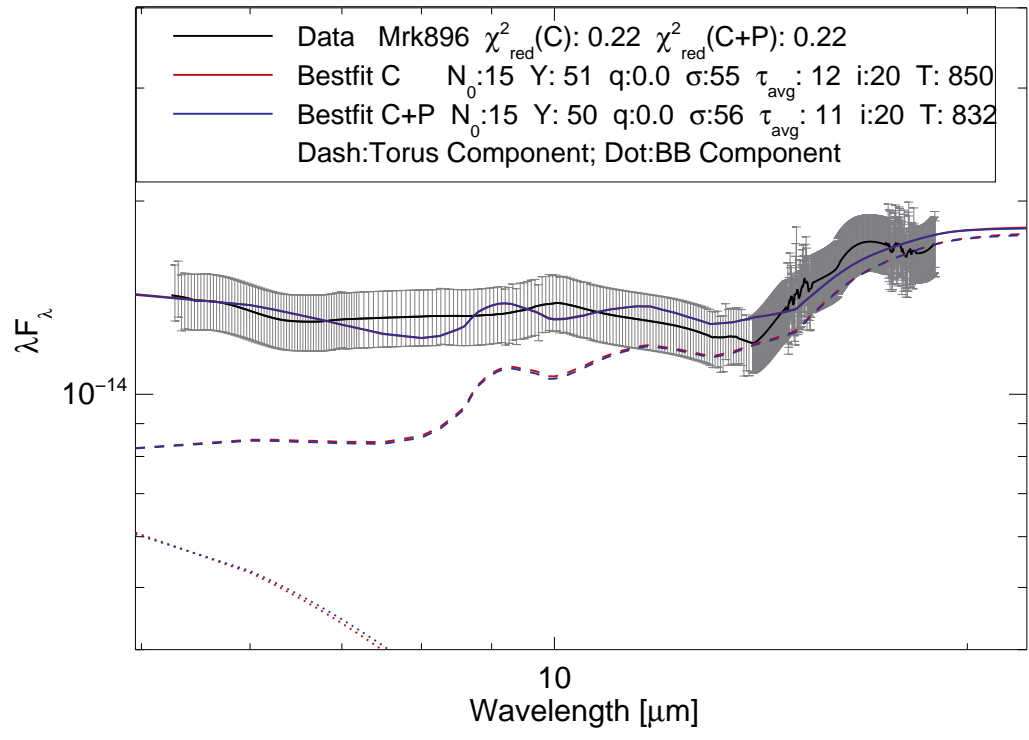
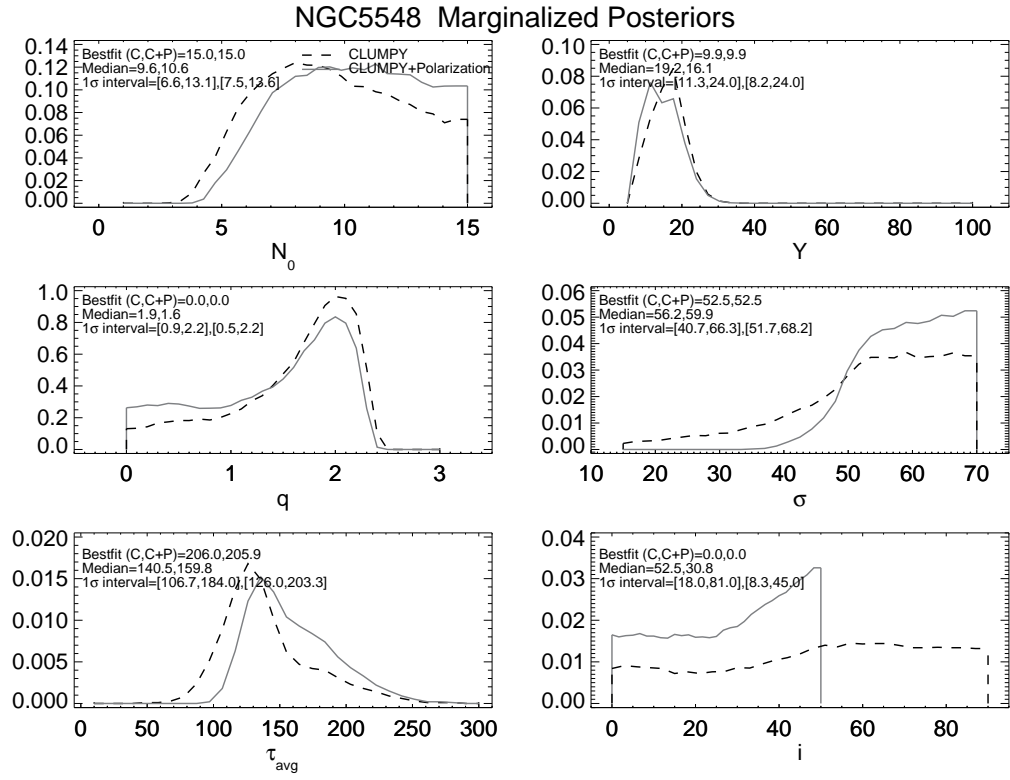


Figure A.1i Same as Figure 7.19 but for Mrk 896.



Data with CLUMPY and CLUMPY+Polarization Bestfits

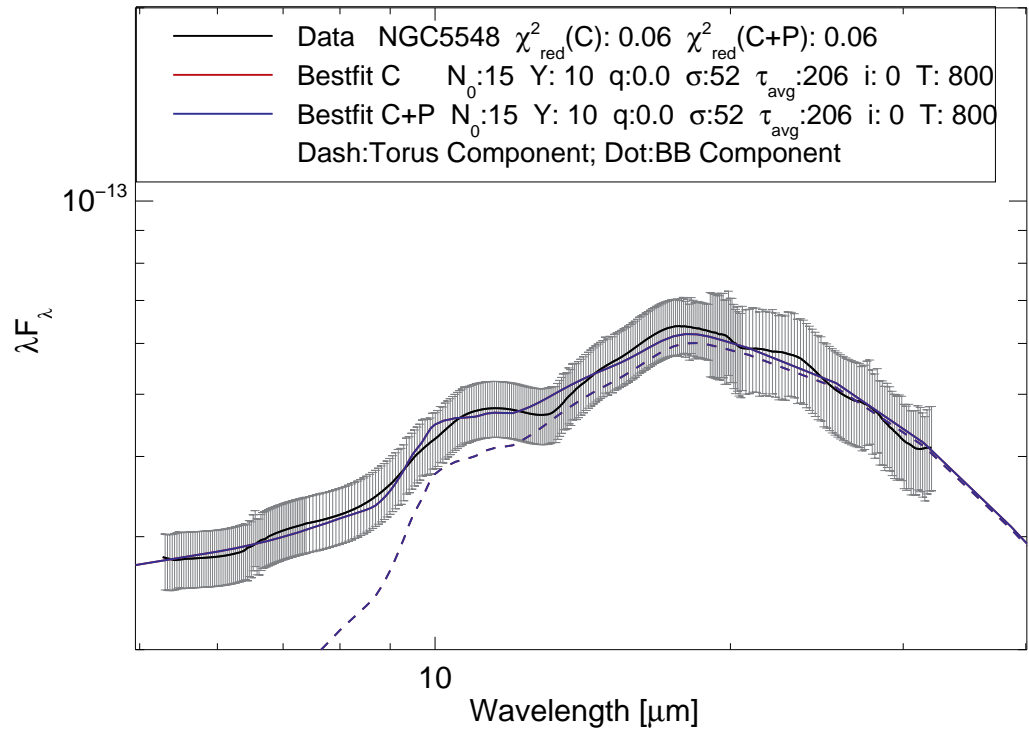


Figure A.1j Same as Figure 7.19 but for NGC 5548.

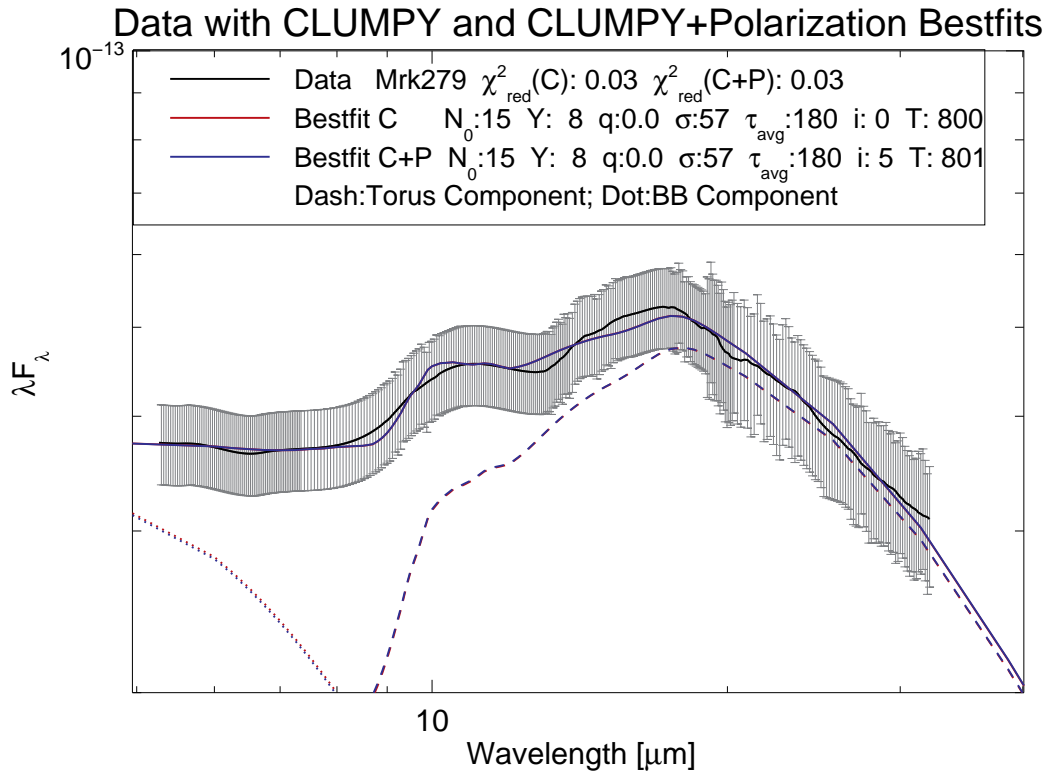
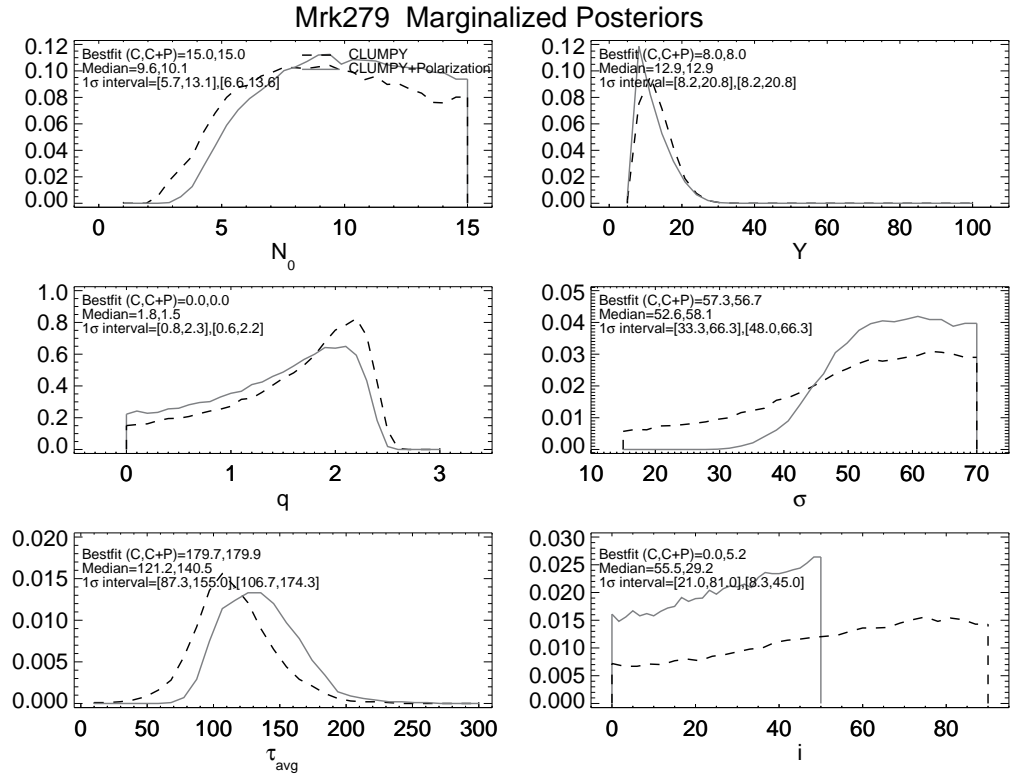
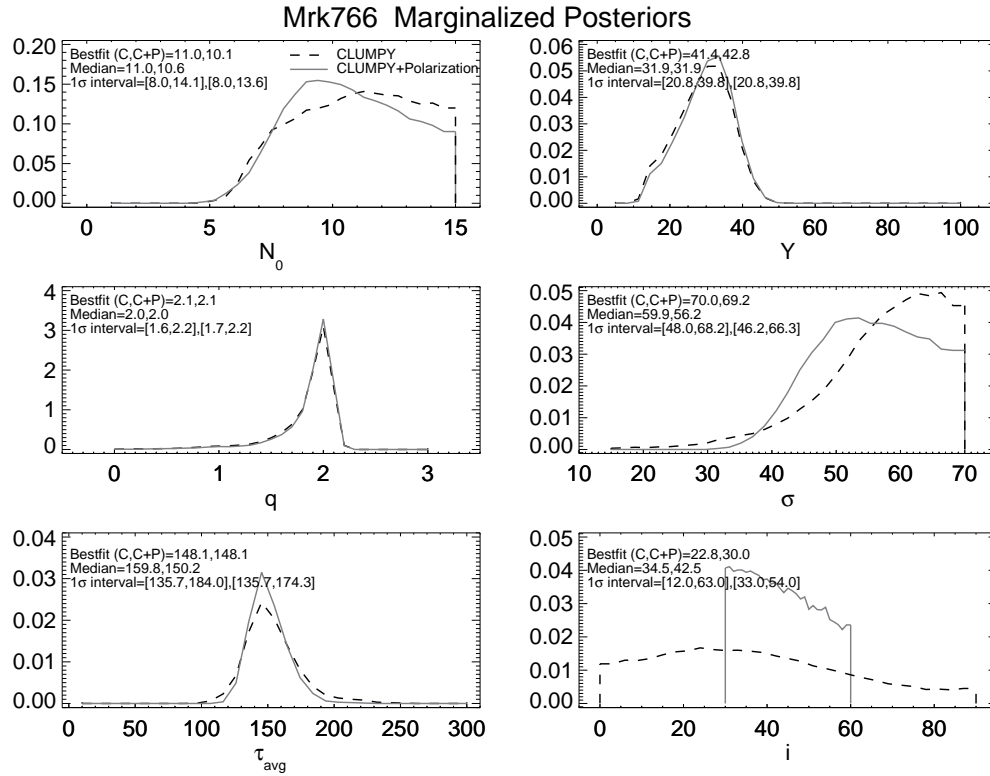


Figure A.1k Same as Figure 7.19 but for Mrk 279.



Data with CLUMPY and CLUMPY+Polarization Bestfits

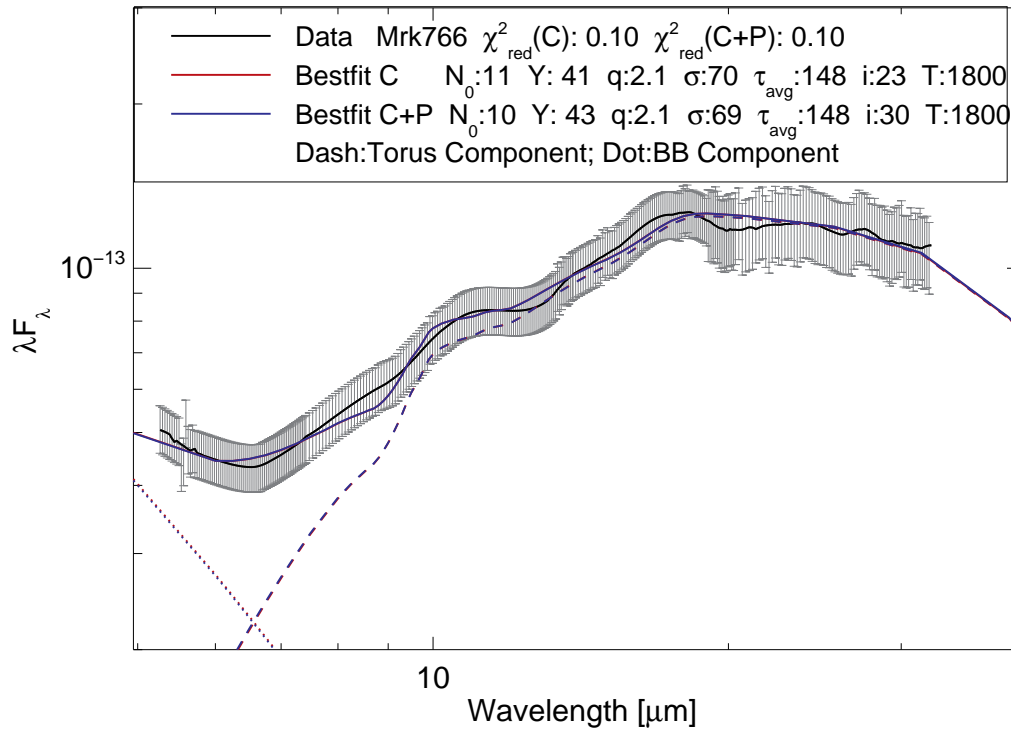
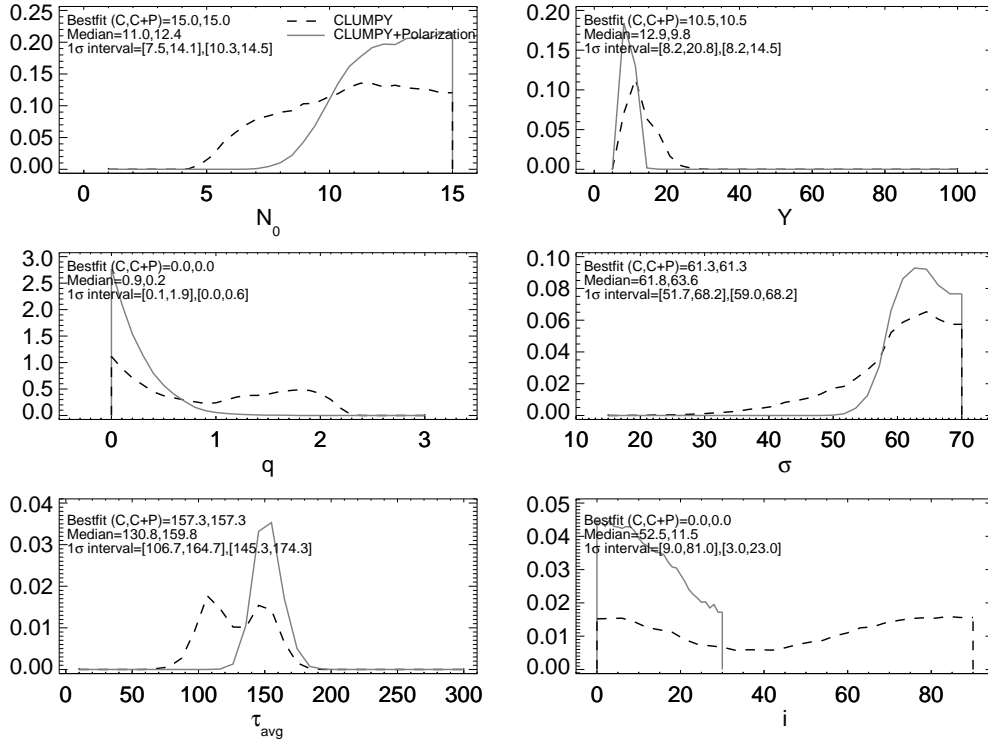


Figure A.11 Same as Figure 7.19 but for Mrk 766.

Mrk915 Marginalized Posteriors



Data with CLUMPY and CLUMPY+Polarization Bestfits

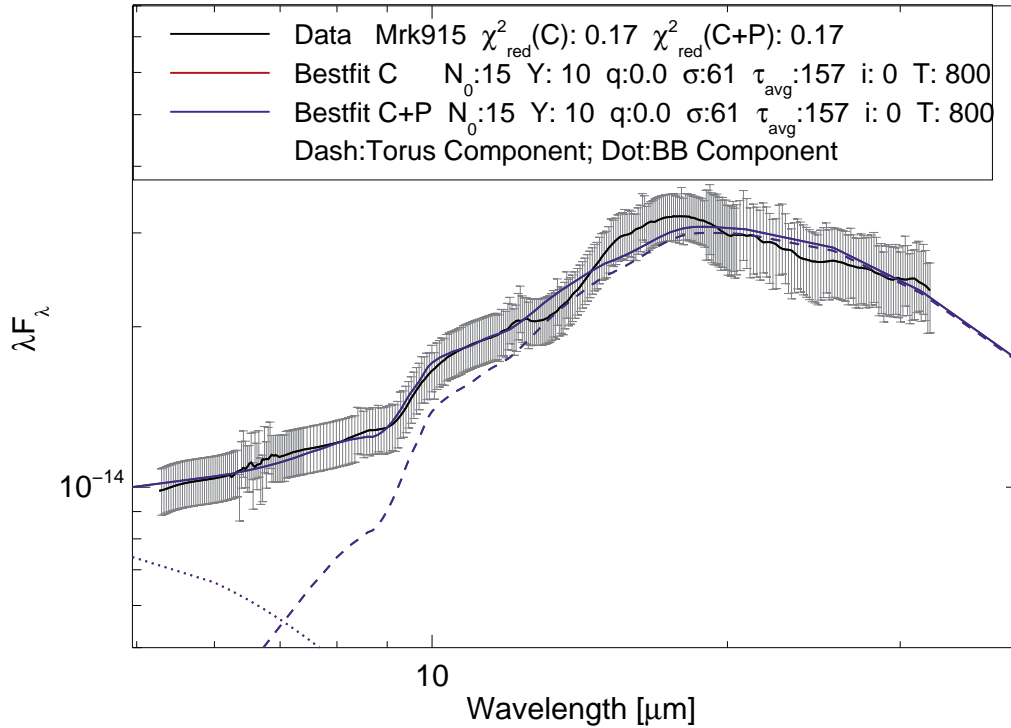
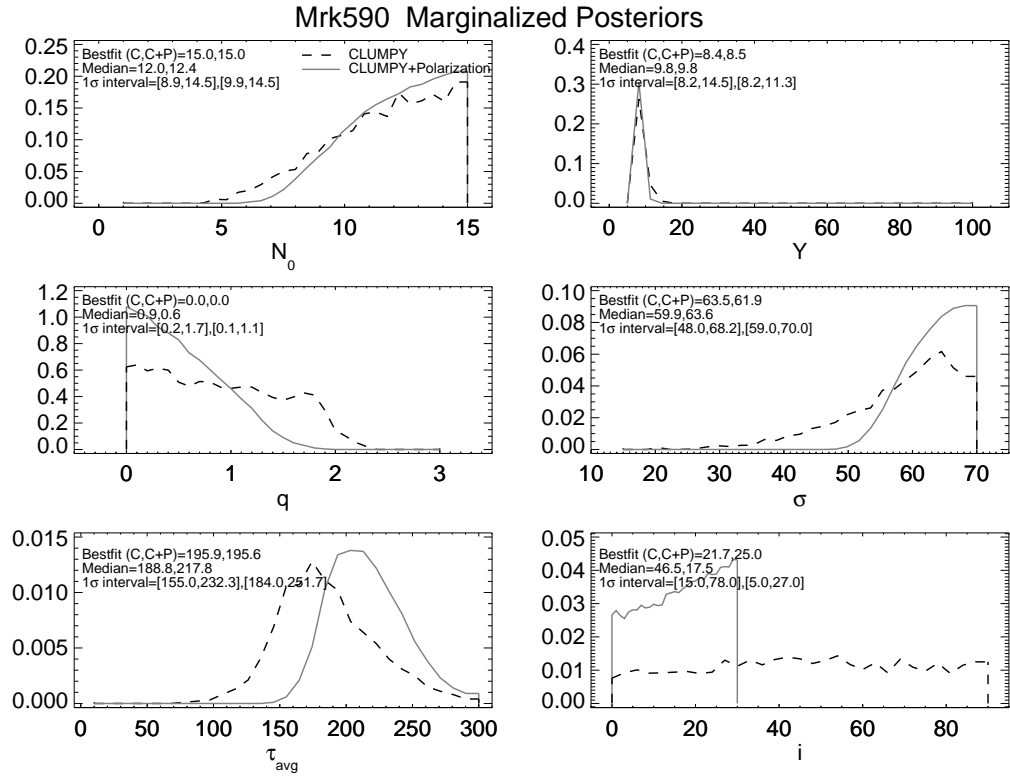


Figure A.1m Same as Figure 7.19 but for Mrk 915.



Data with CLUMPY and CLUMPY+Polarization Bestfits

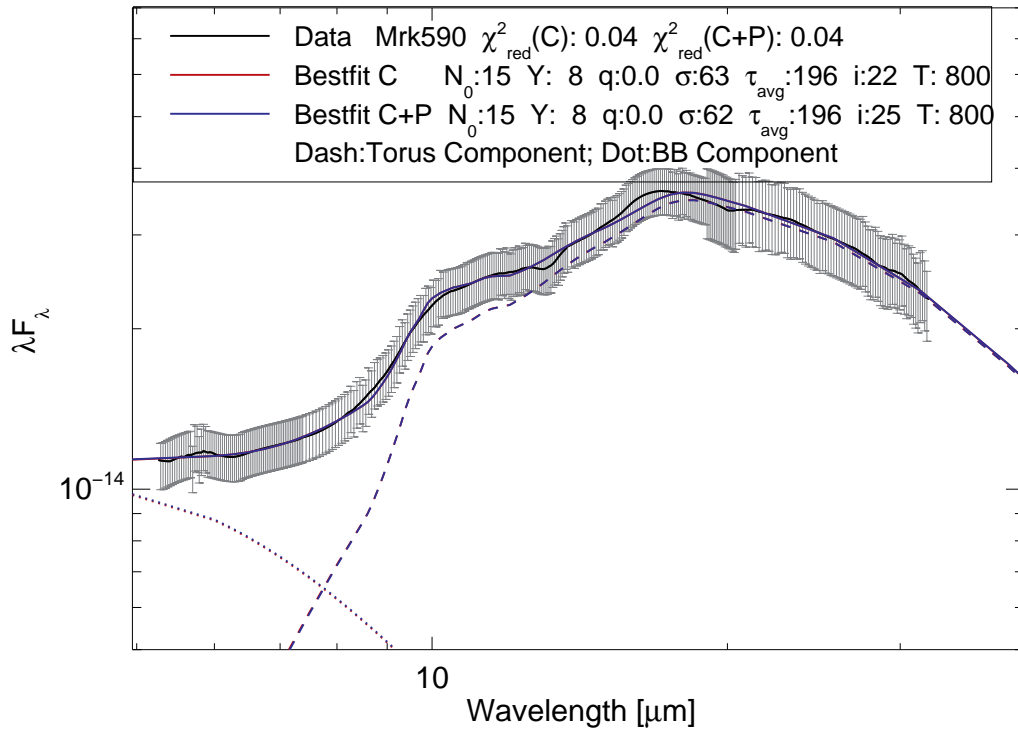
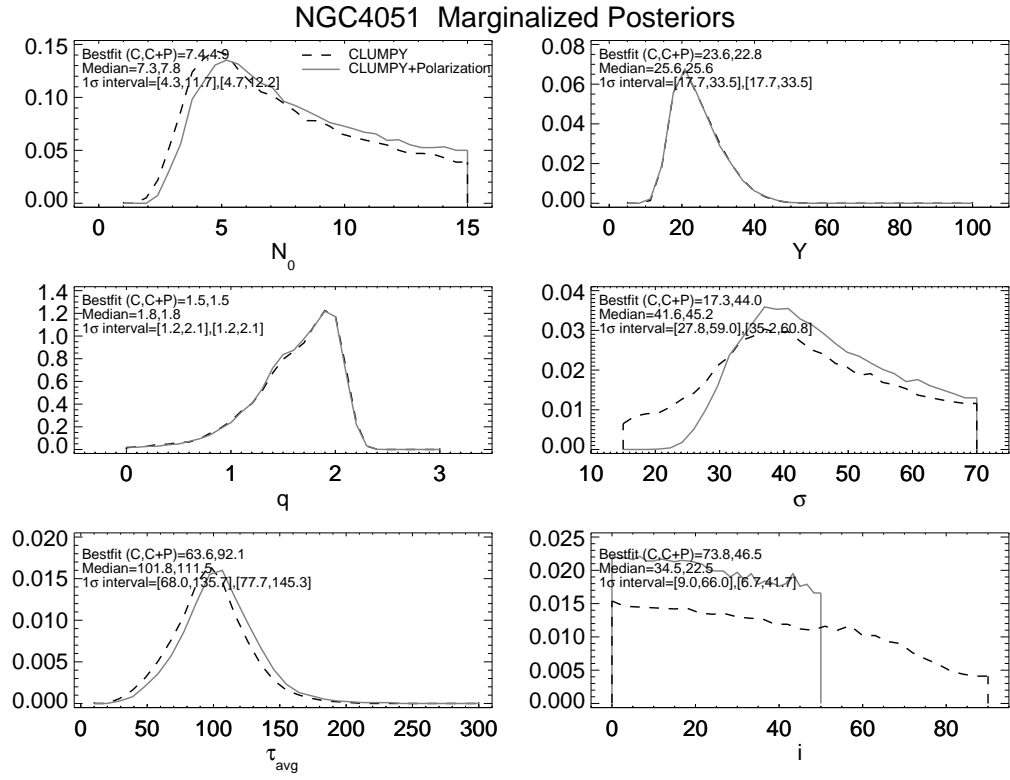


Figure A.1n Same as Figure 7.19 but for Mrk 590.



Data with CLUMPY and CLUMPY+Polarization Bestfits

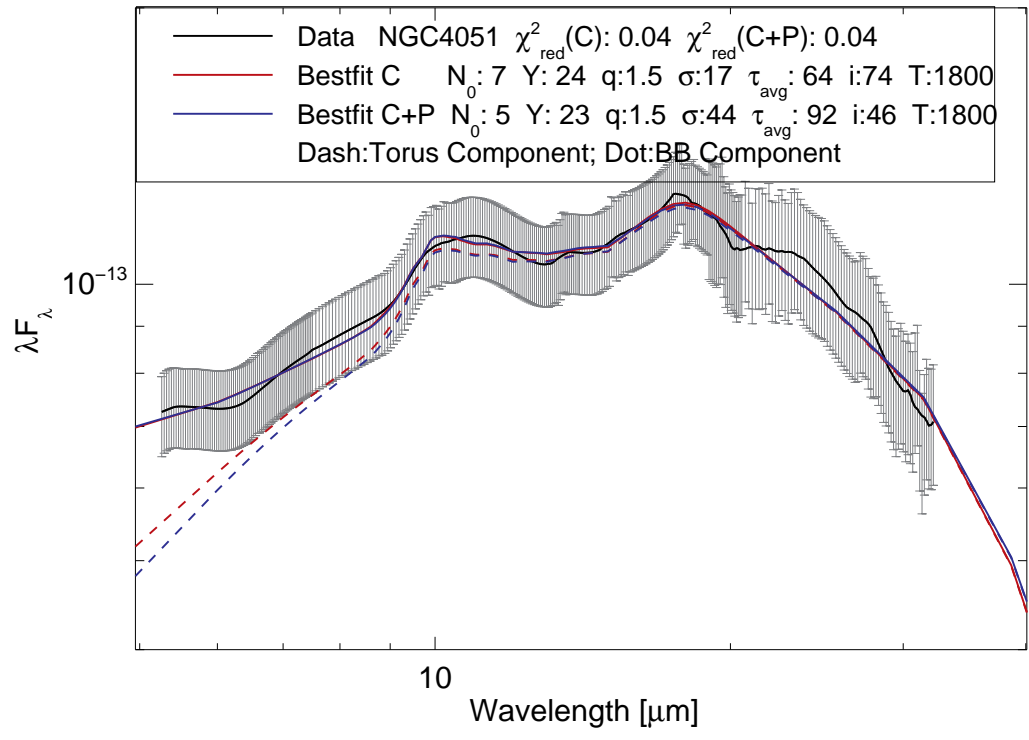
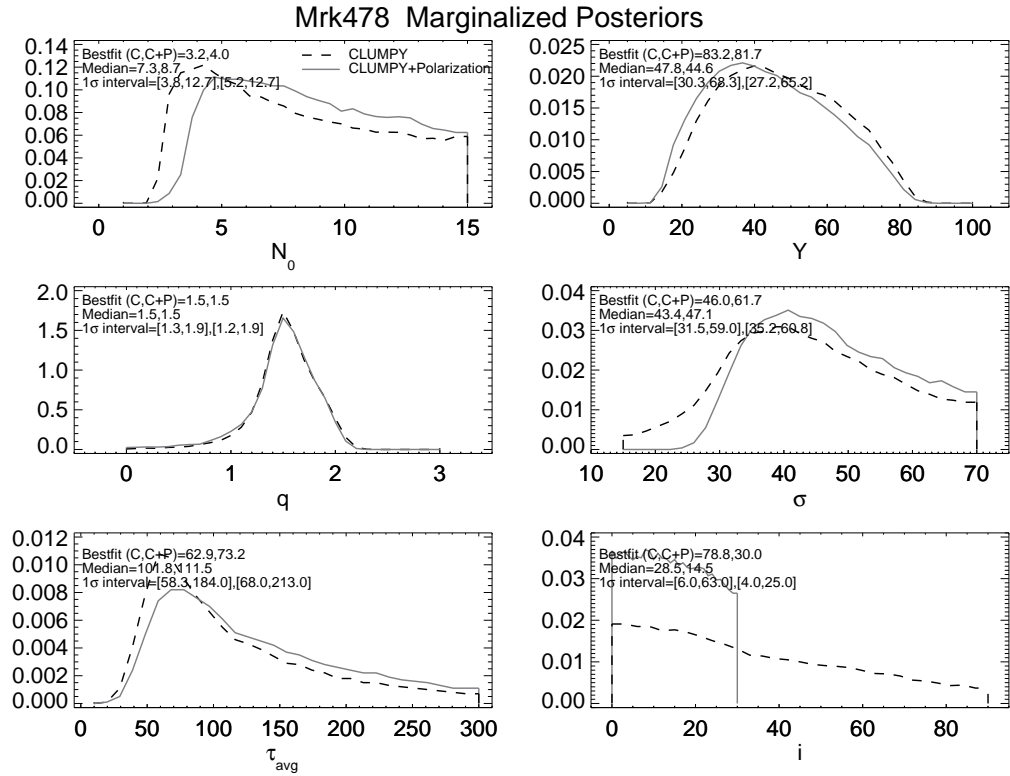


Figure A.1o Same as Figure 7.19 but for NGC 4051.



Data with CLUMPY and CLUMPY+Polarization Bestfits

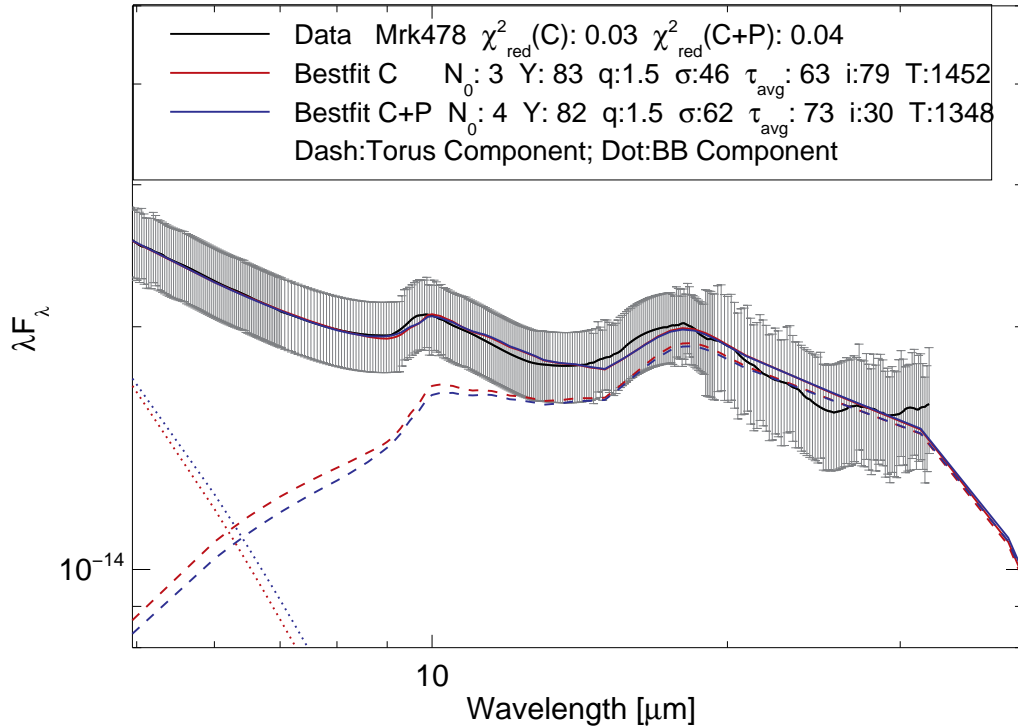


Figure A.1p Same as Figure 7.19 but for Mrk 478.

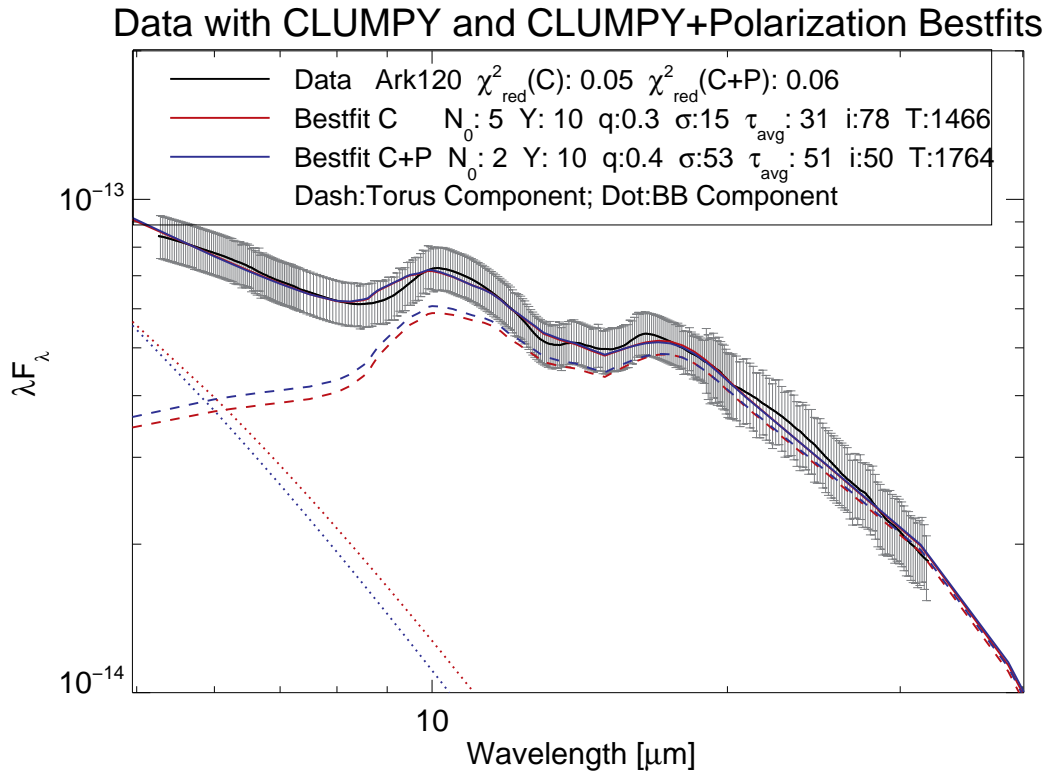
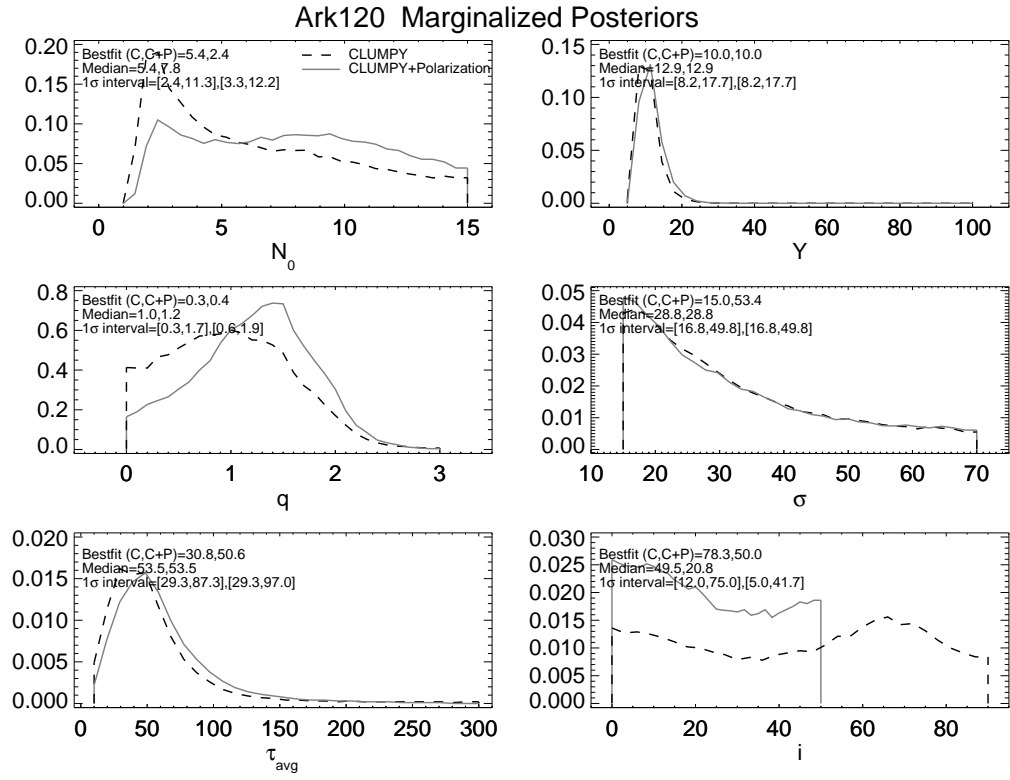
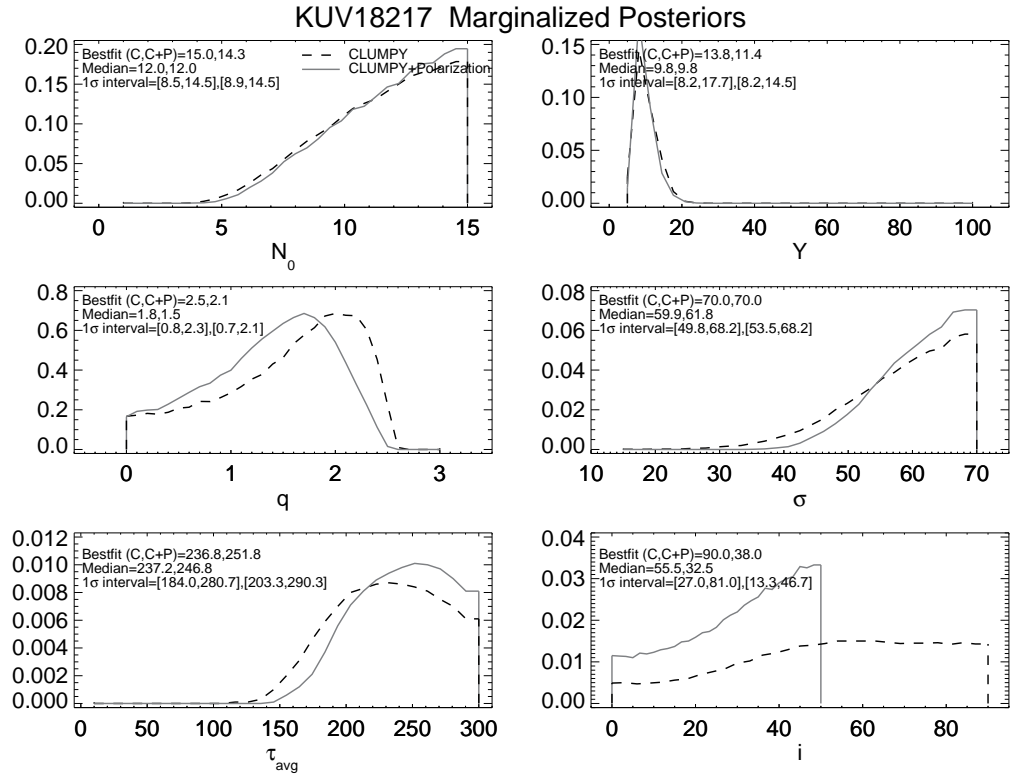


Figure A.1q Same as Figure 7.19 but for Ark 120.



Data with CLUMPY and CLUMPY+Polarization Bestfits

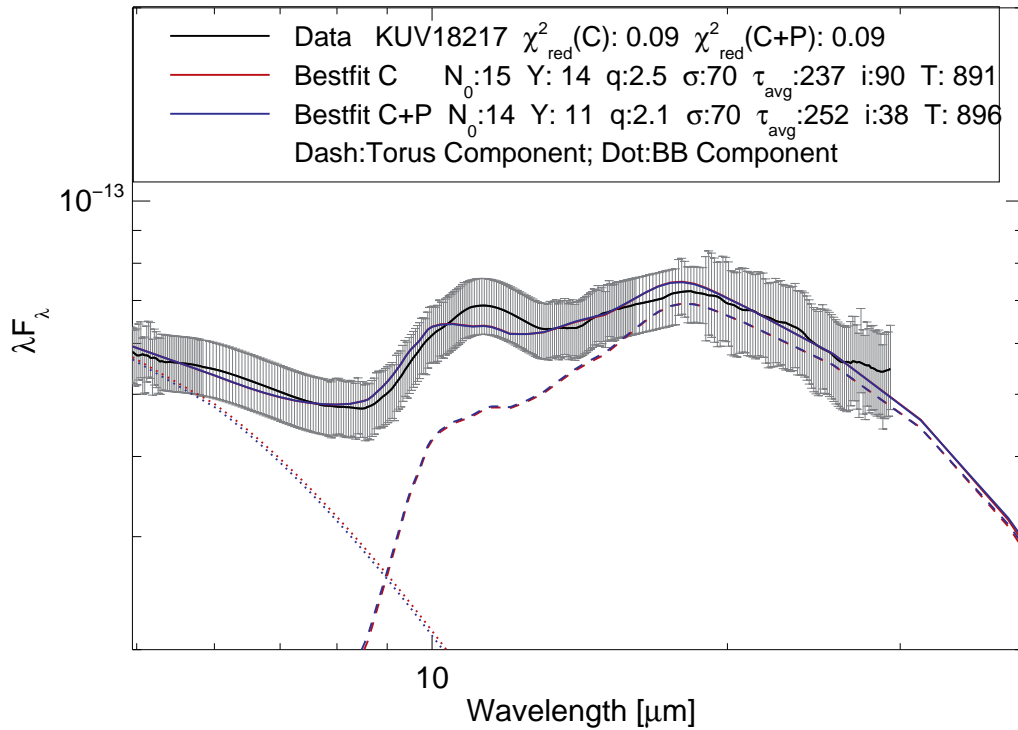
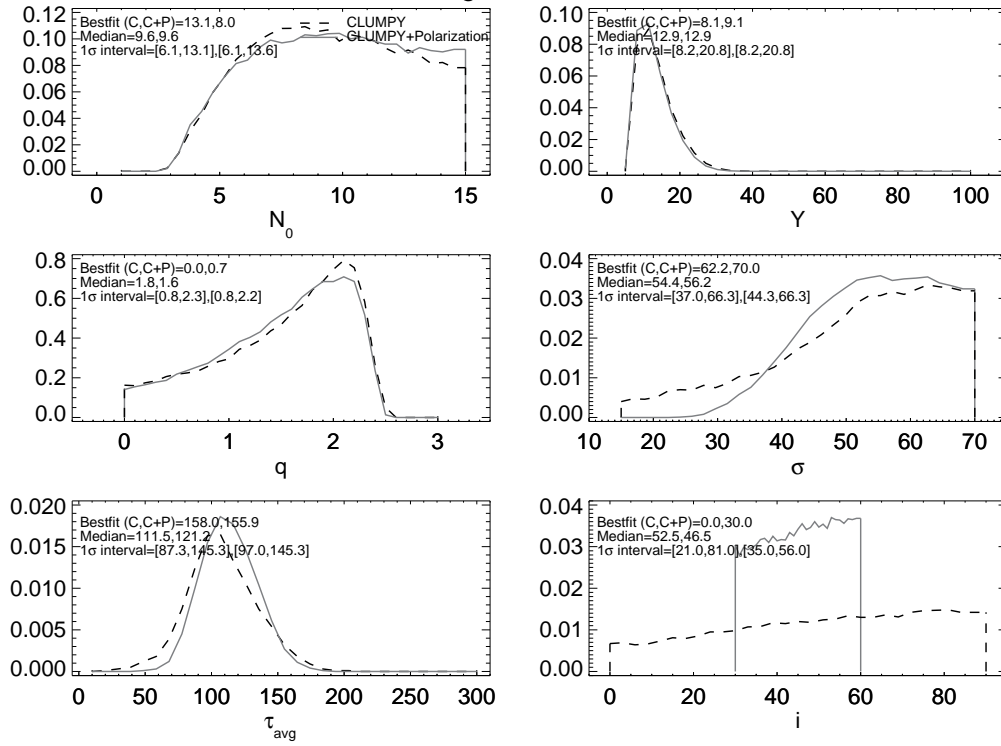


Figure A.1r Same as Figure 7.19 but for KUV 18217+6419.

M63015 Marginalized Posteriors



Data with CLUMPY and CLUMPY+Polarization Bestfits

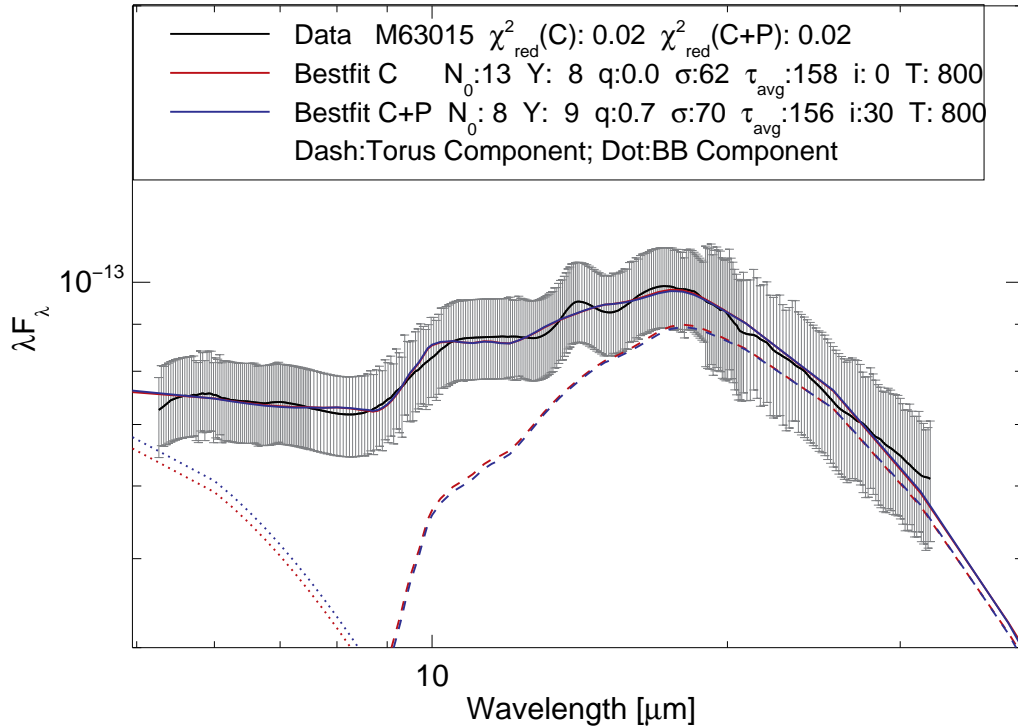
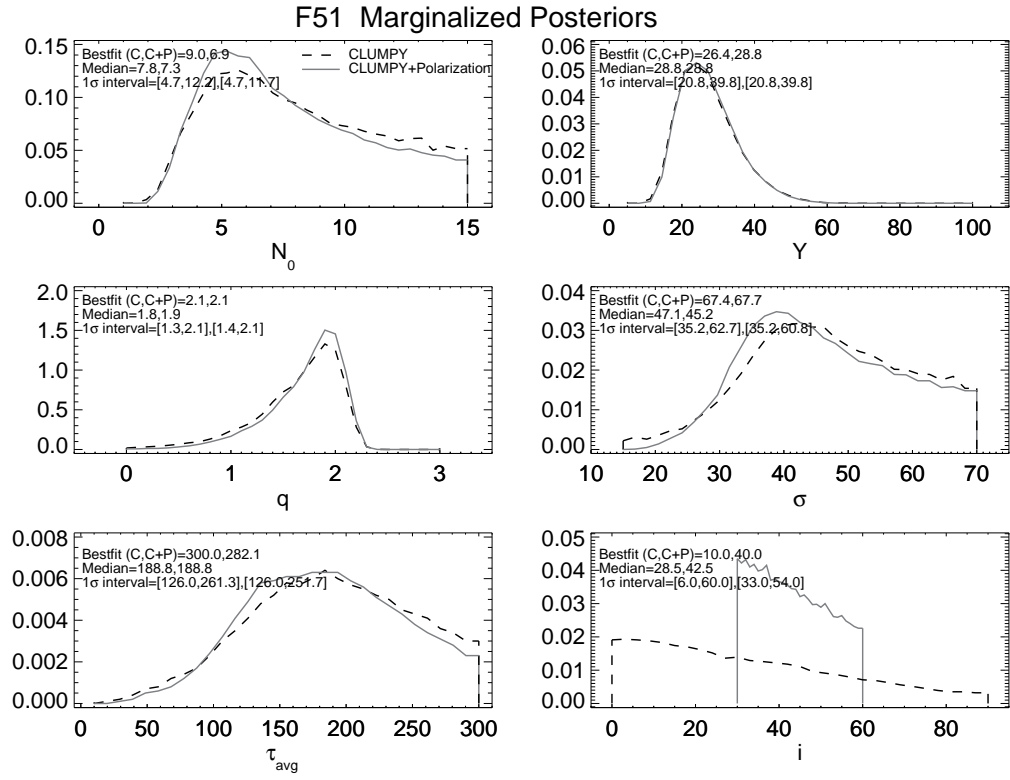


Figure A.1s Same as Figure 7.19 but for MCG -06-30-015.



Data with CLUMPY and CLUMPY+Polarization Bestfits

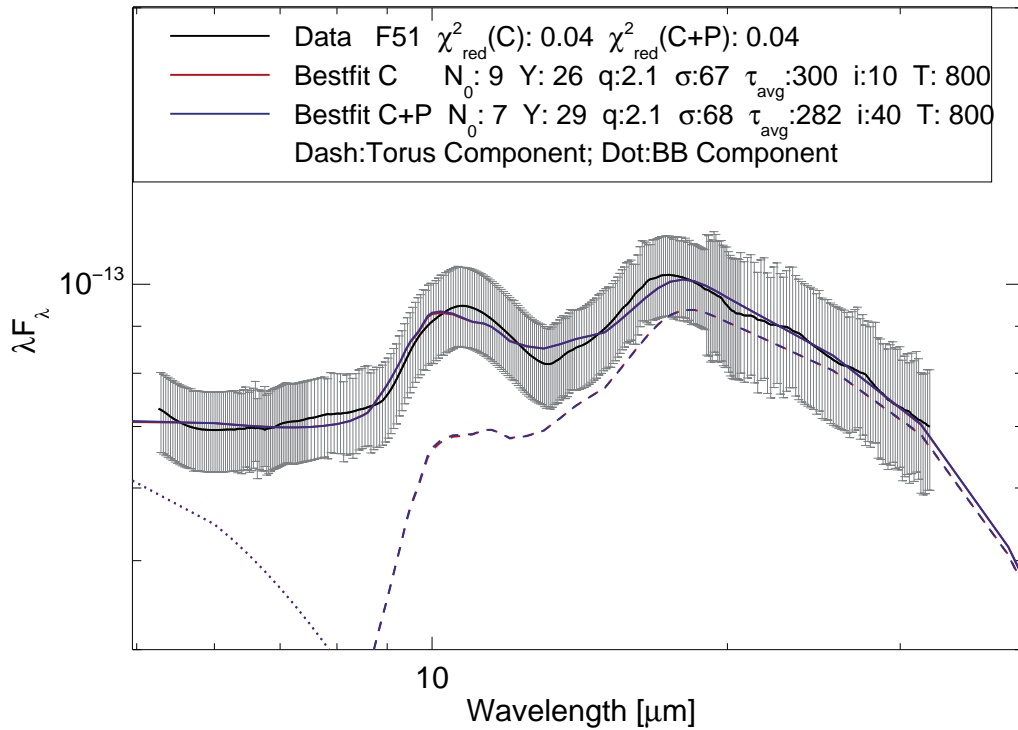
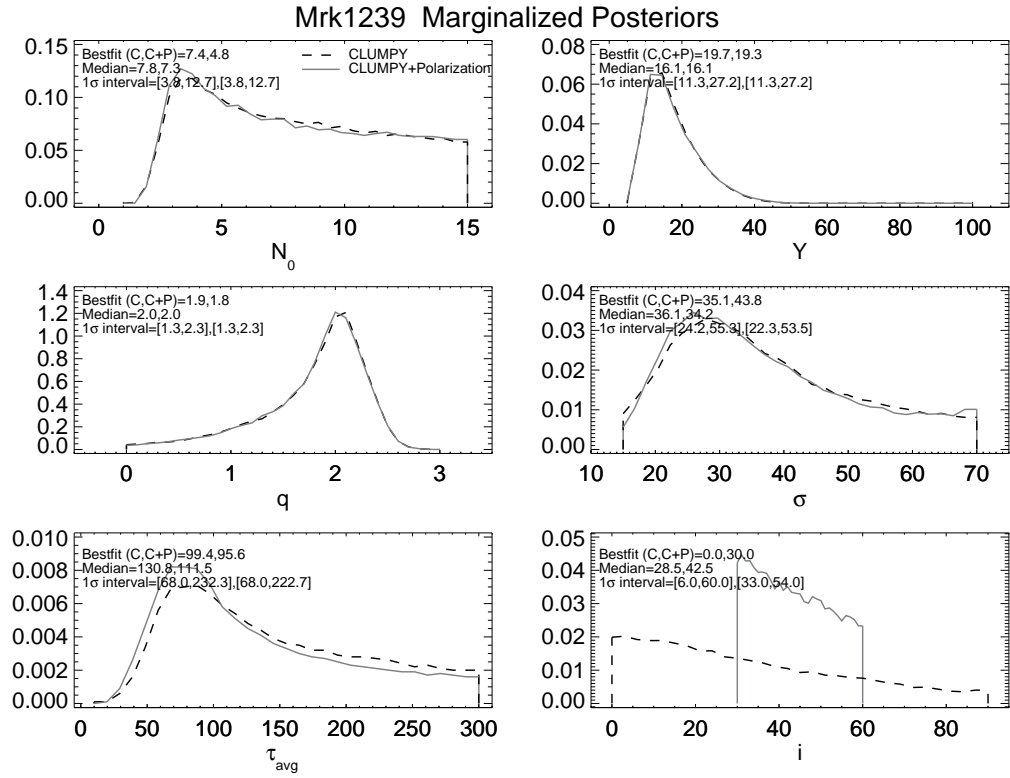


Figure A.1t Same as Figure 7.19 but for Fairall 51.



Data with CLUMPY and CLUMPY+Polarization Bestfits

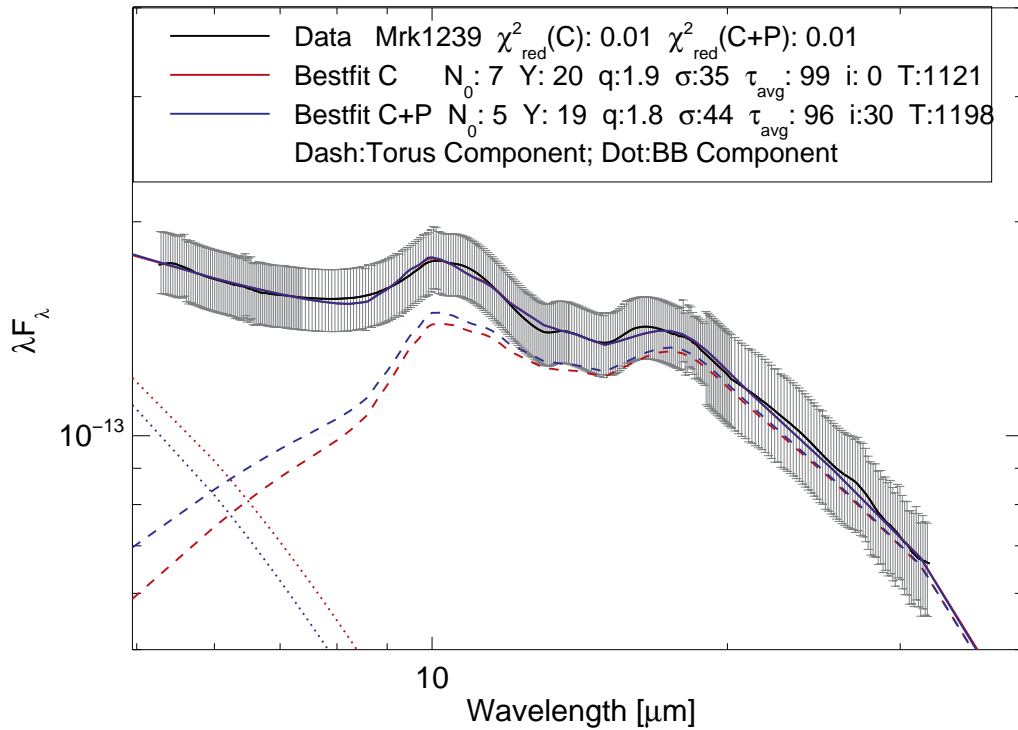
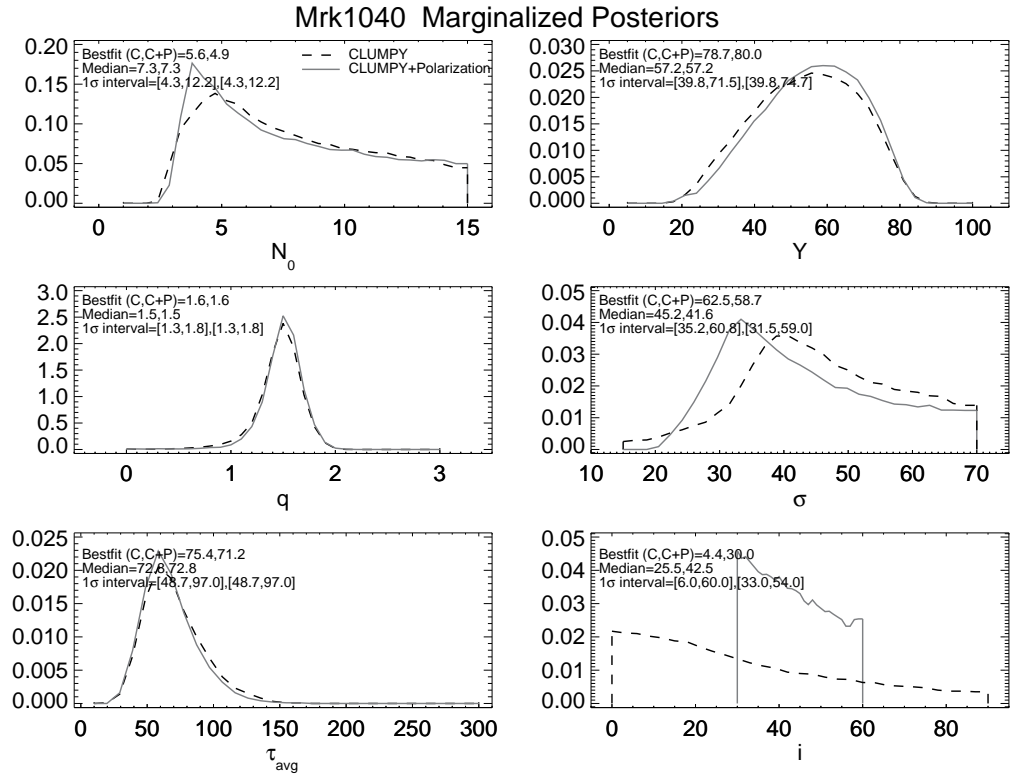


Figure A.1u Same as Figure 7.19 but for Mrk 1239.



Data with CLUMPY and CLUMPY+Polarization Bestfits

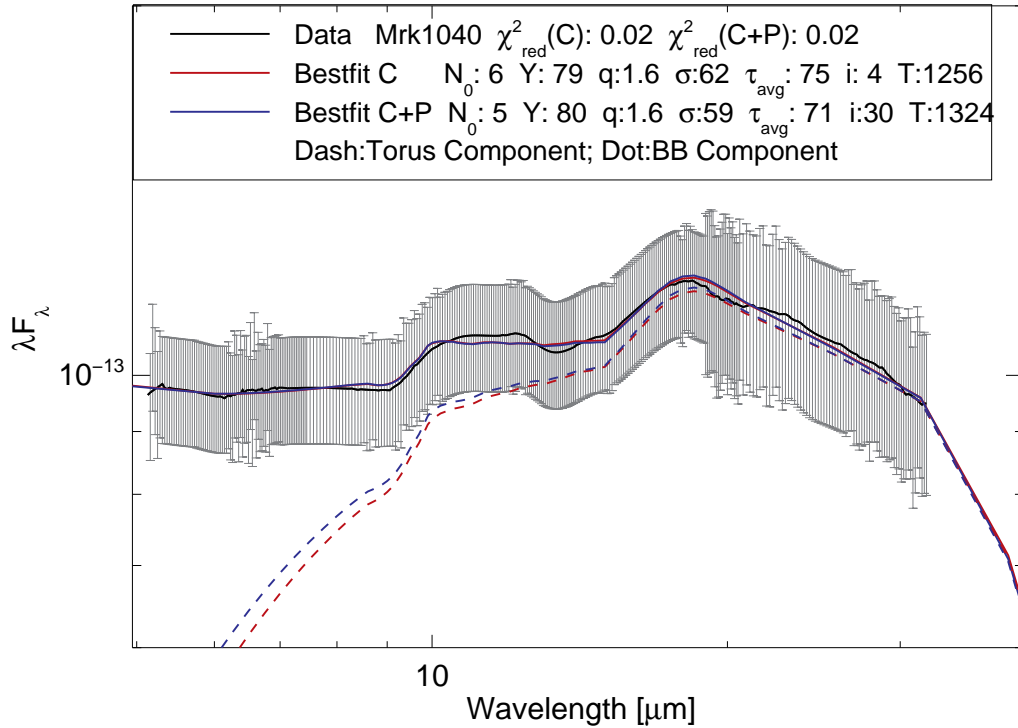
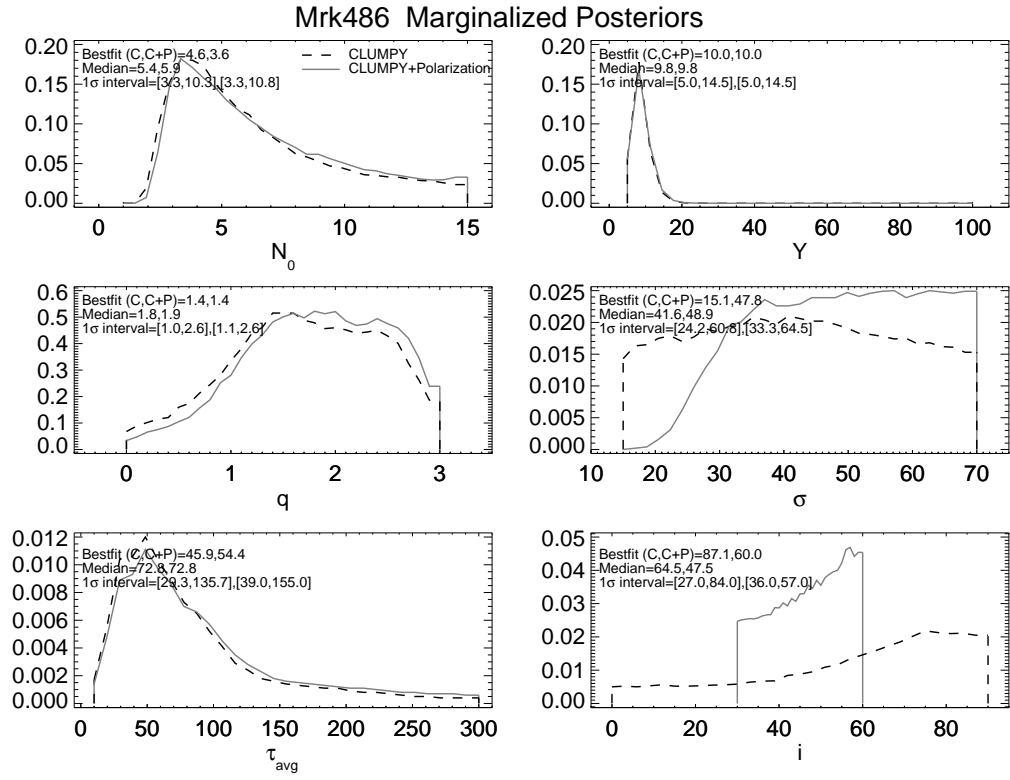


Figure A.1v Same as Figure 7.19 but for Mrk 1040.



Data with CLUMPY and CLUMPY+Polarization Bestfits

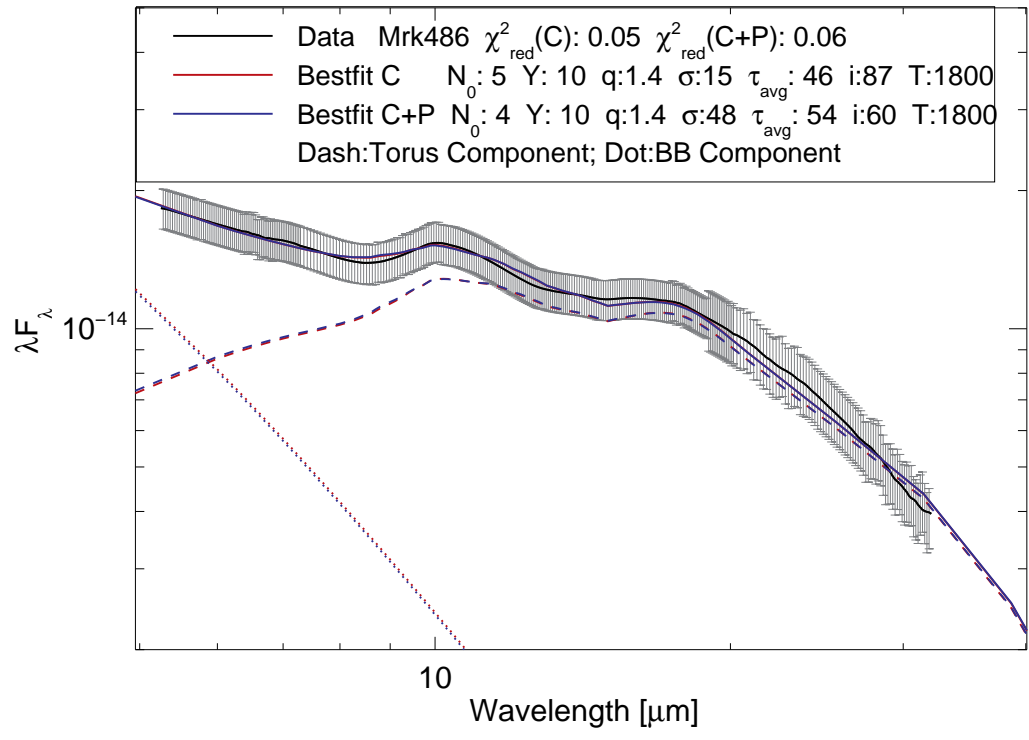
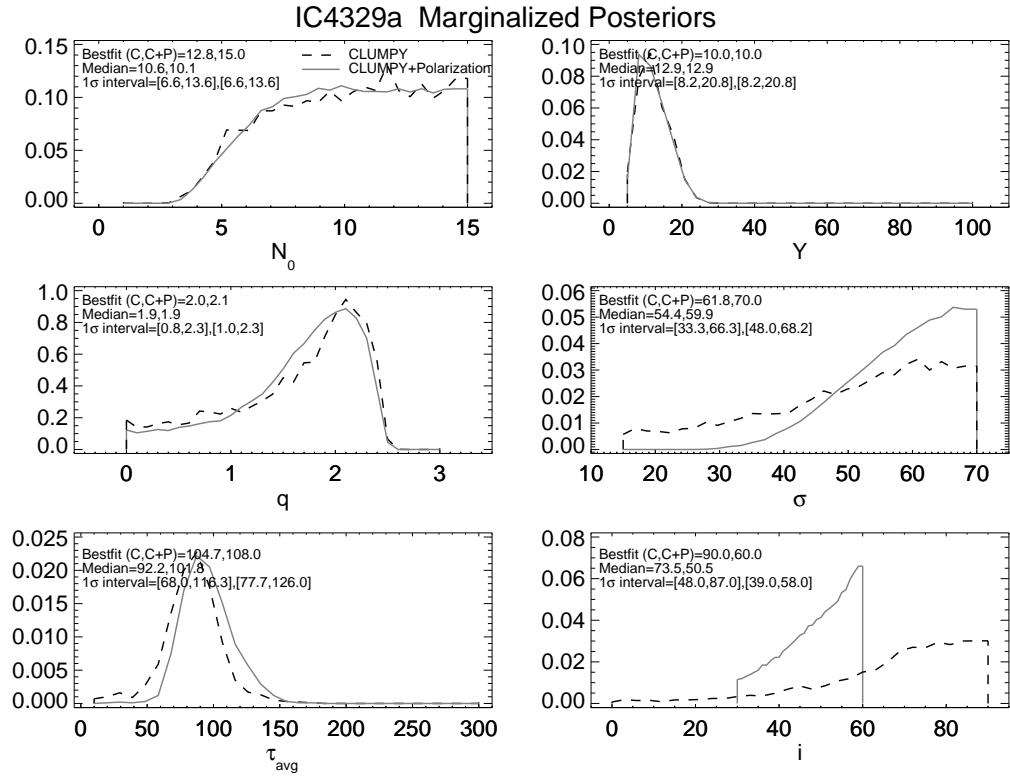


Figure A.1w Same as Figure 7.19 but for Mrk 486.



Data with CLUMPY and CLUMPY+Polarization Bestfits

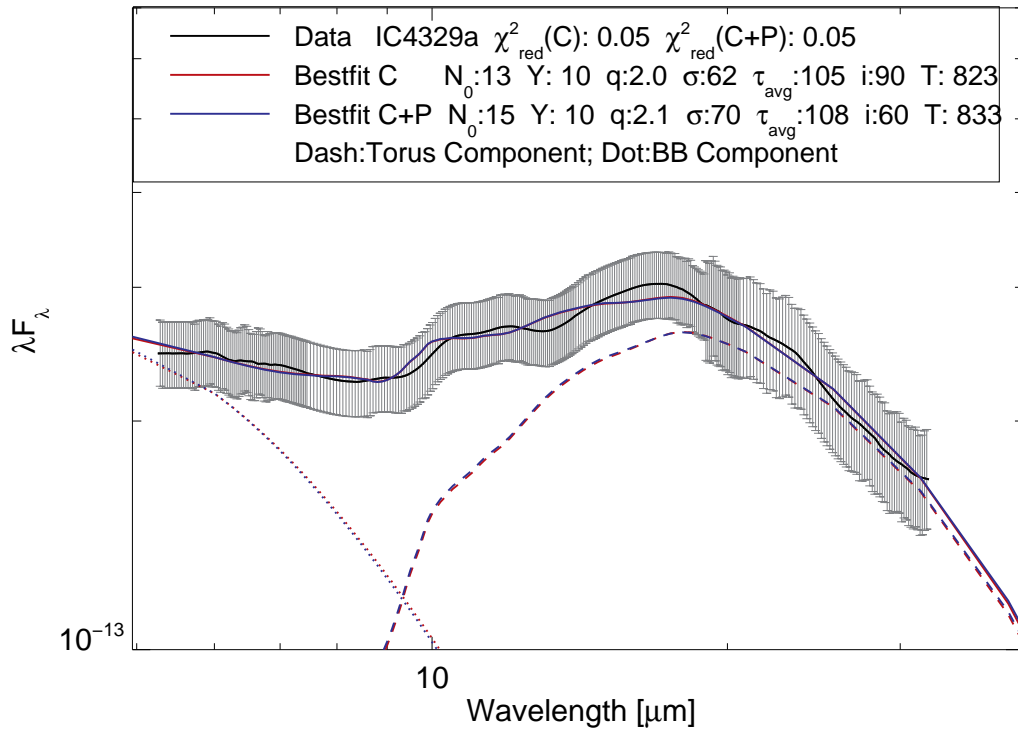
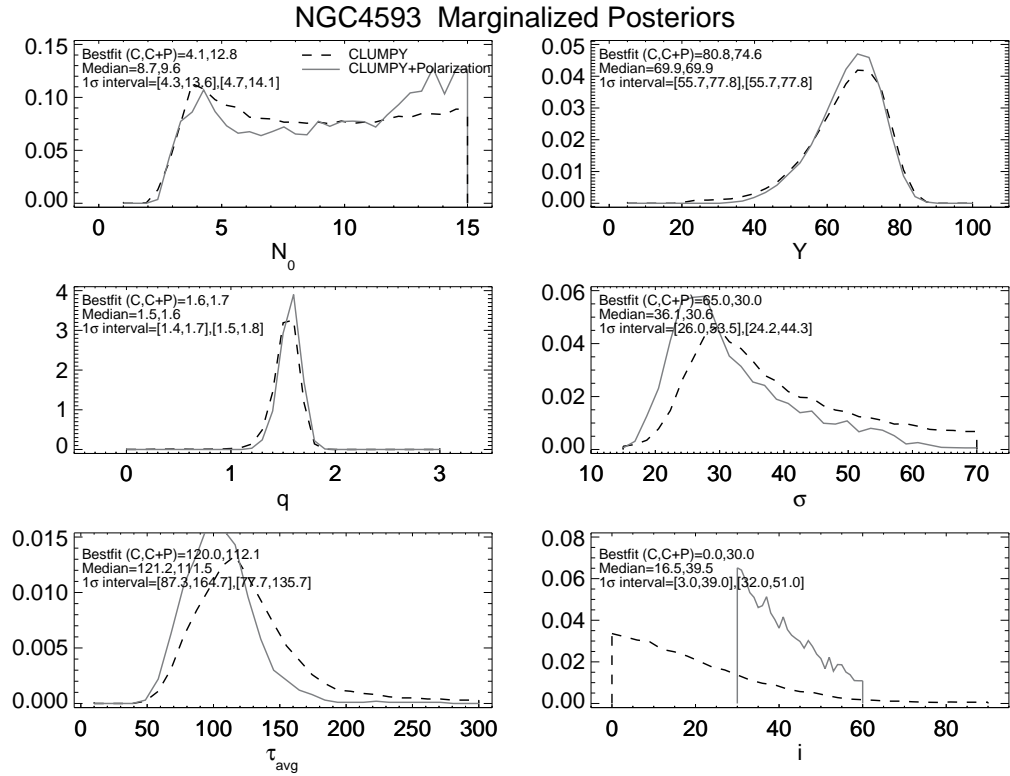


Figure A.1x Same as Figure 7.19 but for IC 4329A.



Data with CLUMPY and CLUMPY+Polarization Bestfits

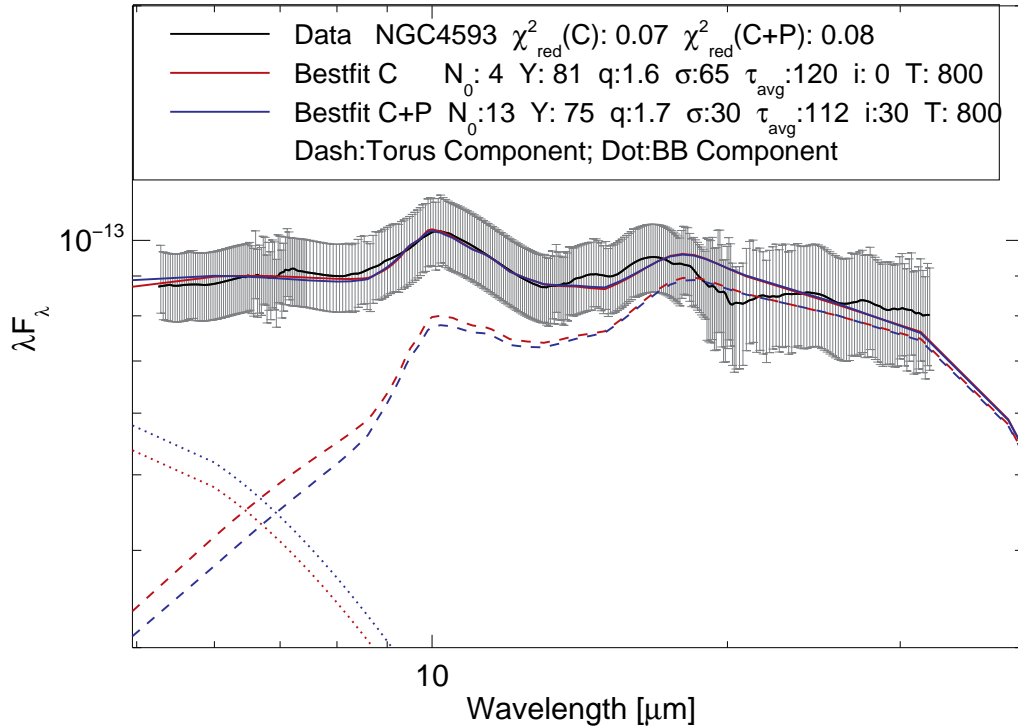
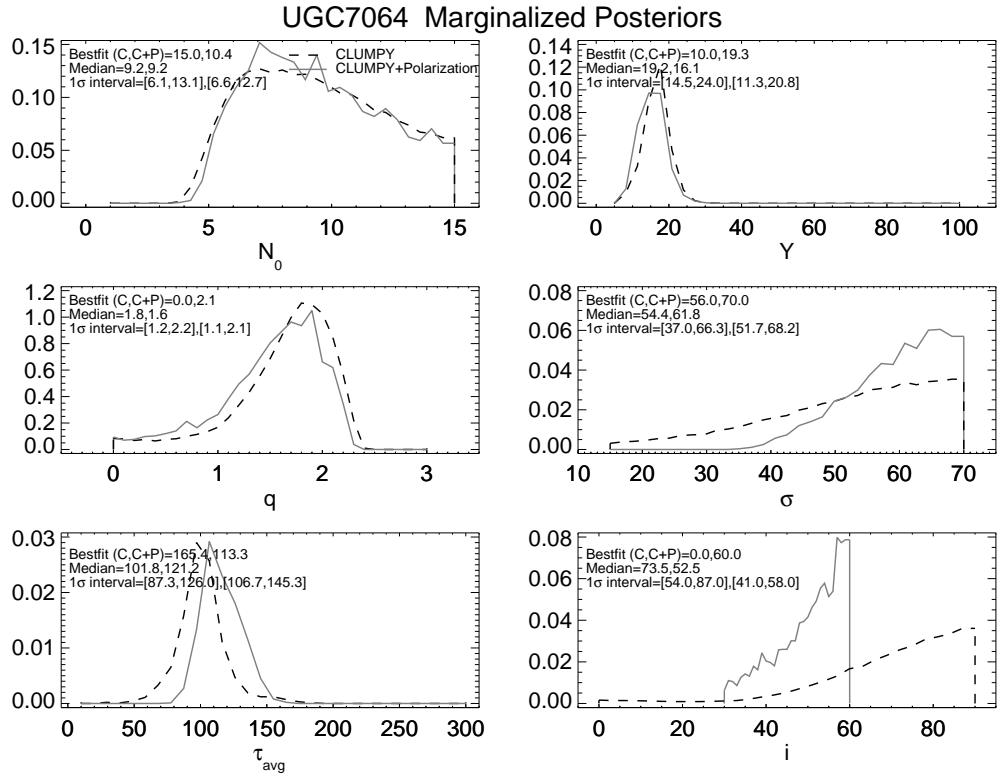


Figure A.1y Same as Figure 7.19 but for NGC 4593.



Data with CLUMPY and CLUMPY+Polarization Bestfits

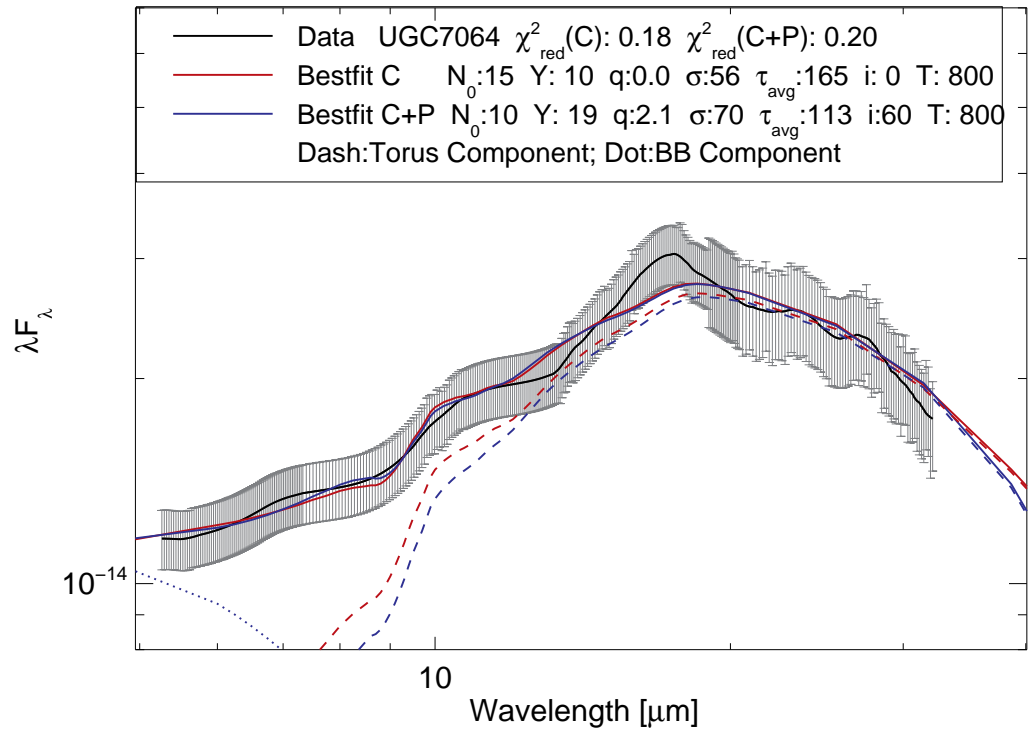


Figure A.1z Same as Figure 7.19 but for UGC 7064.

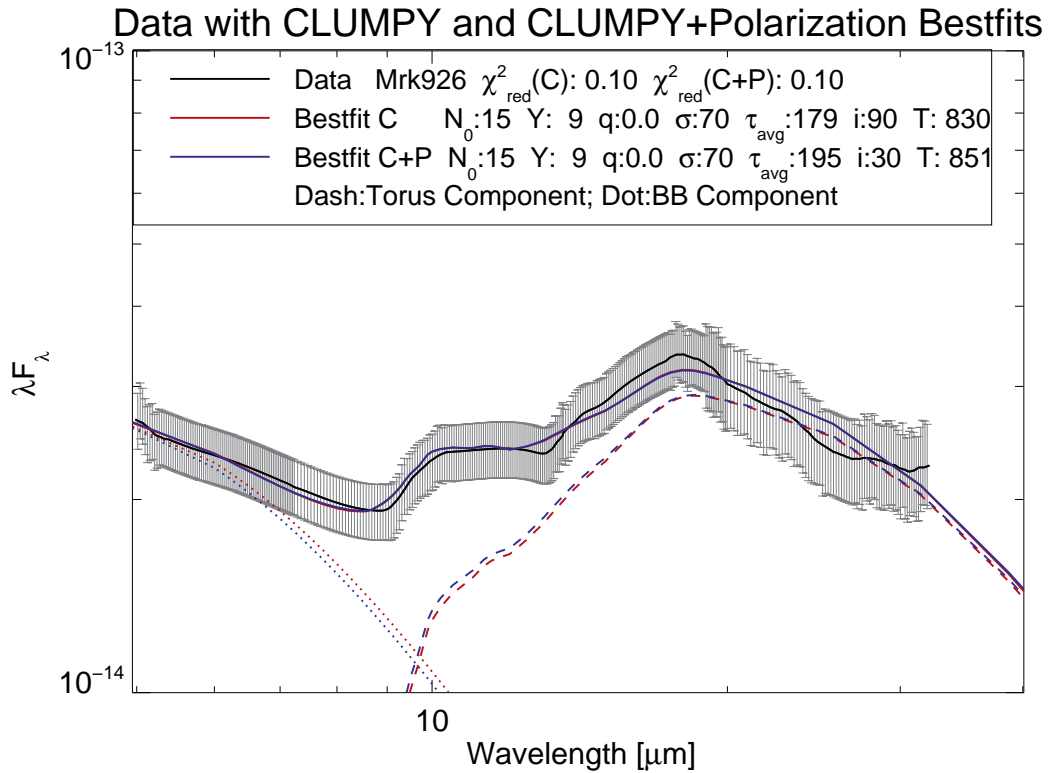
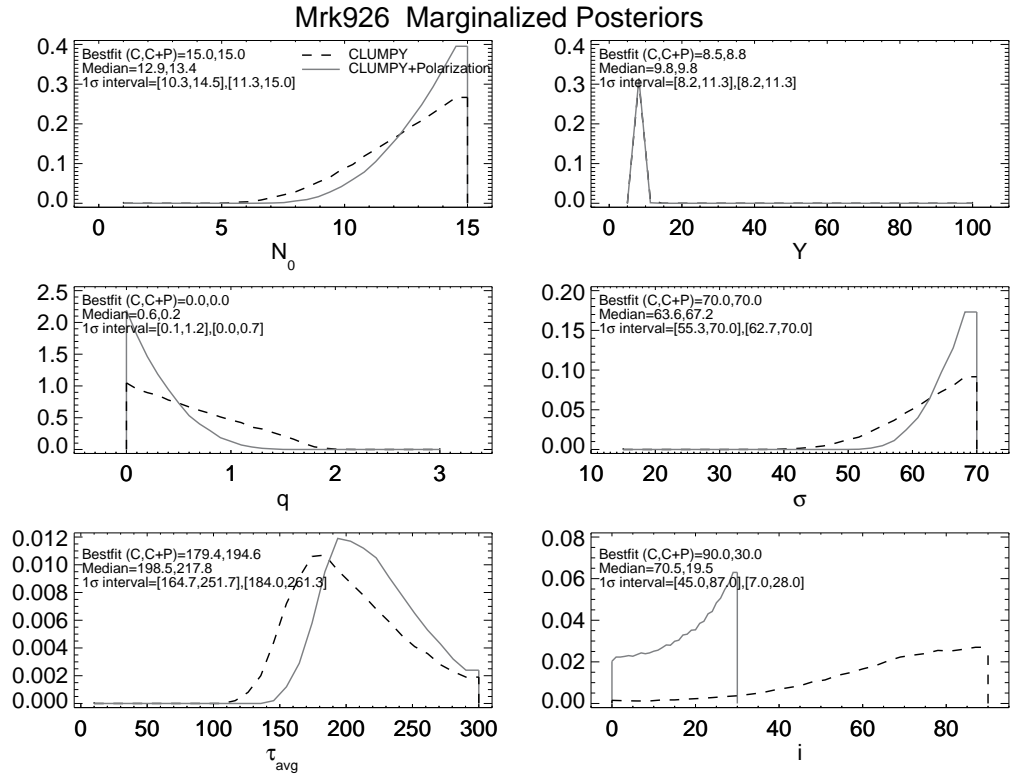
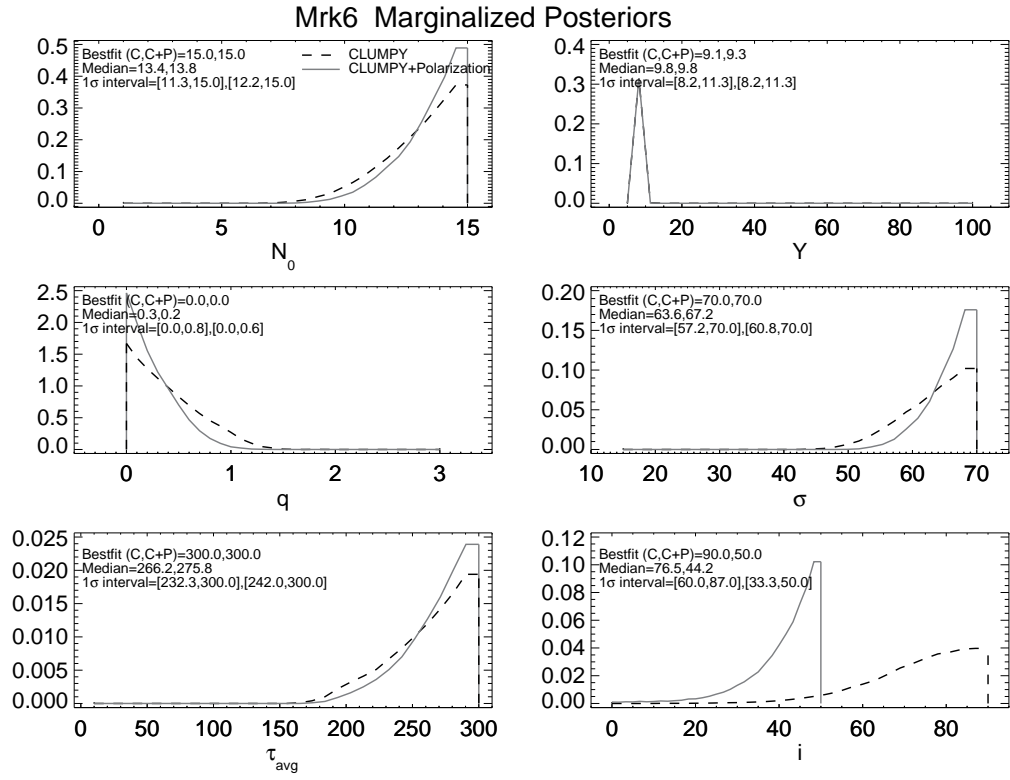


Figure A.1aa Same as Figure 7.19 but for Mrk 926.



Data with CLUMPY and CLUMPY+Polarization Bestfits

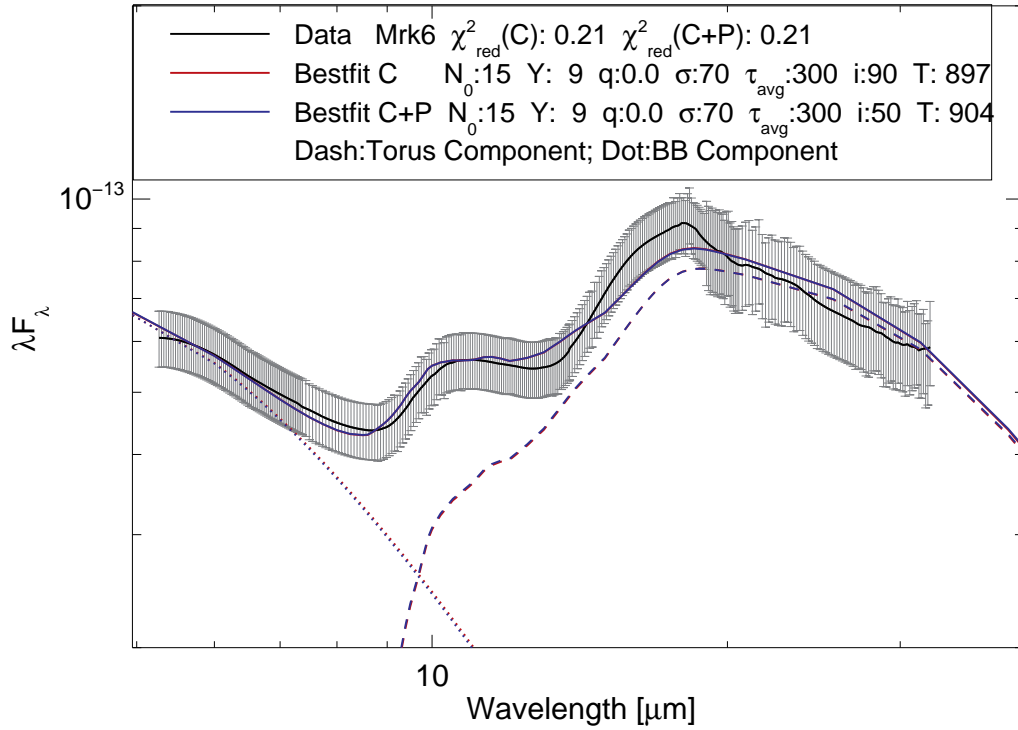


Figure A.1bb Same as Figure 7.19 but for Mrk 6.

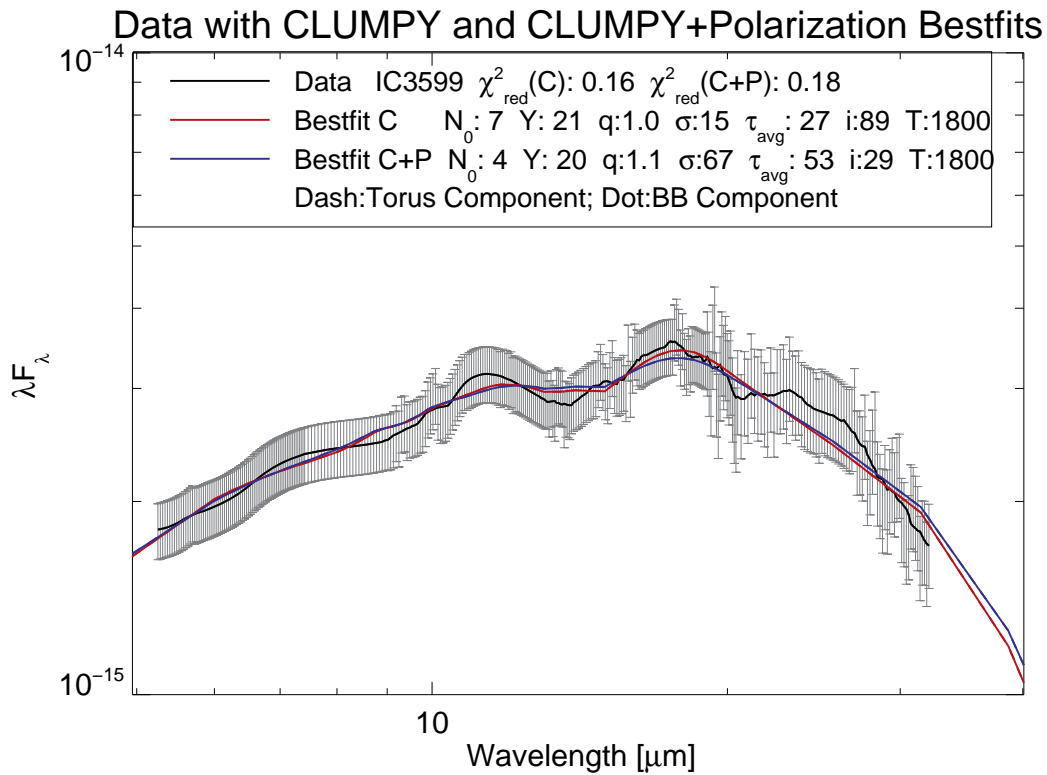
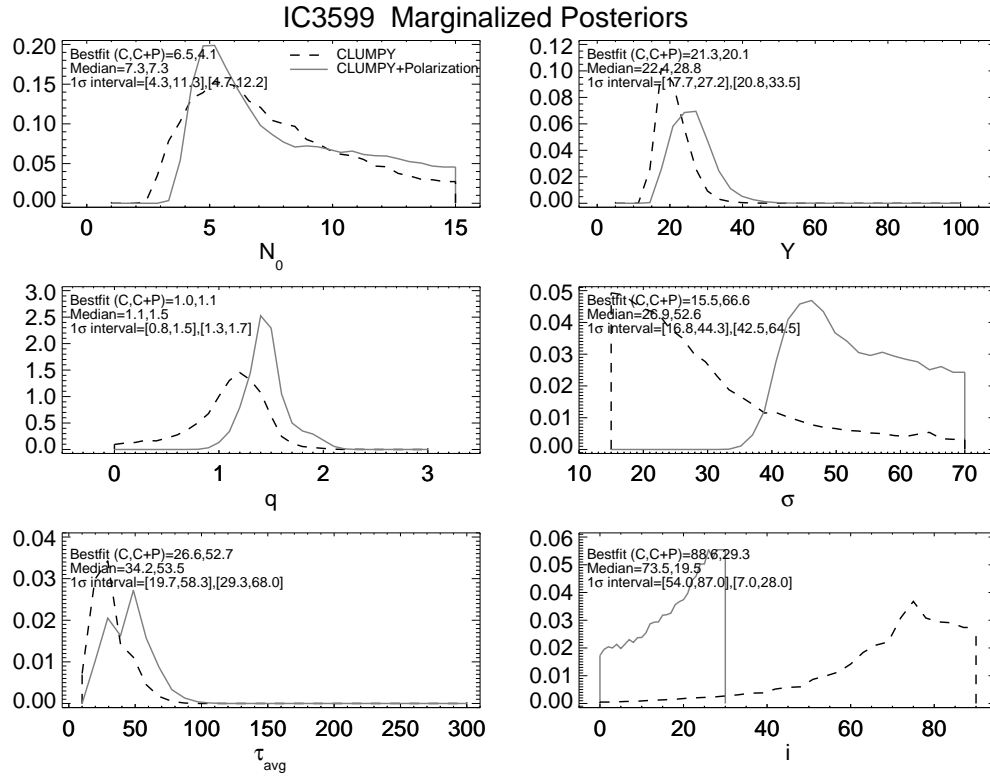
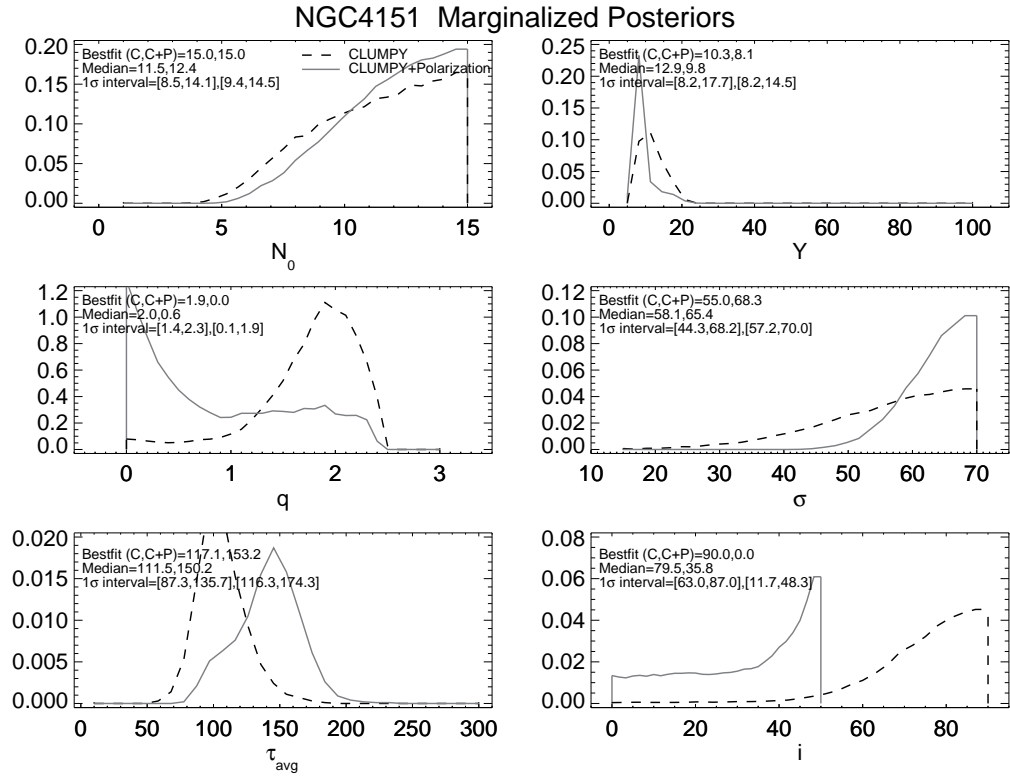


Figure A.1cc Same as Figure 7.19 but for IC 3599.



Data with CLUMPY and CLUMPY+Polarization Bestfits

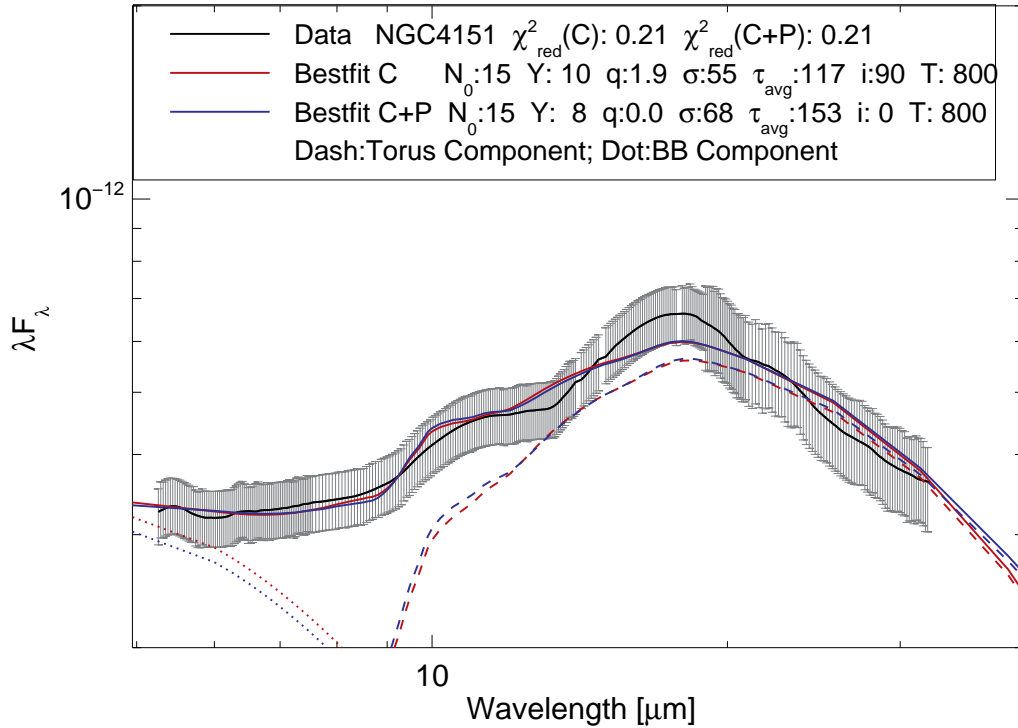
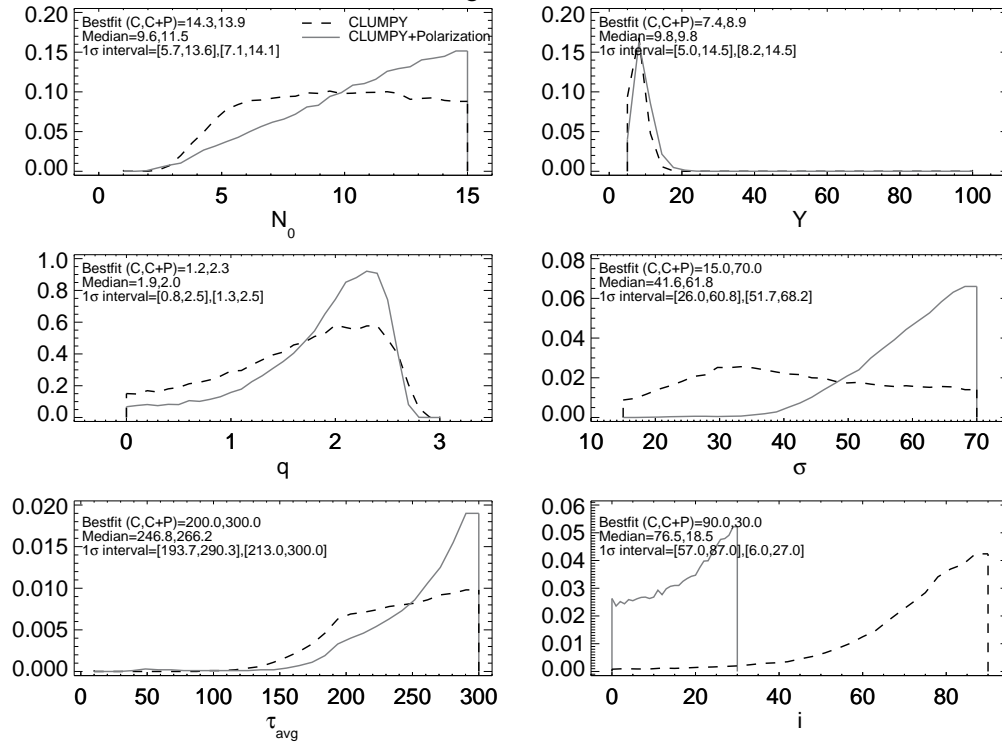


Figure A.1dd Same as Figure 7.19 but for NGC 4151.

PG1211 Marginalized Posteriors



Data with CLUMPY and CLUMPY+Polarization Bestfits

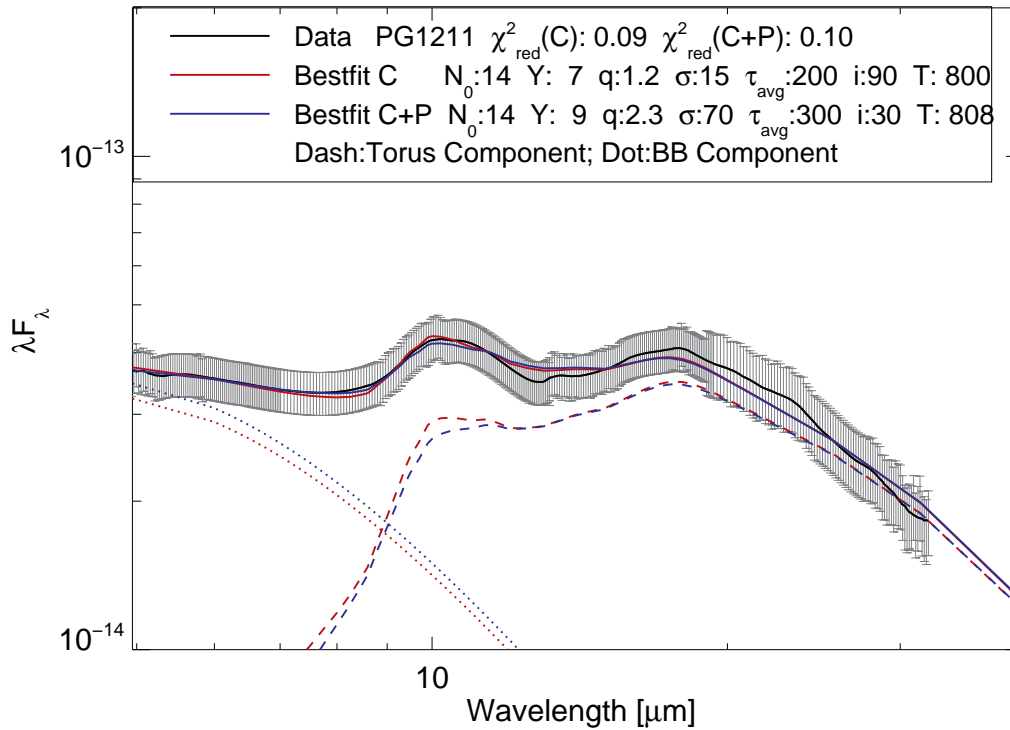
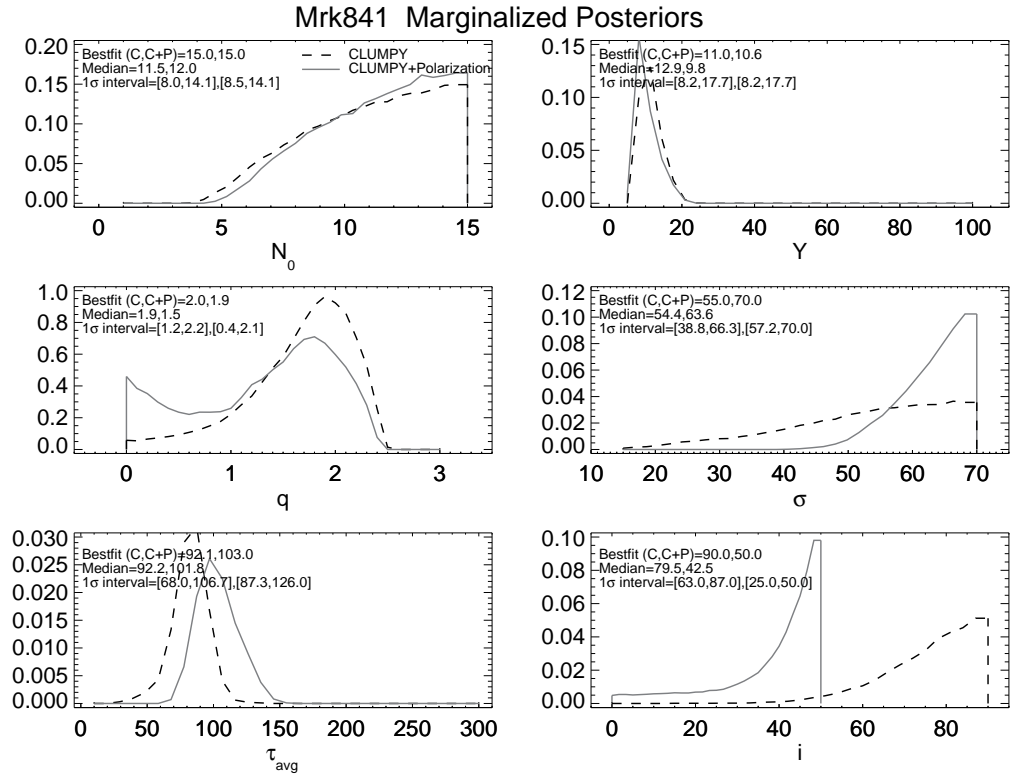


Figure A.1ee Same as Figure 7.19 but for PG 1211+143.



Data with CLUMPY and CLUMPY+Polarization Bestfits

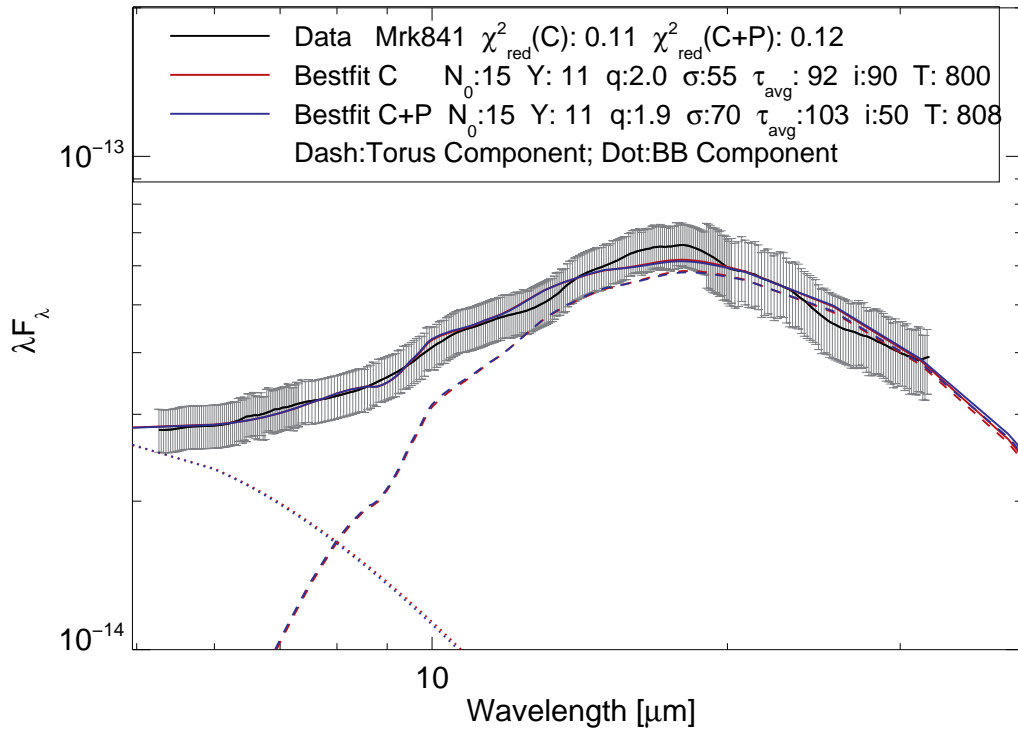
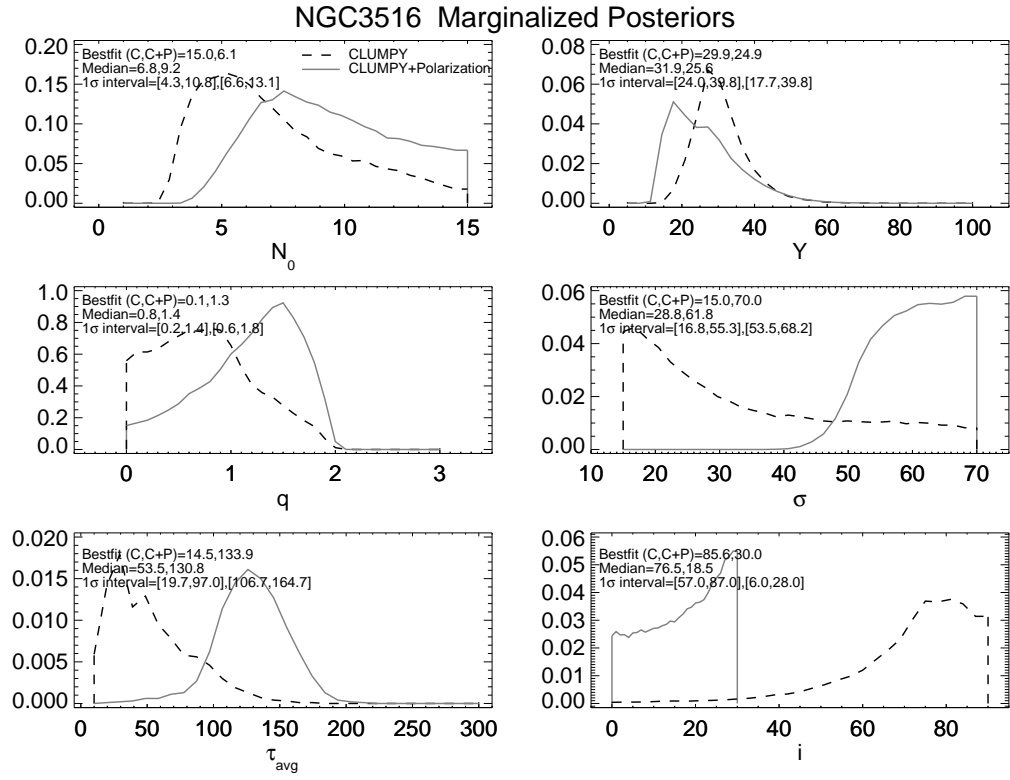


Figure A.1ff Same as Figure 7.19 but for Mrk 841.



Data with CLUMPY and CLUMPY+Polarization Bestfits

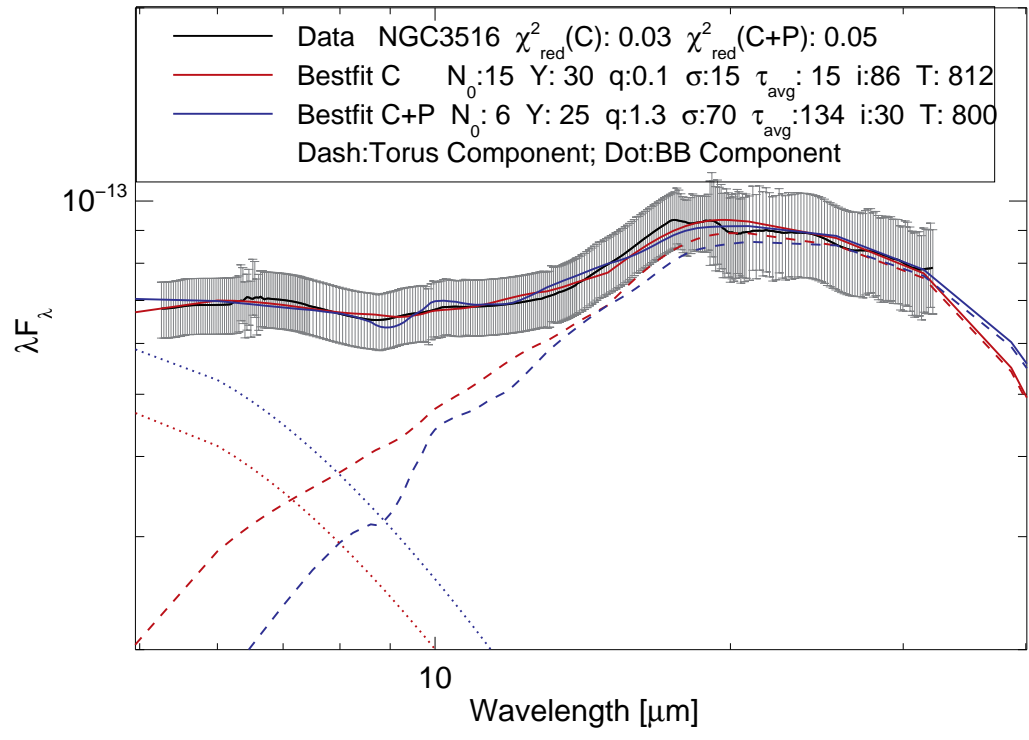
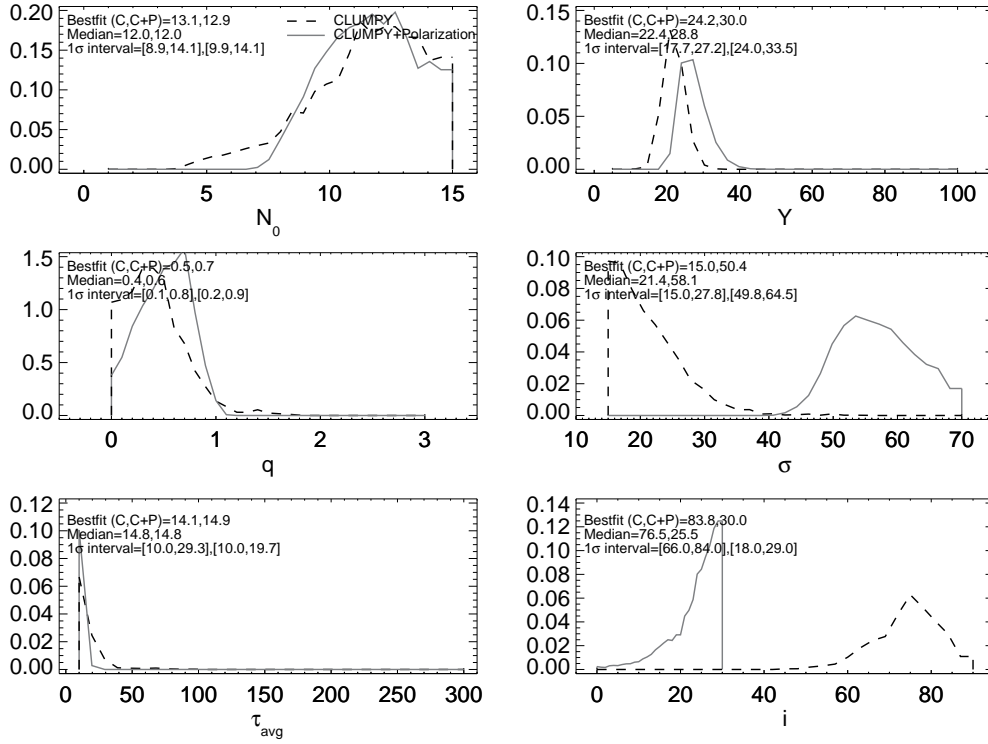


Figure A.1gg Same as Figure 7.19 but for NGC 3516.

PG1612 Marginalized Posteriors



Data with CLUMPY and CLUMPY+Polarization Bestfits

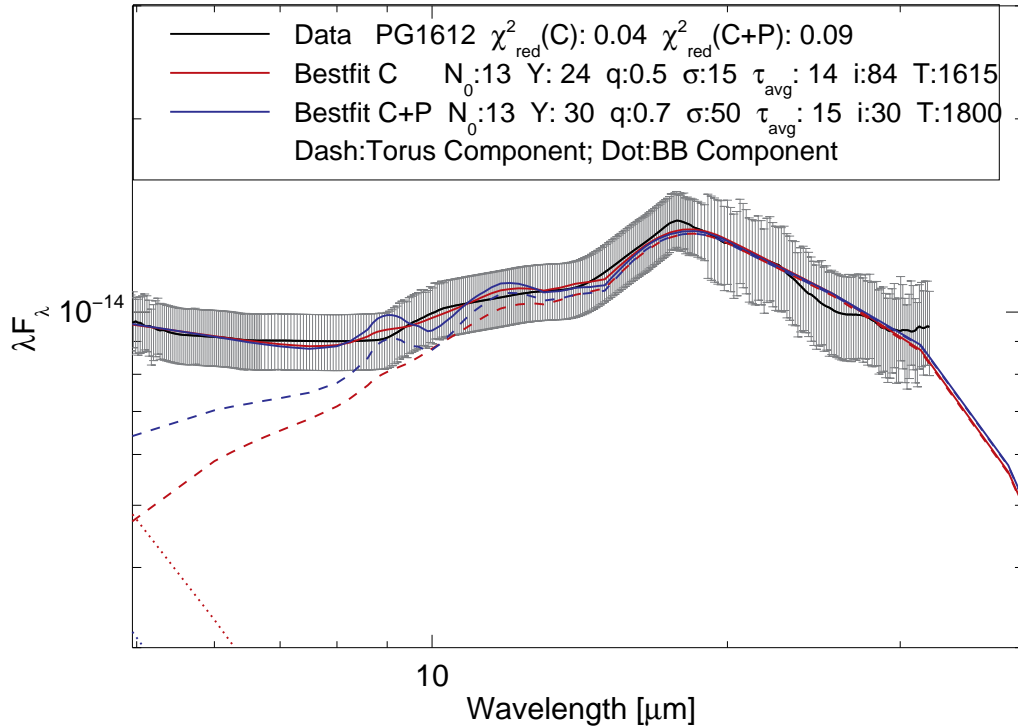


Figure A.1hh Same as Figure 7.19 but for PG 1612+261.

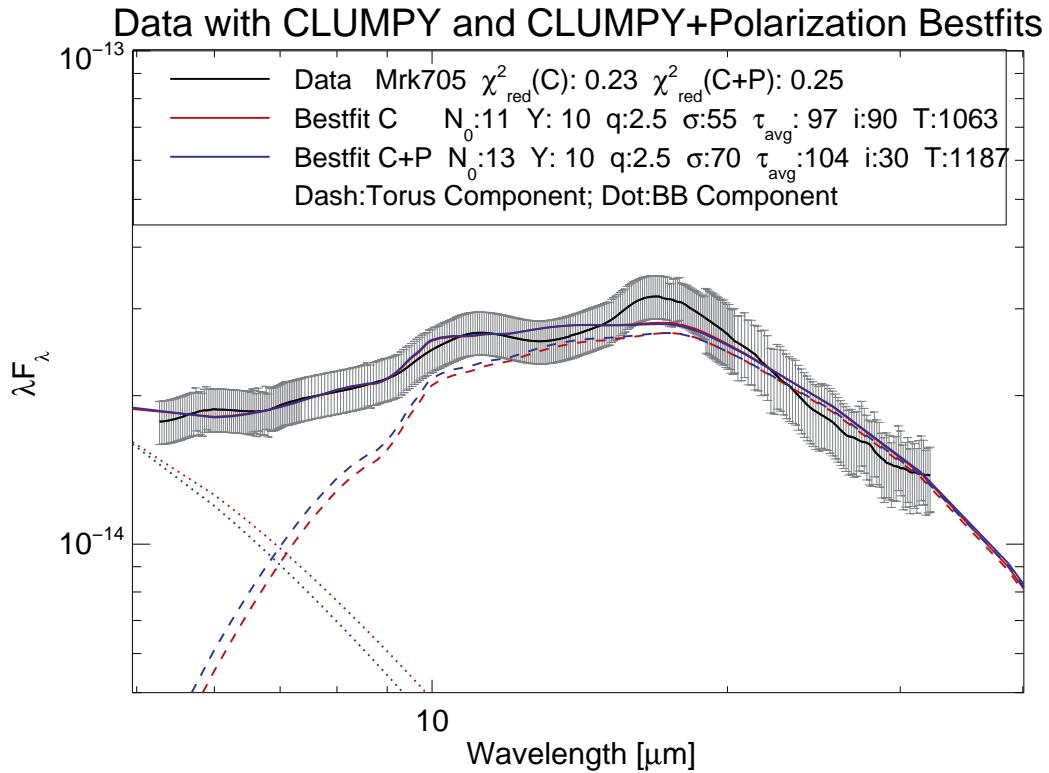
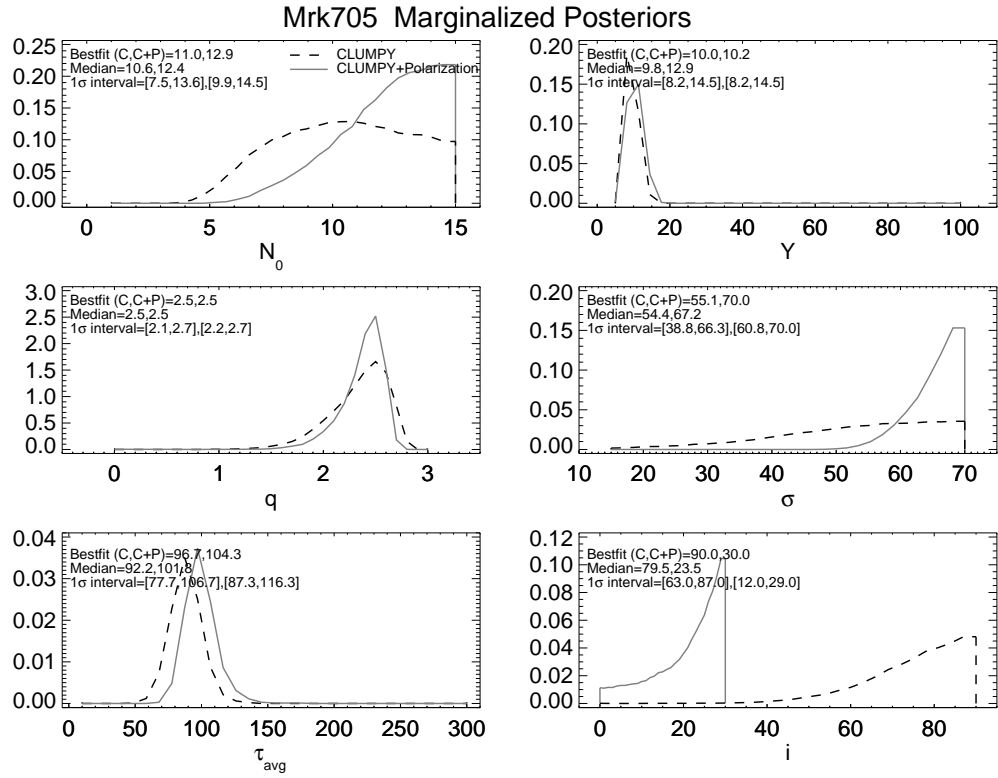


Figure A.1ii Same as Figure 7.19 but for Mrk 705.

A.2 Seyfert 2 Source Summaries

This section presents fitting results of the Seyfert 2 sources within our sample.

MCG -05-23-016 – Classification: Seyfert 2; Polarization class: Polar;

Percentage of overlapping area: 100%; See Figure A.2a

The exact best-fit models and posterior distributions are produced by fitting with and without prior polarization knowledge. The MIR emission of this source is fit well by models which have high inclination angles. Restricting the parameter range of i made no difference. The number of clouds encountered along angle i is nearly 15 clouds in this relatively compact, large scale height torus.

Mrk 463E – Classification: Seyfert 2; Polarization class: Polar;

Percentage of overlapping area: 100%; See Figure A.2b

The i posterior for both the C and C+P fits strongly favors high inclination angles. Since the best-fit models and the posteriors overlap nearly perfectly, polarization and MIR emission are in agreement. The fit models a torus which is somewhat compact whose opening angle is around 45° .

NGC 4388 – Classification: Seyfert 2; Polarization class: Polar;

Percentage of overlapping area: 100%; See Figure A.2c

The i posterior for both the C and C+P fits strongly favors high inclination angles. Like Mrk 463E, since the best-fit models and the posteriors overlap nearly perfectly, polarization and MIR emission are in agreement.

IRAS 05189-2524 – Classification: Seyfert 1; Polarization class: Polar;

Percentage of overlapping area: 100%; See Figure A.2d

Like the previous sources, both fitting methods yield the exact same result. However, this source is described by a spatially large torus, in both radius and scale height.

NGC 5252 – Classification: Seyfert 2; Polarization class: Polar;

Percentage of overlapping area: 99%; See Figure A.2e

The results of the C+P fit are in complete agreement with those of the C fit. The inclination angles are determined to be large, and using the median values of i , σ and N_0 show that an observer encounters many clouds for this compact torus.

IRAS 20210+1121 – Classification: Seyfert 2; Polarization class: Polar;

Percentage of overlapping area: 97%; See Figure A.2f

IRAS 20210+1121 is modeled by an extremely dense torus who strongly favors high values of i and σ . The MIR emission clearly identified the source as a type 2. The two fitting methods are consistent.

IRAS 18325-5926 – Classification: Seyfert 2; Polarization class: Polar;

Percentage of overlapping area: 87%; See Figure A.2g

The MIR analysis with and without polarization clues yield similar results. High i values are preferred in a compact torus with a small scale height and several clouds encountered in the direction i .

IC 5063 – Classification: Seyfert 2; Polarization class: Polar;

Percentage of overlapping area: 62%; See Figure A.2h

Polarization estimates are in accordance with the results of MIR emission. The chance of photons to escape from this small torus is essentially zero.

IRAS F15480-0344 – Classification: Seyfert 2; Polarization class: Polar;

Percentage of overlapping area: 55%; See Figure A.2i

The unrestricted fit's posteriors match those of the C+P fit. The polarization predictions are upheld by MIR emission. The torus in this source is extremely compact and optically thick.

IRAS 20460+1925 – Classification: Seyfert 2; Polarization class: Polar;

Percentage of overlapping area: 3%; See Figure A.2j

The MIR emission analysis shows that this source favors lower values of i for a compact torus. Though the posteriors show i tends toward 0, the best-fit model chose 34° which is just outside the range permitted by polarization. Since the limit is $i = 40^\circ$, the best-fit models are similar with differences in the posteriors arising from the limited models in the database. However, the posteriors yield the same general results for a compact torus with many clouds, and since both the C and C+P models describe the data well, we conclude that the two methods are in agreement.

NGC 7674 – Classification: Seyfert 2; Polarization class: Polar;

Percentage of overlapping area: 68%; See Figure A.2k

This is the first source in which the polarization restrictions influenced the i posterior distributions, and therefore they slightly tweaked the other posteriors. NGC 7674 favors inclination angles around 50° at least in the posteriors; however, the C fit prefers lower inclinations of which the C+P fit cannot attain. Since the C+P fit would like to describe the data in similar fashion as does C, it compensates with a completely different best-fit model but still produces the same overall posteriors as the C fit. Since both fits describe the data well and yield similar posteriors, the polarization and MIR emission are in agreement.

3C234 – Classification: Seyfert 2; Polarization class: Polar;

Percentage of overlapping area: 35%; See Figure A.2l

The i parameter slightly favors lower values, and imposing the restriction inhibits the C+P model to choose the same best-fit model as the C fit. σ is decreased in order to compensate for the increased i , yet both fits yield a few clouds encountered along direction i . Since a torus model can describe the source well and utilize the information provided by the polarization to do so, the MIR emission technique used to obtain inclination angles confirms that of polarization.

TOL 1238-364 – Classification: Seyfert 2; Polarization class: Polar;

Percentage of overlapping area: 20%; See Figure A.2m

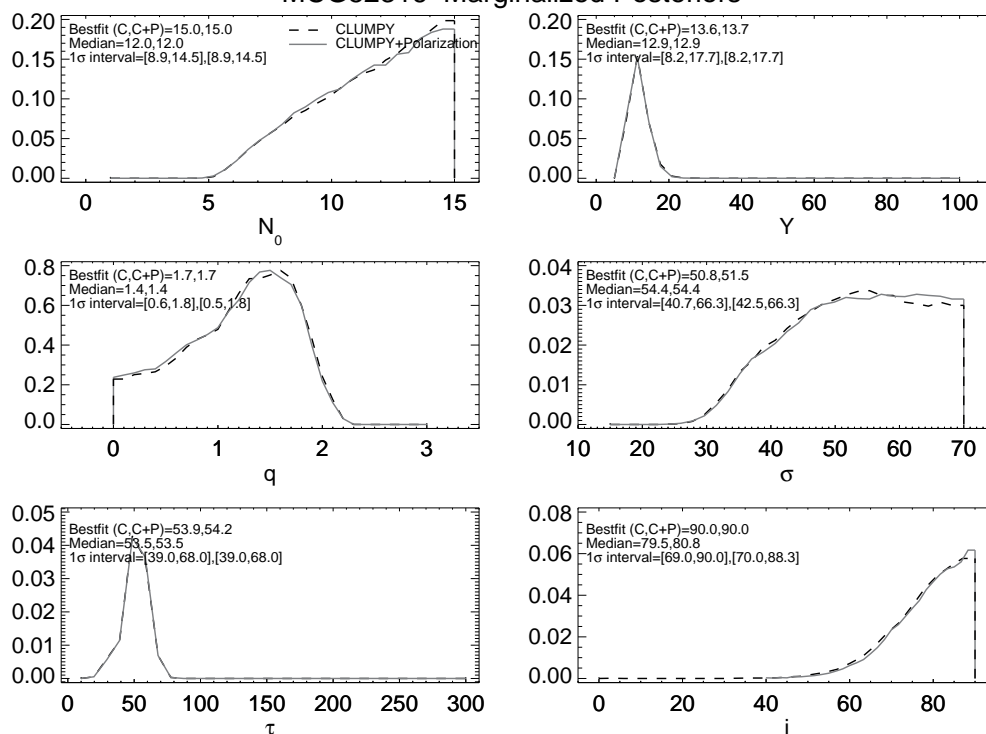
Polarization predictions are confirmed by MIR emission in this source since the χ_R^2 values of the C+P and C fits are similar and within the threshold value. The C fits obviously favored lower inclination values, and upon imposing the restriction, i favored the smallest values possible, those at the lower boundary. Though parameter values change with the different fits, the torus is described by both to be compact with a large scale height.

IRAS F04385-0828 – Classification: Seyfert 2; Polarization class: Polar;

Percentage of overlapping area: 0%; See Figure A.2n

This source has a strong silicate absorption feature, yet strongly prefers to be modeled by small inclination angles. Since the polarization estimates restrict $i > 40^\circ$, the C+P model chooses $i = 40^\circ$ to produce the same emission as the entire database's best-fit model. To reproduce a similar fit while encompassing the restriction, the C+P fitting techniques derives a model with completely different parameter values. As seen in the bottom SED comparisons, the two best-fit models are different but describe the data within $\chi_R^2 \leq 0.25$, so we say the two methods are in accordance with each other.

MCG52316 Marginalized Posteriors



Data with CLUMPY and CLUMPY+Polarization Bestfits

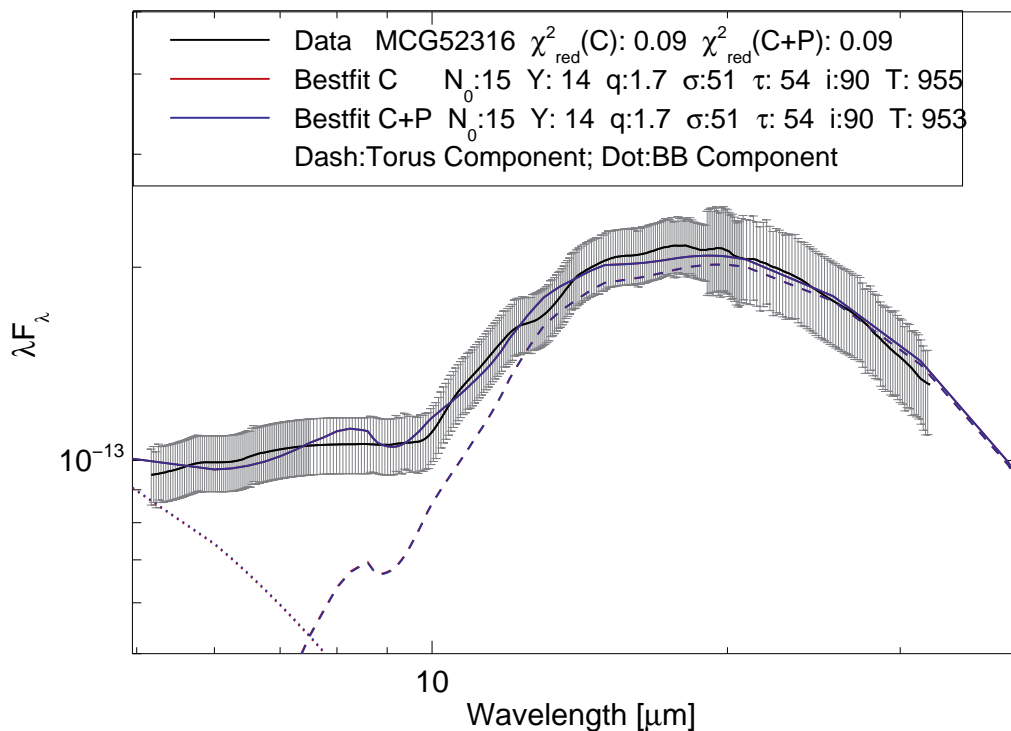
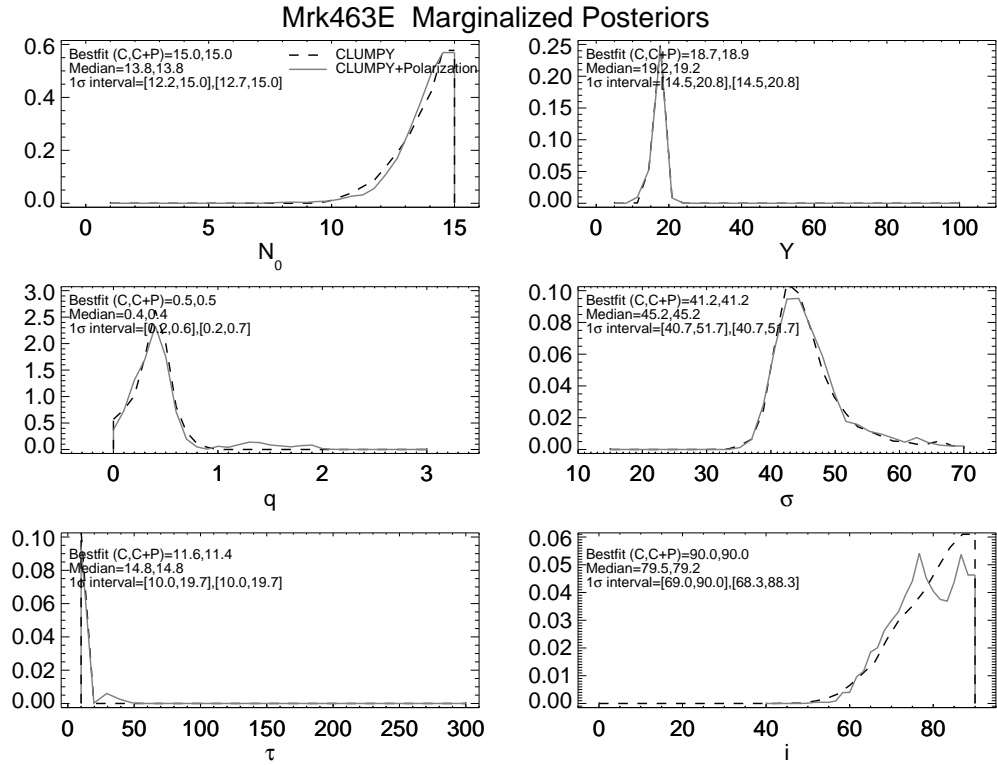


Figure A.2a Same as Figure 7.19 but for MCG -05-23-016.



Data with CLUMPY and CLUMPY+Polarization Bestfits

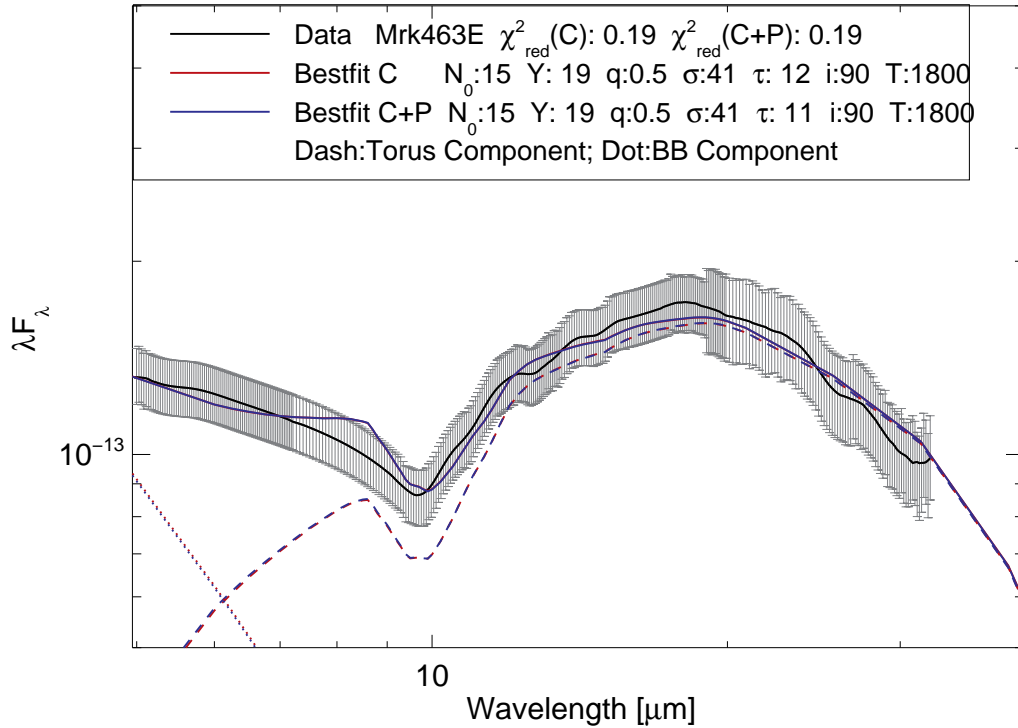
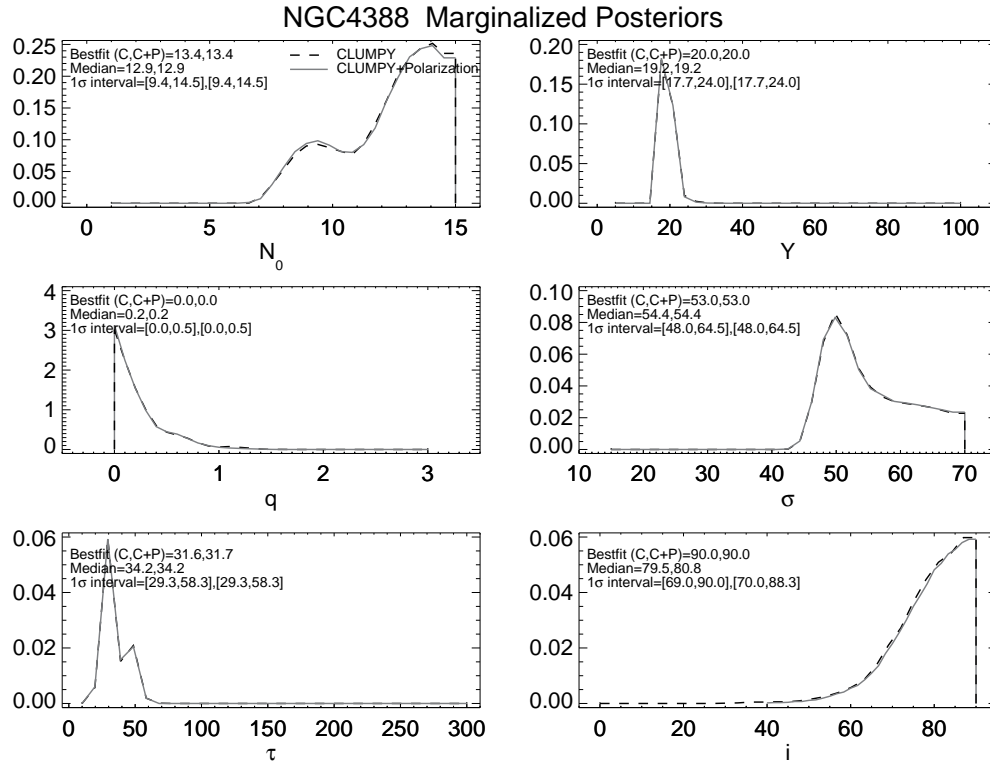


Figure A.2b Same as Figure 7.19 but for Mrk 463E.



Data with CLUMPY and CLUMPY+Polarization Bestfits

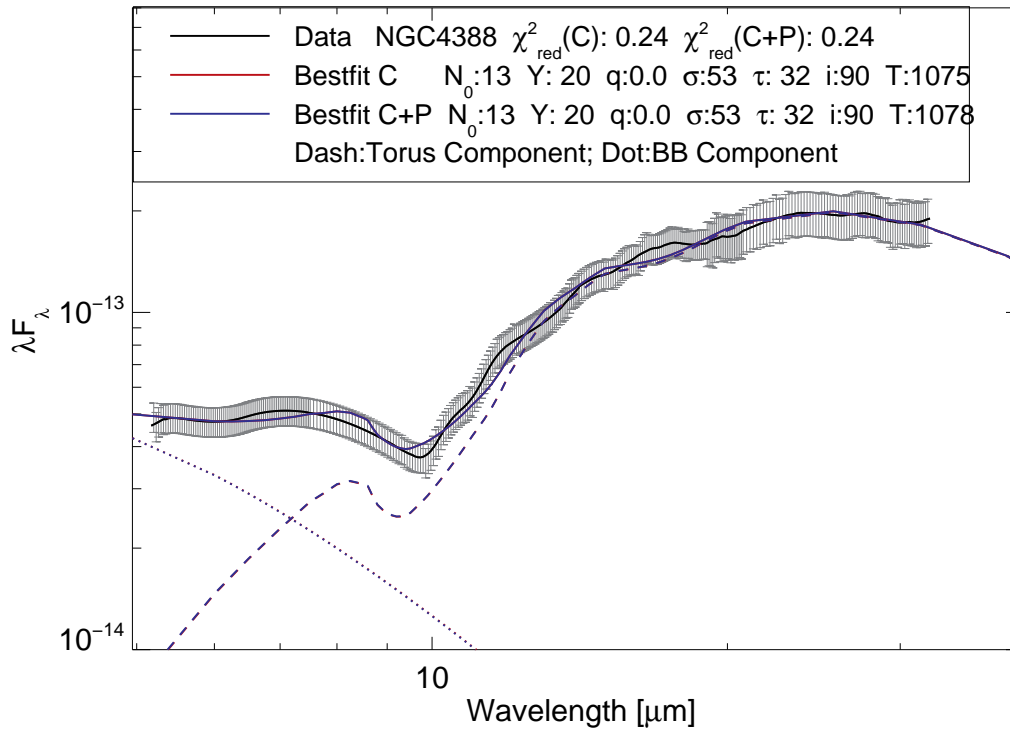
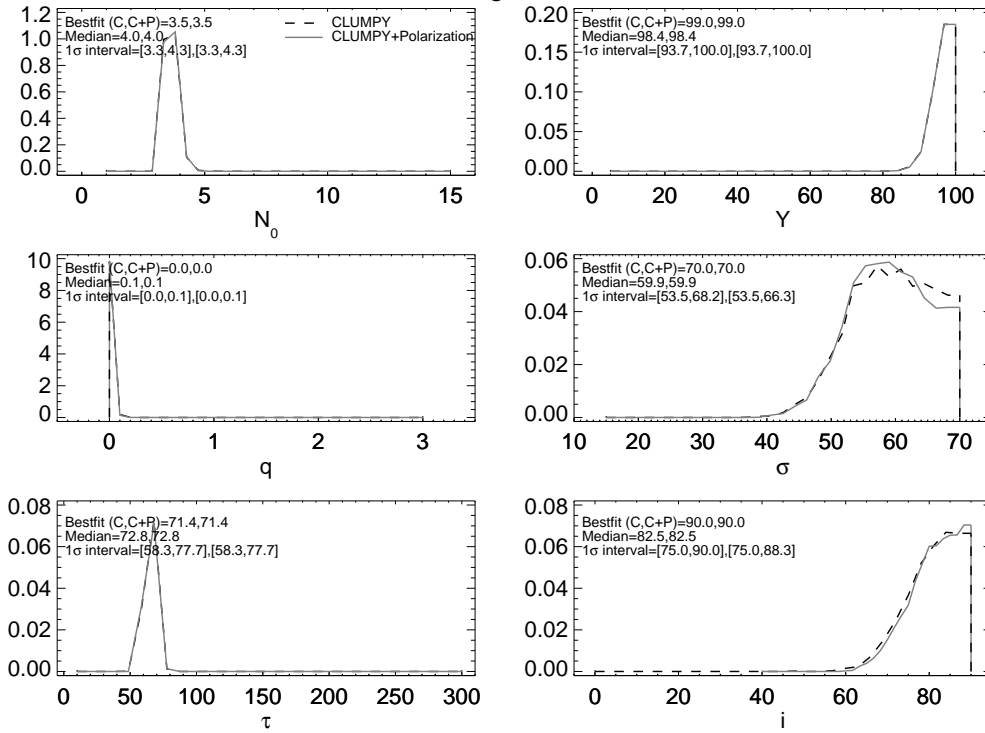


Figure A.2c Same as Figure 7.19 but for NGC 4388.

IRAS05189 Marginalized Posteriors



Data with CLUMPY and CLUMPY+Polarization Bestfits

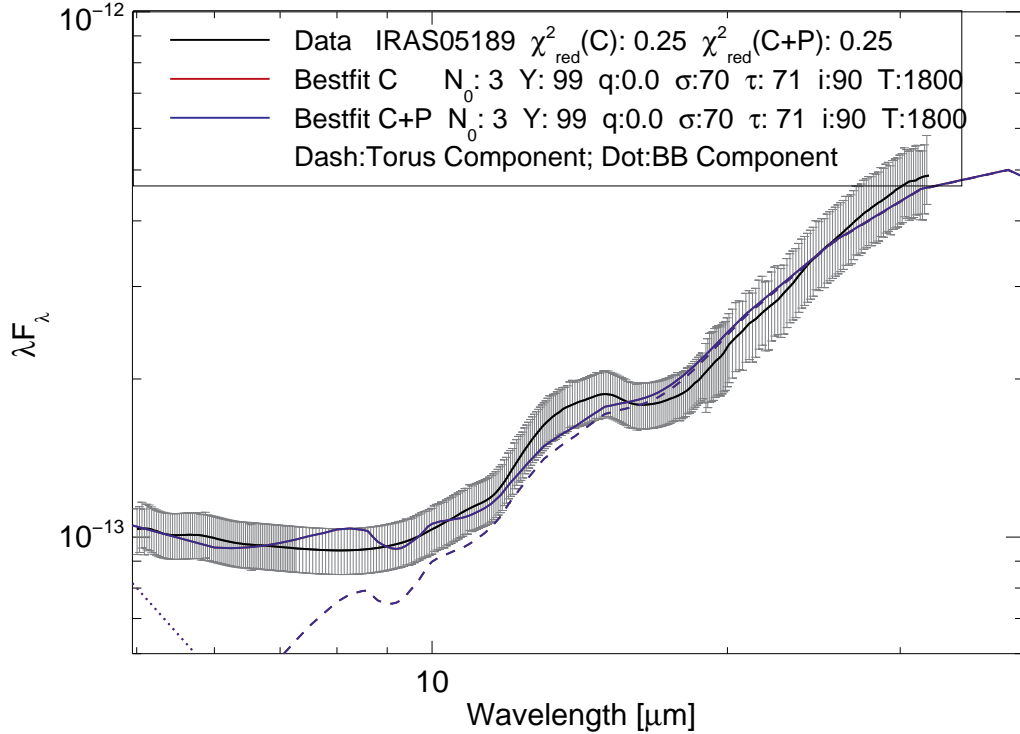
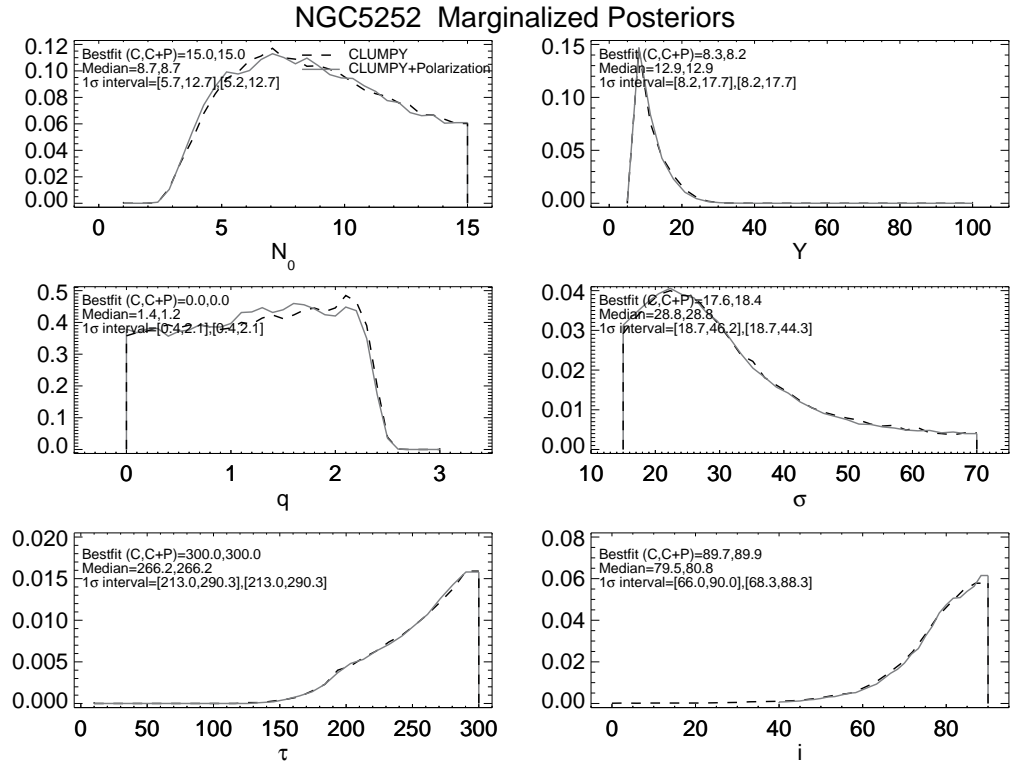


Figure A.2d Same as Figure 7.19 but for IRAS 05189-2524.



Data with CLUMPY and CLUMPY+Polarization Bestfits

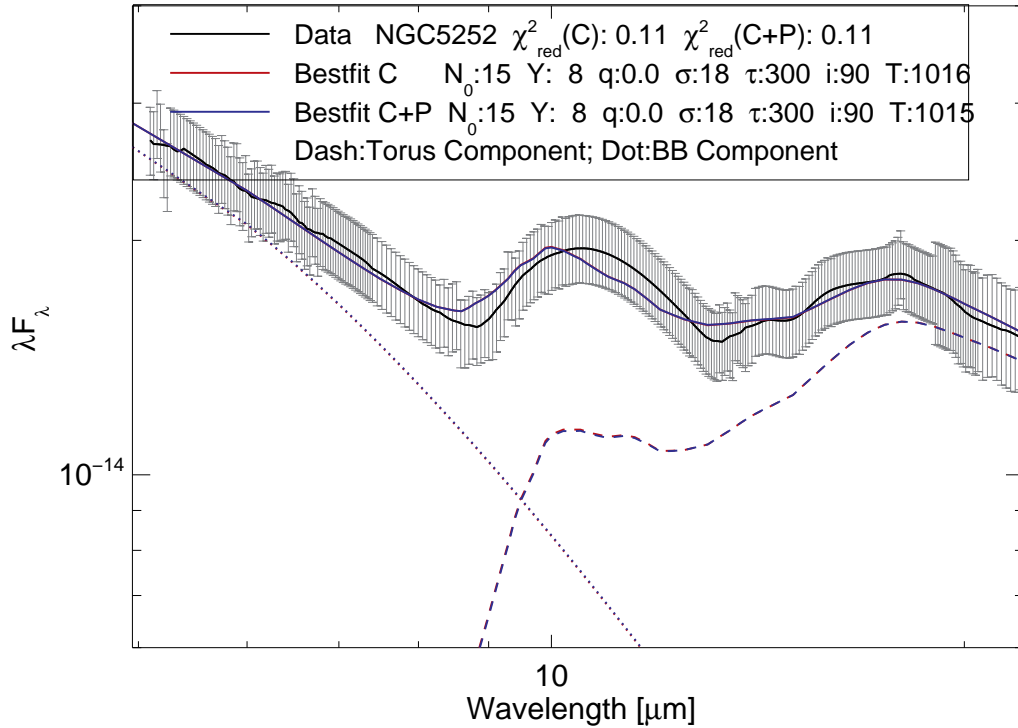
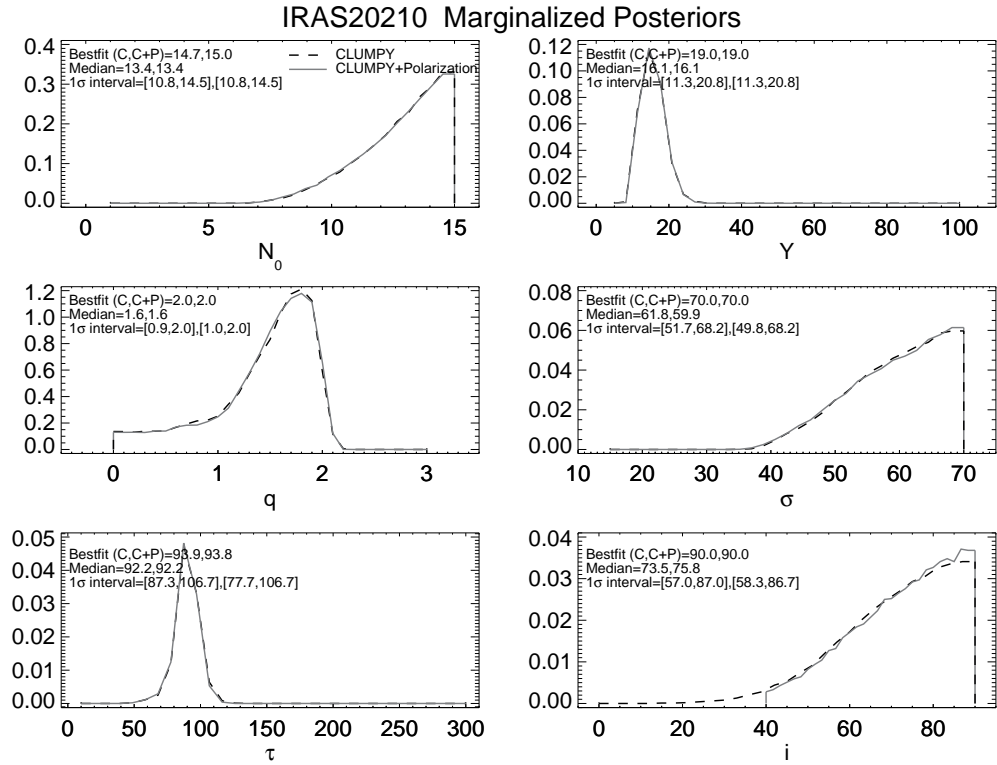


Figure A.2e Same as Figure 7.19 but for NGC 5252.



Data with CLUMPY and CLUMPY+Polarization Bestfits

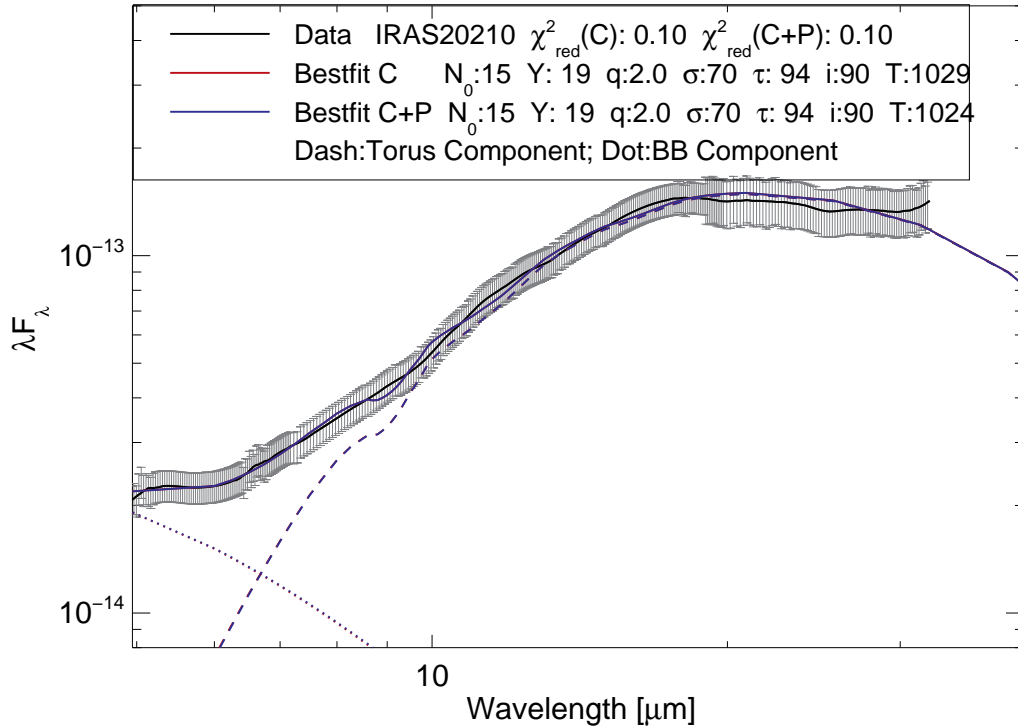
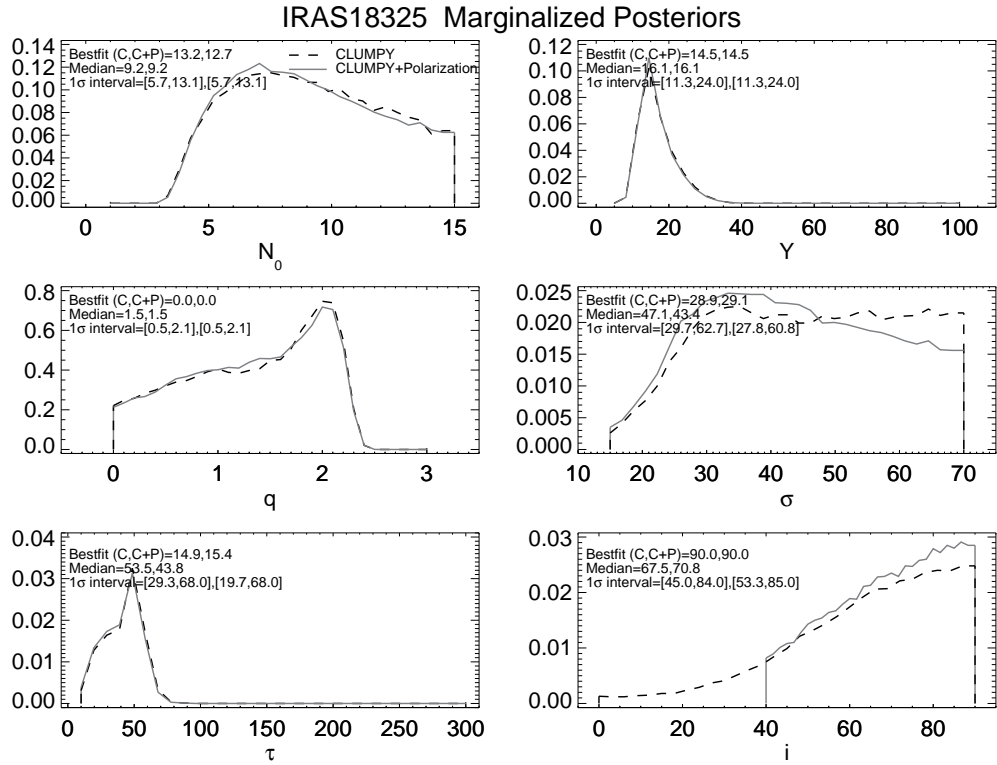


Figure A.2f Same as Figure 7.19 but for IRAS 20210+1121.



Data with CLUMPY and CLUMPY+Polarization Bestfits

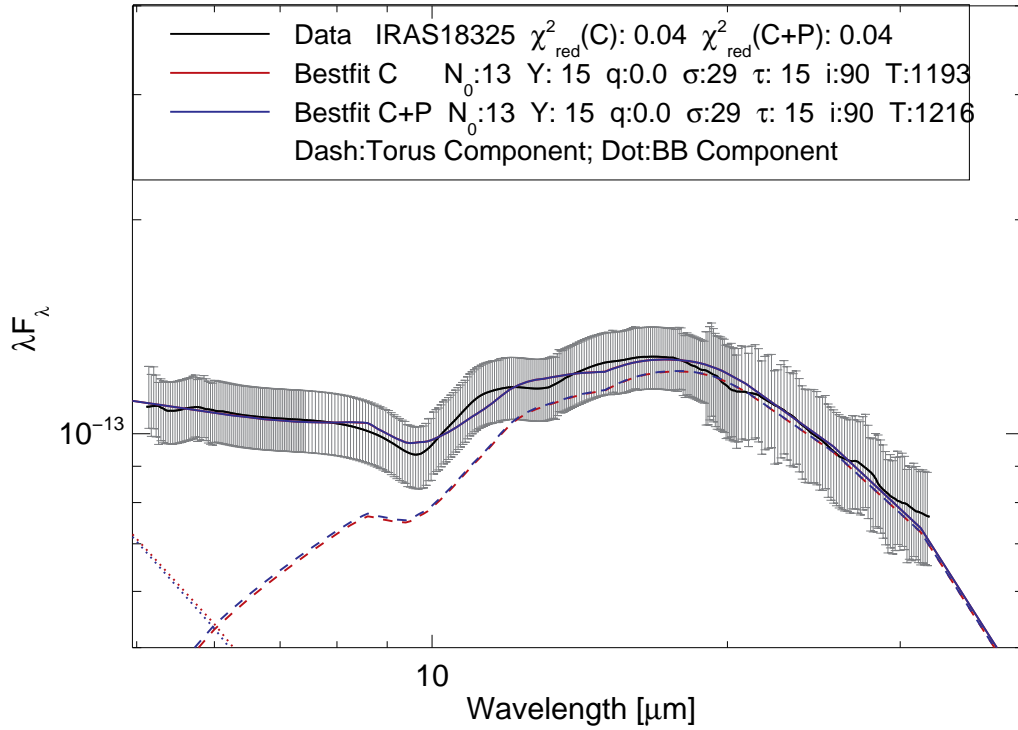
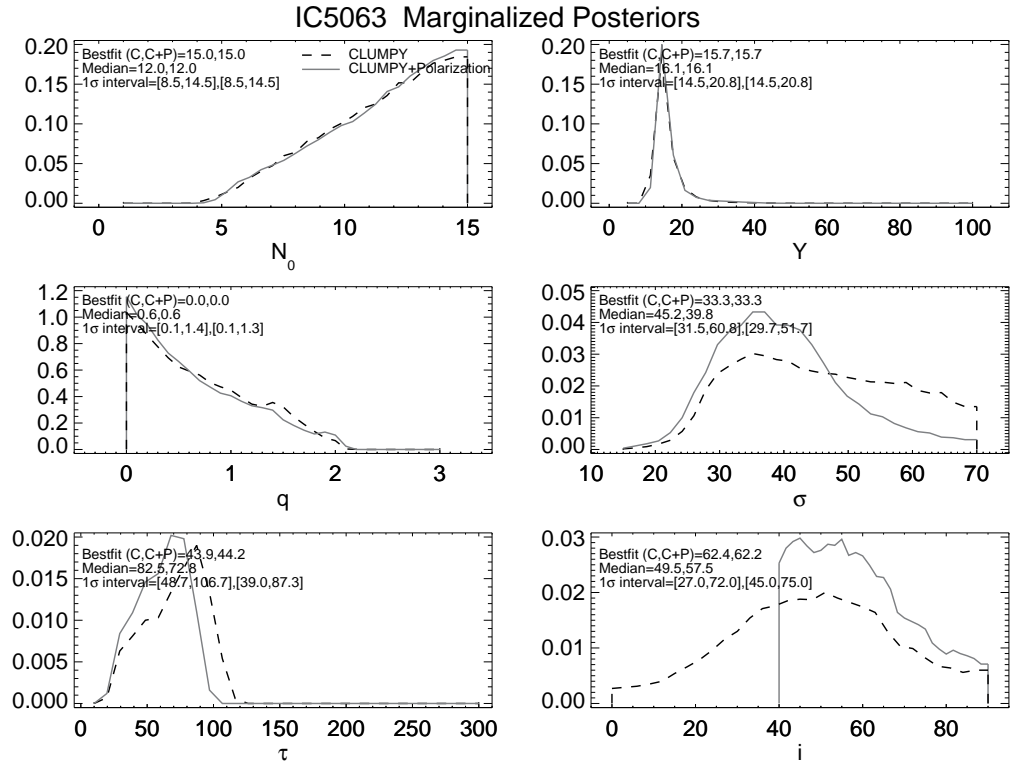


Figure A.2g Same as Figure 7.19 but for IRAS 18325-5926.



Data with CLUMPY and CLUMPY+Polarization Bestfits

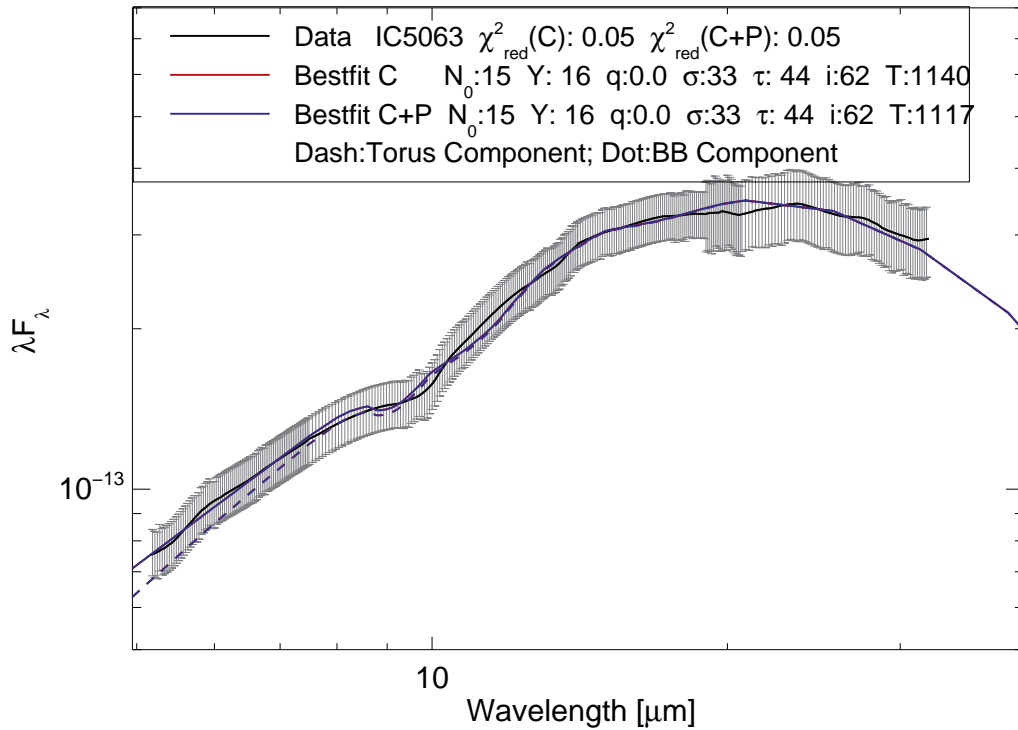
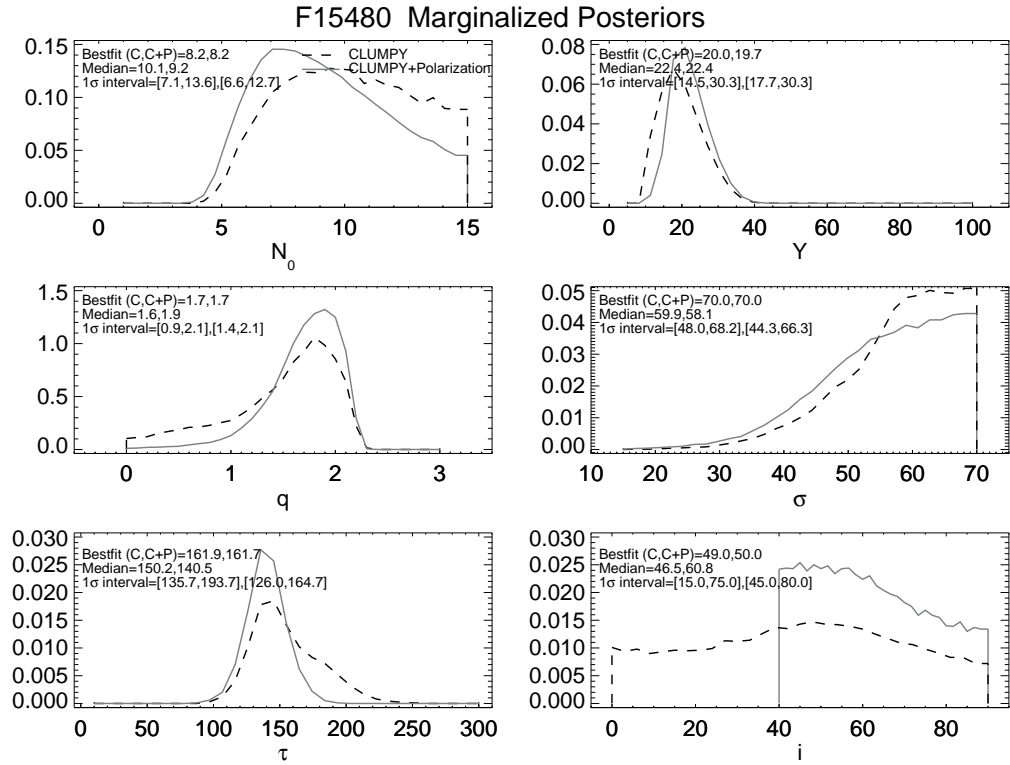


Figure A.2h Same as Figure 7.19 but for IC 5063.



Data with CLUMPY and CLUMPY+Polarization Bestfits

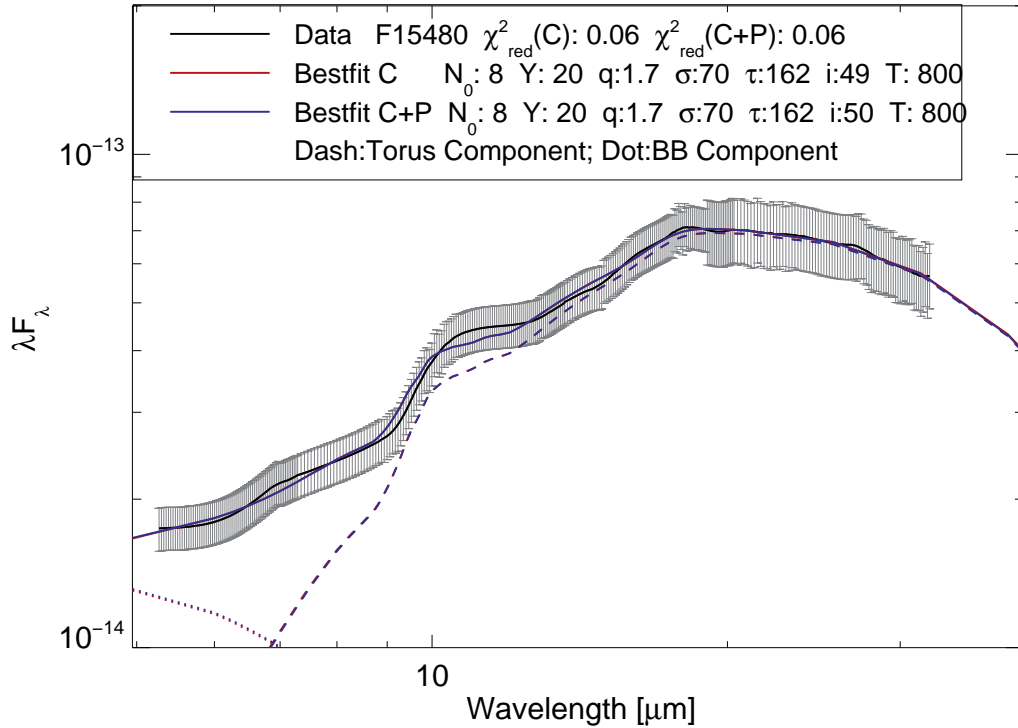
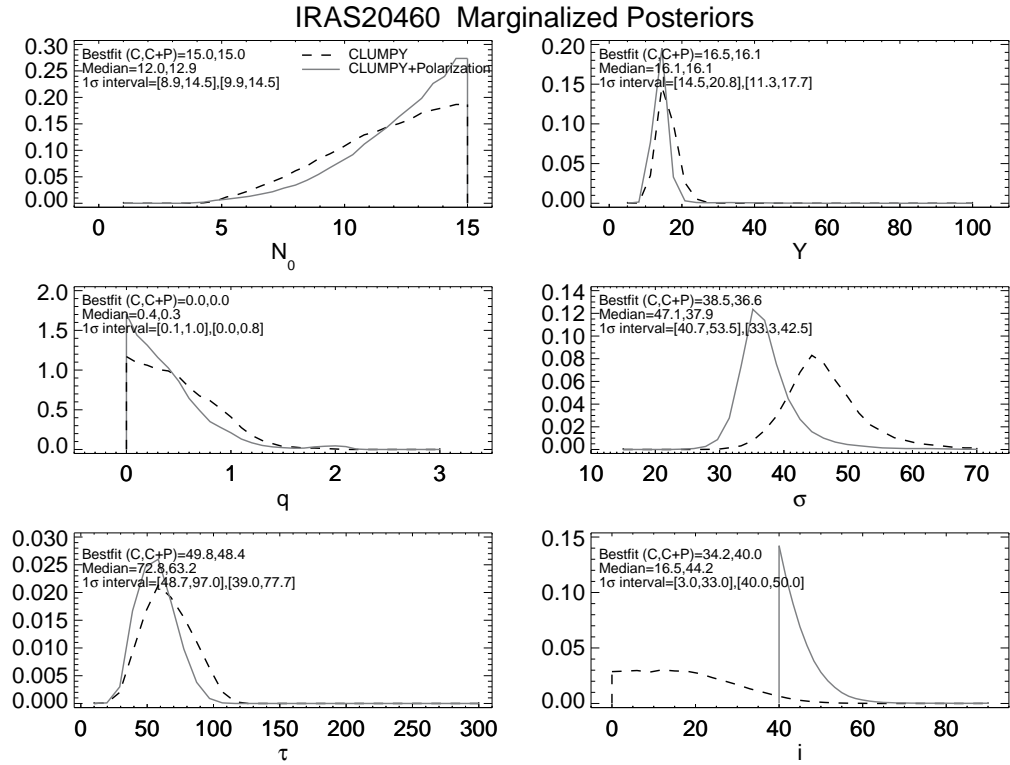


Figure A.2i Same as Figure 7.19 but for IRAS F15480-0344.



Data with CLUMPY and CLUMPY+Polarization Bestfits

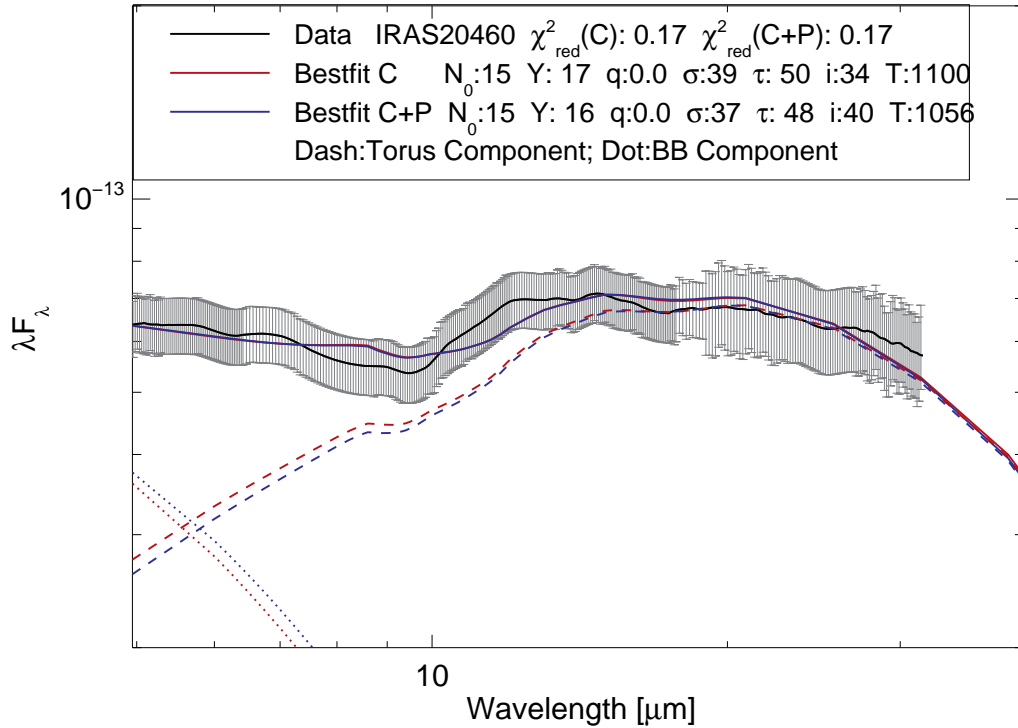
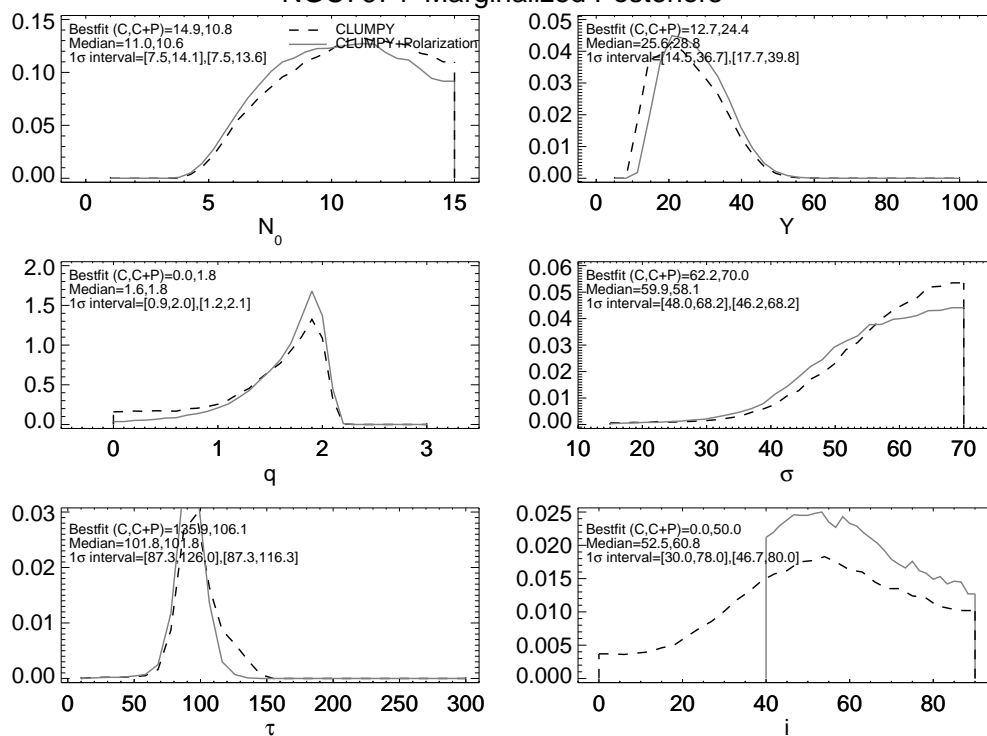


Figure A.2j Same as Figure 7.19 but for IRAS 20460+1925.

NGC7674 Marginalized Posteriors



Data with CLUMPY and CLUMPY+Polarization Bestfits

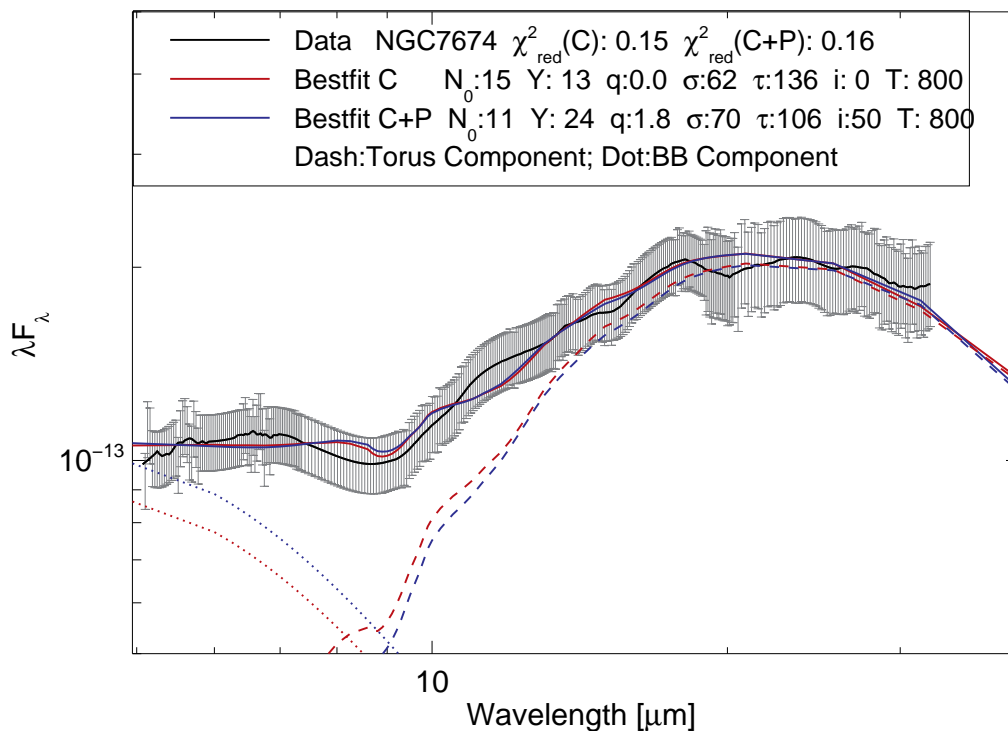


Figure A.2k Same as Figure 7.19 but for NGC 7674.

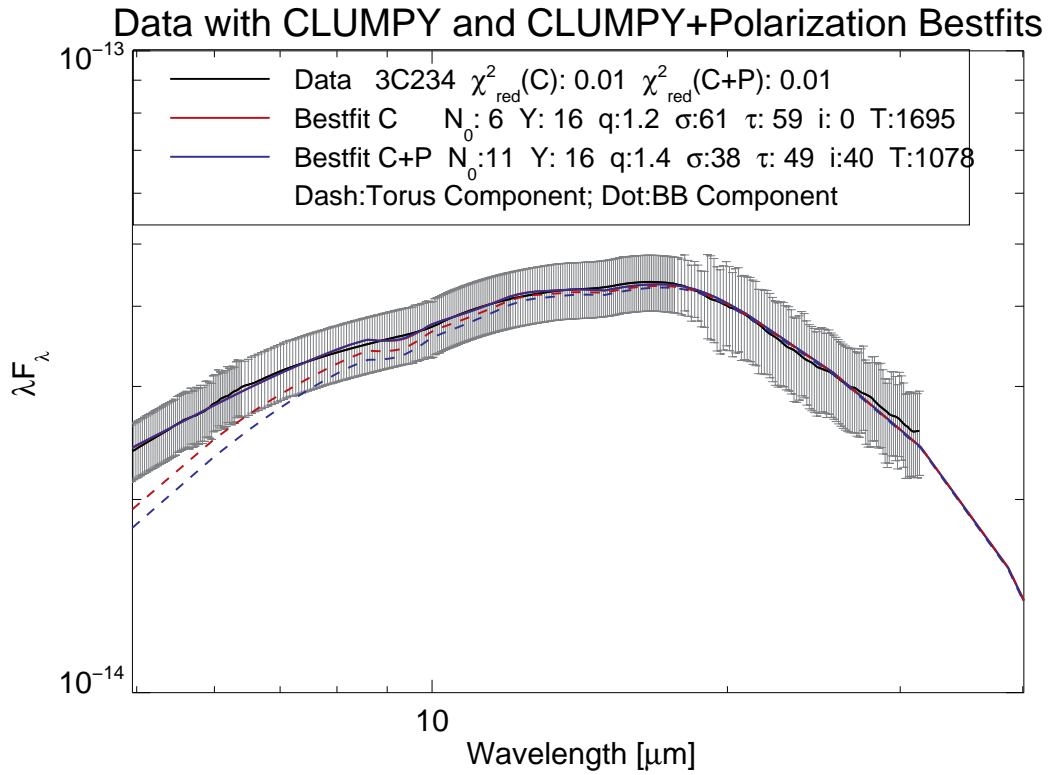
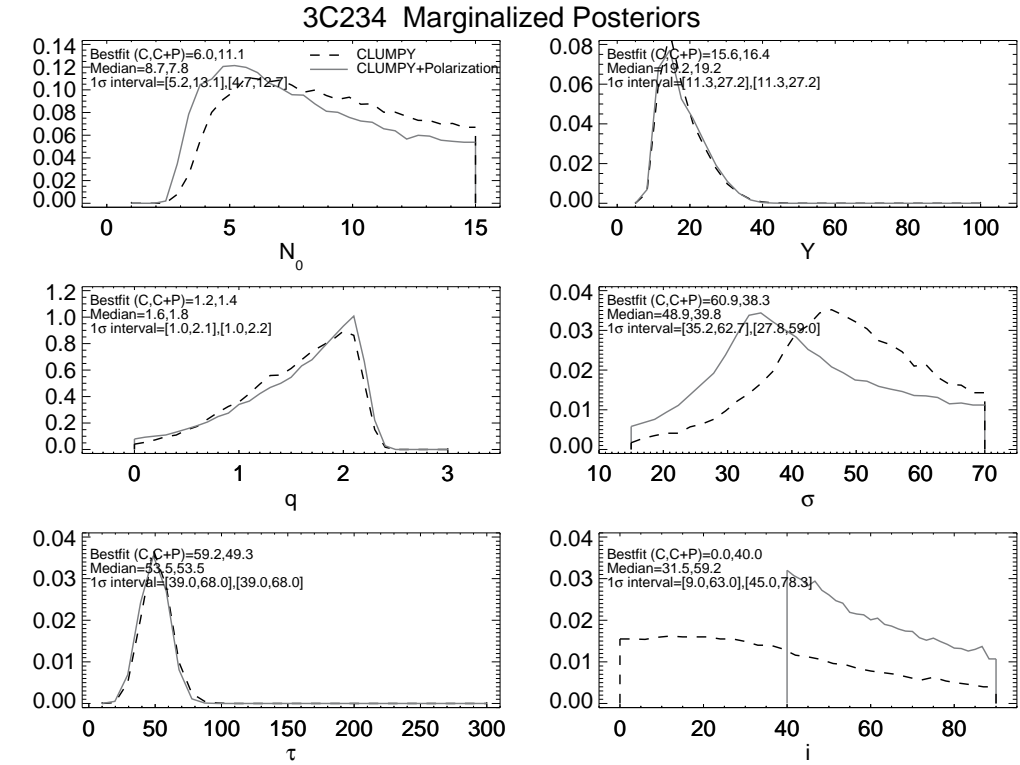
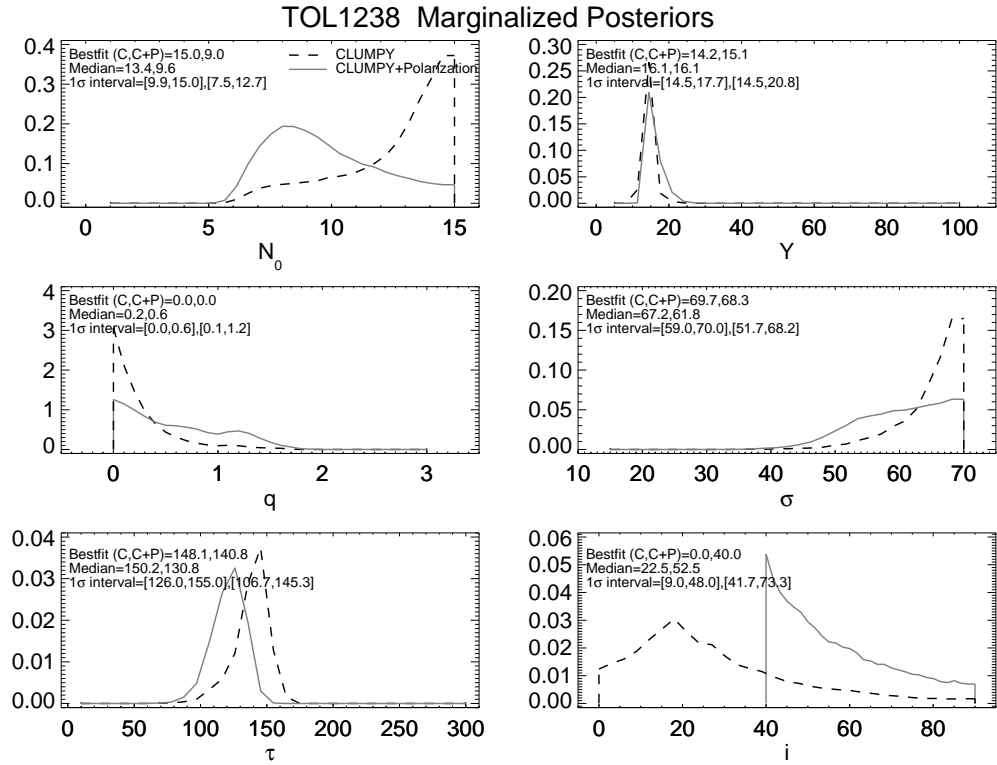


Figure A.2| Same as Figure 7.19 but for 3C234.



Data with CLUMPY and CLUMPY+Polarization Bestfits

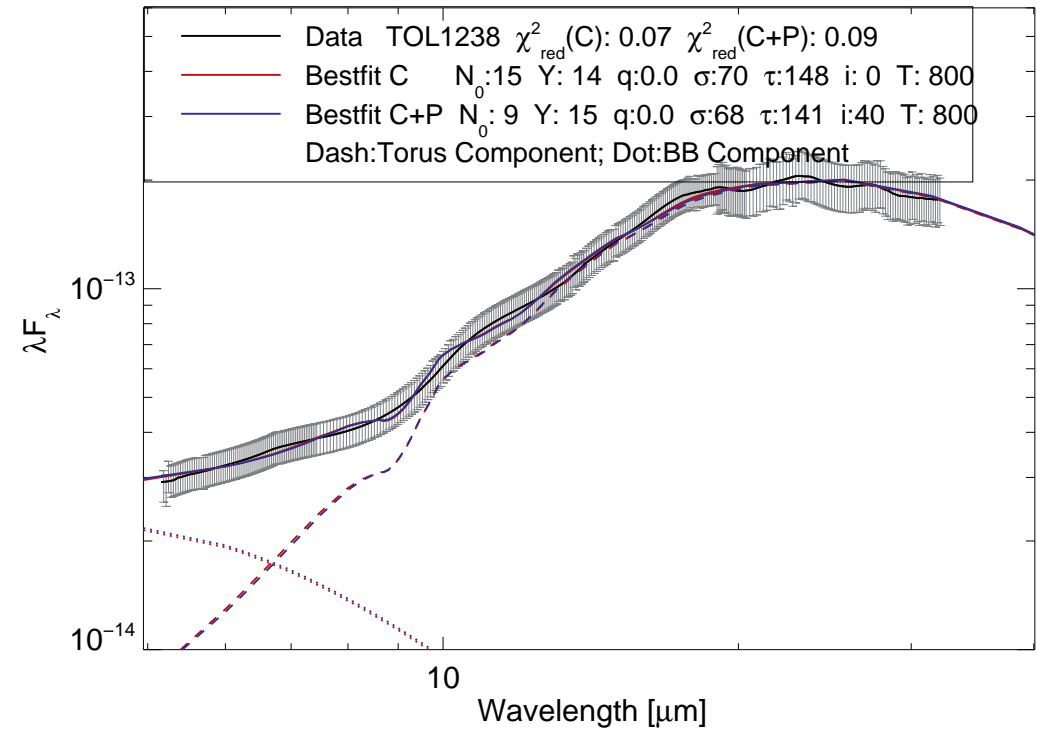
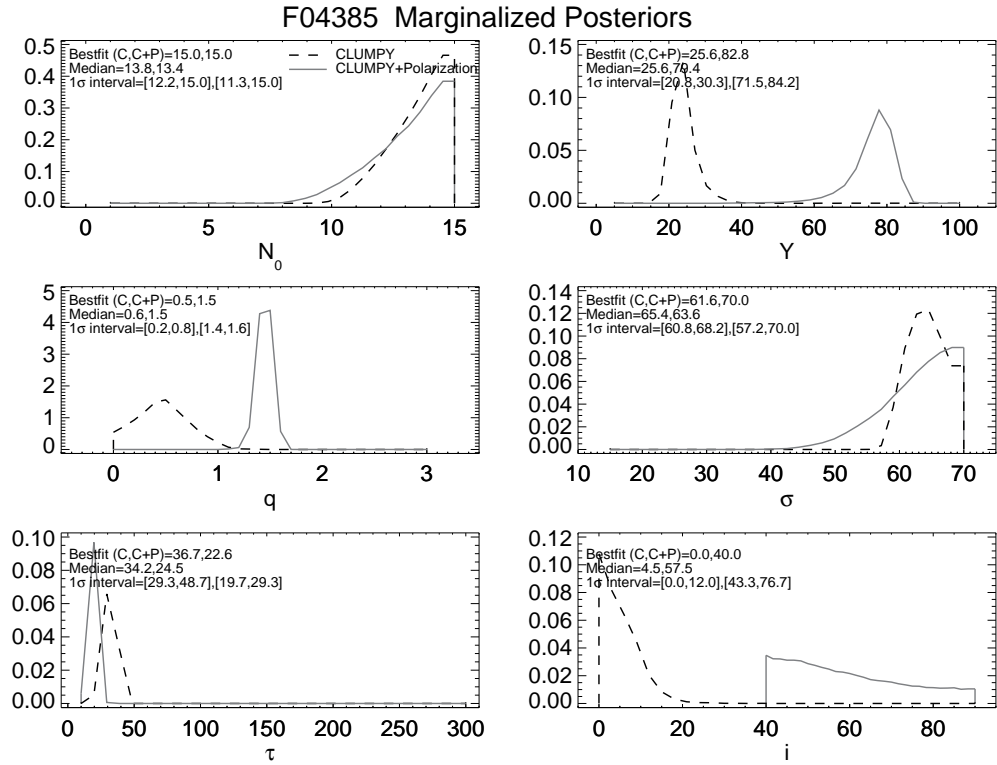


Figure A.2m Same as Figure 7.19 but for TOL 1238-364.



Data with CLUMPY and CLUMPY+Polarization Bestfits

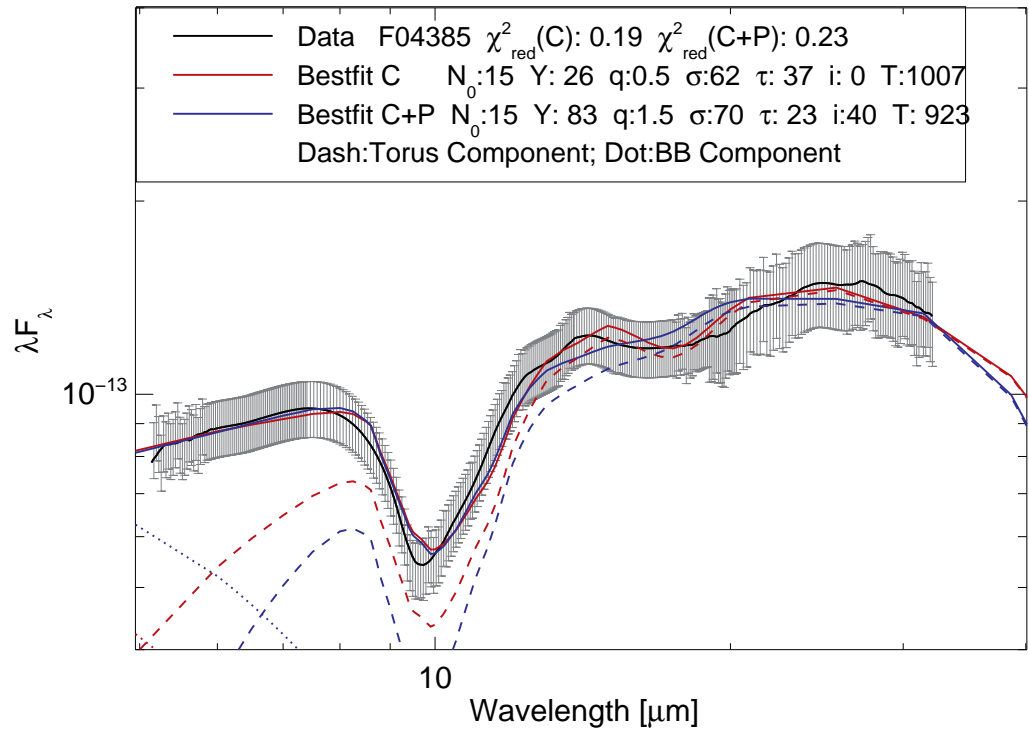


Figure A.2n Same as Figure 7.19 but for IRAS F04385-0828.

A.3 Poorly Fit Sources

Of our sample of 41 Seyfert 1 sources and 20 Seyfert 2s, only 36 of the former and 14 of the latter could be described well ($\chi_R^2 \leq 0.25$) by CLUMPY torus models. For each of the remaining 11 sources, a reason exists as to why the sources could not be fit, and we describe each source in this section.

Mrk 231 – See Figure A.3a.

The best-fit model chosen to characterize the torus has $\chi_R^2 = 0.47$, thus this source is not well described by the models. This type 1 source appears to have strong silicate absorption features with strengths $S_{10} = -0.503$ and $S_{18} = -0.284$, which the torus models have difficulty in reproducing. The CLUMPY models, by the inherent distribution of clouds in a clumpy geometry that allows views of hot cloud faces through many viewing situations, never produce deep silicate absorption features, and for this reason, Mrk 231 is not fit successfully.

Mrk 507 – See Figure A.3b.

This type 1 source had limited *Spitzer* observations thus our wavelength range is restricted between 5-19 μm . Though the star formation template removal process rid only 1% of the total flux, the shorter wavelength PAH features were deleted and the long wavelength emission lowered. Even so, there tends to be a slight hint of a broad PAH residual present near 11 μm and another at 17 μm . These together may alter the shape of the spectrum in such a way to prohibit the models to acceptably describe the torus.

Mrk 509 – See Figure A.3c.

When fit by the clumpy torus SEDs, the model that best describes the MIR emission does so with a $\chi_R^2 = 0.39$, a value that exceeds the threshold defined to describe a ‘well-fit’ model. This source appears to have strong emission peaks near 10 and 18 μm , which are attributed to silicate dust. Calculating the silicate strengths for

this source, we found $S_{10} = 0.203$ and $S_{18} = 0.127$ for each feature respectively, which is not out of the ordinary for strength values. Though crucial detail was involved in removing the star formation component from this source, of which we found contributed nearly 12% of the total emission, it is possible that the broad 17 μm PAH band was not completely removed. This potentially remaining PAH feature in combination with the long wavelength emission that was decreased as the star formation template was removed may lead to the unordinary spectral shape that cannot be described by SEDs that model torus emission. It is also possible that this source is one that has strong 18 μm emission that the torus models cannot explain, such as NGC 3281 and NGC 7582 of Ramos Almeida et al. (2011) whom also attempt to fit clumpy torus models to Seyfert SEDs.

NGC 3227 – See Figure A.3d.

The silicate features for this type 1 source are in weak and intense emission for the 10 and 18 μm features respectively, with $S_{10} = 0.067$ and $S_{18} = 0.209$. Like Mrk 509, the 18 μm region of this spectrum is dominant with the torus models unable to explain ($\chi_R^2 = 0.57$) the strong emission. Ramos Almeida et al. (2009) examined this source and similarly found a virtually absent 10 μm feature, though they did not have 18 μm data to confirm our results.

NGC 7213 – See Figure A.3e.

A type 1 source whose original flux was $\sim 17\%$ star formation contributed, NGC 7213 has very strong silicate emission features, $S_{10} = 0.600$, $S_{18} = 0.203$. The star formation removal removed long wavelength emission, causing the spectral shape to appear fluctuating. Including the blackbody component to represent the hot dust component within the torus' sublimation radius, the best fit model has $\chi_R^2 = 0.62$, outside of the threshold for a 'good fit', but still somewhat imitating the shape of the spectrum.

In addition to the Seyfert 1 sources, 6 of 20 Seyfert 2s could not be modeled by our CLUMPY torus SEDS. A large reason these sources lacked the ability to be de-

scribed well by the models lay in their shapes, i.e., the spectral shapes are not those of AGNs. It is likely that some of these sources are dominated by emission from star formation, or perhaps there is contaminating emission along the line-of-sight to the galaxy leading to the non-AGN-like spectral shapes. We have ground-based spectroscopy available for some of these sources (See Section 7.3), and we will see that the high-resolution ground-based observations, which capture what is believed to be mostly AGN emission, do not always agree with the observations of *Spitzer*. This points out that the large aperture *Spitzer* observations gather quite more than the central AGN emission, and this addition flux from the host galaxy can distort the spectra.

3C321 – See Figure A.3f.

There appears to be an emission peak near $15 \mu\text{m}$ for this source whose fit of $\chi_R^2 = 0.40$ is not acceptable. This peak may stand out simply because the $18 \mu\text{m}$ feature is slightly absorbed, as the best model predicts. In this case, enhanced absorption is expected near $10 \mu\text{m}$ though no data is present as any star formation presence near the $7.7 \mu\text{m}$ PAH was deleted when the nearly one quarter of the original flux star formation contribution was removed.

NGC 1068 – See Figure A.3g.

The archetypal Seyfert 2 cannot be described well by the CLUMPY torus models, though this statement is limited to a *Spitzer* analysis, as authors have examined this source using ground based observations (Mason et al., 2006; Alonso-Herrero et al., 2011). Upon comparing *Spitzer* spectroscopy to the *Gemini* observations of Mason et al. (2006); Alonso-Herrero et al. (2011) we find that the spectral shapes are not in agreement. That is to say, the large aperture *Spitzer* observations capture much more than the nuclear emission than *Gemini* does, thereby contaminating the observation with non-AGN emission and altering the spectral shape. Figure 7.11 overplots the observations, and it is clear to see that long wavelength emission is not in accordance between the two data sets. We therefore must dismiss the *Spitzer* analysis of this

source, as we are sampling more than just the AGN emission that the high-resolution ground-based observations are assumed to measure.

NGC 2992 – See Figure A.3h.

Like some of the Seyfert 1s, this source has a strong emission peak near $18 \mu\text{m}$ which inhibits the torus models from describing it. Comparing the ground-based observations with those of *Spitzer*, the N-band spectroscopy and Q-band photometric point agree, alluding that similar emission is gathered in both observations. However, the fall-off of long wavelength emission makes it difficult for the torus models to describe the data.

NGC 5506 – See Figure A.3i.

The *Spitzer* spectrum of this source is uncharacteristic of an AGN. The extremely deep absorption feature at $10 \mu\text{m}$ ($S_{10} = -0.67$) is itself difficult for the clumpy torus models to explain as they do not produce strong absorption features. There tends to be an ULIRG-type spectral shape for this source with strong $10 \mu\text{m}$ absorption with a minimal $18 \mu\text{m}$ feature. This deep absorption is not reflected in ground-based photometry, but upon assessing N-band spectroscopy, it is evident that deep absorption is prevalent even at small spatial scales. For this reason, we believe this source has extinction along the line of sight.

NGC 5728 – See Figure A.3j.

This type 2 source has a unique spectral shape that cannot be explained at all by the torus models. We immediately dismiss this source from our *Spitzer* analysis since the dominant contributor to the original flux was star formation (65%).

NGC 7582 – See Figure A.3k.

Also with an unique spectral shape, we dismiss NGC7582 from our *Spitzer* study since we find in our ground-based study that extended emission contaminates the total emission even for small spatial scales. This is in agreement with Ramos Almeida

et al. (2009) who find the clumpy torus fits to ground-based photometry unreliable.

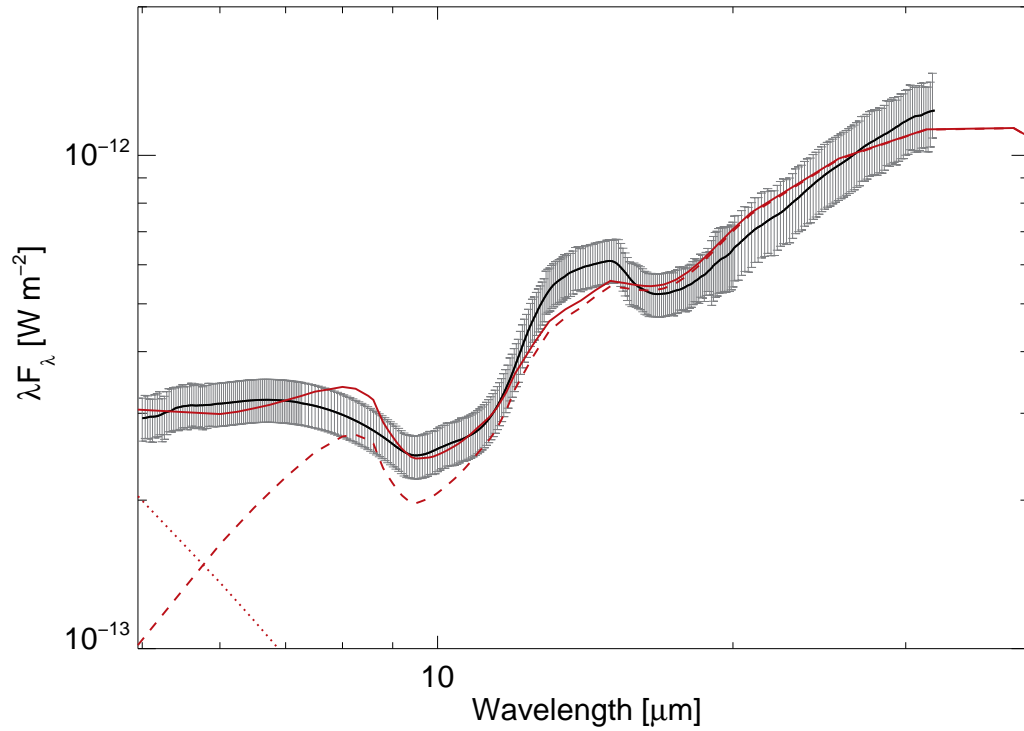


Figure A.3a The *Spitzer* spectrum of Seyfert 1 Mrk 231 (black with gray error bars) is fit by a 2-component (torus-dash and blackbody-dot) model whose goodness-of-fit $\chi_R^2 = 0.47$. Since this value exceeds the limit of $\chi_R^2 = 0.25$, we exclude it in the analysis of the overall sample.

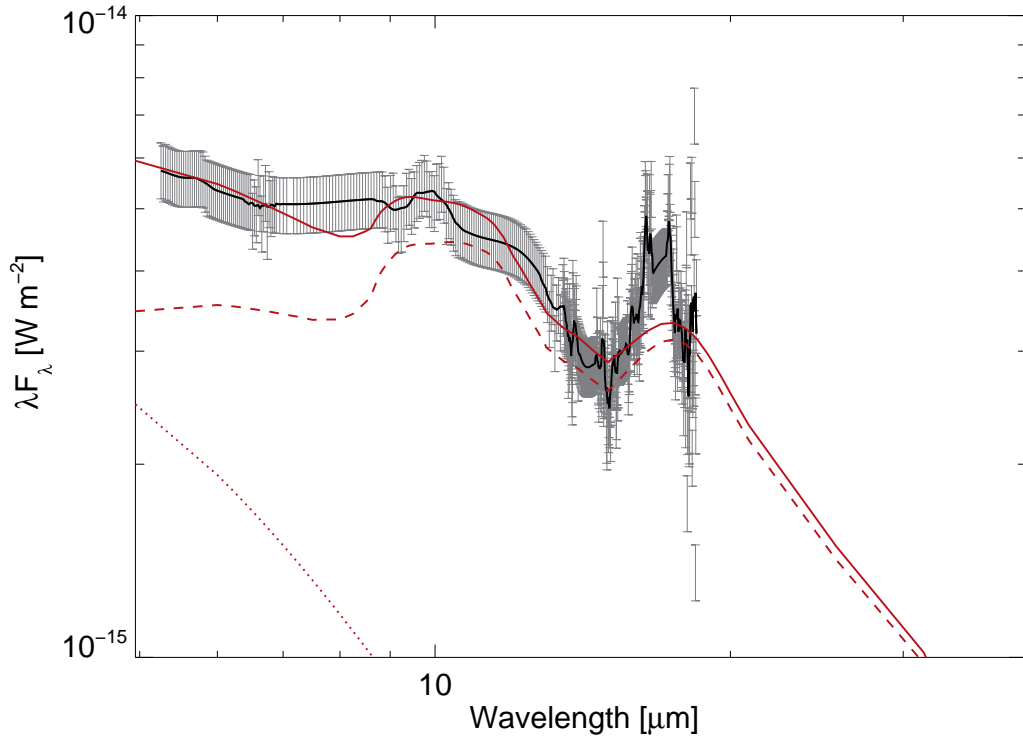


Figure A.3b Same as Figure A.3a but for Mrk 507. $\chi_R^2 = 2.38$.

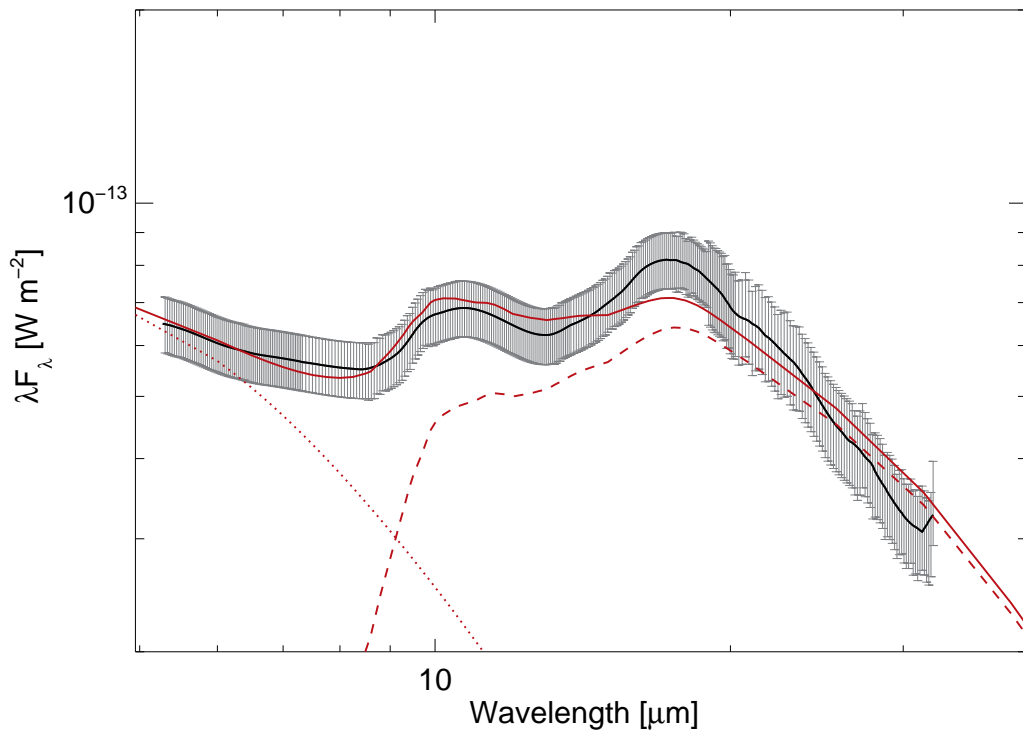


Figure A.3c Same as Figure A.3a but for Mrk 509. $\chi_R^2 = 0.39$.

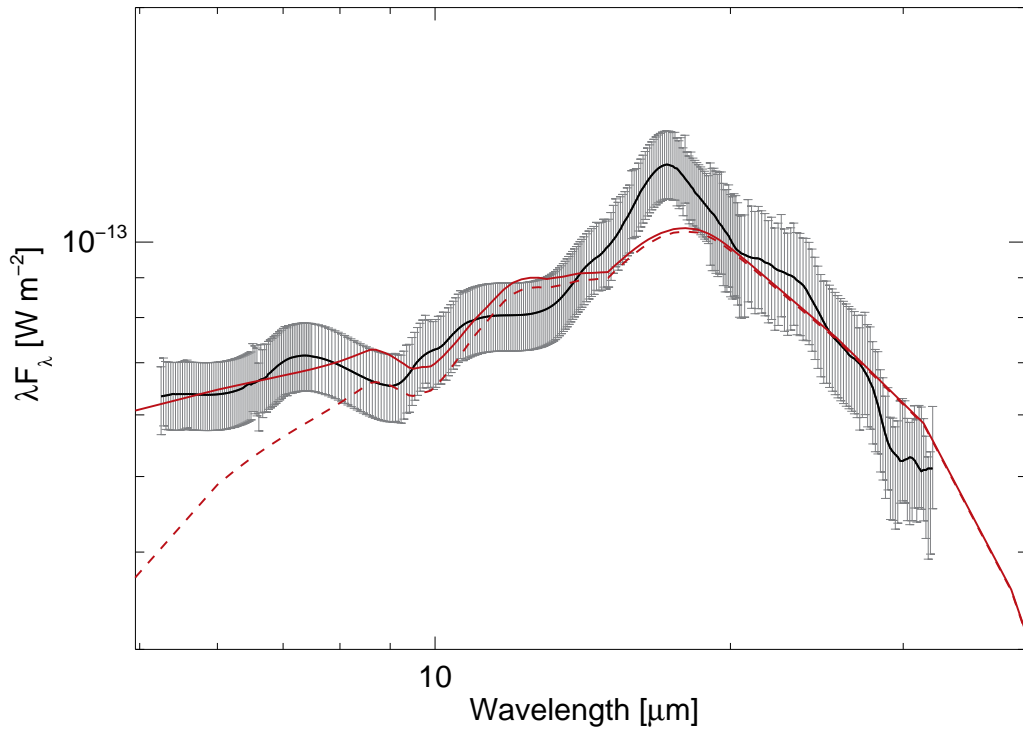


Figure A.3d Same as Figure A.3a but for NGC 3227. $\chi_R^2 = 0.57$.

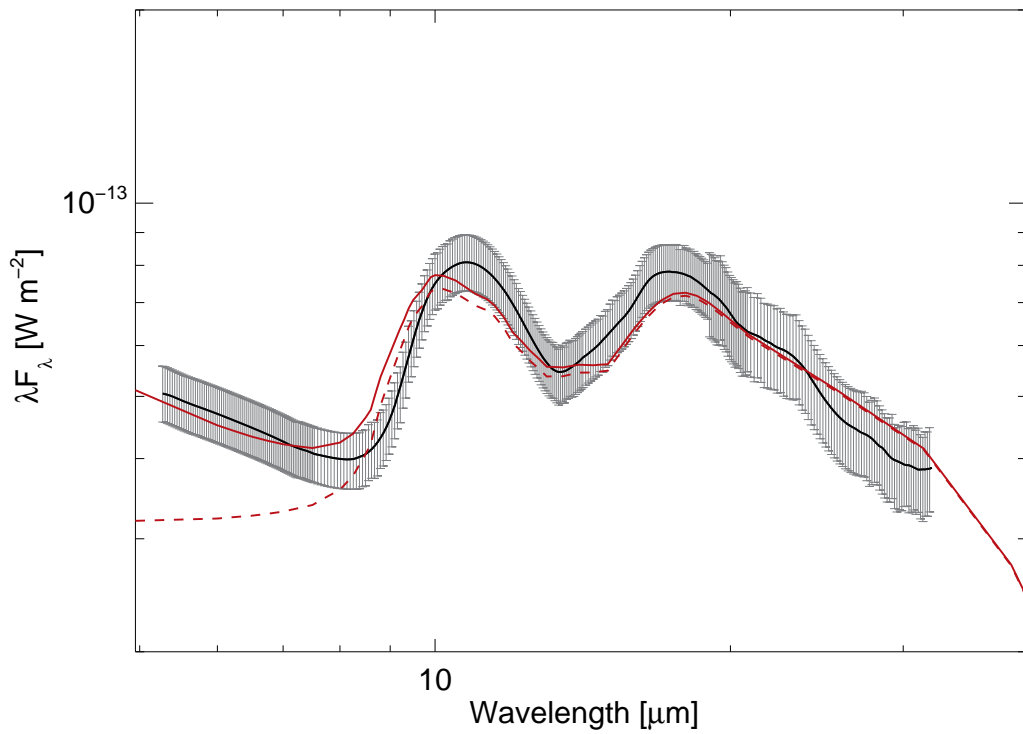


Figure A.3e Same as Figure A.3a but for NGC 7213. $\chi_R^2 = 0.62$.

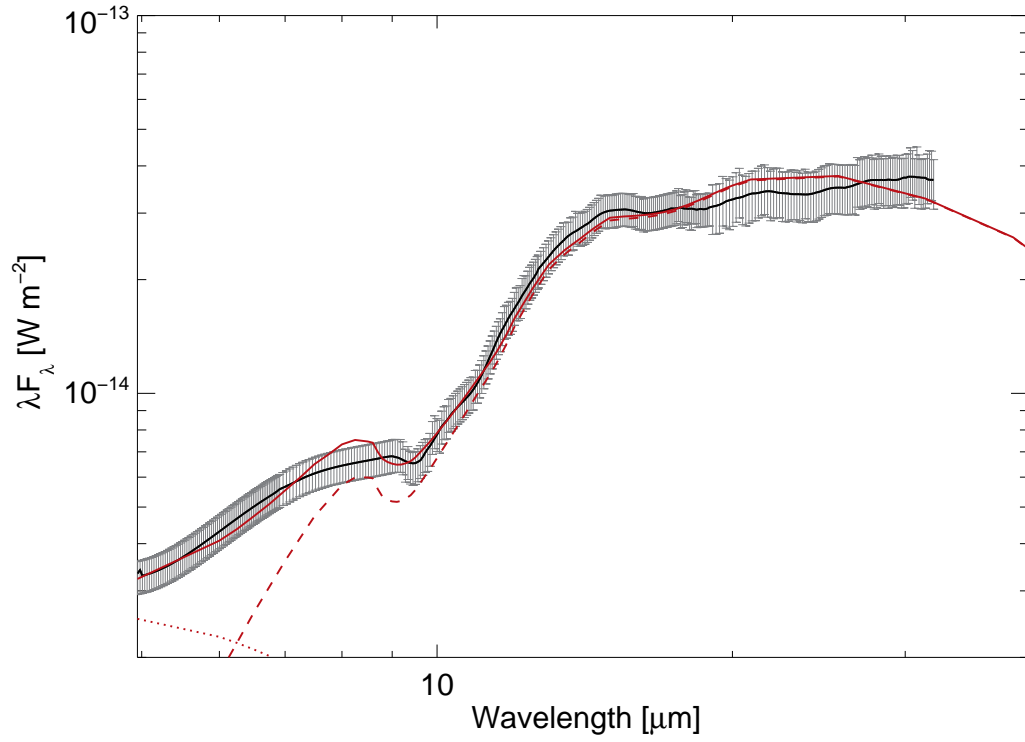


Figure A.3f Same as Figure A.3a but for 3C321. $\chi_R^2 = 0.40$.

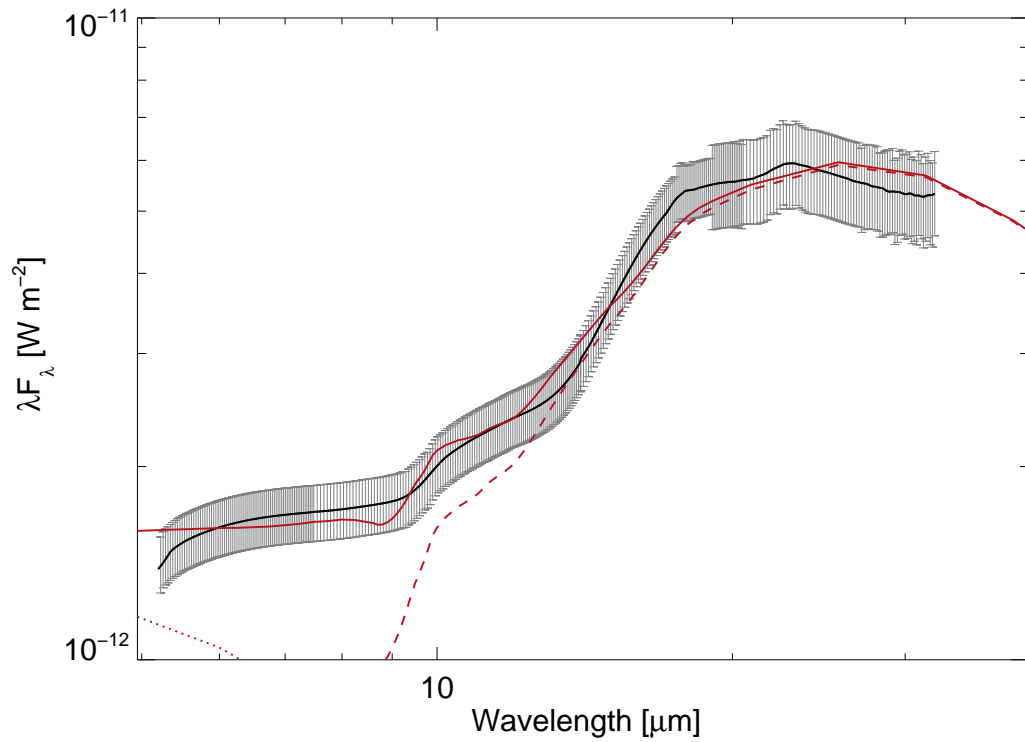


Figure A.3g Same as Figure A.3a but for NGC 1068. $\chi_R^2 = 0.27$.

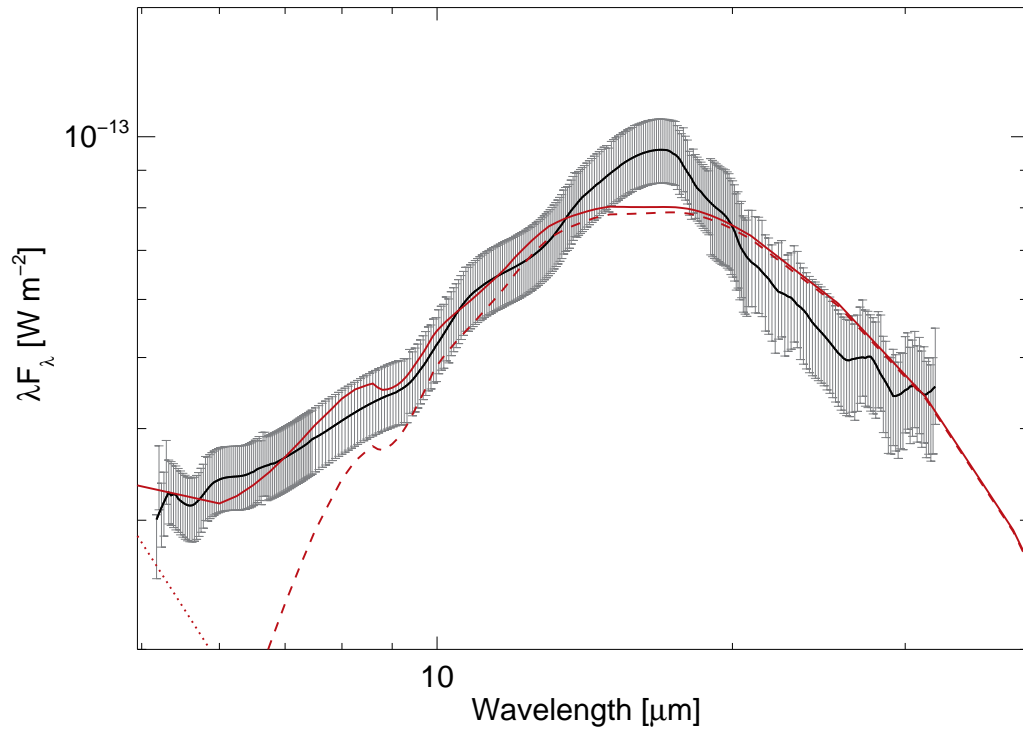


Figure A.3h Same as Figure A.3a but for NGC 2992. $\chi_R^2 = 0.51$.

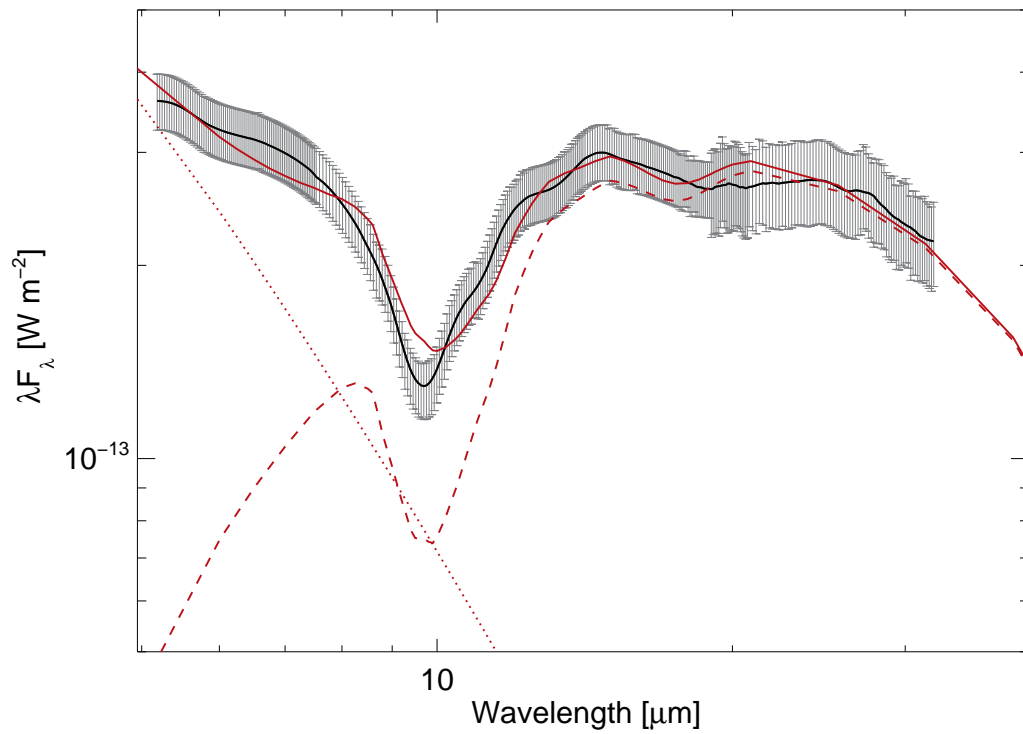


Figure A.3i Same as Figure A.3a but for NGC 5506. $\chi_R^2 = 0.40$.

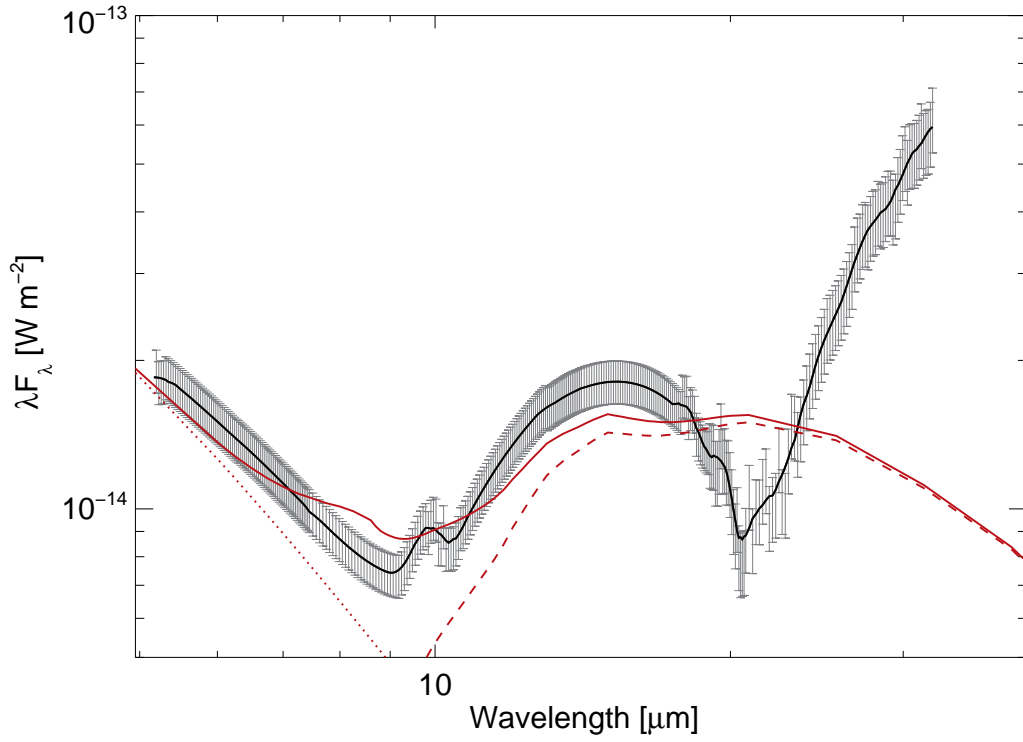


Figure A.3j Same as Figure A.3a but for NGC 5728. $\chi_R^2 = 5.06$.

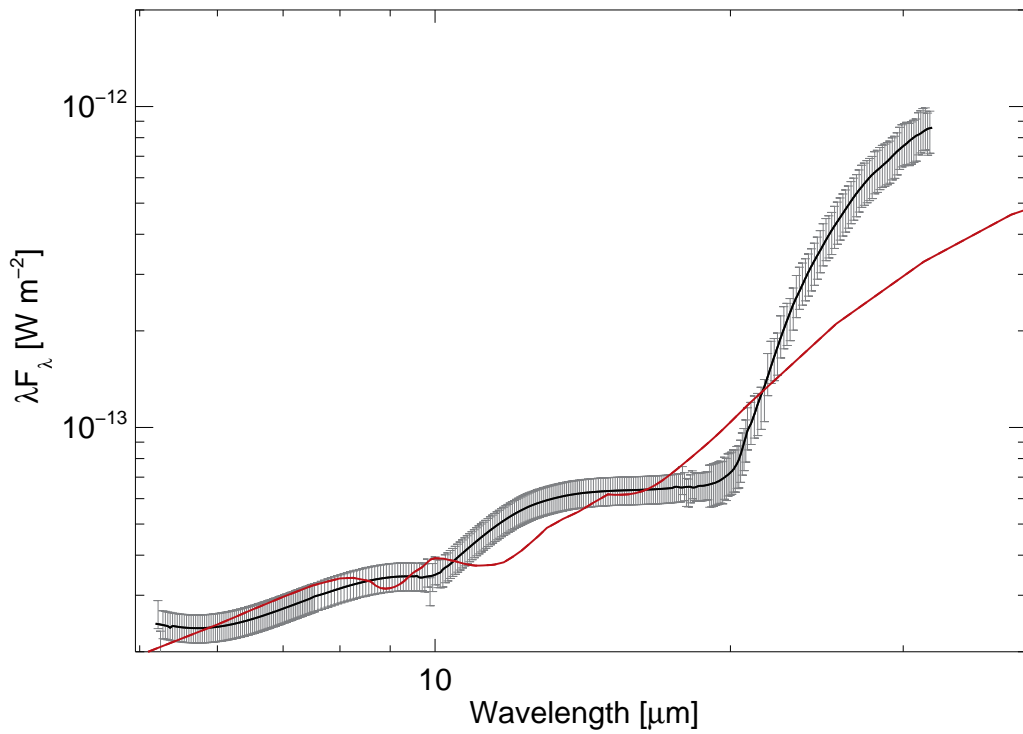


Figure A.3k Same as Figure A.3a but for NGC 7582. $\chi_R^2 = 4.02$.

Bibliography

- Alonso-Herrero, A., Quillen, A. C., Simpson, C., Efstathiou, A., & Ward, M. J. 2001, *AJ*, 121, 136
- Alonso-Herrero, A., Quillen, A. C., Rieke, G. H., Ivanov, V. D., & Efstathiou, A. 2003, *AJ*, 126, 81
- Alonso-Herrero, A., et al. 2006, *ApJ*, 640, 167
- Alonso-Herrero, A., Colina, L., Packham, C., Díaz-Santos, T., Rieke, G. H., Radomski, J. T., & Telesco, C. M. 2006, *ApJ*, 652, L83
- Alonso-Herrero, A., Ramas Almedia, C., Mason, R., Asensio Ramos, A., Roche, P. F., Levenson, N. A., Elitzur, M., Packham, C., Rodriguez Espinosa, J. M., Young, S., Díaz-Santos, T., & Pérez-García, A., M. 2011, *ApJ*, 736, 82
- Antonucci, R. R. J. 1983, *Nature*, 303, 158
- Antonucci, R. R. J. 1984, *ApJ*, 278, 499
- Antonucci, R. 1993, *ARA&A*, 31, 473
- Antonucci, R., & Miller, J. 1985, *ApJ*, 297, 621
- Asensio Ramos, A., & Ramos Almeida, C. 2009, *ApJ*, 696, 2075
- Bailey, J., Axon, D. J., Hough, J. H., Ward, M. J., McLean, I., & Heathcote, S. R. 1988, *MNRAS*, 234, 899
- Barmby, P., et al. 2006, *ApJ*, 642, 126
- Beckert, T., Driebe, T., Hönig, S. F., & Weigelt, G. 2008, *A&A*, 486, 17
- Brightman, M. & Nandra, K. 2011, *MNRAS*, 414, 3084
- Brindle, C., Hough, J. H., Bailey, J. A., Axon, D. J., Ward, M. J., Sparks, W. B., & McLean, I. S. 1990, *MNRAS*, 244, 577
- Buchanan, C. L., Gallimore, J. F., O’Dea, C. P., Baum, S. A., Axon, D. J., Robinson, A., Elitzur, M., & Elvis, M. 2006, *AJ*, 132, 401
- Burtscher, L., Jaffe, W., Raban, D., Meisenheimer, K., Tristram, K. R. W., & Röttgering, H. 2009, *ApJ*, 705, L53
- Draine, B. T. 2003a, *ApJ*, 598, 1017
- Draine, B. T. 2003b, *ApJ*, 598, 1026

- Drain, B. T. & Li, A. 2007, ApJ, 657, 810
- Efstathiou, A., & Rowan-Robinson, M. 1995, MNRAS, 273, 649
- Elvis, M., et al. 1994, ApJS, 95, 1
- Elvis, M., Risaliti, G., Nicastro, F., Miller, J. M., Fiore, F., & Puccetti, S. 2004, ApJ, 615, L25
- Fritz, J., Franceschini, A., & Hatziminaoglou, E. 2006, MNRAS, 366, 767
- Gandhi, P., Horst, H., Smette, A., Hönig, S., Comastri, A., Gilli, R., Vignali, C., & Duschl, W. 2009, A&A, 502, 457
- Genzel, R., et al. 1998, ApJ, 498, 579
- Gillett, F. C., Kleinmann, D. E., Wright, E. L., & Capps, R. W. 1975, ApJ, 198, L65
- Glasse, A. C., Atad-Ettedgui, D. I., & Harris, J. W. 1997, Proc. SPIE, 2871, 1197
- Goodrich, R. W., & Miller, J. S. 1994, ApJ, 434, 82
- Granato, G. L., & Danese, L. 1994, MNRAS, 268, 235
- Granato, G. L., Danese, L., & Franceschini, A. 1997, ApJ, 486, 147
- Gu, Q., & Huang, J. 2002, ApJ, 579, 205
- Hao, L., et al. 2005, ApJ, 625, 75
- Hao, L., Weedman, D. W., Spoon, H. W. W., Marshall, J. A., Levenson, N. A., Elitzur, M., & Houck, J. R. 2007, ApJ, 655, 77
- Ho, L. C., & Keto, E. 2007, ApJ, 658, 314
- Hönig, S. F., Beckert, T., Ohnaka, K., & Weigelt, G. 2006, A&A, 452, 459
- Hönig, S. F., Smette, A., Beckert, T., Horst, H., Duschl, W., Gandhi, P., Kishimoto, M., & Weigelt, G. 2008, A&A, 485, 21
- Hönig, S. F. & Kishimoto, M. 2010, A&A, 523, 27
- Horst, H., Smette, A., Gandhi, P., & Duschl, W. J. 2006, A&A, 457, 17
- Houck, J. R., et al. 2004, ApJS, 154, 18
- Inglis, M. D., Brindle, C., Hough, J. H., Young, S., Axon, D. J., Bailey, J. A., & Ward, M. J. 1993, MNRAS, 263, 895
- Inglis, M. D., Young, S., Hough, J. H., Gledhill, T., Axon, D. J., Bailey, J. A., & Ward, M. J. 1995, MNRAS, 275, 398

- Ivezić, Z. & Elitzur, M. 1997, MNRAS, 287, 799
- Ivezić, Z., Nenkova, M., & Elitzur, M. 1999, User Manual for DUSTY Univ. of Kentucky Internal Report (arXiv:astro-ph/9910475)
- Jaffe, W., et al. 2004, Nature, 429, 47
- Keremedjiev, M., Hao, L., & Charmandaris, V. 2008, arXiv:0806.2910.
- Klaas, U., et al. 2001, A&A, 379, 823
- Kleinmann, D. E., Gillett, F. C. & Wright, E. L. 1976, ApJ, 208, 42
- Knacke, R. F., & Thomson, R. K. 1973, PASP, 85, 341
- Krolik, J. H., & Begelman, M. C. 1988, ApJ, 329, 702
- LaMassa, S. M., Heckmann, T. M., Ptak, A., Martins, L., Wild, V., Sonnentrucker, P., & Hornschemeier, A. 2011, ApJ, 729, 52
- Levenson, N. A., Sirocky, M. M., Hao, L., Spoon, H. W. W., Marshal, J. A., Elitzur, M., & Houck, J. R. 2007, ApJ, 654, 45
- Levenson, N. A., Radomski, J. T., Packham, C., Mason, R. E., Schaefer, J. J., & Telesco, C. M. 2009, ApJ, 703, 390
- Lutz, D., Sturm, E., Genzel, R., Spoon, H. W. W., Moorwood, A. F. M., Netzer, H., & Sternberg, A. 2003, A&A, 409, 867
- Lutz, D., Maiolino, R., Spoon, H. W. W., & Moorwood, A. F. M. 2004, A&A, 418, 465
- Mason, R. E., Geballe, T. R., Packham, C., Levenson, N. A., Elitzur, M., Fisher, R. S., & Perlman, E. 2006, ApJ, 640, 612
- Mason, R. E., Levenson, N. A., Shi, Y., Packham, C., Gorjian, V., Cleary, K., Rhee, J., & Werner, M. 2009, ApJ, 693, L136
- Mathis, J. S., Rumpl, W., & Nordsieck, K. H. 1977, ApJ, 217, 425
- Meléndez, M., et al. 2008, ApJ, 682, 94
- Meisenheimer, K., et al. 2007 A&A, 471, 453
- Miller, J., Goodrich, R., & Mathews, W. 1991, ApJ, 378, 477
- Mor, R., Netzer, H., & Elitzur, M. 2009, ApJ, 705, 298
- Nandra, K. & Iwasawa, K. 2007, MNRAS, 382, 1
- Nenkova, M., Ivezić, Ž., & Elitzur, M. 2002, ApJ, 570, 9

- Nenkova, M., Sirocky, M. M., Ivezić, Ž., & Elitzur, M. 2008a, ApJ, 685, 147
- Nenkova, M., Sirocky, M. M., Nikutta, R., Ivezić, Ž., & Elitzur, M. 2008b, 685, 160
- Netzer, H., et al. 2007, ApJ, 666,806
- Nikutta, R., Elitzur, M., & Lacy, M. 2009, ApJ, 705, 1550
- Nikutta, R., et al. 2012, in preparation
- Ossenkopf, V., Henning, T., & Mathis, J. S. 1992, A&A, 261, 567
- Packham, C., Radomski, J. T., Roche, P. F., Aitken, D. K., Perlman, E., Alonso-Herrero, A., Coline, L., & Telesco, C. M. 2005, ApJ, 618, L17
- Pier, E. A., & Krolik, J. H. 1992, ApJ, 401, 99
- Prieto, M. A., Reunanen, J., Tristram, K. R. W., Neumayer, N., Fernandez-Ontivero, J. A., Orienti, M., & Meisenheimer, K. 2010, MNRAS, 402, 724
- Polletta, M., et al. 2007, ApJ, 663, 81
- Raban, D., Jaffe, W., Röttgering, H., Meisenheimer, K., & Tristram, K. 2009, MNRAS, 394, 1325
- Radomski, J. T., et al. 2003, ApJ, 587, 117
- Radomski, J. T., et al. 2008, ApJ, 681, 141
- Ramos Almedia, D., et al. 2009, ApJ, 702, 1127
- Ramos Almedia, D., et al. 2011, ApJ, 731, 92
- Richards, G. T., Lacy, M., Storrie-Lombardi, L. J., Hall, P. B., Gallagher, S. C., Hines, D. C., Fan, X., Papovich, C., Vanden Berk, D. E., Trammell, G. B., Schneider, D. P., Vestergaard, M., York, D. G., Jester, S., Anderson, S. F., Budavári, T., & Szalay, A. S. 2006, ApJ, 166, 470
- Rieke, G. H. & Low, F. J. 1975a, ApJ, 197, 17
- Rieke, G. H. & Low, F. J. 1975b, ApJ, 199, L13
- Risaliti, G., Elvis, M., Fabbiano, G., Baldi, A., Zezas, A., & Salvati, M. 2007, ApJ, 659, L111
- Risaliti, G. & Elvis, M. 2004, in Supermassive Black Holes in the Distant Universe, ed. A. J. Barger (Dordrecht: Kluwer), 308, 187
- Roche, P. F., et al. 2001, MNRAS, 248, 606
- Roche, P. F., Packham, C., Telesco, C. M., Radomski, J. T., Alonso-Herrero, A., Aitken, D. K., Colina, L., & Perlman, E. 2006, MNRAS, 367, 1689

- Rush, B., Malkan, M. A., & Spinoglio, L. 1993, *ApJS*, 89, 1
- Sanders, D. B., & Mirabel, I. F. 1996, *ARA&A*, 34, 749
- Sani, E., Lutz, D., Risaliti, G., Netzer, H., Gallo, L. C., Trakhtenbrot, B., Sturm, E., & Boller, T. 2010, *MNRAS*, 403, 1246
- Sargsyan, L., Weedman, D., Lebouteiller, V., Houck, J., Barry, D., Hovhannisyan, A., & Mickaelian, A. 2011, *ApJ*, 730, 19
- Schartmann, M., Meisenheimer, K., Camenzind, M., Wolf, S., Tristram, K. R. W., & Henning, T. 2008, *A&A*, 482, 67
- Schmitt, H. R., Antonucci, R. R. J., Ulvestad, J. S., Kinney, A. L., Clarke, C. J., & Pringle, J. E. 2001, *ApJ*, 555, 663
- Schweitzer, M., et al. 2006, *ApJ*, 649, 79
- Schweitzer, M., et al. 2008, *ApJ*, 679, 101
- Shi, Y., et al. 2006, *ApJ*, 653, 127
- Siebenmorgen, R., Krügel, E., & Spoon, H. W. W. 2004, *A&A*, 414, 123
- Siebenmorgen, R., Haas, M., Krügel, E., & Schulz, B. 2005, *A&A*, 436, 5
- Singh, V., Shastri, P., & Risaliti, G. 2011, *A&A*, 533, 128
- Sirocky, M. M, Levenson, N. A., Elitzur, M., Spoon, H. W. W., & Armus, L. 2008, *ApJ*, 678, 729
- Smith, J. E., Young, S., Robinson, A., Corbett, E. A., Giannuzzo, M. E., Axon, D. J., & Hough, J. H. 2002, *MNRAS*, 335, 773
- Smith, J. E., Robinson, A., Alexander, D. M., Young, S., Axon, D. J., & Corbett, E. A. 2004, *MNRAS*, 350, 140
- Smith, J. E., Robinson, A., Young, S., Axon, D. J., & Corbett, E. A. 2005, *MNRAS*, 359, 846
- Smith, J. D. T., Draine, B. T., Dale, D. A., et al. 2007 *ApJ*, 656, 770
- Soifer, B. T., et al. 2000, *AJ*, 119, 509
- Spoon, H. W. W., Keane, J. V., Cami, J., Lahuis, F., Tielens, A. G. G. M., Armus, L., & Charmandaris, V. 2005, in *IAU Symp. 231, Astrochemistry: Recent Successes and Current Challenges*, ed. D. C. Lis, G. A. Blake, & E. Herbst (Cambridge: Cambridge Univ. Press), 281
- Sturm, E., Lutz, D., Tran, D., Feuchtgruber, H., Genzel, R., Kunze, D., Moorwood, A. F. M., & Thornley, M. D. 2000, *A&A*, 358, 481

- Sturm, E., et al. 2005, ApJ, 629, 21
- Sturm, E., Hasinger, G., Lehmann, I., Mainieri, V., Genzel, R., Lehnert, M. D., Lutz, D., & Tacconi, L. J. 2006, ApJ, 642, 81
- Telesco, C. M., Pina, R. K., Hanna, K. T., Julian, J. A., Hon, D. B., & Kisko, T. M. 1998, Proc. SPIE, 3354, 534
- Teplitz, H. I., et al. 2006, ApJ, 638, 1
- Thompson, G. D., Levenson, N. A., Uddin, S. A., & Sirocky, M. M. 2009, ApJ, 697, 182
- Tran, H. D. 2003, ApJ, 583, 632
- Tristram, K. R. W., et al. 2007, A&A, 474, 837
- Tristram, K. R. W., et al. 2009, A&A, 502, 67
- Trumpler, R.J. 1930, PASP, 42, 214
- van Bemmell, I. M., & Dullemond, C. P. 2003, A&A, 404, 1
- Vasudevan, R. V., Fabian, A. C., Gandhi, P., Winter, L. M., & Mushotzky, R. E. 2010, MNRAS, 402, 1081
- Verma, A., et al. 2003, A&A, 403, 829
- Winter L. M., Veilleux S., McKernan, B., Kallman, T. R. 2012, ApJ, 745, 107
- Werner, M. W., et al. 2004, ApJS, 154, 1
- Woo, J.-H., & Urry, C. M. 2002, ApJ, 579, 530
- Wu, Y., Charmandaris, V., Huang, J., Spinoglio, L., & Tommasin, S. 2009, ApJ, 701, 658
- Young, S., Hough, J. H., Axon, D. J., Bailey, J. A., & Ward, M. J. 1995, MNRAS, 272, 513
- Young, S., Hough, J. H., Efstathiou, A., Wills, B. J., Bailey, J. A., Ward, M. J., & Axon, D. J. 1996, MNRAS, 281, 1206
- Young, S., Corbett, E. A., Giannuzzo, M. E., Hough, J. H., Robinson, A., Bailey, J. A., & Axon, D. J. 1999, MNRAS, 303, 227
- Yuan, T.-T., Kewley, L. J., & Sanders, D. B. 2010, ApJ, 709, 884

VITA

Grant David Thompson

- **Date and place of birth:**

- March 12, 1984; Kirksville, Missouri

- **Educational institutions attended and degrees awarded:**

- M.S. in Physics & Astronomy, University of Kentucky, 2009

- B.S. in Physics & Astronomy, University of Missouri, 2005

- **Professional positions held:**

- Instructor, University of Kentucky, 2010-2012

- Research Assistant, University of Kentucky, 2009-2012

- Research Assistant, University of Kentucky, 2007-2009

- Research Assistant, University of Missouri, 2005-2006

- **Scholastic and professional honors:**

- Summa Cum Laude, University of Missouri, 2005

- Valedictorian, Kirksville Senior High School, Kirksville, Missouri 2002

- American Astronomical Society, member

- **Professional publications**

- **Thompson, G. D.**, Levenson, N. A., Uddin, S. A., and Sirocky, M. M., 2009, “Dust Emission from Unobscured Active Galactic Nuclei,” *Astrophysical Journal*, 697, 182.

- Speck, A. K., Corman, A. B., Wakeman, K., Wheeler, C. H., and **Thompson, G. D.**, 2009, “Silicon Carbide Absorption Features: Dust Formation in the Outflows of Extreme Carbon Stars,” *Astrophysical Journal*, 691, 1202.

- **Thompson, G. D.**, Corman, A. B., Speck, A. K., and Dijkstra, C., 2006, “Challenging the Carbon Star Dust Condensation Sequence: Anarchist C Stars,” *Astrophysical Journal*, 652, 1654.

- Speck, A. K., **Thompson, G. D.**, and Hofmeister, A. M., 2005, “The Effect of Stellar Evolution on SiC Dust Grain Sizes,” *Astrophysical Journal*, 634, 426.